EXPERIMENTAL STUDIES OF FLOW THROUGH DEFORMABLE SILICONE AND TISSUE ENGINEERED VALVES

A DISSERTATION
SUBMITTED TO THE FACULTY OF THE GRADUATE SCHOOL
OF THE UNIVERSITY OF MINNESOTA
BY

Devesh M. Amatya

IN PARTIAL FULFILLMENT OF THE REQUIREMENTS
FOR THE DEGREE OF
DOCTOR OF PHILOSPHY

Ellen K. Longmire, Advisor

December, 2009

Acknowledgements

In my 29 years of pursuit for higher knowledge, I am truly indebted to my mother who gave me the inspiration that even though I am behind at the start I will finish ahead. As a child coming to a foreign country, I spoke very little very little English. As a result, I could not reap the full benefits of a public school system in my beginning year. I would come home daily crying. So, my mother decided to take her time off from the pursuit of the American dream to make sure I would not jeopardize mine. She taught me English daily until I felt comfortable to speak English in public. One day I said 'It is hard to bok.' referring to my book bag. This sentence was a combination of English and Nepali, my native language. This sentence was neither correct grammatically nor in the same language; however, this statement symbolizes that I was confident enough to communicate my thoughts, and most importantly, the audience understood it. I hope the reader of this manuscript, regardless of the academic background, is able to understand the little bit of knowledge I imparted.

My mother took me through the symbolic path of knowledge, but I had many important mentors in my life that advised and educated me and I hope to follow in their footsteps. Professor, Dr. Ellen Longmire, my latest influential mentor and research advisor, Department of Aerospace Engineering & Mechanics at the University of Minnesota, has steered me in the last four years to become a meticulous researcher. Professor Longmire challenged my reasonings at times and supported my arguments when appropriate. Under her guidance, I have learned the nuisances of the research community and am greatly indebted to her for any future success in my academic career. I would also like to acknowledge Professor of Biomedical Engineering at the University of Minnesota, Dr. Victor Barocas, for temporarily taking me in as a surrogate graduate student. He took me under his wings as a fresh inexperienced researcher, instilled in me the faith that I had the ability to conduct doctoral research. Even though my niche was destined for experimental research under Professor Longmire, I am truly privileged to say I had the great opportunity to be advised in my graduate studies by these two leading researchers in the respective areas. Finally, I would like to acknowledge my undergraduate advisors Dr. Susan Blanchard and Dr. Peter Mente, former Professor and Professor, respectively at North Carolina State University, who inspired me to pursue my doctoral degree.

Finally I would equally like to thank other mentors and research committee members, my research colleagues and lab/shop technicians, academic sponsors, friends, and family who have been supportive educationally, financially, and emotionally through both the rough and the smooth times. It would be inappropriate for me to overlook my father's contribution as just family, because I know, he as a doctoral researcher/scientist, not only encouraged me to this path, but will also be the first one to read this manuscript. My father is by far the most dedicated researcher I have ever come across. According to my mother, he is sometimes guilty of putting research priorities over family and friends. I hope to carry his work ethic, but carry it realizing that being well-educated means more than just being the best in your field, it also means understanding every aspect of life to the best of your ability.

Abstract

Annually, approximately 250,000 repair/replacement heart valve surgeries are performed world-wide. Currently the two options available for valve replacement are mechanical or bioprosthetic valves. Thrombosis (blood clots) and embolic events (movement of the clots through the blood vessels) have been linked with the mechanical valves, so that life-long anticoagulant therapy is required. Deterioration of the structural integrity, in part due to calcification, has been linked with bioprosthetic valves. The current paradigm is to replace a living, but incompetent valve with a non-living valve, be it mechanical or biological prosthetic. A living prosthetic valve grown with patient donor-based tissue engineering paradigm may be a possible solution.

The primary objective of this study was to characterize the *in vitro* performance of the tissue engineered valve equivalents in a cardiovascular pulse duplicator and assess their potential for clinical use as valve replacement prostheses. A second objective was to conduct experiments under different flow conditions with synthetic silicone polymer valves of various geometries and materials similar in mechanical properties to those of the valve equivalents that are more amenable to experimental measurements of velocity and structural deformation using two-dimensional particle image velocimetry of high spatial resolution, three-dimensional velocimetry of volumetric measurements, and hot film anemometry of high temporal resolution. These measurements are needed to validate computational codes incorporating fluid-structure interaction and may be applied towards tissue engineered heart valve design and optimization.

All of the silicone materials tested showed a neo-Hookean material response at engineering strains less than 0.5. The silicone linear elastic modulus was similar in order to the values measured in native aortic valve leaflets. The diaphragm valves with an orifice deformed to a concave shape with respect to the upstream flow for both steady and pulsatile flow conditions, along with orifice expansion at increasing flow rates. The orifice expansion (up to 75% increase in area) led to reduced pressure drops as compared with non-expanding or rigid diaphragm valves. A jet with significant inward radial velocity was present immediately downstream of the deformed diaphragm valves for both steady and pulsatile flows. This inward flow was associated with vena contracta. For low Reynolds number, laminar steady upstream flow conditions, the diaphragm valve supported the formation of relatively large scale vortices with passage frequency of St = 0.34. For pulsating flow, a leading vortex ring followed by a trailing jet was present during forward flow acceleration. Phase-averaged velocity measurements show lower fluctuations during the acceleration phase than during the deceleration phase of the flow.

The deformation of the transparent bileaflet silicone valve in the pulsating flow showed leaflets deforming in similar concave state with respect to the upstream forward flow of systole and towards the lower pressures during diastole. The bileaflet silicone valve showed asymmetry in root deformation and a slot-like elliptical jet flow profile through the leaflets unlike the circular profile of the diaphragm valve. Downstream flow stagnation and recirculation were present during systole and areas of recirculation were present both upstream and downstream. These flow features were less organized for the latter during diastole.

The tissue engineered valve equivalents harvested after development in the bioreactor and placed within a rigid housing were able to withstand pressures of ~50 mmHg, pressure drops of ~40 mmHg, and flow rates of ~25 L/min throughout the loading of the right ventricular cardiac cycle. The temporal pressures and flow signatures replicated right physiological conditions. The flow downstream indicated an elliptical jet during systole similar to the bileaflet silicone valve. The locations of tissue engineered valve equivalent failures were at the leaflet commissure and Dacron cuff-valve root interface.

Table of Contents

List of Tables

List of Figures

Nomenclature

Latin symbols

2L	Bileaflet valve tissue engineered valve equivalent
3L	Trileaflet valve tissue engineered valve equivalent
ALE	Arbitrary Lagrangian Eulerian
AV	Aortic Valve
C2C	Commissure to commissure plane
CCD	Charged couple diode
CPD	Cardiovascular pulse duplicator
C_d	Discharge coefficient
c	V3V particle triplet centroid
D	Pipe, diaphragm valve, silicone or tissue engineered valve root diameter
D_o	Jet orifice diameter
D_R	Diameter of the leading vortex ring
DV	Diaphragm valve
Def	Velocity gradient tensor
d	Diaphragm valve orifice diameter
dP	Pressure drop
d_{eff}	Diaphragm valve effective orifice diameter
d_g	Distance between two velocity vectors
d_s	Half the distance between two velocity vectors
Eu	Euler number
FSI	Fluid structure interaction
f	Frequency
G1	Generation one tissue engineered valve
G2	Generation two tissue engineered valve
I	Vortex ring impulse
$I_{1,2,3}$	Tensor invariants
K	Velocity gradient

L	Piston stroke length
LC	Laminar upstream flow compliant diaphragm
LED	Light emitting diode
LR	Laminar upstream flow rigid diaphragm
M	PIV magnification factor
MV	Mechanical valve
P, p	Pressure
PIV	Particle image velocimetry
PV	Pulmonary valve
pC2C	Plane perpendicular to commissures
Q	Volumetric flow rate
Q_{avg}	Time average flow rate
Re	Reynolds Number
R	Cross correlation intensity function
RMS	root mean squared
r	Radial direction polar coordinate
St	Strouhal number
SV	Silicone valve
s	Engineering stress
TC	Turbulent upstream flow complaint diaphragm
TR	Turbulent upstream flow rigid diaphragm
T	Time
$\overline{U}$	Time averaged velocity
U	Mean streamwise velocity, Cartesian and cylindrical coordinates
U_{avg}	Average velocity based time-averaged volumetric flow rate and flow diameter
U_{bulk}	Upstream bulk velocity measured by the flow meter
U_c	Jet centerline velocity
U_m	Maximum jet velocity
U_o	Jet exit velocity
u	Instantaneous streamwise velocity, Cartesian and cylindrical coordinates
u_{rms}	u velocity root mean square fluctuations

V	Mean Spanwise velocity, Cartesian and cylindrical coordinates
V3V	Volumetric 3-component velocimetry
VE	Tissue engineered valve equivalent
VIA	Ventricular impedance chamber
v	Instantaneous spanwise velocity, Cartesian and cylindrical coordinates
v_{rms}	v velocity root mean square fluctuations
x,X	Streamwise direction Cartesian and cylindrical coordinates
y,Y	Spanwise direction Cartesian coordinate, V3V planar measurement
Zi	Arterial impedance
z	Spanwise direction Cartesian coordinate, V3V depth measurement
zcomp	Complex roots

Greek symbols

α	Womersley number
θ	Phase angle
φ	Phase
Γ	Circulation
Δ	Discriminant
ρ	Density
η	Dynamic viscosity
γ	Kinematic viscosity
μ	Shear modulus
ε	Engineering strain
λ	Laser wavelength
δ	Uncertainty
ω	Vorticity
τ	Principal shear stress
τ_{max}	Maximum principal shear stress
σ^2	Signal variance

Chapter One: Introduction

1.1 Motivation

Congenital defects, aging or structural wear, and pathological reasons may lead to the requirement for mitral or aortic human heart valve replacement. Annually, approximately 250,000 repair/replacement heart valve surgeries are performed world-wide (Liao et al., 2008). Currently the two options available for valve replacement are mechanical or bioprosthetic based. Different types of prosthetic valves have been clinically utilized for more than 50 years since the first implant done by Charles Hufnagel at the University of Minnesota in 1952. The choice of mechanical or bioprosthetic is mostly patient specific and is at the discretion of the cardiovascular surgeon. Unfortunately, neither valve can truly replicate the native valve, and the 10 year mortality after replacement is 30-55%. Thrombosis (blood clots) and embolic events (movement of the clots through the blood vessels) have been linked with the mechanical valves, so that life-long anticoagulant therapy is required. Deterioration of the structural integrity, in part due to calcification, has been linked with bioprosthetic valves. The current paradigm is to replace a living, but incompetent valve with a non-living valve, be it mechanical or biological prosthetic.

A living prosthetic valve may be a possible solution. The idea is to have a quasi-autologous (patient donor cells) living valve, which is able to grow and remodel under physiological conditions. The rationale is that an autologous valve would not require anticoagulant therapy, and the valve would be capable of remodeling under physiological loading conditions, thus less likely to have structural failure. The novel living prosthetic valves which could be grown in a laboratory setting and implantable in patients are herein identified as tissue-engineered valve equivalents (VE). The potential of having a VE as an option for implant is gaining great interest in the cardiovascular community. The Tranquillo Laboratory at the University of Minnesota is currently growing and harvesting VEs of fibrin based constructs seeded with human dermal fibroblasts (Robinson et al., 2008, Syedain et al., 2008). With the tissue-engineered approach, it is still critical that

the living form of the VEs should not limit its intended function. The VE should allow uni-directional blood flow with similar flow characteristics as native valves, while maintaining its structural integrity throughout the lifetime of the implant.

Before any bioprosthesis can be deemed implantable in patients, it must go though rigorous testing protocols. For the VE, it is reasonable to expect both the form and function to be similar to that of the native valve. The current work will focus mainly on validating the VE function and the reader is directed to literature detailing the form of the VE (Robinson et al., 2008, Syedain et al., 2008). The function of the valve can be tested experimentally on a bench-top or clinically with animal and human studies. A thorough bench-top, *in vitro* performance of the VE will be evaluated in this dissertation. However, clinical tests are not the scope of the current work.

Another area of research conducted in this dissertation is the experimental study of fluid and structure interaction. Fluid structure interactions (FSI) occur in a range of engineering problems. For example, the macro-scale flows resulting in aerodynamic flutter of wings and transient loads on bridges and buildings to micro-scale flows through MEMS devices such as silicone pressure sensors and Ahmed valves used to maintain intraocular pressure for glaucoma patients are the flow scales incorporating FSI. Computational modeling of fluid structure interaction is a developing field and the accuracy of these models is important in predicting structural failure modes. The diversity in FSI and the importance of accurate computational models being noted, the focus of the current dissertation will be towards experimental cardiovascular valve-type flows conducted to validate computational in-house code.

There is great interest in understanding the role of FSI in cardiovascular flows. Within the human heart, the pulsatile trans-mitral flow results in mitral valve annulus displacement (Kheradvar and Gharib, 2007). Additionally, the various valve leaflets open and close over 3 billion times during their lifespan under the pulsatile flow interaction. The dynamics of FSI may even differ from valve to valve. For example, the mitral valve opens passively as a result of the flow and is held closed actively by the parachute-like strings of the chordae tendineae. The aortic valve both opens and closes passively as a result of the flow. Note that the active expansion and contraction of the heart is also coupled with the valve dynamics.

Accurately-modeled computational works can be used as a predictive method to gain insight into the performance of the VEs, which may otherwise be limited by strictly experimental trials. There is a need to validate the accuracy of the different computational methods by appropriate experimental studies. For example, the valve leaflets encounter large deformations and strains as a result of the blood flow. The ability of computational models to capture accurately these flow induced large deformations is still a challenge. These large deformations may lead to valve failure. Additionally, the computational accuracy in capturing the dominant and secondary structures in the flow with respect to size and duration is important. These flow dynamics may have direct physiological implications such as blood cell damage. An ideal experiment to validate the computational methods would be *in vivo* measurements of fluid structure interaction of clinical valve implants. However, computational methods incorporating macro and micro structural tissue mechanics along with flow interactions have not advanced far enough to capture fully the true valve dynamics. Additionally, clinical data of the prototype valves may not be practical with respect to cost and the measurement techniques may be limited in resolving the complete flow and structural dynamics. Simple *in vitro* experiments with quantifiable valve material and deformation along with the flow dynamics might be sufficient to validate the merit of the current computational fluid structure interaction models.

1.2 Previous Work

This section first reviews the native and prosthetic heart valve hemodynamics. Second, the progress in computational and experimental FSI studies with a focus on heart valve flows will be discussed. Third, the well-studied dynamics of quasi-steady and pulsatile jet flows representative of heart valve flow dynamics will be introduced.

1.2.1 Valve Hemodynamics

The human heart has four valves that allow unidirectional flow of oxygenated and de-oxygenated blood to the peripheral vasculature and lungs, respectively (see Fig. 1-1 for anatomy and nomenclature used throughout this manuscript). A proportionally large volume of literature has been focused on the aortic valve, followed by the mitral valve,

and to a lesser extent the tricuspid and pulmonary valves. The focus of this manuscript will be introducing the aortic valve hemodynamics, because the ultimate intent of the VEs is to function as replacements for malfunctioning native aortic valves. The hemodynamics of the native pulmonary valve will also be introduced because the VEs will also be tested in the pulmonary position.

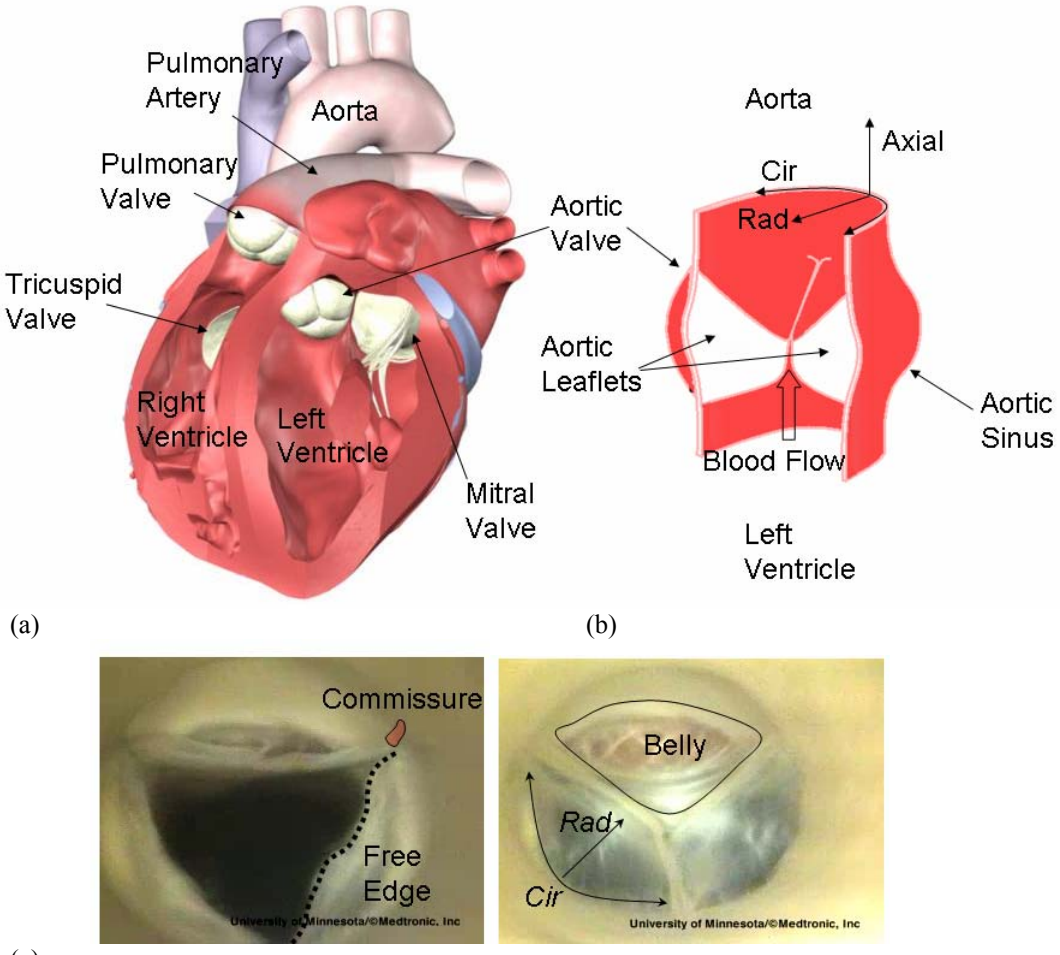

Figure 1-1. (a) Heart anatomy modified from Atlas of Human Cardiac Anatomy, University of Minnesota (b) Cut-away of the aortic root. Two of the three aortic leaflets and sinuses are shown, a polar coordinate system indicating the axial, rad. = radial, and cir. = circumferential directions are shown along with the axial flow of blood from the left ventricle to the aorta (c) Close-up of the porcine aortic valve leaflets from aortic view, left: open (systole) and right: closed (diastole). Commissure, intersection of the two leaflets on the root wall; belly, the non-coapting surfaces of the leaflet; Images obtained from the Visible Heart Project®, University of Minnesota. http://www.vhlab.umn.edu/

1.2.1.1 Native Aortic Valves

The aortic valve is situated between the aorta and left ventricle. A competent aortic heart valve ensures unidirectional blood flow from the left ventricle to the aorta with minimal obstruction and regurgitation (Mirnajafi et al., 2006). The three leaflets of the valve open and close encountering substantial mechanical stress and strain at a rate of approximately once-per-minute or 40 million times a year and 3 billion times over an average lifetime. During diastole (see Fig.1-2), the ventricular filling phase, the closed aortic valve must withstand a pressure gradient across the leaflets of approximately 80mmHg. During this phase, the leaflets are highly stretched and bulge inwards towards the ventricle with surface strains of 10.1% and 30.8% in the circumferential and radial directions, respectively (Thubrikar, 1990). Throughout diastole, leaflets must maintain a complete seal preventing backflow of the blood. At each commissure location, or the intersection of adjacent leaflets contiguous with the sinus (the base of the aorta also referred to as the root), large tensile stresses are encountered (Mirnajafi et al., 2006). *In vitro* biaxial tensile testing results have shown that aortic heart leaflets are in general independent of strain-rate during physiological loading (381 ± 47.2%/s circumferential and 1183.8 ± 51.3%/s radial). The tests also reveal low levels of viscous dissipative effects (hysteresis), negligible creep, but significant directional dependent stress relaxation (Stella et al., 2007). During systole, the contraction of the heart, the aortic valve leaflets open, and the main mode of leaflet deformation is flexure. At the commissure, large bending deformations of the leaflets occur, approximately 65º measured with respect to the closed position of the leaflets (Mirnajafi et al., 2006). The leaflets bulge outwards at the belly in the direction of the aorta where the curvature is reversed from the diastolic state. Additionally, i*n vitro* results show that the aortic root dilates approximately 9% when aortic pressure in the root is increased from 80 mmHg to 120 mmHg during the systolic phase. The expanding sinuses 'pull' at the commissure of the leaflets allowing smooth leaflet opening and minimizing bending. By contrast, in diastole the contracting root 'releases' the leaflets at the commissure. The 'pull-and-release' mechanism is purported to minimize the stresses on the aortic valve leaflets.

During early systole, the opened phase of the aortic valve, a pressure difference of a few millimeters of mercury (i.e., larger ventricular pressure than aortic) rapidly accelerates the flow of blood through the valve. The velocity profile of the blood, as it ascends the aortic arch, is skewed towards the inner wall. Flow rates reach maximum values of 30 L/min (Yoganathan et al., 2004). The peak in streamwise velocity migrates towards the outer wall of the aortic arch during early to mid systole with the flow separation from the wall of the aorta causing retrograde flow. Right-handed helical (non-axial components of velocity reach 29 ± 5 cm/s) flow becomes evident in the ascending aorta according to phase-averaged MRI results (Kilner et al., 1993). During mid to late systole, the flow decelerates at a lower rate than the initial acceleration with helical and reverse flow still present. It is thought that the helical flow may delay flow separation and minimize turbulence (Kilner et al., 1993). Secondary recirculating flows due to adverse pressure gradients are present towards the end of systole at the sinuses downstream of the aortic valve (Kilner et al., 1993, Yoganathan et al., 2004). The recirculating flow at the sinuses aiding in the smooth closure of valve leaflets was first hypothesized during the Renaissance Period by Leonardo da Vinci (1513). This has been empirically and computationally validated by pioneers in heart valve mechanics Bellhouse and Talbot (1969) and Peskin *et al. (1982)*, respectively.

The forces on the macrostructure of the valve described in the previous paragraphs have close synergy with the response in the microstructure at the cellular level. Collagen fibers align in the circumferential loading direction of the leaflet at the onset of diastole when the difference in aortic and ventricular pressure rises from 0 to 4 mmHg. The macro-micro relationship is explained comprehensively by Schoen. If homeostasis or stable internal environment is maintained, where endothelial cells maintain thromboresistance and interstitial cells promote matrix (i.e., collagen fiber) turnover, the valve is competent throughout the lifetime.

There are many factors that may disrupt the homeostasis. Aging and calcification may lead to stiffening of the valve leaflets, resulting in valve stenosis (the narrowing of valve opening). Mechanical factors such as high stresses are thought to potentiate calcification (Thubrikar et al., 1986). A stenotic valve requires higher pressure drops during systole to generate the same amount of forward flow as a non-stenotic valve. The

higher resistance to flow can be temporarily accommodated by ventricular hypertrophy (enlargement) resulting in stronger ventricular contraction. The enlarged heart eventually decreases the cardiac output (amount of blood ejected by the ventricle) and fails. Congenital malformation such as a bi-leaflet valve in place of a trileaflet valve predisposes one to valve stenosis. Pathological conditions such as Myxomatous disease damage the collagen microstructure weakening the leaflets, which may result in valve prolapse (excessive leaflet bulging) and blood regurgitation. Rheumatic fever causes fibrotic thickening, which may make the valve stenotic and regurgitant. Infective endocarditis disease leads to degradation of valve microstructure and potential perforation of valve leaflets making a valve regurgitant. If medical intervention with drug treatment is not sufficient then valve repair or replacement surgery can improve a patient's quality of life and may even be life-saving.

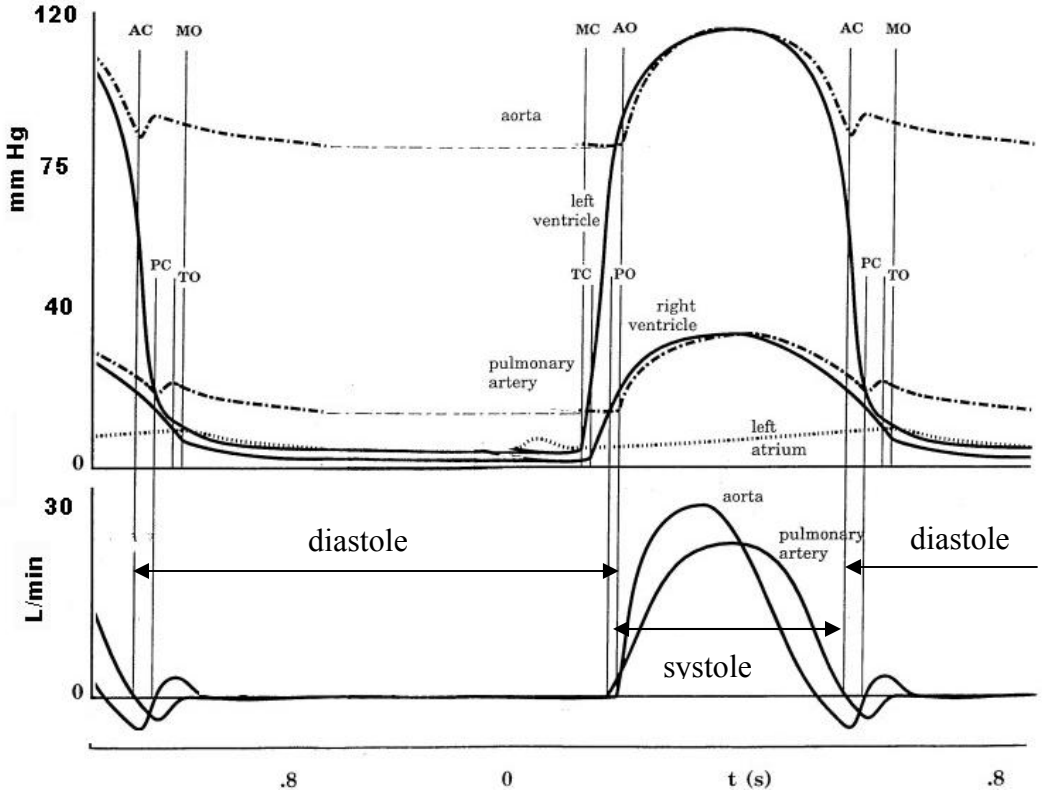

Figure 1-2. Representative cardiac cycle for aortic and pulmonary blood flow. AC: aortic valve close, PC: pulmonary valve close, MO: mitral valve open, TO: tricuspid valve open, TC: tricuspid valve close, MC: mitral valve close, AO: aortic valve open, and PO: pulmonary valve open. http://www.bg.ic.ac.uk/

1.2.1.2 Native Pulmonary Valves

The pulmonary valve is a tri-leaflet valve that allows unidirectional deoxygenated blood flow from the right ventricle into the pulmonary artery. Pulmonary valves have been shown to have similar tensile properties as that of aortic valves (Stradins et al., 2004). These valves function at much lower pressure loading conditions than aortic valves. However, the pressure and flow time signatures are similar in profile to that of aortic valves shown in Fig. 1-2. The peak systolic pressure reaches approximately 35 mmHg. The pulmonary artery pressure is maintained at approximately 10-15 mmHg during diastole. The peak streamwise velocities during systole reach 75 ± 15 cm/s (Weyman, 1994) and clockwise rotation of the peak velocity location downstream of the pulmonary valve has been noted during ventricular ejection (Sloth et al., 1994). The peak velocities and corresponding peak flow rates are lower than for the range aortic valves (71 to 143 cm/s) because of the larger diameter of the pulmonary artery and pulmonary valve as compared with the aortic counterparts. Also, the duration of the pulmonary ejection period is longer within the pulmonary artery to maintain the same time averaged flow rates (Nichols and O'Rourke, 2005). The failure of pulmonary valves is not as common as aortic valves; however, failures through calcification, stenosis, and pathological conditions still occur.

1.2.1.3 Replacement Valves

It is well established in the literature that the current options in aortic and mitral heart valve replacement prosthesis introduce unwanted hemodynamics effects in the case of mechanical valves (see Fig. 1-3a for a representative mechanical valve) and have limited lifetime in the case of the bioprosthetic valves (see Fig. 1-3b for a representative bioprosthetic valve). This leads to re-operation or death within 10 years postoperatively in a large percentage of patients with both of these types of replacement valve. However, the driving force in the clinical application of these valves for over 50 years has been the native valve-like hemodynamic function in the case of bioprosthetic valves and the durability of the mechanical valves. Note that allograft (human donor) and autograft in the Ross Procedure (native pulmonary valve replaces the malfunctioning aortic valve) both fall under the bioprosthetic valve category. The former is limited in donor supply

and the latter still requires a bioprosthetic valve in the pulmonary position to replace the harvested native pulmonary valve. The following paragraphs describe the more commonly implanted mechanical and animal-donor based bioprosthetic valves.

The current generation of mechanical heart valves can be classified into the tilting disc, bileaflet prosthesis, and the lesser used caged ball. The St. Jude Medical (SJM) Regent bileaflet, the most commonly used (Fig 1-3a), is constructed of pyrolytic carbon, which has excellent durability. The same material is also used for other mechanical valves currently on the market. Each of the two leaflets rotates about a hinge and has an opening angle of 85º under minimal mean systolic pressure drops of 9 mmHg. In practice, the flow through all of these mechanical valves may cause thrombo-emboli or be limited by thrombotic occlusions. Therefore, a valve recipient must undergo anticoagulant therapy throughout his/her lifetime. Anticoagulant therapy results in high risk of hemorrhage. Other concerns with these valves mentioned in recent literature are hemolysis and cavitation (Herbertson et al., 2008, Rambod et al., 2007). It is important to introduce a brief history of the experimental hemodynamic studies of the mechanical valve and elaborate on the potential links between the mechanical valve and adverse hemodynamic physiological response. A comprehensive history of prosthetic valves is given by Zilla *et al. (2008).*

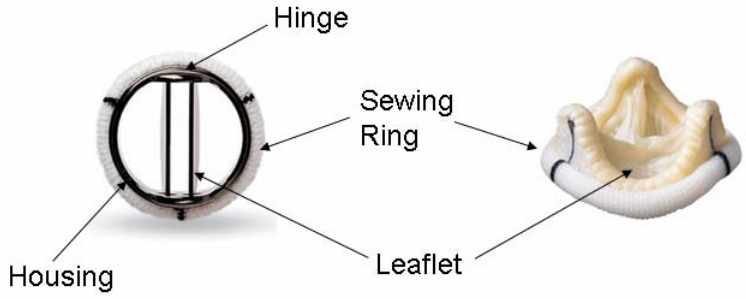

(a) (b)

Figure 1-3. Replacement heart valves: (a) replacement St. Jude Regent bileaflet mechanical valve (b) replacement St. Jude Medical Biocor pericardial trileaflet valve.

Early hemodynamic studies (late 1960s to early 1970s) of replacement heart valves were performed in *in vitro* cardiovascular pulse duplicators (CPD), and the prosthetic valve performance was assessed by bulk pressure drop and flow performance such as valve opening area and regurgitant volume. In the late 1970s and 1980s, replacement valve flow fields were visualized by illuminating tracer particles with a laser source highlighting vortices shed by the valve leaflets (Chandran et al., 1983, Gross et al., 1988). More quantitative velocity measurements were obtained using laser Doppler velocimetry (Yoganathan and Corcoran, 1979) and hot-film anemometry (Swope and Falsetti, 1976). Stein and Sabbah (1976) were first to obtain *in vivo* velocity measurements using hot-film anemometer probes. In the early 90s, particle image velocimetry (PIV) gained popularity in quantifying prosthetic valve flow fields with seminal works conducted by Lim *et al. (1994)*. Currently, three-dimensional high spatial resolution (Leo et al., 2006) and high temporal resolution PIV measurements (Pierrakos et al., 2004) give better insight into *in vitro* hemodynamics. MRI (Kilner et al., 1993) and ultrasound measurement (Travis et al., 2004) techniques in the clinical setting give insight into *in vivo* hemodynamics, but could use further improvement in resolution and accuracy. Additionally, developing computational work with replacement heart valves is a powerful tool for investigating the hemodynamics (Carmody et al., 2006, Cheng et al., 2003, de Hart et al., 2003, Ge et al., 2008, Peskin and McQueen, 1989).

Thrombosis is a physiological response to platelet activation. It results in clot formation and may lead to embolism, which is the movement of these clots in the blood stream. The thrombosis may block blood supply to the coronary vessels and peripheral organs, and this is the most serious complication of mechanical valves. Tilting disc valves are prone to thrombus formation in the smaller opening outflow and hinge regions (Bluestein et al., 2000). Thrombus formation in bileaflet valves occurs primarily at the hinge of the leaflets (Simon et al., 2007). The putative hemodynamic factor leading to thrombus formation is high shearing flow between the hinge and the valve housing, which activates platelets and leads to thrombus formation in areas of prolonged flow residence time such as in possible stasis or recirculation zones within valve sinuses. However, the exact value of the shear stress required to activate platelets as cited in literature varies by almost 4 orders of magnitude. Brown *et al.* (1975) cite a peak shear

stress of 10 N/m^2 for 300 seconds, a well accepted value. Bernstein *et al.* (1977) cite a peak shear stress of 1E5 N/m^2 for 0.002 seconds. A compilation of the various data collected is presented in the shear stress-exposure time plot of Fig. 1-4. Essentially, the longer duration of shear stress exposure on platelets correspond with a lower threshold of shear stress required to activate platelets and vise versa. Experimental and computational results have shown that the shearing stresses downstream of the St. Jude Medical Regent bileaflet valve may be sufficient to induce platelet damage (Ge et al., 2008). The hinge region is characterized by unsteady flow, vortex structures, and stagnation zones where platelets are subjected to long duration of shearing stresses. Higher magnitude of shear stress can be expected during backward flow of blood through the hinge gaps. Dumont *et al.*'s (2007) work with a laminar computational model indicates that the shear stresses are sufficient for platelet activation at the hinge region. Simon *et al. (2007)* spatial-temporal hinge flow analysis of a 'Lagrangian-type' model accounts for platelet shear stress exposure time. The findings indicate that the shear stresses measured do not meet the threshold for platelet activation or hemolysis (the lysis of red blood cells). Hemolysis threshold can be assumed to be an order of magnitude higher in shear stress levels (between 150 and 400 N/m^2 of exposure time ~ order of minutes) as compared with platelet activation (Ge et al., 2008). This trend is shown in Fig. 1-4.

Cavitation is the rapid formation, growth, and collapse of vapor bubbles due to reduction in static pressure below the vapor pressure of the fluid. This process is thought to induce red blood cell trauma (Herbertson et al., 2008). When cavitation is present, the collapse of the bubbles generates intense shock waves and high-speed reentrant jets leading to surface pitting and erosion on the leaflet and housing of Duromedic heart valves (Kafesjian et al., 1989, Klepetko, 1989). Local pressure oscillations, vortices shed by leaflet tips, and squeeze jets through valve hinges lead to reduction in local pressure and have been hypothesized to induce cavitation. So far cavitation has been documented only upstream (left atrium) of the mechanical valves used in mitral implants (Yoganathan et al., 2004).

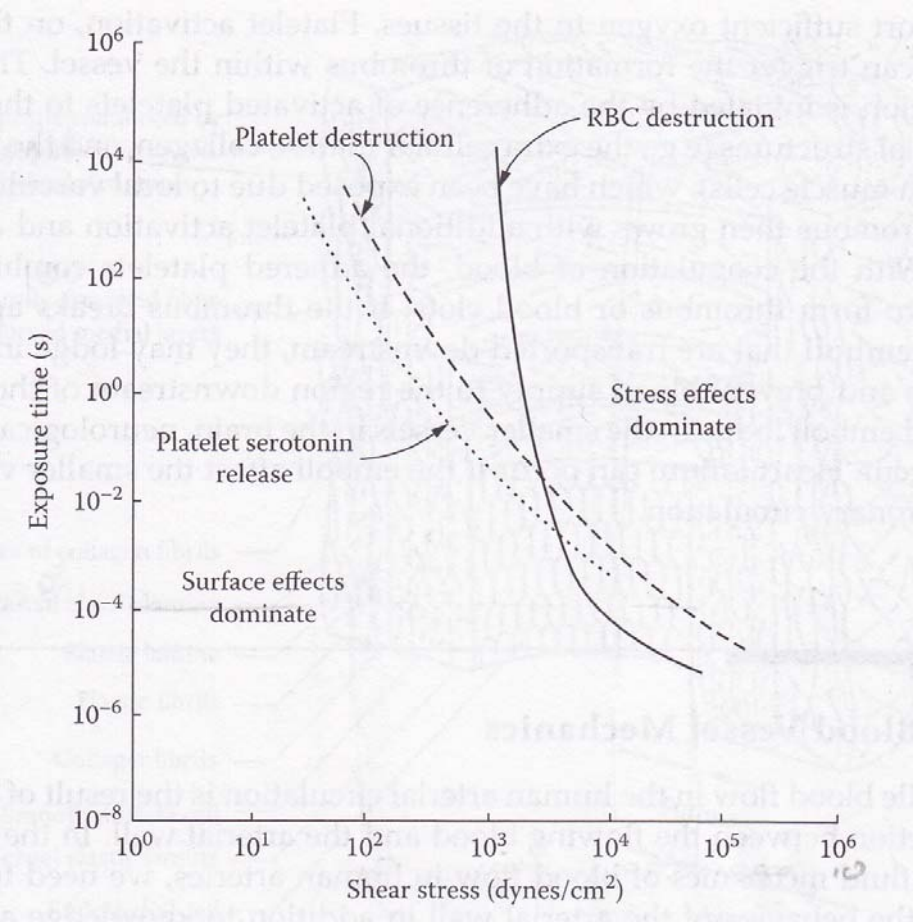

Figure 1-4. Shear stress versus exposure time plots for threshold of hemolysis of red blood cells and destruction of platelets. Chart obtained from Chandran et al. (2007)

Bioprosthetic stented trileaflet valves exhibit higher systolic pressure drops than mechanical or native valves. Non-stented valves offer larger opening area and result in lower pressure drops than stented, but are larger than most mechanical valves. Bioprosthetic valves are chemically treated with glutaraldehyde to reduce immunogenicity. However, the stiffening of the leaflets by the chemical treatment results in smaller than ideal opening area of the valve leaflets. The leaflets may encounter large bending under the larger pressure drops (Zilla et al., 2008). Bioprosthetic valves are also prone to leaflet calcification and non-calcific structural damage. Calcification results in a stenotic valve and eventual structural failure. Calcification is purported to be a physiological response caused by precipitation of calcium-phosphate minerals on predominantly unviable endothelial and interstitial cells after glutaraldehyde fixation

(Schoen, 2008). Additionally, the actual fixation process, or the cross-linking of collagen fiber may promote calcification (Zilla et al., 2008). As with native valves, the calcification process is thought to be accelerated at areas of higher stress (Liao et al., 2008). It is evident that the exact cause of calcification is still debatable, but it occurs more frequently in bioprosthetic valves than in native valves.

1.2.2 Fluid-Structure Interaction

Fluid-structure interaction is described to underscore the importance of experimental validation of the various nascent computational schemes used for heart valve flow simulations. Flows around and through flexible and deformable structures and vessels occur frequently in both industrial and physiological applications. Often, these flows are extremely complicated to model theoretically or computationally. For example, human heart valves are complex in shape, material, and dynamics, which has been described in the Section 1.2.1. As mentioned earlier, the thin leaflets flex and strain significantly and coapt under loading of large pressure drops. The flow through the valves is typically unsteady and three-dimensional, including flow reversal, three-dimensional separation and vortex formation and shedding (Yoganathan et al., 2005). All of these complexities are challenging to model individually, let alone collectively. The linking theme is that the movement of the structure affects the flow of the fluid and the flow of the fluid affects the movement of the structure. More specifically, the inherent interaction between the flowing blood (generalized as a fluid continuum) and the valve (generalized as the deformable solid structure) requires coupling of the conservation of mass and momentum equations of fluids and solids. The solids equation must account for inhomogeneity, anisotropy, and non-linear material and geometric deformations of the three-dimensional valve. Meanwhile, the nonlinear Navier-Stokes equations must handle variations in three-dimensional space, including the scales of the flow (i.e., from an inertia dominated central jet to smaller eddies on the periphery) and time (i.e., low frequency of the heart-beat to high passage frequency of small eddies). There is great interest in correctly modeling the FSI incorporating the complexities in the heart valve physiological flow.

Computational schemes incorporating FSI will be discussed briefly to give the state of the art in modeling cardiovascular flows. Early valve simulation works were either fluid-only or solid-only; with the former, the valve was introduced as a rigid body and the governing flow equations were solved (Ge et al., 2003, Ge et al., 2005) and with the latter, the fluid forces were prescribed as the pressure on the moving solid (Kim et al., 2008). Also, there have been attempts to prescribe explicitly the rigid body movement and solve the fluid equations with the updated state of the rigid body (Cheng et al., 2003, Dasi et al., 2007).

In a general sense, computational schemes discretize the flow domain into finite elements or volumes and solve the governing partial differential equations (i.e., Navier-Stokes) at the nodes or intersection of these elements or volumes. In cardiovascular valve flows, FSI requires the coupling of the mass and momentum equations for the solid (heart valve) and fluid (blood). For example, the velocity of the fluid (blood) must match the velocity of the solid (valve leaflets) at the interface throughout the cardiac cycle. The computational challenge arises when the boundary of the flow domain is moving, in the case of an opening valve. Broadly, the two methods implemented to handle a moving interface are the deforming grid and fixed-grid methods (Liu et al., 2009, van Loon et al., 2006). For the deforming grid method, the elements that make up the mesh of the flow domain are moving with the solid interface in time, also referred to as Arbitrary Lagrangian Eulerian method (ALE). However, with large translations and rotations of the solid interface, the mesh becomes strongly distorted, requiring remeshing. Remeshing is computationally costly and information may be lost. For the fixed-grid method, the fluid elements are stationary and the nodal values of velocity for example of the moving solid are coupled to the interpolated fluid velocity at that point. The seminal work with this method was done by Peskin and McQueen (1989) and is referred to as the Immersed Boundary Method.

Carmody et al. (2006) used the arbitrary Lagrangian-Eulerian (ALE) algorithm for a three-dimensional FSI model of an ideal aortic valve as defined by Thubrikar (1986). They compared the spatial and temporal opening/closing of porcine valve leaflets in a pulse duplicator system to their computational results of an idealized aortic valve with three deformable leaflets. They showed good qualitative correspondence, but suggested

that detailed quantitative comparison was inappropriate. Cheng et al. (2003) tracked temporal leaflet position of a rigid mechanical valve simulating a single closing event using a two-dimensional ALE algorithm. They compared the computational and experimental results and showed that the trend in opening angle versus time was similar, but that the computational opening angle lagged in time. They attributed the discrepancy to three-dimensionality in the experiment.

de Hart et al. (2000), using their fictitious domain method, a variation of the Immersed Boundary Method, performed two-dimensional simulations of a flexible leaflet in a rigid sinus cavity under pulsatile flow. For experimental validation, they observed a rectangular rubber (EPDM) sheet mounted within a pulse duplicator system. The sheet exhibited some deflection perpendicular to the viewing plane due to three-dimensional motion in the flow. A thicker, stiffer leaflet yielded motion that was more two-dimensional. The leaflet motion and fluid flow, measured by laser Doppler velocimetry, were predicted well by the simulation. The fluid velocity patterns were similar for both computational and experimental cases with the exception of a secondary vortex near the leaflet fixation point present only in the computational case that was attributed to a mesh refinement issue.

Stijnen et al. (2004) followed up this study by examining a two-dimensional rotating Lexan leaflet. Particle image velocimetry (PIV) was used to determine velocity fields. Once again, the trends in leaflet motion were similar in the experiments and computations. Discrepancies in leaflet motion were attributed to the boundary layer flow near the sidewalls of the experimental set-up, which did not exist in the two-dimensional simulation. The computed and experimental flow patterns were very similar, although some discrepancies resulted from the difference in the valve motion. The same experimental approach was used to validate additional computational simulations of flow through rigid valves (Dumont et al., 2007).

Separately, Ge and Sotiropoulos performed three-dimensional direct numerical simulation on flow through mechanical bileaflet valves using experimental data to prescribe the leaflet kinematics and a variation of the immersed boundary solver (Dasi et al., 2007). They claim that a full non-linear fluid-structure interaction would have to account for friction coefficient at the hinge, which is valve specific and would require

extensive calibration to determine. Borazjani *et a*l. (2007) added FSI to the 3D simulation, but still neglected the hinge mechanisms and matched experimental data reasonably well.

1.2.3 Jet Flows

For the current work, axisymmetric steady and pulsatile incompressible jets having similar flow conditions to those of native and prosthetic heart valves will be discussed. The idea behind the following paragraphs is to introduce the nomenclature and familiarize the reader with the physics of jet flow, which will be used to assess the experiments conducted in this dissertation.

The flow through both native and prosthetic valves is jet-like during systole. Fig 1-5a) shows a velocity vector field obtained by MRI indicating jet-like flow from the left ventricular outflow tract at an oblique viewing plane cutting through the sinuses (Kilner et al., 1993). The flow is from bottom right (left ventricle) to top left (aorta). The vectors in the left ventricle are directed inwards and elongate at the location of the valve. The fluid upstream with significant momentum generated by the contracting heart passes through a confined area such as the valve into an area of much larger cross section such as the aorta resulting in jet-like flow downstream. The recirculating vectors at the periphery of the jet and near the valve occur at the location of the sinuses. This recirculation aids in the smooth closure of the valve leaflets as described in Section 1.2.1.1. Fig. 1-5b shows velocity measurements made during peak systole using stereoscopic PIV one cm and three cm downstream of a Carbomedic bileaflet mechanical valve placed in a rigid tubular housing connected to a cardiovascular pulse duplicator (Kaminsky et al., 2008). There are three distinct jets at z = 1 cm, with the two side jets reaching a higher velocity than the central jet as indicated by the color contour and heights of the peaks. This flow profile is typical for bileaflet mechanical valves. Further downstream at z = 3 cm, the velocity profile has a bimodal distribution. Fig. 1-5c also shows velocity measurements (profile indicating streamwise velocity magnitude and planar velocity gray-scale contour) using stereoscopic PIV five mm downstream of a bovine pericardial valve placed in a rigid tubular housing and connected to a cardiovascular pulse duplicator (Marassi et al., 2004). Unlike the bileaflet mechanical

valve flow, there is only a central jet. It is clear that the jet profiles are influenced by the geometry of the valve and the geometry of the valve boundaries such as the sinuses.

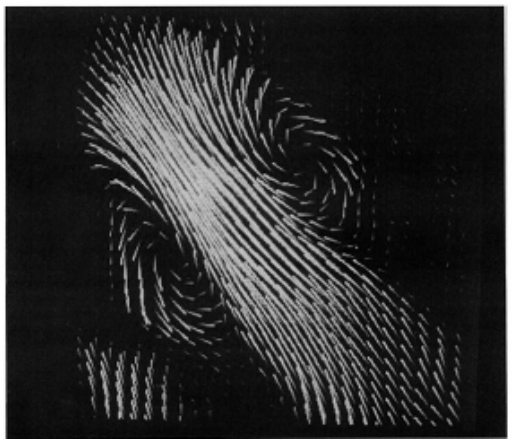

(a)

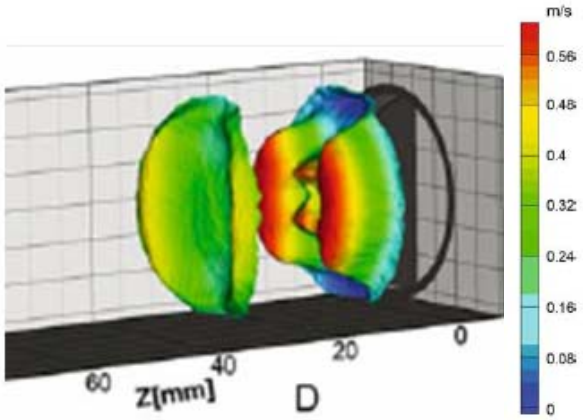

(b)

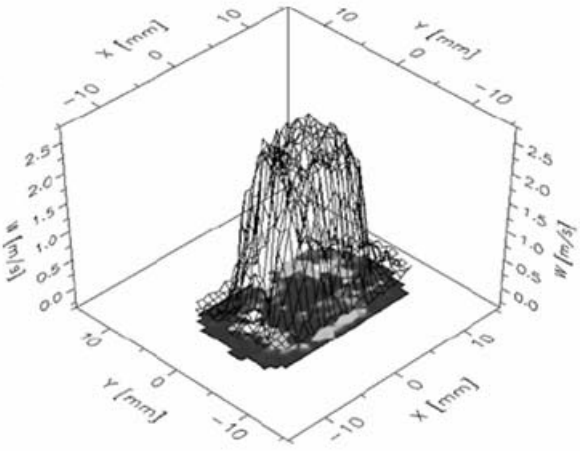

(c)

Figure 1-5. (a) Jet flow velocity vector field through the native aortic valve viewed at the oblique plane of the two sinuses. MRI data obtained from Kilner et al 1993, (b) bimodal side jets with a weaker central jet velocity profile at two streamwise planes downstream of Carbomedic bileaflet mechanical valve *in vitro* stereo-PIV measurements, Kaminsky *et al. 2008,* and (c) central jet streamwise velocity profile with planar velocity contour downstream of a bovine pericardial valve *in vitro* stereo-PIV measurements by Marassi *et al* 2004.

The velocity variation within a jet is influenced by the initial and upstream boundary conditions. The upstream geometry and the type of area contraction can influence the downstream flow. The axisymmetric jet exiting a nozzle (see Fig. 1-6) and entering a stationary ambient fluid has been studied extensively. Within the nozzle, there is a thin layer of fluid called the boundary layer in which the viscosity plays a role. The fluid velocity at the nozzle surface is zero by the no-slip condition. The reduction in diameter through the nozzle leads to an increase in velocity or spatial acceleration of the fluid. The acceleration is proportional to the square of the reduction in flow diameter based on mass conservation. If the contraction is gradual, any separation of the flow from the nozzle surface is less likely. At the nozzle exit, the velocity profile is flat, and the streamwise component of the velocity is U_0. The flat velocity profile defines the diameter of the potential core within which viscous forces are negligible. At the edge of the jet, the velocity drops from peak value to zero along the radial direction (r). This radial distance establishes the initial jet shear layer thickness and is affected by the boundary layer upstream. The linear growth of the shear layer along the streamwise direction (z) is indicated by the average velocity profile becoming more Gaussian. Additionally, the boundary of the shear layer and the surrounding fluid is defined where the streamwise velocity $u \approx 0$. The streamwise distance to the location where the top and bottom shear layers meet, or the location where the centerline velocity changes from U_o defines the length of the jet's potential core. After this streamwise location, the velocity approaches and maintains a self-similar shape.

Fig 1-7 shows a schematic provided by Yule et al. (1978) identifying the instantaneous flow features expected in an axisymmetric jet with Reynolds number >> 1. Reynolds number is defined as the ratio of inertial forces to viscous forces (Re of the jet = jet velocity * jet diameter / kinematic viscosity of the fluid). The instability in the shear layer (Crow and Champagne, 1971) and surrounding disturbances (Moore, 1977) cause the periodic roll up of circumferentially coherent ring vortices. The normalized frequency or Strouhal number (St = frequency * jet diameter / jet velocity) indicating the passage of these coherent vortices is approximately 0.3 in a jet exiting a nozzle (Crow and Champagne, 1971, Danaila et al., 1977).

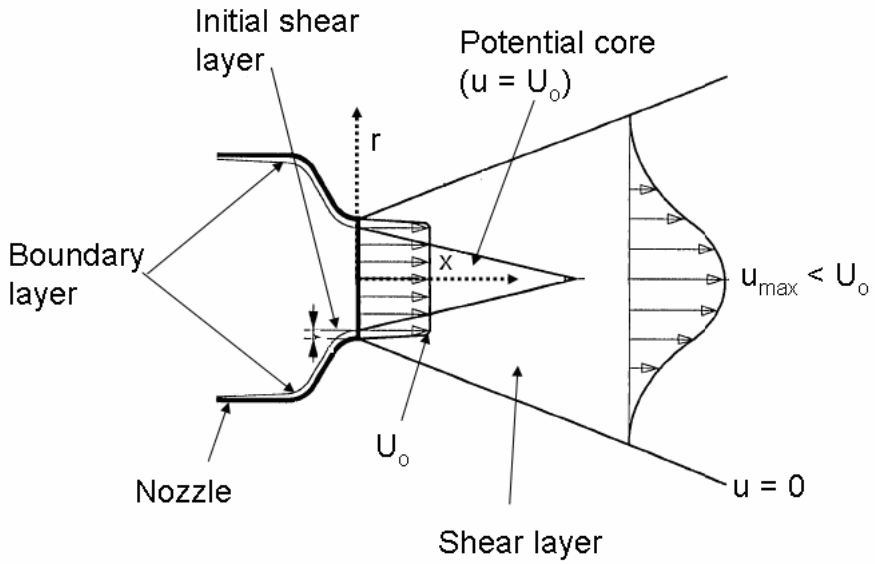

Figure 1-6. Axisymmetric jet exiting a nozzle. Re >> 1. Modified from Bumsoo Han, *Instantaneous Energy Separation in a Jet Flow*, PhD Thesis. 2001

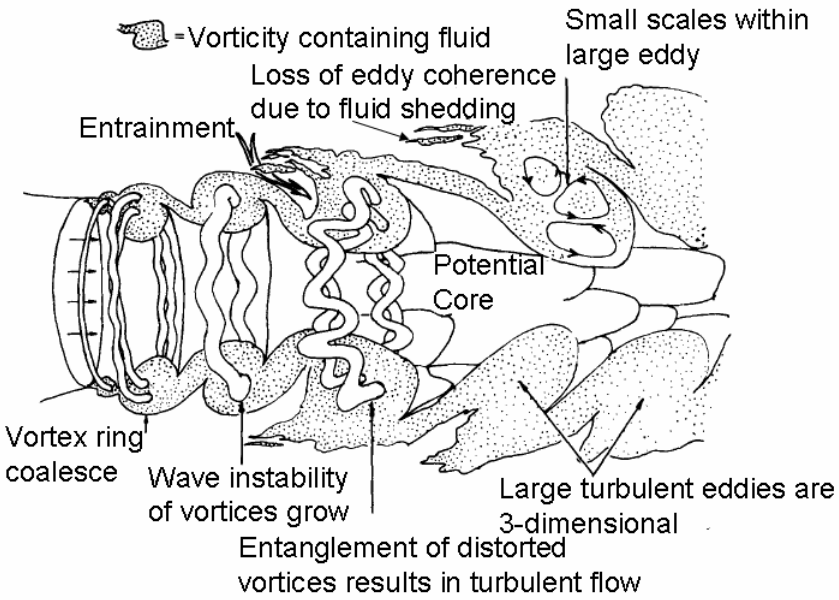

Figure 1-7. Instantaneous flow features of a quasi-steady jet. Reynolds number >> 1. Schematic modified from Yule *et al.* 1978.

The instability, called the Kelvin-Helmholtz instability, is well predicted by the Orr-Sommerfeld linear stability theory (Batchelor and Gill, 1962). The vortices may grow in size as they entrain the surrounding fluid and decrease in spacing as they coalesce with neighboring ones. Three dimensional instabilities as seen in the waviness along the azimuthal direction of the vortex ring can grow and break the symmetry. Additionally, these vortices shed fluid and also engulf smaller eddies (coherent vorticity-containing regions of fluid) in the flow. An early review of jet flows has been done by Abramovich (1963). Han (2001) has summarized the works done by various researchers in current understanding of flow dynamics in a jet.

In the context of cardiovascular flows, pulsating jets are of interest. Gharib *et al.* (Dabiri and Gharib, 2005, Gharib et al., 1998, Kheradvar and Gharib, 2007, Krueger and Gharib, 2003) have done extensive studies on leading vortex rings along with trailing jets generated by starting flows. Using a piston/cylinder arrangement, a starting jet through a nozzle was generated (See Fig. 1-8a). They showed the formation of a leading vortex ring with and without a trailing jet by using flow visualization (See Fig. 1-8b). The vortical structures in the trailing jet are due to Kelvin-Helmholtz instability similar to quasi-steady jets. The flow exiting the nozzle rolls up into a vortex ring when the piston displaces, and grows in size by entraining the ambient irrotational fluid. The strength or circulation of the leading vortex ring is dependent on the vorticity flux provided by the trailing shear layer. The maximum circulation (Γ = area-integrated vorticity) of the leading vortex ring that can be achieved is dependent on the formation number ($\overline{U}T/D_o$), which is equal to the stroke ratio (L/D_o). $\overline{U}$ is the time-averaged velocity, T is the time duration of fluid ejection, D_o is the diameter of the orifice through which the fluid is ejected, and L is length of a column of fluid ejected. The authors have shown that for a stroke ratio $\geq$ approximately 4, the trailing jet is evident. The normalized time (formation number) for maximum circulation of a vortex ring was within the range of 3.6-4.5, beyond which no additional circulation enters the ring and pinch-off from the trailing jet occurs.

Dabiri and Gharib (2005) conducted studies with temporally varying exit nozzle diameters and showed that increasing the diameter with time led to rings with higher

impulse, but the pinch-off or formation time along with mass entrained was unaffected. The vortex ring impulse (I) is defined as $I = (1/4)\pi\rho\Gamma D_R^2$, where ρ is the density of the fluid and D_R is the diameter of the leading vortex ring. Meanwhile, temporally decreasing the nozzle diameter led to an increase in the formation number, but a decrease in vortex ring impulse and fluid entrained in the ring. These studies have clinical and biophysical relevance. The flow of blood through the mitral valve into the left ventricle during diastole generates a leading vortex ring. Clinical diagnoses of stenotic mitral valves show an increase of an order of magnitude in formation times from 3.6-4.5 due to valve orifice diameter reduction by stenosis. However, in hearts with left ventricle cardiomyopathy, the formation time drops to 1.5-2.5 due to an increased valve orifice diameter D_o (Krueger and Gharib, 2003). In terms of biological fluid transport, increasing orifice size to maximize impulse and ejecting an entire volume of fluid as a vortex ring within the formation time approaching 4 was purported to be the most efficient system (Dabiri and Gharib, 2005).

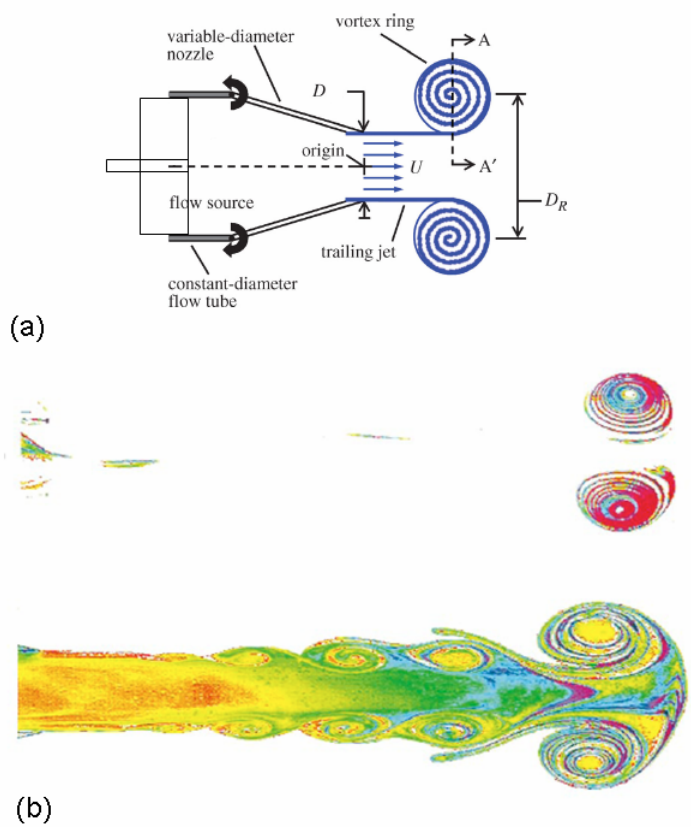

Figure 1-8. (a) piston cylinder arrangement of a starting pulsatile jet through a nozzle with exiting vortex ring, drawing obtained from Krueger *et al.* Physics of Fluids 2003. (b) top, a leading vortex ring without a trailing jet; bottom, a leading vortex ring with a trailing jet.

1.3 Objective and Approach

The primary objective of this study was to characterize the *in vitro* performance of the VEs in a cardiovascular pulse duplicator and assess their potential for clinical use as valve replacement prostheses. A second objective was to conduct experiments with synthetic polymer valves of various geometries and materials similar in mechanical properties to those of the VE, but more amenable to measurements of flow velocity and structural deformation using the current experimental protocols. These measurements are needed to validate computational codes incorporating FSI and may be applied towards tissue engineered heart valve design and optimization.

1.3.1 VE in vitro Performance

A pulse duplicator system that replicated both right and left ventricular cardiac loading conditions was designed to test the performance of the VEs in both the aortic and pulmonary positions. The time-dependent pressures, volumetric flow rates, velocity fields, and vorticity fields were quantified in accordance with L.4.2.3 of ANSI/AAMI/ISO 5840:2005, Cardiovascular Implants-Cardiac valve prosthesis standards. The VE was photographed at all stages of the cardiac cycle in accordance with L.4.2.7 and failure modes were assessed. Parts of the Test procedures L.4.3 were followed to quantify the VE performance. The exact protocol could not be rigorously followed because of the novelty in the valve design.

1.3.2 Flow and Structural Deformation of Polymer Valves

The complexity in valvular flow is in part attributed to FSI and requires a close synergy and integration between experiment and computational models in order to validate the computational models as predictive tools. The experimental objective was to develop simple yet suitable test cases for validating computational FSI codes specifically for structures that encounter significant deformation and strains as would be the case for VEs. Compression-molded silicone polymer served as the flexible valves, and the deformation was quantifiable *in situ*. Varying the silicone material properties, which were measured independently, allowed adjustment of the valve compliance. Additionally, valve geometries were varied to give multiple flow conditions. The initial flow condition was also varied by implementing both steady and unsteady pulsatile flows. The flow rate or Reynolds numbers yielding significant deformation and strain were considered along with physiological frequencies.

Chapter Two: Experimental Methods

2.1 Facilities

A pipe flow facility generating steady controllable laminar and turbulent flows was set up. Additionally, a flow facility simulating physiological cardiovascular conditions was set up. Some parts of the flow facility were fabricated in the machine shop of the Electrical Engineering Department at the University of Minnesota. Other parts were purchased from part suppliers as required for the experimental facilities.

2.1.1 Pipe Flow Facility

An image of the pipe flow facility is shown in Fig. 2-1 accompanied by a schematic in Fig. 2-2 with the major components labeled. An acrylic pipe with an inner diameter D of 2.54 cm, a wall thickness of 0.3 cm, and a length of 170.2 cm was used. These dimensions were chosen to match approximate aorta diameter, minimize optical distortion, and ensure the flow through the pipe was fully developed, respectively. The pipe was sectioned to mount a diaphragm valve 152.4 cm (60D) downstream of the entrance and 18.6 cm (7.3D) upstream of a flow reservoir.

A visualization box was placed external to the pipe at the location of the diaphragm. The box was fabricated from acrylic for optical clarity as required for particle image velocimetry (PIV) measurements. A schematic of the visualization box with the pipe running through the box is shown in Fig. 2-3. The visualization box was filled with sodium iodide solution 60% by weight of which the refractive index was matched to that of the acrylic pipe (~1.5) resulting in minimal optical distortion caused by the pipe wall curvature. The solid colored pieces around the pipe as shown in the 3-D view were used to seal the internal sodium iodide fluid of the box. The box of 5 mm wall thickness was dimensioned such that stereoscopic and planar PIV could be performed. The maximum planar PIV field of view was 7.6 cm x 5.5 cm as shown in the side camera view. See Section 2.5.1 for details on PIV measurements. Stereoscopic PIV measurements are not reported in this dissertation.

A flow conditioner was located upstream of the pipe section to minimize disturbances. The flow conditioner included three components. First, the unconditioned flow entered a diffuser with an inlet diameter of 2.54 cm, outlet diameter of 7.62 cm, and length of 19.5 cm. Next, the flow passed through a 30.5 cm long settling chamber containing a perforated plate with holes of 1.2 cm diameter, a honeycomb section with 0.2 cm diameter tubes and 2.5 cm length, and a stainless steel screen (mesh size 0.2 cm). These components acted to eliminate swirling motion and decrease flow non-uniformity over the cross section. Finally, the conditioned flow passed through a nozzle with diameter ratio of 3:1. The contraction followed a 5^{th}-order polynomial fit which ensured smooth transition of the working fluid into the pipe section.

An Iwaki centrifugal pump drove the working fluid (0.9% by weight NaCl solution, $\rho = 1.005$ g/cm^3, and $\mu \sim 1.02$ mPa•s), and the flow rate was controlled by a needle valve. A Carolina Medical electromagnetic flow meter with ±5% accuracy when operating at 3 to 5 L/min, positioned inline upstream of the flow conditioner, was used to monitor the steady volumetric flow rates. Additionally, a Transonic Systems ultrasonic flow meter (4% accuracy of the 2 L/min full-scale) external to the flow was used to monitor flow rates at low Reynolds numbers. Pressure taps were located one diameter upstream and downstream of the diaphragm valve location. Vivitro Systems Inc. transducers monitored pressures with an accuracy of 1 mmHg. An additional differential pressure transducer having an accuracy of 0.1% of the 0.75 mmHg full-scale (Druck Incorporated) was used at low flow rates.

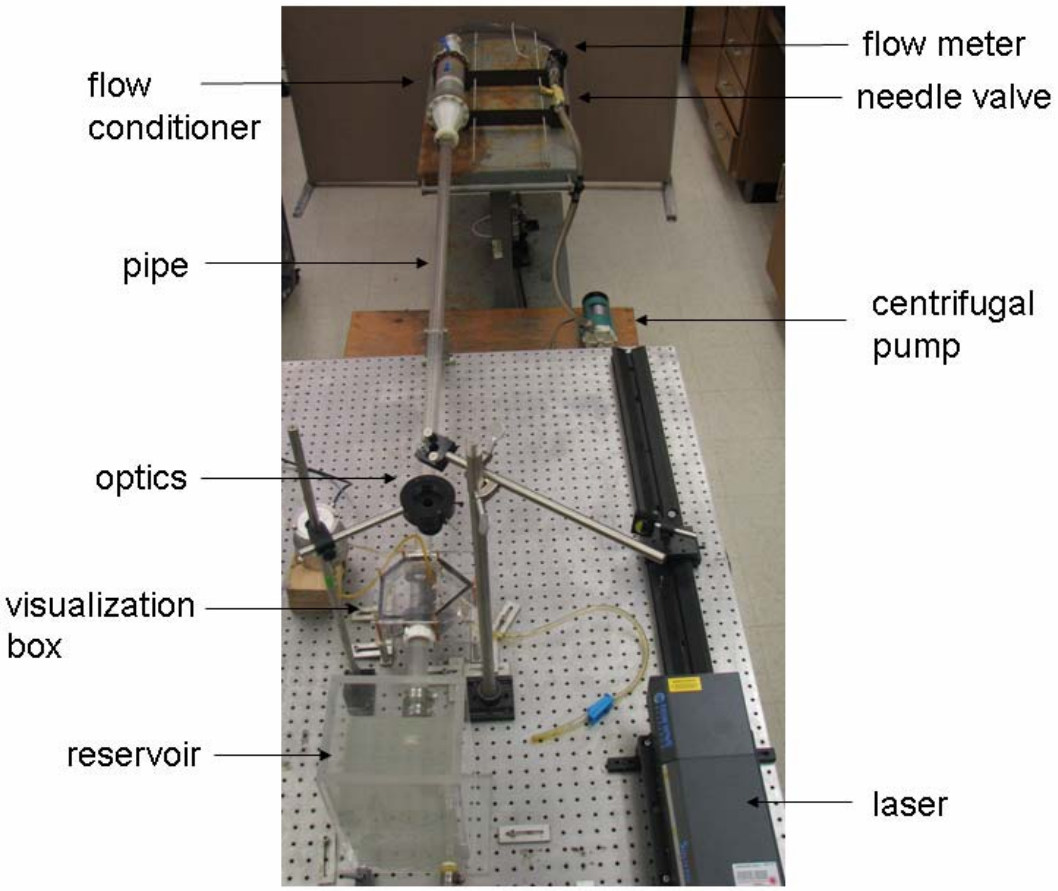

Figure 2- 1. Steady flow facility.

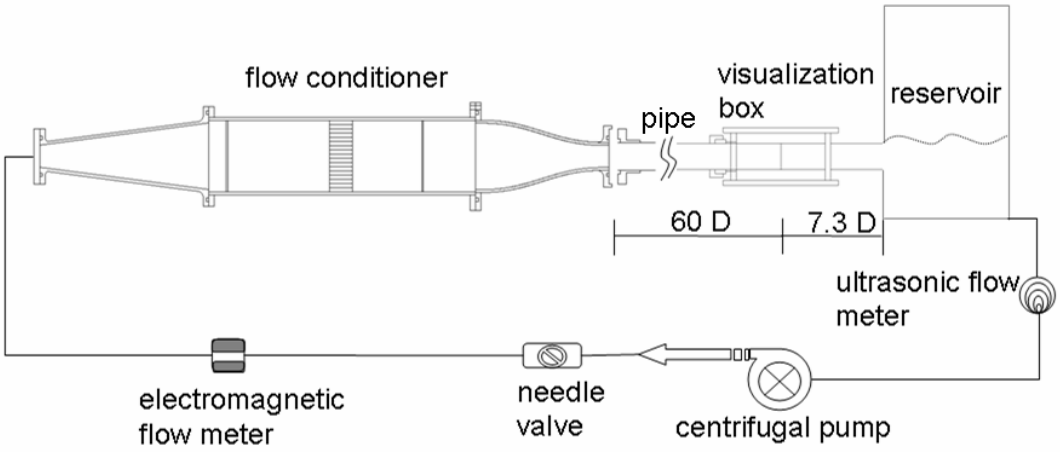

Figure 2- 2. Steady flow schematic, not drawn to scale.

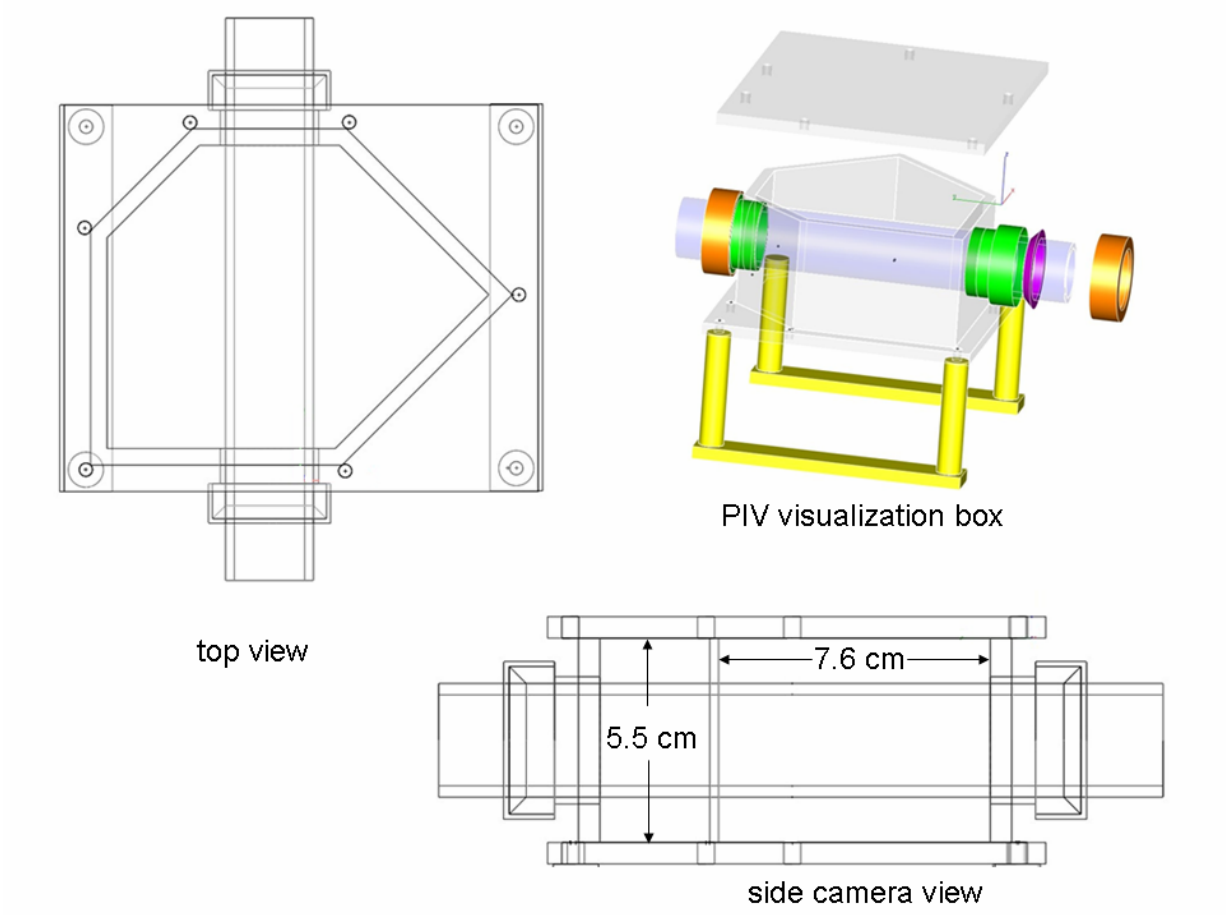

Figure 2- 3. Visualization PIV Box schematic showing the top view, side PIV camera view, and the 3-D view.

2.1.2 Cardiovascular Pulse Duplicator Facility

The cardiovascular pulse duplicator (CPD) was designed to replicate both left and right cardiovascular normal physiological flow and pressure signatures (aortic and pulmonary signatures shown in Fig. 1-2), which allowed the *in vitro* testing of valves in the aortic and pulmonary positions, respectively.

The CPD consisted of three major components integrated for flow and pressure measurements in the proximity of the testing valve and designed for optical access. The three components were an input flow forcing device, custom-built controllable impedance system, and data acquisition system. A picture of the experimental CPD setup is shown in Fig. 2-4 accompanied by a schematic in Fig. 2-5. The forcing device was a

Vivitro Systems Inc. linear displacement piston pump. The pump was driven by a programmable waveform and amplifier. A modified sinusoidal waveform with a repetition frequency of 1.167 Hz (70 beats/min) was chosen based on *a priori* knowledge of replicating physiological signal of 30% and 70% systolic and diastolic durations, respectively. The programmable waveform generator is shown in Fig 2-6. The normalized voltage-time and frequency spectrum generated diagrams are shown in Fig 2-7. The adjustable waveform amplifier controlled the amplitude of linear piston displacement and therefore the volume of working fluid displaced by the pump in one forward stroke during systole. The pump flow diameter was 7 cm.

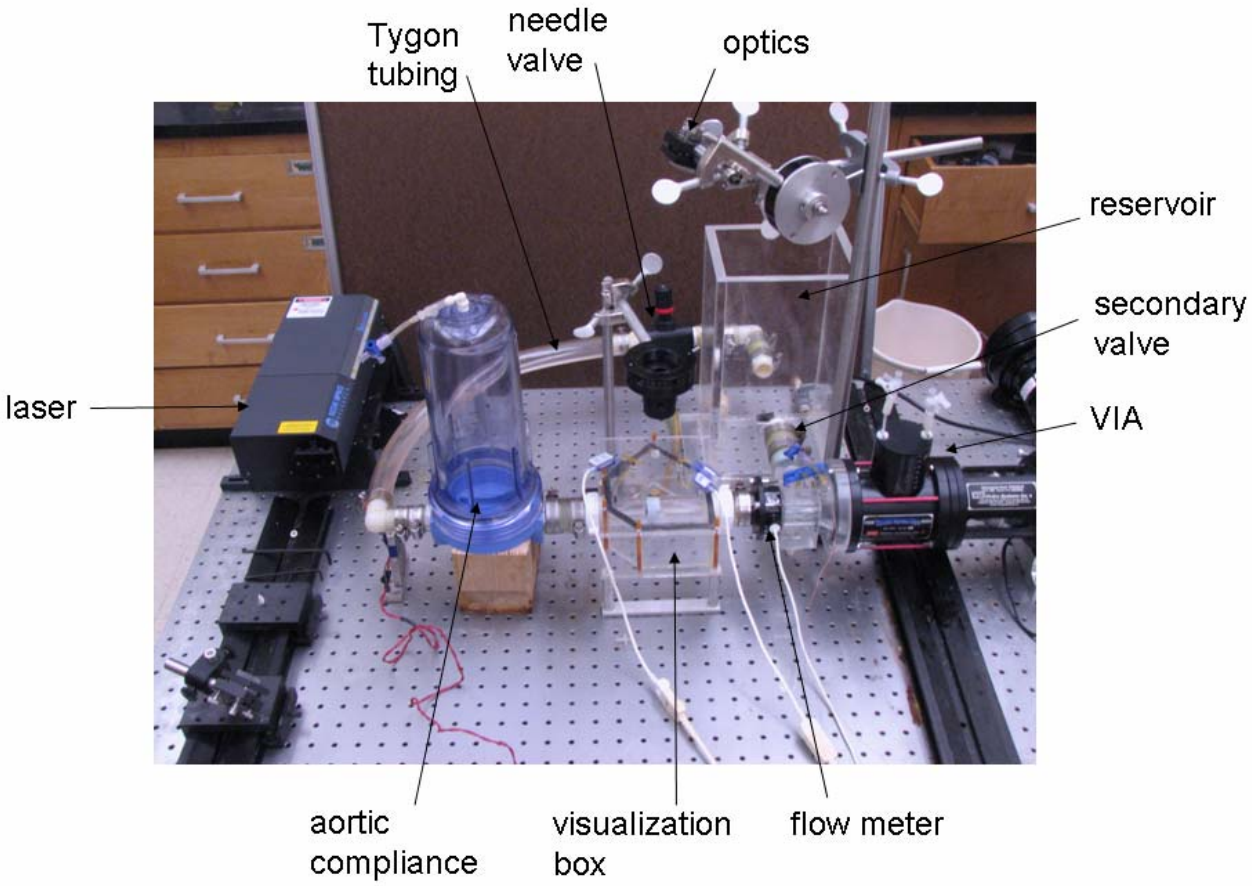

Figure 2- 4. Pulse duplicator facility.

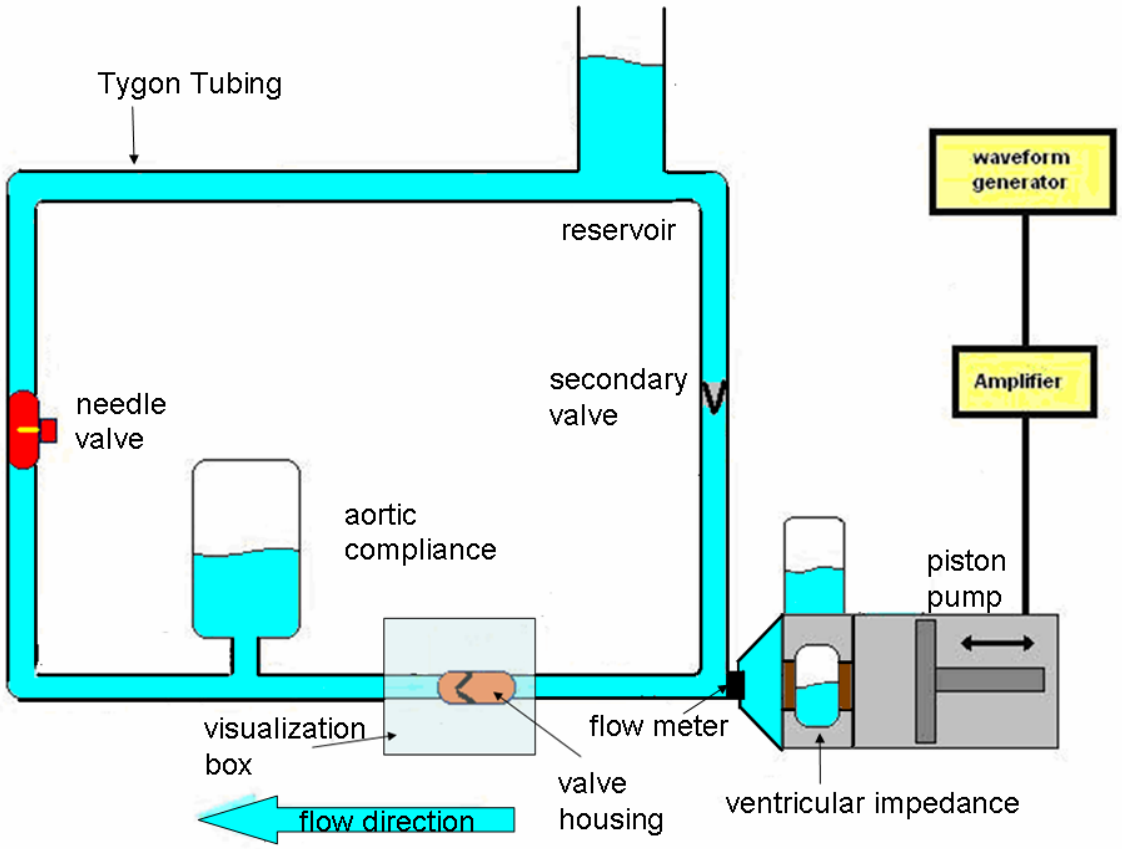

Figure 2- 5. Pulse duplicator flow schematic, not drawn to scale.

The working fluid was either saline solution (0.9% by weight NaCl solution, ρ = 1.005 g/cm^3, and $\eta \sim 1.02$ mPa•s) or water-glycerin solution (40 / 60 % water to glycerin ratio by volume, ρ = 1.15 g/cm^3, $\eta \sim 6.58$ mPa•s). The working fluid passed through a manufactured VSI Inc. left ventricular impedance chamber (VIA) with inner diameter matched to the pump (VIA shown in Fig 2-8). The left ventricular impedance chamber contained three parts: two adjustable compliance chambers with maximum air volumes of 60 mL and 120 mL and an internal finely porous cylindrical resistive unit. Note that the flow exits from the bottom of the compliance chamber as shown in Fig. 2-8c. Immediately downstream of the ventricular impedance was a flow reducer that decreased the flow cross section from the VIA flow diameter down to 2.8 cm. The reducer connects to an acrylic T-junction schematically shown in Fig 2-9. The flat side of the T-junction

has a window to view the secondary valve perpendicular to the streamwise direction of the pump. The Carolina Medical electromagnetic flow meter was mounted to the T-junction and placed inline with the pump. The testing valve was placed downstream of the flow meter. At this location the visualization box was placed external to the valve. The Vivitro Systems Inc. pressure transducers were placed upstream and downstream of the testing valve, and the location depended on the valve tested.

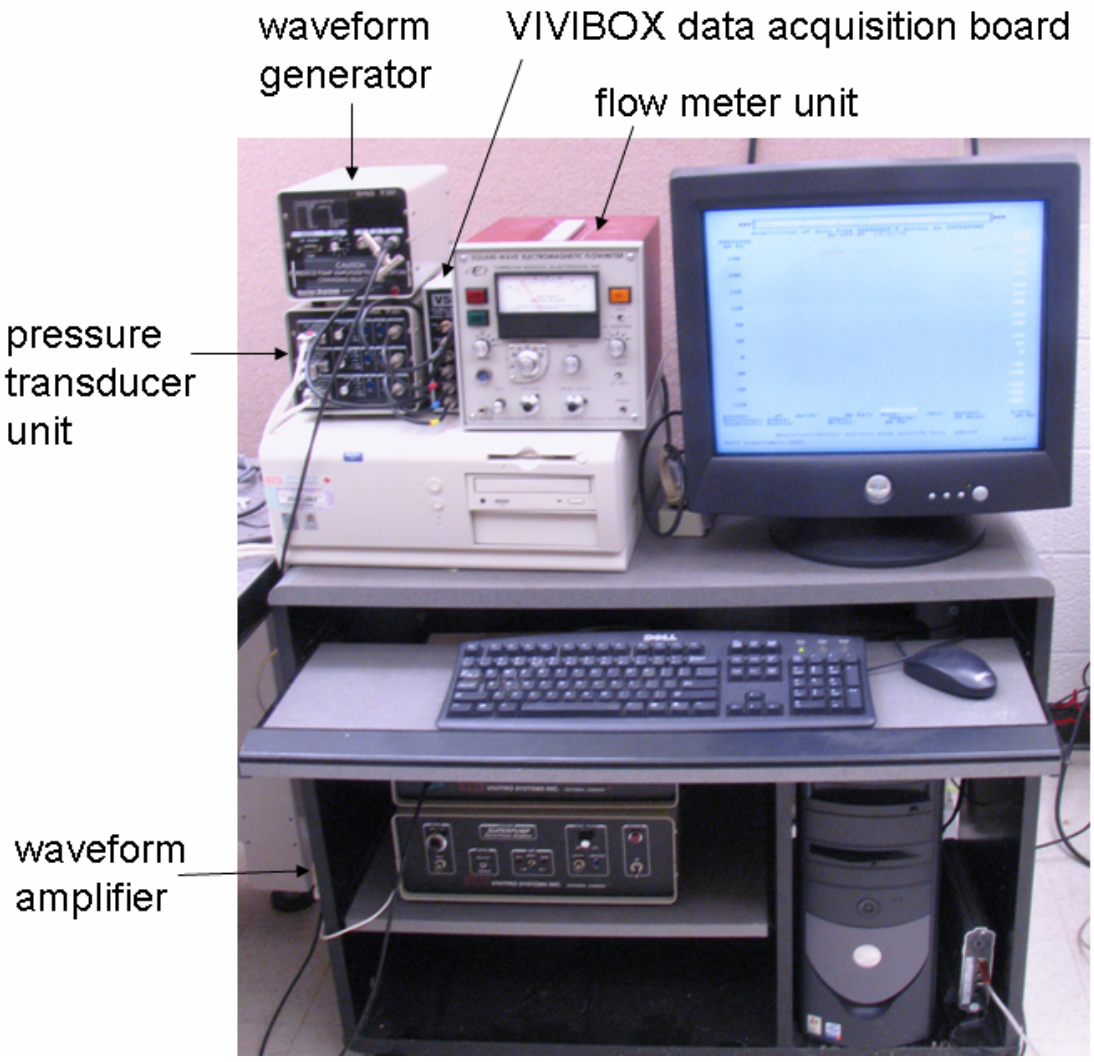

Figure 2- 6. Flow control, monitoring, and data acquisition system.

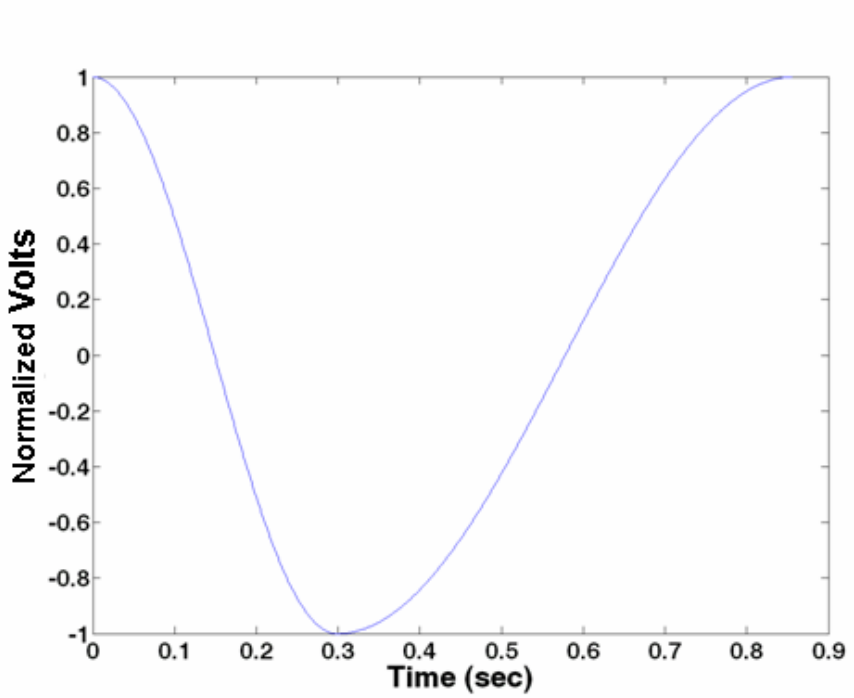

(a)

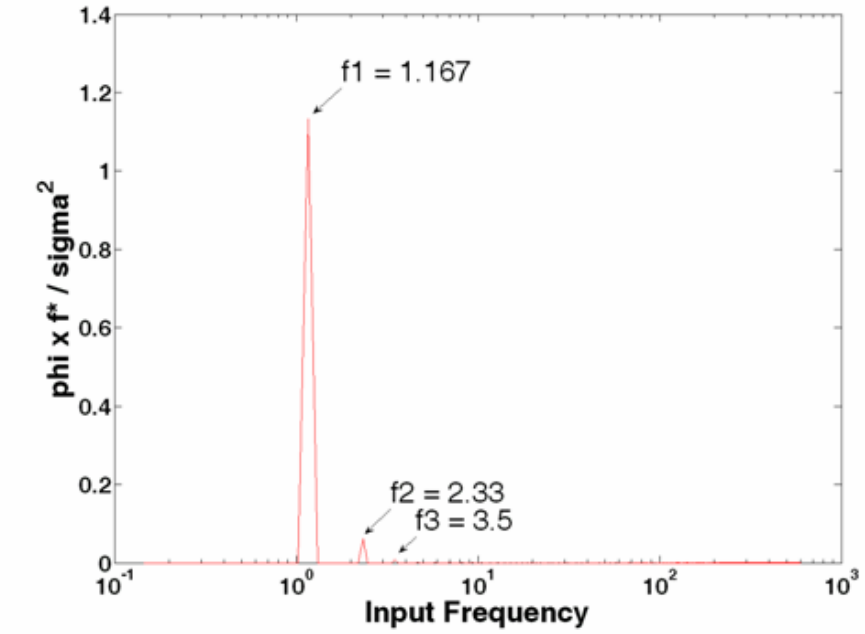

(b)

Figure 2- 7. (a) Input pump displacement waveform and (b) frequency spectrum.

(a)

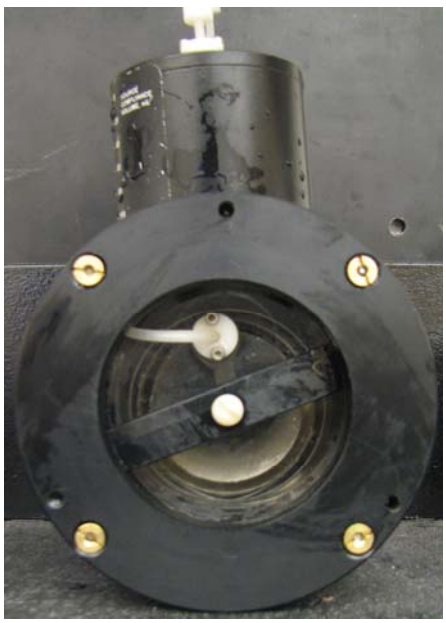

(b)

(c)

Figure 2- 8. (a) Vivitro Systems left ventricular impedance VIA, (b) inlet from pump to VIA, (c) outlet from VIA to CPD.

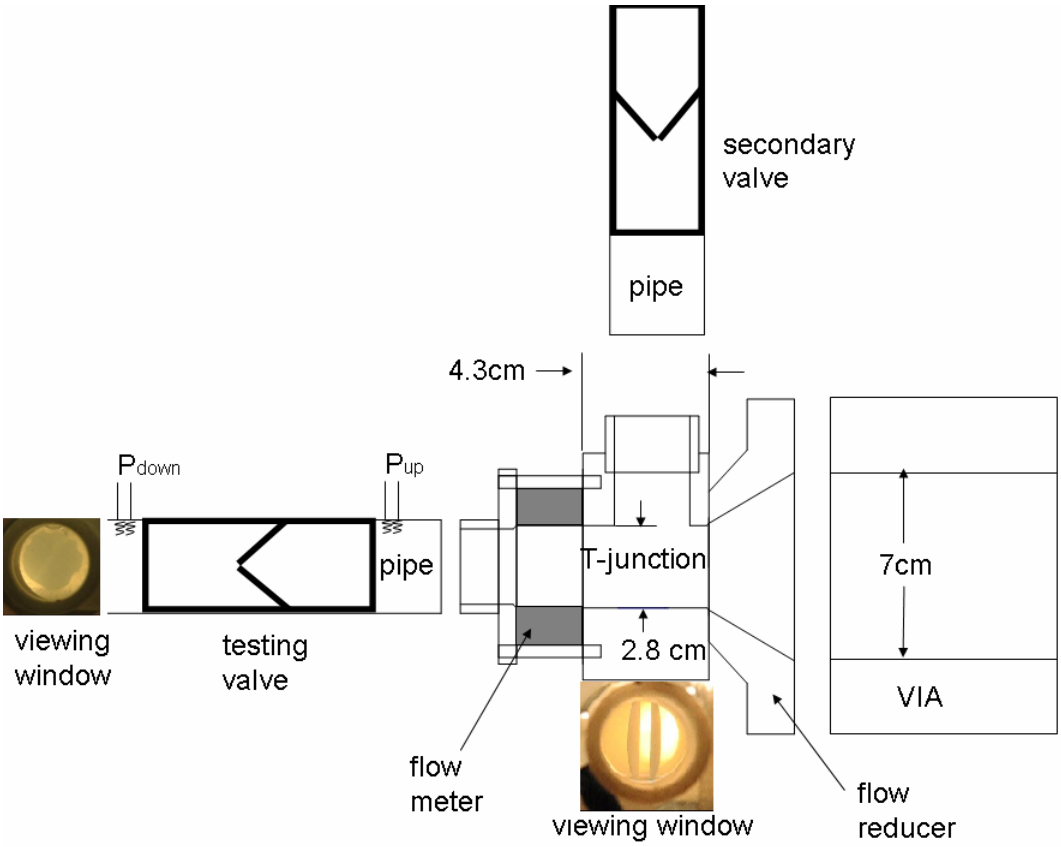

Figure 2- 9. Flow reducer and valve viewing windows. Note compliance chamber not shown downstream of testing valve.

Two visualization boxes were used in conjunction with the CPD. The PIV box discussed in Section 2.1.1 was used. An additional volumetric 3-component velocimetry (V3V) box was fabricated. The V3V visualization box was fabricated from acrylic for optical clarity. The dimensions of the box were chosen for appropriate magnification and field of view as required with V3V calibration and measurements. The length, height, depth, and thickness of the box were 20 cm, 18cm, 6.8 cm, and 0.5 cm, respectively. See Fig. 2-10 for V3V box layout. An orifice was bored through two of the smaller side faces so that a 3.175 cm outer diameter acrylic pipe could be inserted. The fluid in the pipe was separated from the external fluid in the box. The pipe and box were sealed by rubber gaskets and clamps shown as solid pieces in the 3-D view. The external fluid was either sodium iodide (60% by weight) or water glycerin (40/60 % by volume) solution for

testing the mechanical or transparent silicone valve, respectively. The sodium iodide matched the index of refraction of the acrylic tubing (1.49) when testing the mechanical valve. The water glycerin matched the index of refraction of the transparent silicone when testing the transparent silicone valve (1.43). Only the transparent silicone valve data will be reported herein.

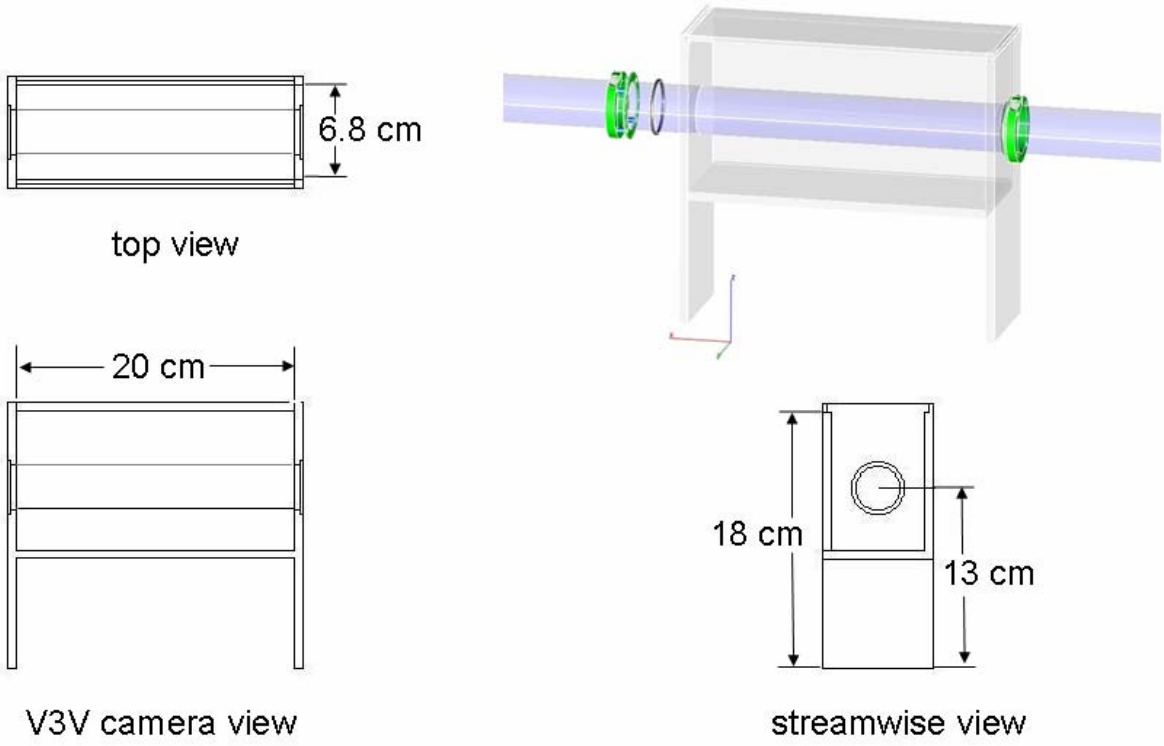

Figure 2- 10. V3V visualization box.

Downstream of the testing valve were the components providing the systemic impedance. The custom-built systemic arterial impedance (Zi) is the measure defining the ratio of the pulsatile pressure (P) to pulsatile flow (Q) as a function of time.

$$Zi \approx \frac{P(t)}{Q(t)} \qquad (2\text{-}2)$$

The impedance is a combination of hydrodynamic resistance due to the viscosity of the working fluid, the material compliance of the pulse duplicator components, and the inertia of the working fluid. The appropriate systemic arterial impedance along with the

upstream VIA results in physiological flow and pressure traces. The components of the systemic impedance were very interdependent, and controllability was a key design concern. A chamber having maximum air volume of 1L immediately downstream of the valve served as the aortic compliance. Downstream of the aortic compliance was a plastic barbed T-junction, which had one branch sealed with a flat acrylic disc used as the end-on viewing window for the testing valve. The VE as seen through the viewing window is shown in Fig 2-9. A needle valve was used to simulate the peripheral arterial resistance. The needle valve opening and closing could be finely controlled with the dial settings on the valve. The needle valve was connected with Tygon tubing of 1.9 cm inner diameter, 0.3 cm wall thickness, and a length of approximately 60 cm. The Tygon tubing was expandable and therefore had some inherent compliance. The flow through the needle valve emptied into a reservoir, which provided further compliance and hydrostatic pressure head. The working fluid in the pulsatile flow loop was also inserted at this location. To complete the unidirectional pulsatile flow loop, a pericardial secondary valve (picture shown with mechanical valve) was placed downstream of the reservoir and upstream of the acrylic T-junction. This valve acted as a check valve to prevent backflow around the loop.

Pressure, flow rate, and piston position data were acquired by the VIVIBOX VB2001 12-bit resolution with maximum sampling rate of 100 ksamples/s of ±10 volt range DAS-1600 data acquisition board. In the experiments described, the data were sampled at 300 Hz. A low pass filter of 30 Hz was set for the pressure and flow measurements. The system components are shown in Fig. 2-6. The supporting software Analyze Vivitro Systems Inc. was programmed in Borland C++. The software allowed collecting of pressure and flow time signatures. Ten consecutive cycles were averaged for all pressure and flow rate data recorded. The data was saved as a text file and post-processed with calibration parameter using Excel.

Fig. 2-11 show plots of *in vitro* CPD data of replicating aortic (AV) and pulmonary (PV) valve pressure and flow time signatures. Zero mmHg represents baseline atmospheric pressures. The testing or primary valve was a St. Jude Medical bileaflet mechanical valve. The secondary valve was a St. Jude Medical Biocor trileaflet bioprosthetic valve. Both valves are shown in Fig. 1-3. The input condition was piston

stroke volume of 70 mL operated at 70 beats per minute. This results in maximum pressure readings of approximately 115 and 50 mmHg during systole for the AV and PV conditions, respectively. The primary valve opens at a systolic pressure difference of approximately 10 mmHg. There is a sustained pressure difference (upstream – downstream) of at least -80 and -10 mmHg during diastole for the AV and PV conditions, respectively. The ventricular pressures drop slightly below zero due to the backward stroke and vacuum like effect of the piston-pump for both AV and PV cases. The negative pressures may occur physiologically during expansion of the ventricles. The peak flow rates are approximately 30 L/min and 25 L/min for both AV and PV conditions, respectively. The forward flow occurs earlier for PV than for AV. The average flow rate of 4.8 L/min is larger for the PV as compared to the 4.1 L/min of the AV. From 0.36 seconds to 0.4 seconds there is a reverse flow of the working fluid as recorded by the flow meter. This corresponds to approximately a 5 mL regurgitant volume of the mechanical valve. At time ~ 0.18 and 0.42 second there are higher frequency oscillations in the pressure signature for both the AV and PV conditions. This pressure fluctuation is a result of the closing of the primary and secondary valves. The pressure and flow conditions as generated by CPD match fairly well with native aortic and pulmonary conditions as discussed in Sections 1.2.1.1 and 1.2.1.2.

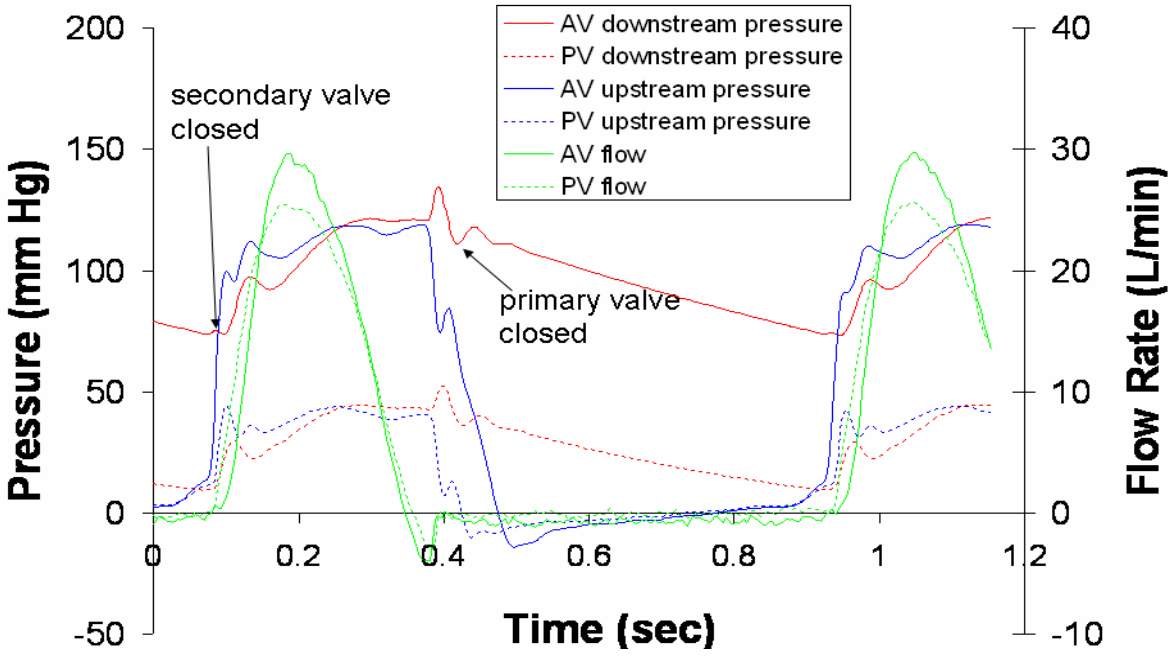

Figure 2- 11 Aortic and pulmonary mechanical valve *in vitro* flow and pressure signatures.

The maximum compliance in the VIA (60 mL and 120 mL of air volume) minimized left ventricular pressure oscillation and also resulted in smoother flow rate waveforms as tested with aortic roots and bioprosthetic valves in a cardiovascular pulse duplicator by Jennings *et al.* (2001). Additionally, the systolic rise in ventricular pressure was closer to clinically accepted value of approximately 1000 mmHg/s with the VIA (full air volume) as compared to 6000 mmHg/s without the VIA (no air volume). Peak flow rates were higher with the VIA as compared to that without VIA. According to the VIA manual, peak flow rates were reached earlier and had larger flow magnitude with the VIA than without the VIA (Jennings et al., 2001). These reported findings were consistent with the current setup. Therefore, the full compliance VIA setting was maintained with the current experimental testing. Aortic compliance was required to maintain downstream diastolic pressures. A domed chamber having air ports for adding and bleeding air volumes was used to simulate aortic compliance. Decreasing the air volume or compliance resulted in an overall increase in upstream and downstream systolic pressures. Decreasing the air volume also increased the ratio of maximum to minimum downstream pressures. An air volume of approximately 1L resulted in reasonable physiological pressure and flow traces. The 1L air volume was larger than the 640 mL air volume used in the commercial Vivitro System Super-Dup'r Model Left Heart. Like the aortic compliance, the needle valve regulated the downstream diastolic pressure and overall pressure signatures. A fully opened valve resulted in lower overall pressures and downstream diastolic pressures along with lower instantaneous flow rates. The aortic compliance and needle valve worked in tandem to replicate peripheral impedance. Adjusting the fluid height in the reservoir controlled the pressure difference between the internal flow and external environment. The hydrostatic head also drove the fluid through the bioprosthetic secondary valve. Additionally, the piston pump backward stroke induced the fluid through the bioprosthetic secondary valve. A hydrostatic head of approximately 3.8 cm was added to the internal fluid. This hydrostatic head was required for the VE testing. Without this internal hydrostatic pressure, the VEs were not able to support their weight (see Results Section 3.3).

The relative proximity of the CPD components to the location of the pressure and flow transducers affected the measurements. The pressure and flow transducers were kept as close to the testing valve as possible. The location of the CPD components was optimized to replicate the physiological conditions as closely as possible. For example, bringing the aortic compliance and VIA closer to the valves resulted in a decrease in pressure spikes or fluid inertia related 'hammer' effect during closing of the valves. It should be noted that the testing valve geometry and compliance has intrinsic impedance. Therefore, the exact impedance setting could not be replicated from one testing valve to the next, but had to be tuned to match the representative AV and PV pressure and flow traces closely.

2.2 Valves

The following sections present the valves that were tested in the steady flow and CPD facilities. The fabrication and mounting processes of these valves for testing are described in detail.

2.2.1 Valve Equivalent

The valve equivalents (VEs) were grown in the Tranquillo Laboratories at the University of Minnesota. The VEs were composed of a fibrin scaffold seeded with human dermal fibroblasts. A multi-week incubation and cyclic distention in a bioreactor led to collagen deposition with tissue mechanical integrity similar to that of pulmonary valve leaflets. For greater details please read thesis entitled 'Development of a Completely Biological Tissue Engineered Heart Valve' Syedain, Z. 2009 along with published works by Syedain *et al.* (2008) and Robinson *et al.* (2008).

The VEs harvested for *in vitro* pulse duplicator testing were either bileaflets (n = 30) or trileaflets (n = 10). Fig. 2-12 shows a side and downstream (aortic) view of the bileaflet VE. In general these valves were approximately 0.03 cm in thickness for both root and leaflet macrostructure. The VE diameter was 2 cm and the length was approximately 3 cm (measured from the Dacron cuff ends). Note that the VE lengths varied from sample to sample due to tissue compaction during the tissue engineering process. Most VEs had lengths within 2 to 4 cm. The left side image of Fig. 2-12 shows

a side view of the exposed VE root in a water bath with root internal fluid of higher pressure. Without the internal pressure difference, the valve was not able to support its weight. The orientation of the valve is such that the forward internal flow is to the right. In this view of the zero-flow state, the angle inclination of the bottom leaflet is approximately 51º with respect to the x-axis. The lips (horizontal extension of the leaflet along the commissure) of the two leaflets are also shown and the dimensions of the lips were affected by the initial leaflet compaction. An approximation was 0.2 cm in length, 0.1 cm in thickness, and the span of the root diameter. The space at the commissure between the two leaflets is clearly seen. This inherent gap led to incomplete coaptation for all VEs at zero flow. The right side image shows the aortic or downstream view. In this image, the VE is sutured into a silicone sleeve. When the VE is sutured into a silicone sleeve (2 cm ID, 0.2 cm thickness, and variable length specific to the harvested valve), no internal pressure difference is required to keep the valve at its radially expanded state. The Sterling Supplies silicone sleeves were cured at room temperature over a 24-hour period. In about seven of the valves used for testing, the leaflets initially coapted before being exposed to the testing conditions. The majority of the valves did not coapt due to tissue compaction during the VE growth process.

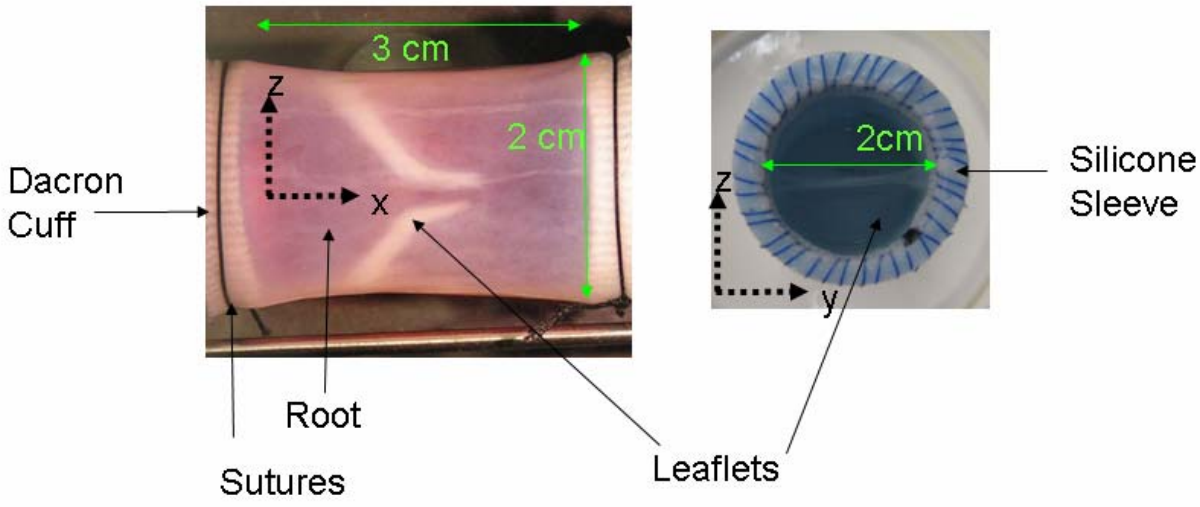

Figure 2- 12. VE side view (flow direction from left to right) and top (aortic) view.

There were multiple modes for mounting the VEs within the visualization boxes. Fig 2-13a shows the expansion constrained mode of mounting the VE. In this approach, the silicone sleeve VE unit was inserted inside an acrylic pipe of inner diameter 2.54 cm. The friction between the outer silicone and inner acrylic surface was sufficient to prevent the forward displacement of the valve and silicone sleeve unit. A set screw (not shown in the schematic) was placed immediately upstream of the valve silicone sleeve preventing backwards displacement of the valve during the backstroke of the piston. The VE, silicone sleeve, and acrylic tube unit was inserted into the visualization box. An exposed to the external fluid bath root mounting was required to accommodate VE root expansion. The schematic for this approach is shown in Fig 2-13b. Teflon diameter reduction fittings (2.54 cm down to 1.6 cm) were placed internal to each of the VE root ends. The ends were sealed by tying sutures with a slipknot over the valve and securing the VEs onto the ends of the Teflon fittings. In the root-exposed mode, the internal pressure within the root needed to be greater (~ 3 mmHg) than the external pressure for the VE to support its weight.

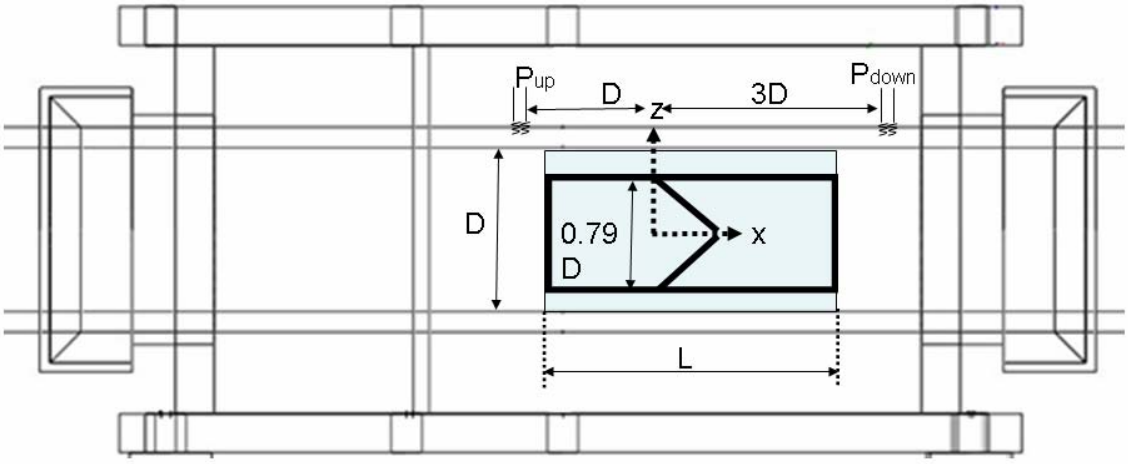

(a)

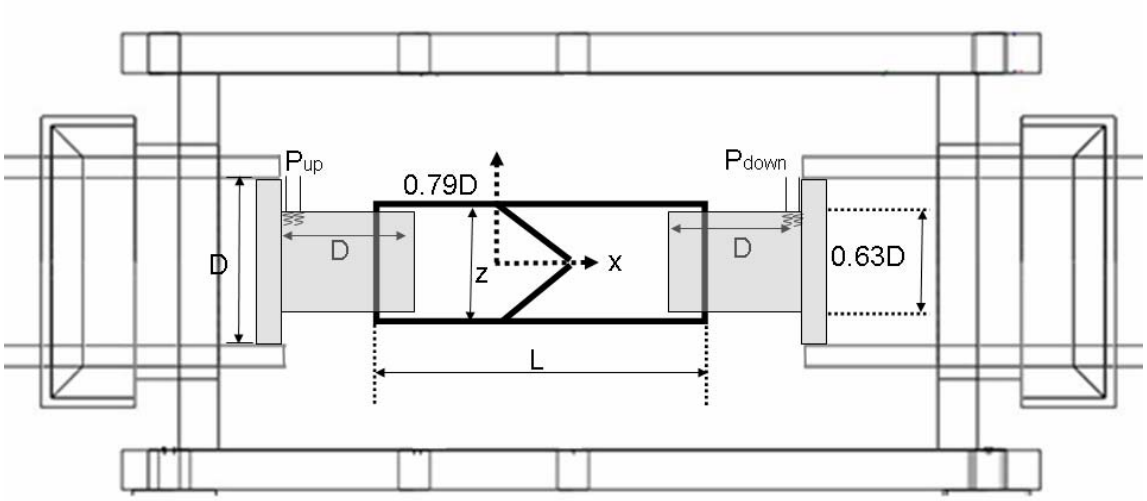

(b)

Figure 2- 13 (a) Valve equivalent silicone sleeve housing root expansion constrained mount and (b) VE root exposed mount inside the visualization box. D = 2.54 cm. The pipe box seal coupler is shown on both ends of the pipe section.

2.2.2 Circular Diaphragm with Orifice

Two-part silicone gels (Nusil Technology) were chosen for the diaphragm valve (DV) material based on the high manufacturer-stated compliance of the cured product. Three gel combinations: MED 4901 (most compliant, stress of 2.2MPa at 1075% strain), MED 4905 (stress of 3.6MPa at 1100 strain), and MED 4-4220 (least compliant, stress of 4.48 MPa at 575% strain) were tested. The silicone gels were compression-molded in an aluminum cavity shown in Fig. 2-14 and cured at 400°F for 20 minutes resulting in circular silicone diaphragm valves as shown in Fig. 2-15 left image.

Each DV had 2.54 cm diameter and 0.1 cm thickness with an outer ring of 0.3 cm thickness for mounting. An orifice of diameter d was punched out from the center of each DV. Most tests were performed with d/D = 0.31 which yielded measurable deformations for the lowest volumetric flow rates examined. For a comparison case, a rigid aluminum diaphragm valve with 0.3 cm thickness and d/D = 0.31 shown in the right image of Fig. 2-15 was used. One DV with a larger orifice (d/D = 0.69, MED 4901) not shown was tested. In total five diaphragms were tested (MED 4901 with d/D = 0.31, MED 4905 with d/D = 0.31, MED 4-4220 with d/D = 0.31, aluminum with d/D = 0.31, and MED 4901 with d/D = 0.69).

The DVs were mounted at the junction of the upstream and downstream acrylic pipe sections as shown in Fig. 2-16. A 0.15 cm radius round was chamfered from the wall of the acrylic pipe to center and align the DV mounting rings. The diaphragm mounting rings were dabbed with vacuum grease to seal the internal fluid.

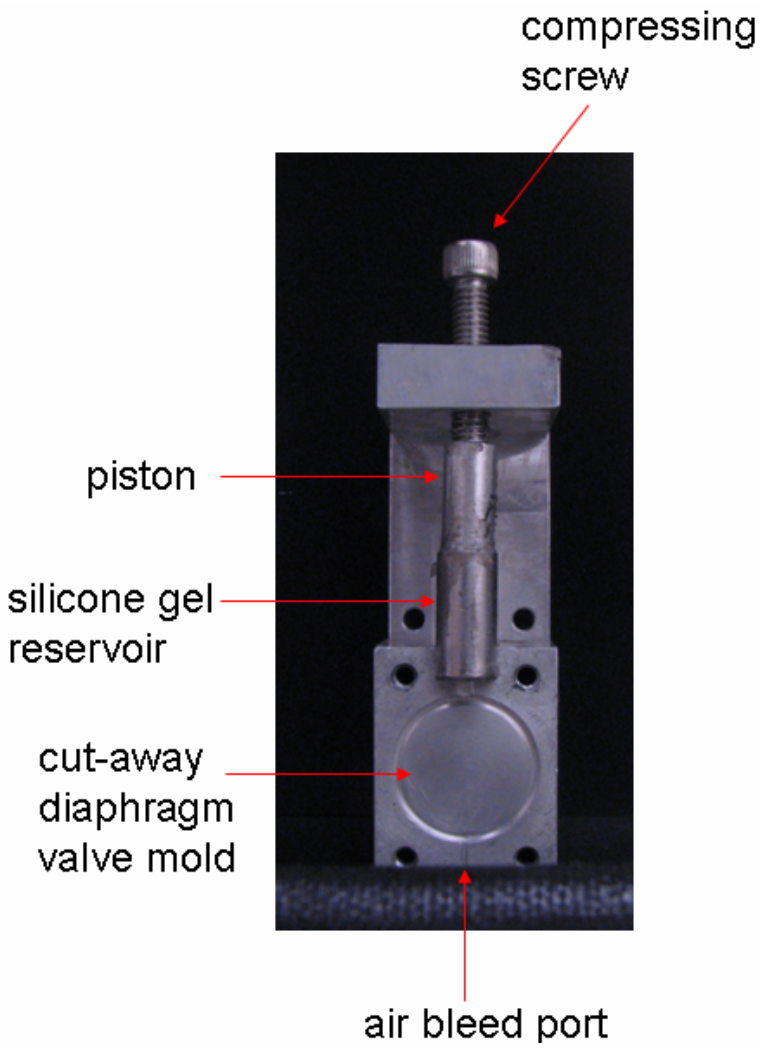

Figure 2- 14. Silicone diaphragm valve mold.

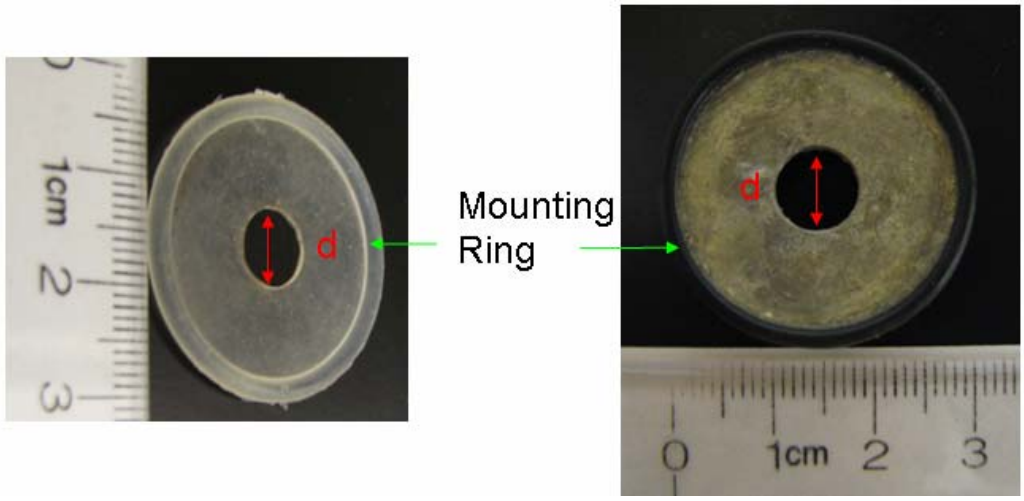

Figure 2- 15. Silicone and aluminum diaphragm valves.

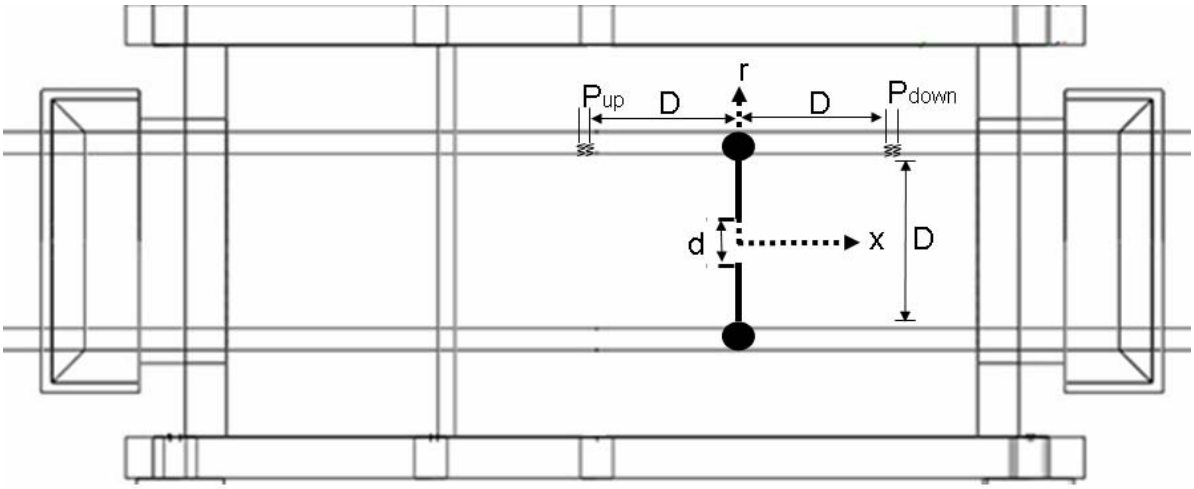

Figure 2- 16 Mounting of the silicone diaphragm valves inside the visualization box. D = 2.54 cm and d = 0.8 cm.

2.2.3 Transparent Silicone Valve

Two-part silicone Sylgard 184 gel (Dow Corning Inc.) was chosen for the optical transparency required to conduct tests on a transparent silicone valve. The transparent silicone valve (SV) was compression-molded in an aluminum cavity (Fig. 2-17) with dimensions chosen to closely match the geometry of the VE (see Fig. 2-12) and cured at 302°F for 10 minutes. The tensile material characteristics are shown in Appendix E.

Fig. 2-18 shows a downstream (aortic) view on the left and side view on the right of the TSV. Fig. 2-19 schematic shows the dimensions of the SV. The SV had a root length of 4 cm and an inner diameter of 2 cm. The base of the leaflet was 1.7 cm from the upstream end of the root and the bottom leaflet was angled at approximately 51 degrees. The leaflet and root were 0.1 cm in thickness. The leaflet opening was approximately 0.1 cm. The free edge of the leaflet had a very thin 'lip' as a result of the molding and the need for a straight leaflet opening. The lip had a length of 0.15 cm along the x-direction and a thickness of less than 0.05 cm.

An exposed-root mounting similar to the VE approach was used to accommodate SV root expansion and the same schematic applies as shown in Fig 2-13b. Unlike the VEs, the SVs were secured onto the Teflon fitting by sealing the junction with Teflon and electric tapes. The SVs were able to support their weight unlike the VEs; therefore, the internal pressure and external pressure could be equivalent during testing. The SV and Teflon fittings were inserted into the V3V visualization box for testing.

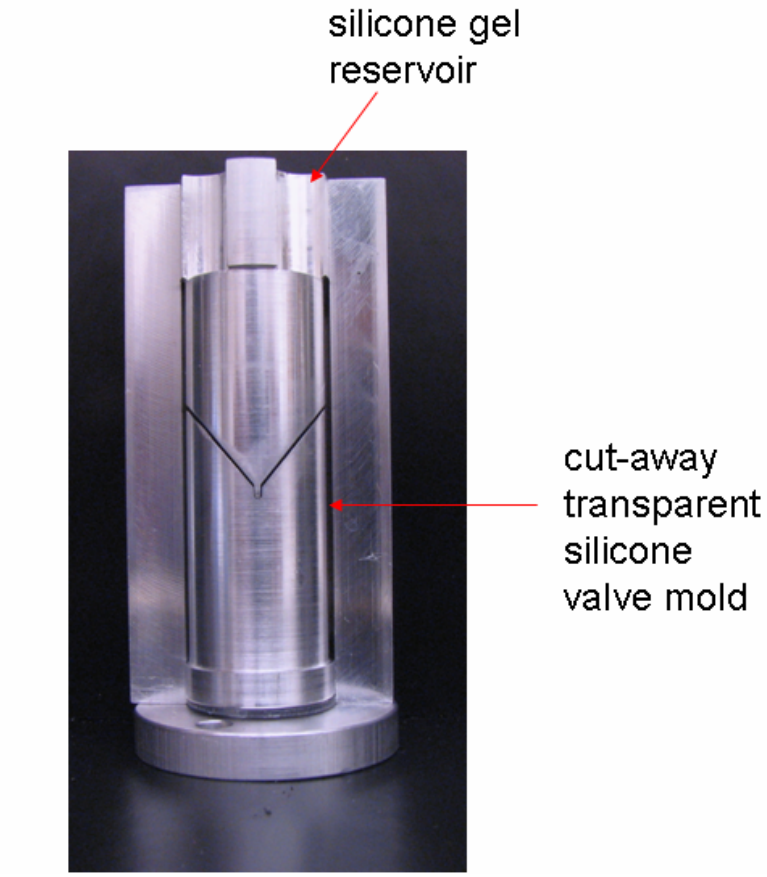

Figure 2- 17. Transparent silicone valve mold.

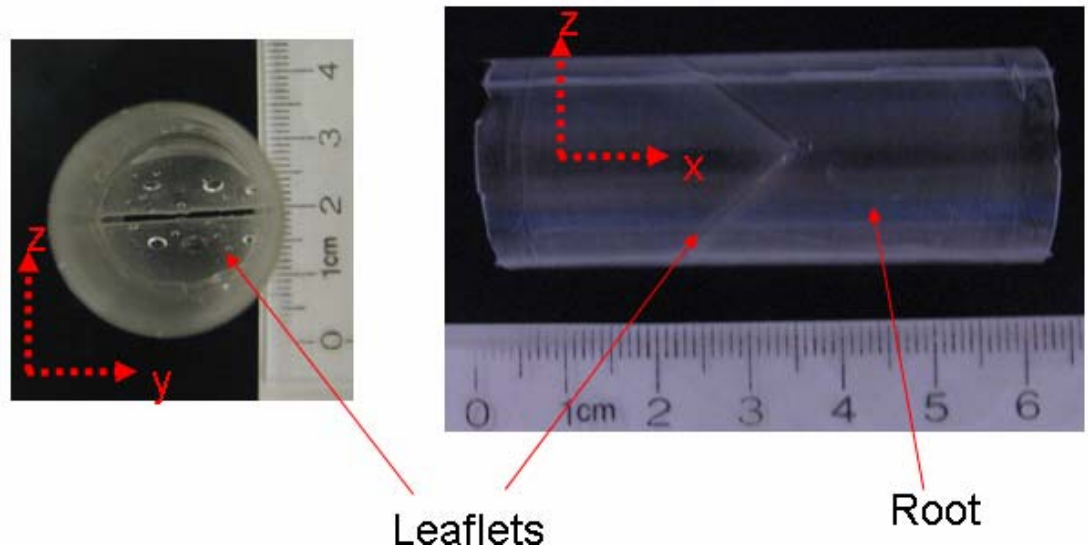

Figure 2- 18. Transparent silicone valve aortic and side views

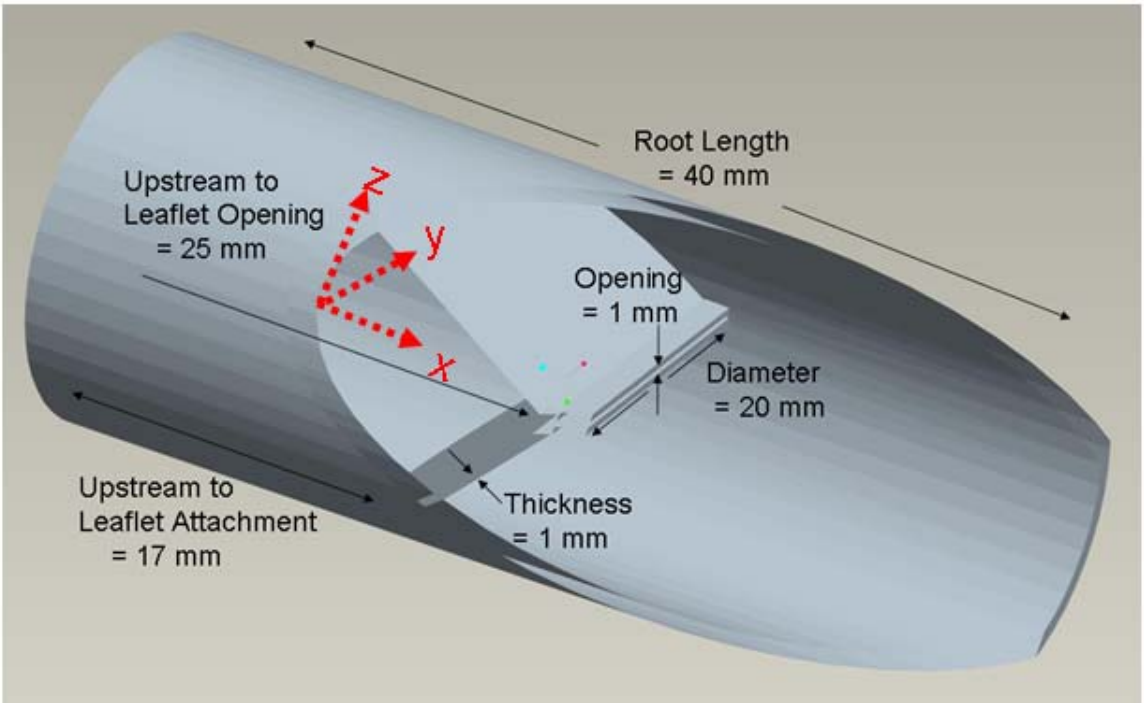

Figure 2- 19. Transparent valve dimensions.

2.2.4 Mechanical Valve

A 21mm St. Jude Medical Regent bileaflet mechanical valve (MV shown in Fig 1-3a) housed inside a Sterling supplies silicone sleeve (2 cm ID, 0.2 cm thickness, and

1.5 cm length) was placed within an acrylic pipe (2.54 cm inner flow diameter). This allowed a press-fit of the mechanical valve with the silicone sleeve within the acrylic pipe (similar to Fig. 2-13a). The MV silicone sleeve acrylic pipe unit was inserted into the PIV visualization box for testing.

2.3 Uniaxial Tensile Testing

Rectangular samples of each silicone type were cut from the DV and SV and tested for mechanical properties. Uniaxial tensile tests were performed with a material testing system (Instron Corp., Canton, MA)**.** Each sample was placed in compressive grips as shown in Fig. 2-20. The nominal gauge length (distance between grips) was measured and used to determine engineering strain (ε). The samples were subjected to a 0.05 N preload and strained at 1%/s increments until reaching a total strain ε of 50%. A 5 ±0.00125 N load cell recorded the corresponding force applied. The force value was normalized by the initial sample cross-sectional area (thickness x width) to obtain a corresponding engineering stress (s). A neo-Hookean hyperelastic model (Equation 1) for incompressible material:

$$s = \mu\left(\varepsilon - \left(\varepsilon + 1\right)^{-2} + 1\right) \qquad (2\text{-}2)$$

was fit to the averaged (N=4) stress-strain data for each silicone material type. A shear modulus (μ) was then extracted by minimizing the sum-of-squares for each material type.

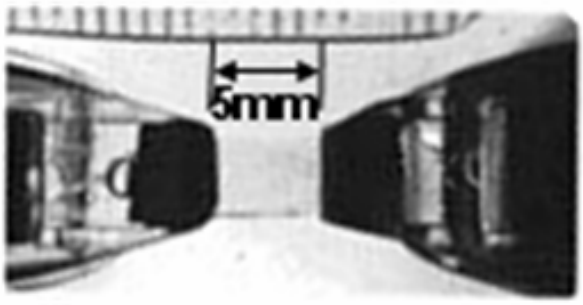

Figure 2- 20. Uniaxial tensile silicone material mechanical testing.

2.4 Digital Video Acquisition

Digital video data was acquired with a Canon Powershot S3 Is 6.0 MP camera. The digital camera recorded valve opening area and failure modes in the cardiovascular

pulse duplicator at 640 X 489 pixel resolution at 30 frames per second. The camera frame rate allowed a recording of approximately 26 phases of the cardiac cycle. The digital video acquisition was synchronized to the piston-pump displacement by having a light emitting diode (LED) in the field of view. The LED was triggered and synchronized with the start of the forward stroke of the piston-pump. The digital video data calibration for spatial magnification was based on *a priori* knowledge of valve dimension with the field of view under zero flow. A sample image is shown in Fig. 2-9 labeled viewing window.

2.5 Velocimetry

2.5.1 2D Particle Image Velocimetry

Particle image velocimetry (PIV) is a quantitative noninvasive method of measuring instantaneous planar velocity fields in fluids. The experimental method is based on the fact that small particles of density similar to that of the working fluid are suspended, and if the fluid acceleration is not too high, the particles follow the fluid motion accurately (Raffel et al., 1998). The number of particles per unit volume of working fluid should be sufficiently low to preserve the original flow dynamics (Crowe et al., 1998, Merzkirch, 1987). However, seeding density should be optimized for registration of the particle movement. Therefore, the velocity of the fluid can be approximated by the velocity of the particle.

For the PIV measurements, 10 μm hollow spherical glass particles (ρ = 1.05 – 1.15 g/cm^3) were seeded into the working fluid. A schematic of the PIV setup is shown in Fig. 2-21. The flow and particles were illuminated by pulsed light sheets from a pair of Nd:YAG New Wave lasers (λ = 532 nm) aimed downward through the pipe cross section. Each laser beam passed through a combination of 25 mm focal length cylindrical and 200 mm focal length spherical lenses resulting in sheets of approximately 1 mm thickness. The light scattered by the particles was acquired by a dual-frame camera (TSI Powerview 4MP) with a resolution of 2048 x 2048 pixels and 12-bit dynamic range charged couple diode (CCD) array. A 200 mm lens (Nikon micro-Nikkor) was mounted on the camera and located approximately 30 cm from the light sheet

resulting in a magnification factor M ~ 55 pixels/mm. An aperture setting of f# 5.6 allowed sufficient illumination for particle identification at a laser intensity of 80mJ/pulse. The pairs of images separated by the laser pulse separation time (ΔT) and focused on the laser sheet plane were recorded. Image pairs were acquired at a repetition rate of 1-2 Hz so that consecutive image pairs could be considered statistically independent. The image pairs and laser were synchronized by a TSI 610034 Laser Pulse Synchronizer of 1ns resolution. The synchronizer enabled the pulses from each laser to straddle neighboring camera frames. Ensembles of image pairs were acquired for each run so that averaged quantities could be determined. A sample image pair schematic of particles is shown in the bottom Fig. 2-21 with the real image pair shown in top row of Fig. 2-22. A vector field is plotted on the right image of the pair. An individual vector was computed based on the following algorithm using INSIGHT3G (TSI Inc.) software.

First, image conditioning was done by subtracting a minimum average pixel intensity from each of the raw images, which diminishes the effects of background light, laser glare, and noise. Fig. 2-22 top row shows background-subtracted raw images of illuminated particles in white and background in black for frames A and B acquired at times t_o (initial location of particles) and $t_o + \Delta T$ (final location of particles due to the movement of the flow field within ΔT), respectively. ΔT was chosen to ensure that the maximum particle displacement was 8 pixels. Each pixel in the image has intensity (I) on a 12-bit dynamic grayscale range. The illuminated particles in white have higher intensity value than the background.

Second, each image was gridded into small interrogation (processing) areas of 64 x 64 pixels shown by the green box, a dimension within the maximum 25% in-plane particle displacement rule (Keane and Adrian, 1990). The center of this interrogation area is the location of the displacement vector to be computed. The interrogation areas are spaced with 50% overlap, meaning neighboring vectors are separated by 32 pixels

Third, cross-correlation was used to find particle displacement between the successive frames in each interrogation area. The cross-correlation function R based on the intensity (I) can be defined as:

$$R_{I_1 I_2}(\Delta X, \Delta Y) = \int I_1(X, Y) I_2(X + \Delta X, Y + \Delta Y) dX dY \qquad (2\text{-}2)$$

where, $I_1$is the intensity at a point (X, Y) of the first image and I_2 is the intensity at a point (X + ΔX, Y + ΔY) of the second image. *R* is maximized for the dominant particle displacement (ΔX, ΔY). The velocity components (U, V) were obtained by dividing the displacement values by the pulse separation time (ΔT). Insight3G performs a Fast Fourier Transform of the Intensity function to compute *R*. The resulting correlation function is shown in the bottom row of Fig. 2-22. A Gaussian fit was used to find the peak intensity. The lower intensity peaks in the periphery represent noise. At this point, one 'pass' of the PIV algorithm was completed.

Finally, iterations or multiple passes were required if the individual particle displacements vary within the interrogation area as a result of local velocity gradients. For example in Fig 2-22, particles near the top right corner within the green interrogation area would move to the left and upwards as indicated by the vector at that corner. Note the interrogation area for each process only computes the vector at the center. Particles near the bottom left corner would move to the right and downwards indicated by the vector at that corner. When the particle displacement gradient is significant within the interrogation area, no dominant peak may occur resulting in an erroneous or no displacement vector computed. A multipass central difference image correction deformation algorithm with 0.1 pixel displacement accuracy (δΔX) was performed to account for any high spatial particle displacement gradient within the 64 x 64 pixel interrogation area. The mathematical details are explained by Wereley and Gui (2001). Two primary passes and one secondary pass were utilized. The first primary pass had been performed by the previous two steps (i.e., image gridding and correlation) and vectors had been computed. The second primary pass used the first pass vector field to deform the grid (shown in red of Fig 2-22) by an integer pixel value in both x and y-directions (opposite directions for frame A and B). The input interrogation is increased to twice the initial interrogation size and then the spot mask (shown in shaded blue) interpolates the velocity gradients from the corner vectors to minimize the peak splintering. The secondary pass used subpixel offset grid deformation. The three total passes resulted in a better signal-to-noise ratio of the Gaussian peak and a more accurate displacement vector. *Vector Validation* was performed after each pass to filter out bad vectors and fill in holes with interpolated vectors. Spurious vectors in each pass were

identified and eliminated using a 2-pixel displacement 5 x 5 local median filter and the missing vectors were interpolated using a 3 x 3 mean interpolation. The processing resulted in 97% or higher valid vectors. See Table 1 for PIV experiments conducted.

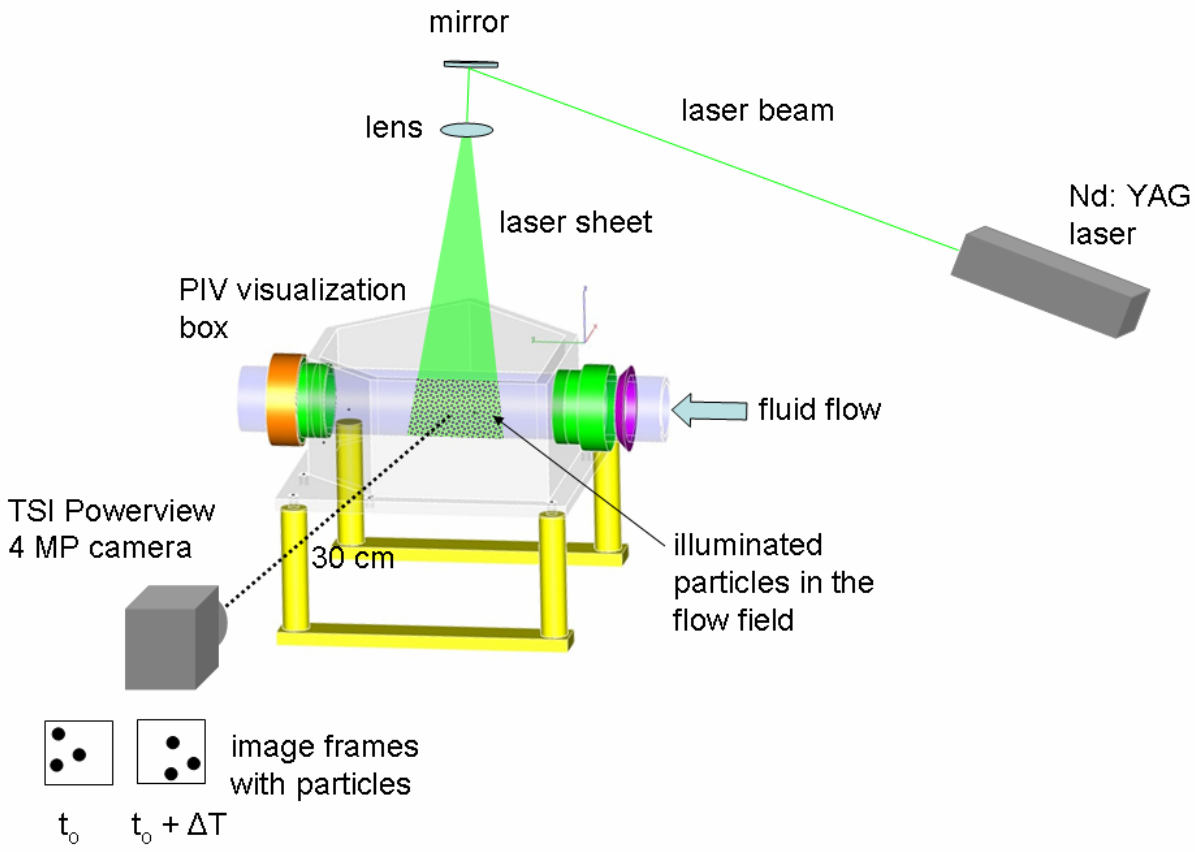

Figure 2- 21. PIV setup.

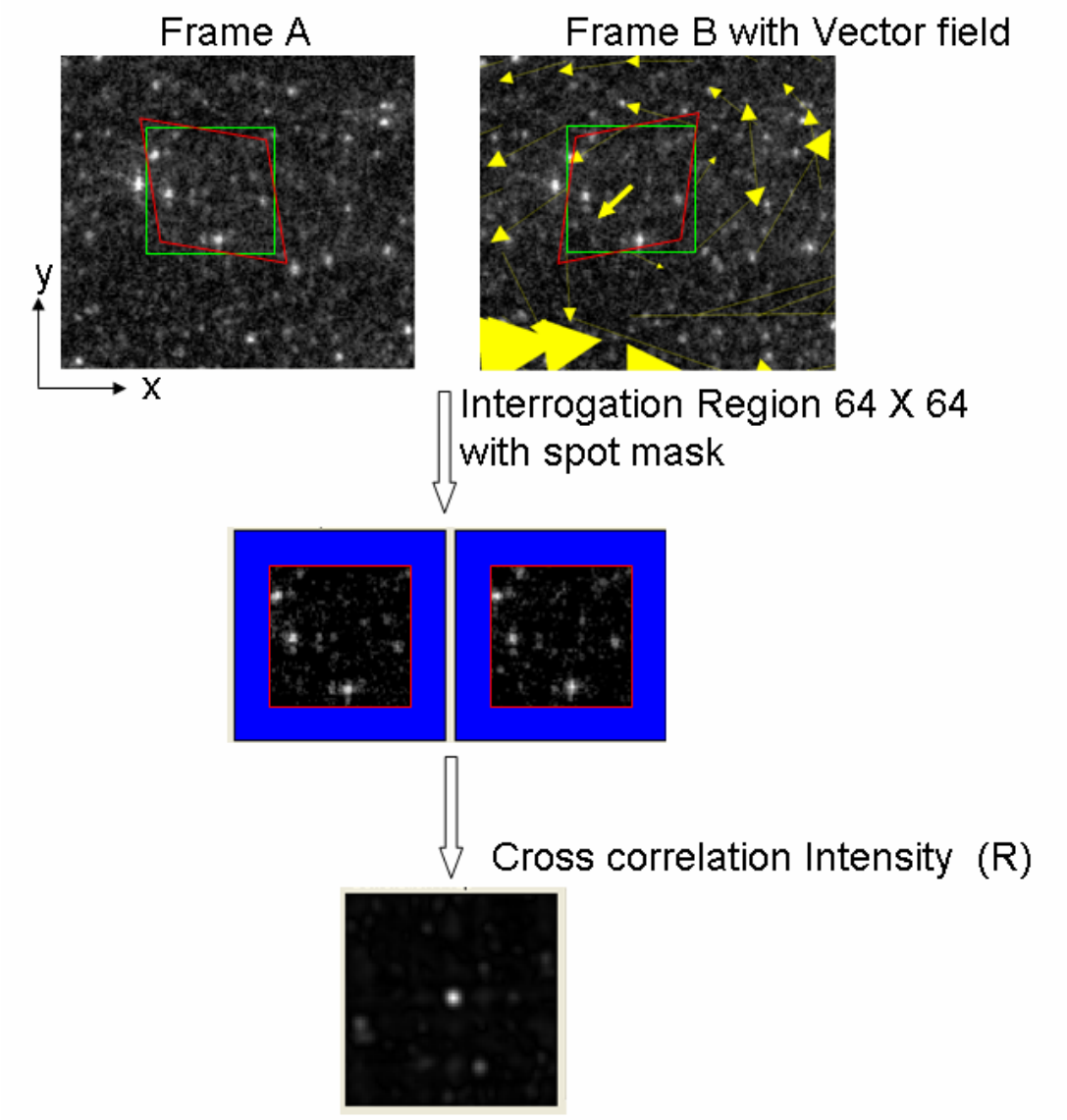

Figure 2- 22. PIV displacement vector processing. Velocity vectors denoted by arrows. Arrowhead size scales with speed.

Table 1. PIV Experiment steady diaphragm valve flow. ε_u and $\varepsilon_{\omega z}$ are the uncertainty in the u-velocity and z-vorticity values.

Steady Flow Experiment Name	Valve Material Geometry	Upstream Flow Rate [L/min] Reynolds Number	Input Flow Frequency [Hz]	Image Pairs	Pulse Separation Time τ [μs]	Vector Field [cm X cm] Vector # (row X col.)	ε_u [cm/s] % of U_{bulk} $\varepsilon_{\omega z}$ [s^{-1}] % of D/U_{bulk}
Upstream Laminar	N/A	0.7 600	N/A	500	5000	2.2 X 2.3 (39 X 40)	0.08 3.5 1.96 2.19
Upstream Turbulent	N/A	4.6 3900	N/A	500	100	2.2 X 2.2 (48 X 48)	1.2 8 29.5 4.92
Downstream	Aluminum DV d/D = 0.31	0.7 600	N/A	275	400	2.3 X 2.3 (40 X 40)	0.5 21 12.3 13.6
Downstream	Aluminum DV d/D = 0.31	4.6 3900	N/A	550	50	2.3 X 2.3 (40 X 40)	3.6 24 88.6 14.8
Downstream	MED 4901 DV d/D = 0.31	0.7 600	N/A	275	400	2.2 X 2.2 (39 X 39)	0.46 20 11.3 12.5
Downstream	MED 4901 DV d/D = 0.31	4.6 3900	N/A	550	80	2.2 X 2.2 (39 X 39)	2.6 17 64 10.6
Downstream	MED 4901 DV d/D = 0.69	10.5 8800	N/A	825	150	2.3 X 2.2 40 X 39	1 3 24.6 1.8

Table 2. PIV Experiment pulsatile diaphragm valve flow. ε_u and $\varepsilon_{\omega z}$ are the uncertainty in the u-velocity and z-vorticity values.

Pulsatile Flow Experiment Name	Valve Material Geometry	Average Flow Rate [L/min]	Input Flow Frequency [Hz]	Image Pairs	Pulse Separation Time τ [μs]	Vector Field [cm X cm] Vector # (row X col.)	ε_u [cm/s] % of U_{bulk} $\varepsilon_{\omega z}$ [s^{-1}] % of D/U_{bulk}
Downstream	MED 4901 DV d/D = 0.31	0.54	1.167	40	Phase dependent	2.3 X 2.2 (46 X 46)	Phase dependent

2.5.2 Volumetric 3-Component Velocimetry

Unlike PIV, volumetric 3-component velocimetry (V3V) uses particle tracking in a three-dimensional space to reconstruct instantaneous volumetric velocity vector fields. V3V particle tracking experiments used a dual-head Nd:YAG laser (λ = 532 nm) with 50 mJ/pulse (see Fig 2-23.). A combination of two 25 mm focal length cylindrical and three 500 mm focal length spherical lenses were mounted in front of the beam exit in perpendicular orientations to produce an ellipsoidal cone of laser light. The three-aperture volumetric cameras (TSI Inc.) were arranged in an equilateral triangle 17 cm apart. Each CCD array had 2048 X 2048 pixels of size 7.4 microns and depth 12 bits. Each camera had a 50 mm Nikon lens with an aperture setting of f#16 and the entire camera lens unit was placed 62.5 – 67.5 cm from the measurement region, which was within the focal depth of the camera. The CCD censors were offset relative to the lens so that all images intersect at the reference plane based on calibration. A pair of laser pulses was separated by ΔT = 50-2500 μs, depending on the experimental conditions, to ensure 25% particle displacement similar to PIV (see Section 2.5.1). Seeding particles, 42 micron silver-coated hollow glass spheres, were identified and tracked in 3D space. The particle density is shown in Fig. 2-24 with the 2D view similar to that of PIV. However, the added depth of the illuminated volume as opposed to a sheet results in a lower seeding density (Pereira et al., 2006). The field of view for testing the transparent silicone valve was approximately 3.6 cm in length (x) and 1.6cm across the diameter of the root (y and z). Initial processing resulted in sufficient particle registration in the flow field. The camera, laser, and the pump piston were triggered by the same synchronizer as

used in the PIV (TSI 610034 1 ns resolution). The synchronizer enabled the pulses from each laser to straddle neighboring camera frames similar to that of PIV. The volumetric velocity vector fields were captured at 7.25 Hz.

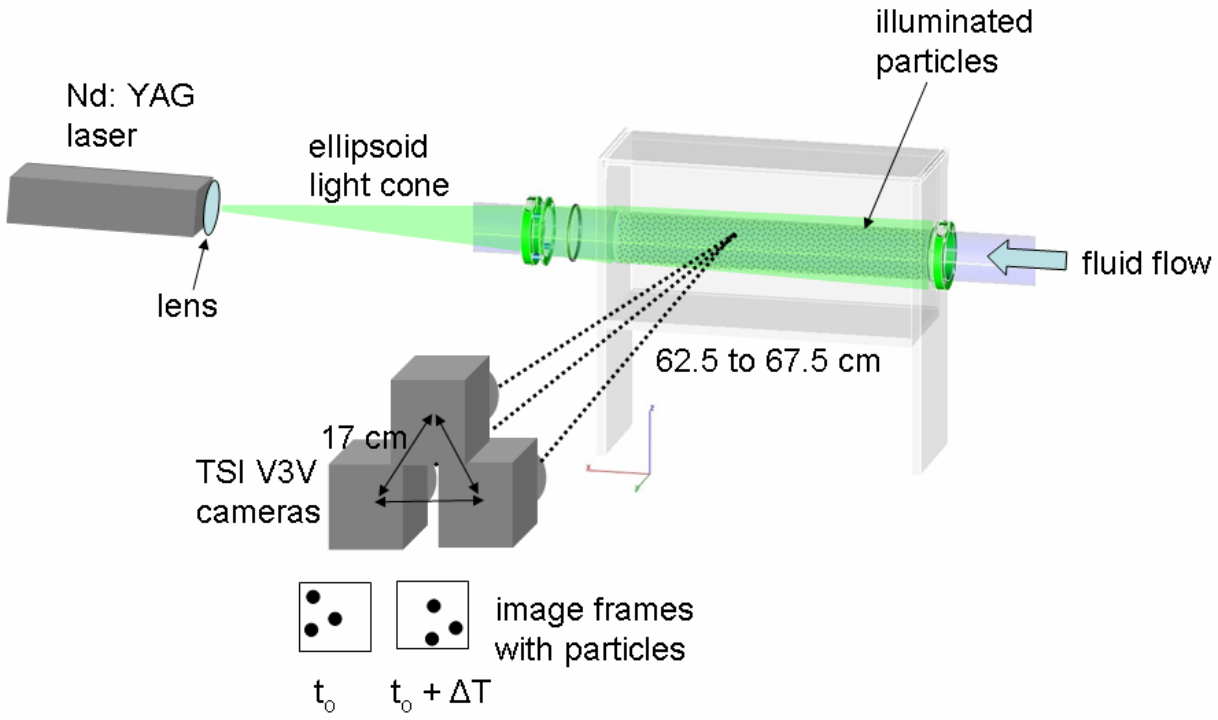

Figure 2- 23. V3V setup. ΔT is laser pulse separation time.

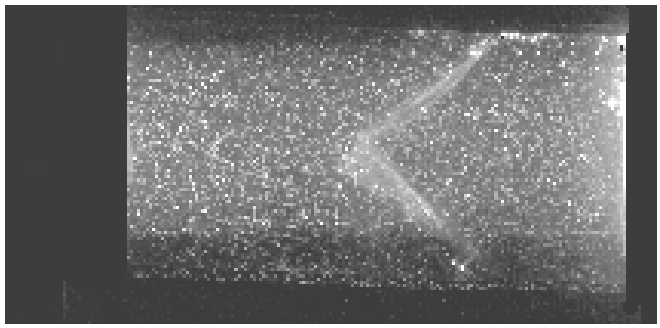

Right camera

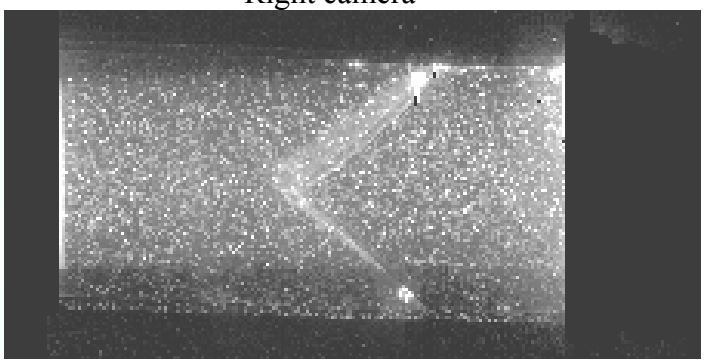

Left Camera

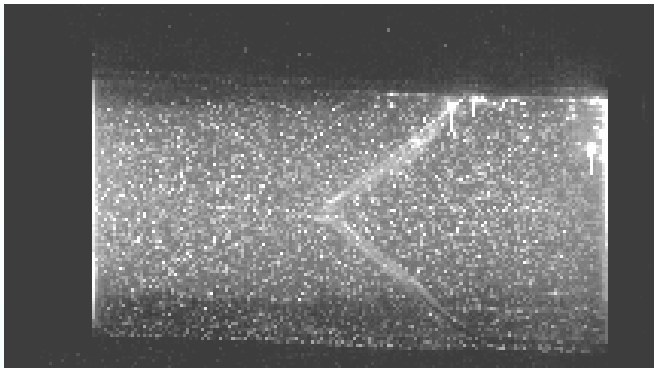

Top Camera

Figure 2- 24. V3V images of transparent silicone valve with illuminated particles.

The instantaneous volumetric velocity vector fields were determined by the algorithm using InsightV3V software (Version 1.0.2. TSI Inc.). A spatial calibration was performed across the volume of the measurement plane to reference the particle location. A calibration target with dots having regular grid spacing of 2.5 mm in the horizontal (x) and vertical (y) directions was placed at a distance of 62.5 cm. The target was traversed a distance of 5 cm in 0.25 cm increments over the depth (z) resulting in the final location of the grid 67.5 cm from the CCD sensor. Fig.2-25 shows calibration dots at -67.5 and -

62.5 cm in z-direction as registered by the CCD sensor. The plane at which the optical axis of all three camera CCD sensors intersected (z = -712.4 and M = 119 pix/cm) defined the reference plane. This was the plane where the x-y location of the calibration dot was the same for all three sensors. As the target was translated, the dot image location on the sensor diverged and was registered as a triangle. The size of the triangle determined the plane location along the depth and defined a signature graph.

The 2D particle locations from each of the three cameras were identified for both frames A (at t_o) and B ($t_o + \Delta T$). In total there were six separate images. A baseline intensity threshold of 35 out of 4096 grayscale along with a local peak intensity threshold ratio of 2 with respect to the background noise was fit, so anything above it was identified as a particle in the 2D plane. A Gaussian intensity profile was fit to the particle image, and the peak represented the center of the particle. Individual particles were identified as '*triplets*' based on the calibration algorithm. The particle to be registered must fall within 0.5 pixels of the triangle defined by the calibration signature graph. Fig.2-26 schematically shows three triplets identifying the three particles on a frame. Each centroid 'c' of the triplets represents the x, y-location of each particle, and the size of the triplet represents the z-location or depth.

The particle 3D displacement was tracked by the movement of these triplets within the flow volume. Generally, multiple particles neighbor one another; therefore, a relaxation method was used to track the 3D particle displacement based on the work of Ohmi (2000) and Pereira (2006). The flow volume was divided into 'clusters'. For example, assume Cluster A has multiple particles. Cluster B was assigned a larger volume based on potential particle displacement out of the initial cluster volume. The particle tracking was based on the assumption that neighboring particles in the cluster move in a similar direction. A match probability P(m,n) was assigned between the particles m in cluster A and n in cluster B. For example, in Fig. 2-26 m = 5 and n = 5. Initially each particle pair was assigned the same probability, 1/N, where N is the number of possible pairs between clusters A and B. Therefore, P(1,1), P(1,2), P(1,3), P(1,4), and P(1,5) = 1/5. An initial displacement 'guess' of particle a_1 to b_1 would give a maximum probability of other neighboring particles matching in displacement within a given tolerance threshold. However, if particle a_1 was paired with b_5, the probability of the

neighboring particles matching in displacement would be greatly reduced. This matching procedure was iteratively recomputed for all particles in the cluster until they converged. The computed vectors were spaced randomly in the 3D volume. However, to compute quantities requiring spatial derivatives such as vorticity and swirl, the random vectors were interpolated onto a Cartesian grid with a spacing of 1 mm. See Table 2 for V3V experiments conducted.

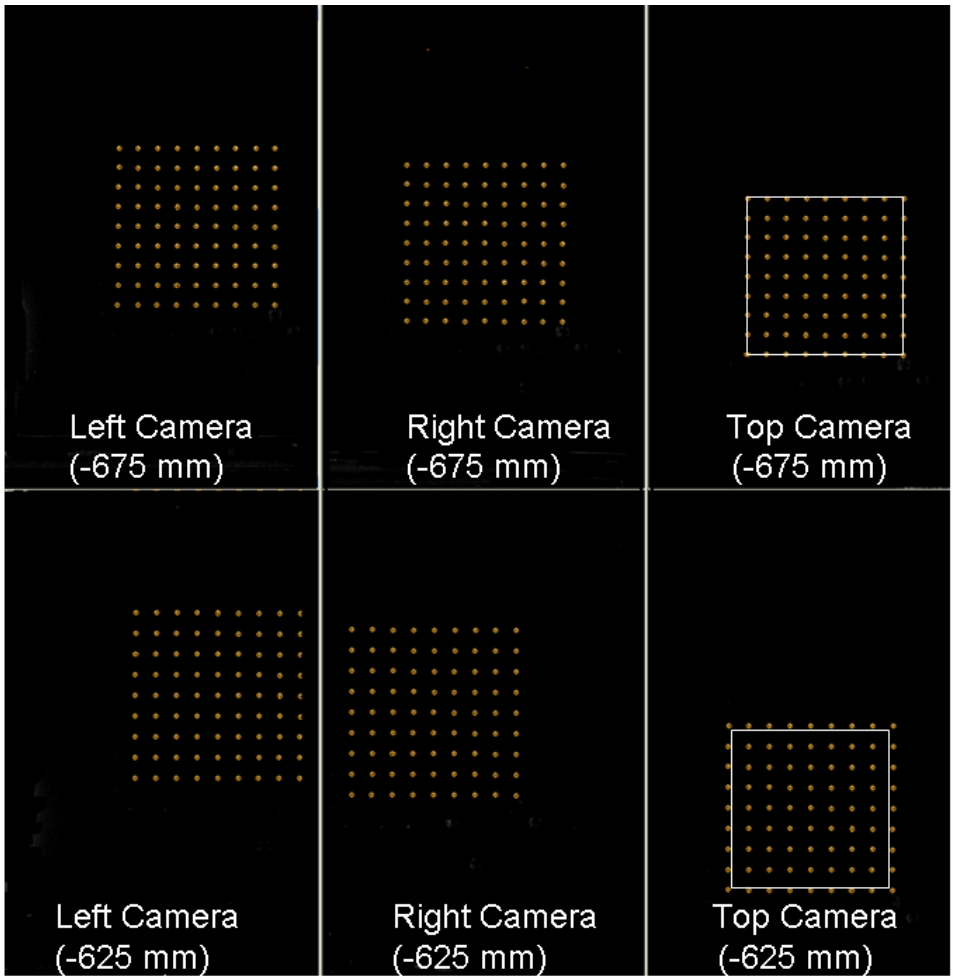

Figure 2- 25. V3V calibration grid and magnification.

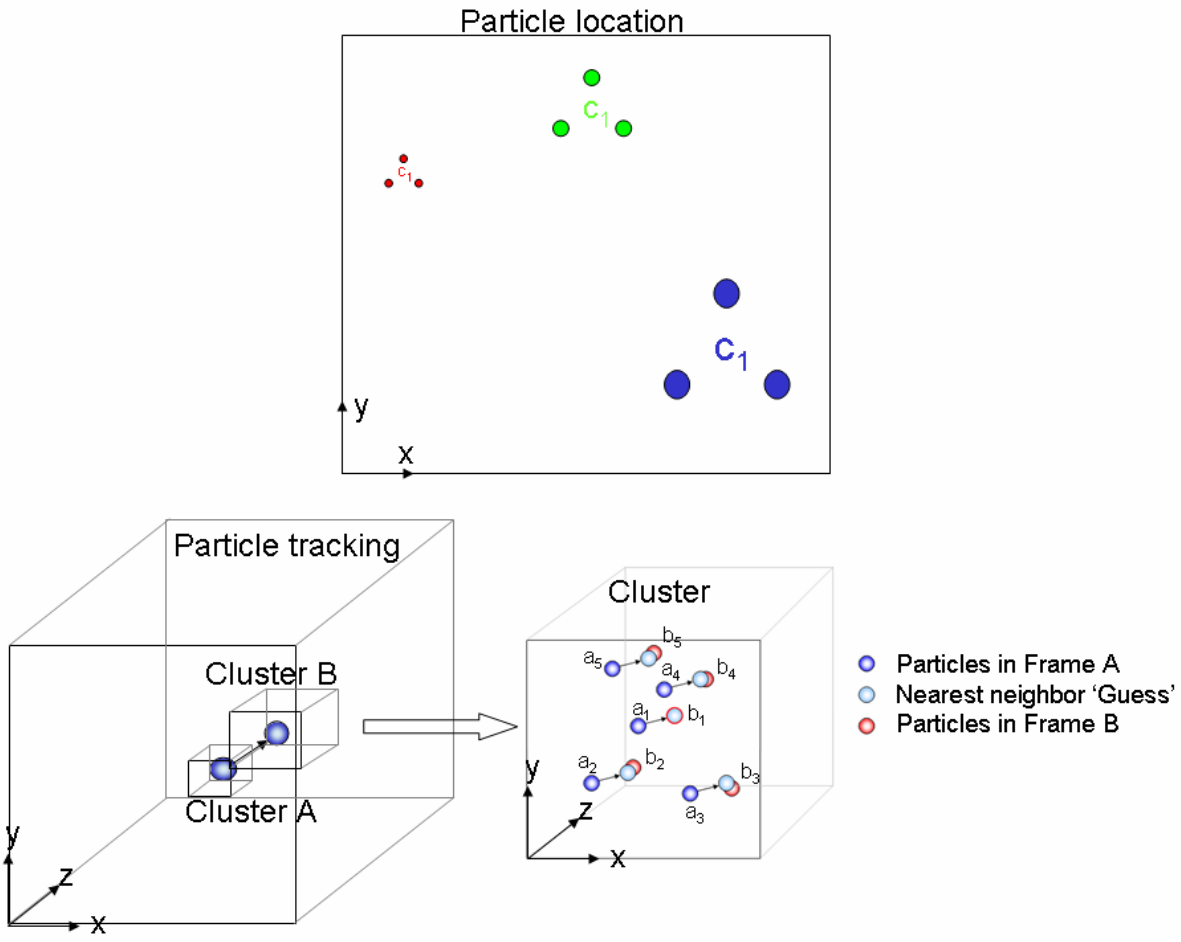

Figure 2- 26 V3V processing.

Table 3. V3V Experiments pulsatile silicone valve. ε_u and $\varepsilon_{\omega z}$ are the uncertainty in the u-velocity and z-vorticity values.

Pulsatile Flow Experiment Name	Valve Material Geometry	Average Flow Rate [L/min]	Input Flow Frequency [Hz]	Image Pairs	Pulse Separation Time τ [μs]	Vector Field [cm X cm X cm] Vector # (x X y x Z)	ε_u [m/s] % of U_{bulk} $\varepsilon_{\omega z}$ [s^{-1}] % of D/U_{bulk}
Transparent Silicone Valve	Valve Sylgard 184	4.21	1.167	5	Phase dependent	3.6 X 1.6 X 1.6 (26 X 13 X 13)	Phase dependent

2.5.3 Hot-Film Anemometry

Since the PIV system provided only instantaneous views of the flow with limited temporal resolution, hot-film anemometry was performed to provide additional point-measurements of power spectra downstream of the diaphragm valves. A Dantec hot-film probe was inserted through a hole in the pipe section at 0.9 pipe-diameters downstream of the diaphragm valve. The spanwise location of the hot-film, which was perpendicular to the flow, was positioned in the developing shear layer downstream of a diaphragm valve. The radial location was chosen as that which yielded the strongest fluctuation energy. The probe was operated in a constant temperature mode at an overheat ratio of 1.2 and attached to an anemometer from AA Lab Systems (AN-1003). Labview systems DAQ NI PCI-6122 data acquisition system having a 16-bit resolution, a maximum transfer rate 100 kS/s, and operating at ±10 V was used. The sampling rate of 1000 Hz (f_s) used resulted in a Nyquist frequency of 500 Hz sufficient for resolving the fluctuation energy at the Reynolds numbers tested. A total of N = 130172 data points were acquired for each case, and power spectra were computed using Matlab Version 7.0 Release 14.

2.6 Experimental Uncertainty Analysis

The uncertainty of an instantaneous velocity vector for PIV is calculated as:

$$\delta u = \frac{\delta \Delta X}{M \Delta \mathrm{T}} \tag{2-2}$$

where, $\delta\Delta X$ is the 0.1 pixel displacement accuracy in the PIV algorithm, M is the magnification factor, and ΔT is the laser pulse separation time. The uncertainty in the instantaneous velocity vector for V3V is calculated as

$$\delta u = u_{\max}\left(\frac{\delta \Delta X}{\Delta X_{\max}}\right) \tag{2-3}$$

note

$$\frac{u_{\max}}{\Delta X_{\max}} = \frac{1}{M \Delta T} \tag{2-4}$$

where, $\delta\Delta X$ = 20μm is the maximum particle x-displacement accuracy in the V3V algorithm, u_{max} is the maximum particle velocity measured, and ΔX_{max} = 1mm is the

maximum particle displacement. $\delta\Delta Y$ and $\delta\Delta Z$ are 20μm and 80μm, respectively. Detailed derivation for Eq. 2-2 and 2-3 are shown in Appendix D.

The velocity gradients (K) are calculated using central difference scheme (see Appendix A). Table 3 above lists the analytical form of the uncertainties for all the gradients of the three velocity components. The grid spacing between the velocity vectors is defined as Δx, Δy, and Δz. The subscripts 1 and 2 for velocity represent the velocity at the two locations used to compute the gradient. These gradients were used to calculate vorticity, swirl, and shear stress values. The detailed derivation is shown in Appendix A.

The statistical uncertainties for all measurements are presented in Table 5.

Table 4. Uncertainties in velocity gradients. K represents any gradient and δK is the uncertainty in the gradient. Δx, Δy, and Δz indicate the spacing between velocity vectors. Detailed calculation is shown in Appendix D.

K	**δK**
$\frac{\partial U}{\partial x}$	$0.707\frac{\delta U}{\Delta x}$
$\frac{\partial U}{\partial y}$	$0.707\frac{\delta U}{\Delta y}$
$\frac{\partial U}{\partial z}$	$\sqrt{\left(\frac{\delta U_1+\delta U_2}{2\Delta z}\right)^2}$
$\frac{\partial V}{\partial x}$	$0.707\frac{\delta V}{\Delta x}$
$\frac{\partial V}{\partial y}$	$0.707\frac{\delta V}{\Delta y}$
$\frac{\partial V}{\partial z}$	$\sqrt{\left(\frac{\delta V_1+\delta V_2}{2\Delta z}\right)^2}$
$\frac{\partial W}{\partial x}$	$0.707\frac{\delta W}{\Delta x}$
$\frac{\partial W}{\partial y}$	$0.707\frac{\delta W}{\Delta y}$
$\frac{\partial W}{\partial z}$	$\sqrt{\left(\frac{\delta W_1+\delta W_2}{2\Delta z}\right)^2}$

Table 5. Statistical uncertainties δ for the mean and rms components.

Experimental condition	Measurement location	δ_{Umean} % of U_{bulk}	δ_{Vmean} % of U_{bulk}	δ_{Urms} % of U_{bulk}	δ_{Vrms} % of U_{bulk}
LR d/D = 0.31	Jet exit centerline	0.03	0.02	0.02	0.01
LR d/D = 0.31	Jet exit shear layer	0.33	0.03	0.02	0.02
LC d/D = 0.31	Jet exit centerline	0.03	0.02	0.02	0.2
LC d/D = 0.31	Jet exit shear layer	0.5	0.07	0.04	0.05
TR d/D = 0.31	Jet exit centerline	0.02	0.02	0.02	0.01
TR d/D = 0.31	Jet exit shear layer	0.32	0.08	0.02	0.04
TC d/D = 0.31	Jet exit centerline	0.03	0.02	0.02	0.01
TC d/D = 0.31	Jet exit shear layer	0.05	0.04	0.03	0.03
TC d/D = 0.69	Jet exit centerline	0.0025	0.001	0.002	0.0007
TC d/D = 0.69	Jet exit shear layer	0.04	0.007	0.03	0.005

Chapter Three: Results

3.1 Diaphragm Valve

A silicone valve with an orifice was mounted inside an acrylic pipe and subjected to both steady and pulsatile flows. The flow rate was controlled, and pressure and diaphragm deformation were recorded along with velocity fields upstream and downstream of the diaphragm. The goal of the experiments conducted was to obtain measurements needed to validate computational codes incorporating fluid-structure interaction.

In the following sections, the streamwise and radial directions of the flow are represented by the cylindrical (x, r) coordinate system with the origin located at the pipe centerline and coincident with the streamwise location of the undeformed diaphragm. The streamwise and radial velocity components are denoted as U and V respectively with $V > 0$ corresponding with outward radial velocity.

3.1.1 Diaphragm Tensile Testing

The engineering stress (s) versus strain (ε) curves, obtained from uniaxial tensile testing, are shown in Fig. 3-1 for the three silicone materials. The mean of four trails for each material is plotted and fell within 13% of the individual measurements. A neo-Hookean material model was curve-fit, and shear modulus values (μ) of 0.016 MPa, 0.03 MPa, and 0.11 MPa were obtained for MED 4901, MED 4905, and MED 4-4220 respectively. These values correspond to a Young's modulus of 0.048 MPa, 0.09 MPa, and 0.33 MPa, respectively, which are of similar order to the values measured in native aortic valve leaflets (Clark, 1973, Mavrilas and Missirlis, 1991). According to the results in Fig. 3-1, within the range of strain $0 < \varepsilon < 0.5$, a neo-Hookean model is sufficient for the three MED materials.

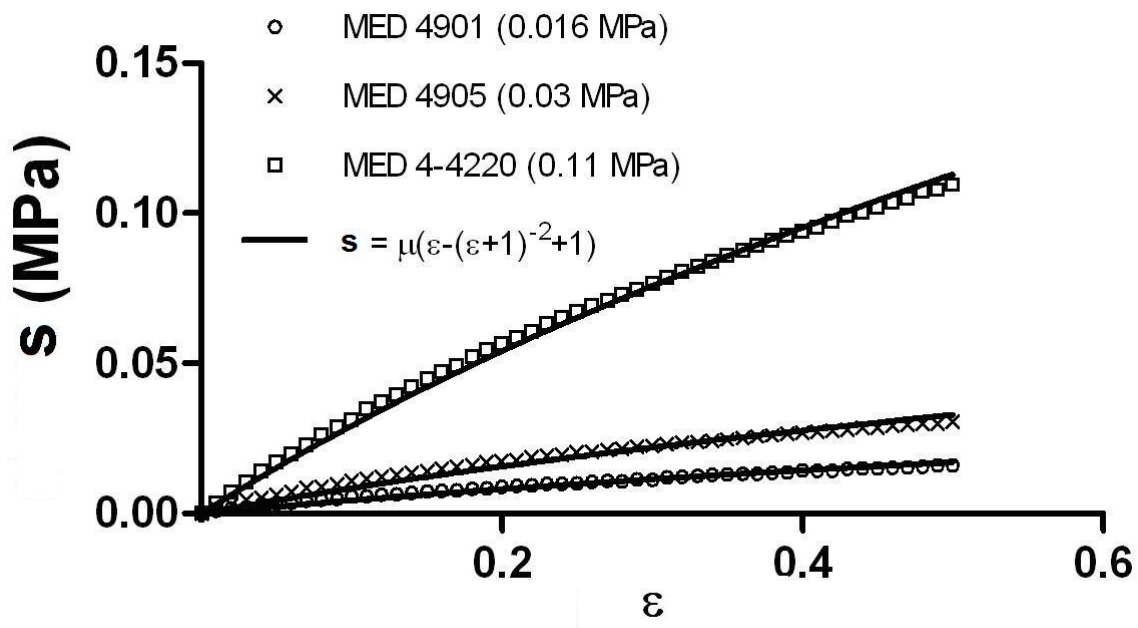

Figure 3- 1. Uniaxial tensile tests of rectangular silicone diaphragm samples. A neo-Hookean material model is curve-fit for MED 4901 (μ = 0.016 MPa), MED 4905 (μ = 0.03 MPa), and MED 4-4220 (μ = 0.11 MPa).

3.1.2 Steady Flow

Pressure, deformation, and flow-rate measurements were carried out over a range of pipe Reynolds numbers Re = 600 - 8800 based on the average velocity over the pipe cross-section U_{bulk} and the pipe diameter D = 2.54 cm. Detailed velocity field measurements were obtained for two volumetric flow rates of 0.7 L/min (Re = 600) and 4.7 L/min (Re = 3900) corresponding with fully-developed laminar (Poiseuille) and turbulent flow upstream of the small orifice (d/D = 0.31) diaphragm, respectively. Both Reynolds numbers yield significant diaphragm deformation and are within the physiological range (Stein and Sabbah, 1976). Additional velocity fields were acquired for flow through the larger orifice diaphragm (d/D = 0.69) at 10.5 L/min (Re = 8800) with the similar intent of producing significant diaphragm deformation.

3.1.2.1 Diaphragm Deformation with Pressure Drop and Flow Rate

Fig. 3-2 shows a side view representation of the deformation for the MED 4901 diaphragm (μ = 0.016 MPa, d/D = 0.31) at Re = 600, 3900, and 8800. For all Reynolds

numbers examined, the diaphragm location was steady and did not vary in time due to fluctuations in the flow. Note that the diaphragm could not be observed from x/D = 0 to 0.04 due to the visual obstruction created by the mounting ring. The diaphragm has a concave deformation with respect to the upstream flow. The undeformed orifice radius is 0.16D. At the lowest Reynolds number of 600, the axial deflection of the diaphragm tip ($\Delta x/D = 0.07 \pm 0.0035$) is more prominent than the radial orifice expansion ($\Delta d/D = 0.015 \pm 0.003$). As Re increases to 8800, however, the radial expansion ($\Delta d/D = 0.20 \pm 0.0035$) becomes comparable to the axial deflection ($\Delta x/D = 0.24 \pm 0.0035$). For this diaphragm, the circumferential strain at the location of the orifice ($\Delta d/d$) increases with Reynolds number as shown in Fig. 3-3. In general, the higher modulus diaphragms, not shown, deforms less at like Reynolds numbers, but exhibits similar concave shapes (not shown). The concave shape occurred also when the orifice size was increased (e.g. d/D = 0.69).

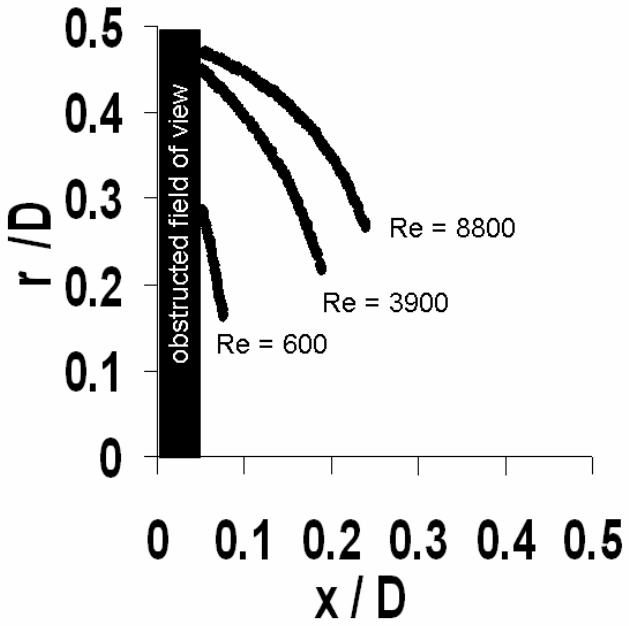

Figure 3- 2. Diaphragm (μ = 0.016 MPa) deformation state for three Reynolds numbers, d/D = 0.31.

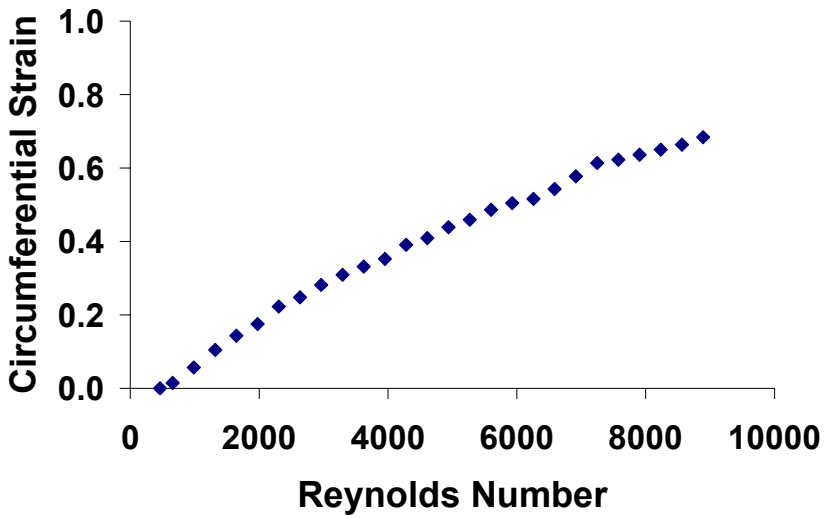

Figure 3- 3. Circumferential strain (Δd/d) measured at the diaphragm (μ = 0.016 MPa) orifice versus Reynolds Number, d/D = 0.31.

Plots of normalized pressure drop (Euler number) versus flow rate (Reynolds number) are shown in Fig. 3-4 for the four diaphragms with d/D = 0.31. The Euler number is defined as

$$Eu = \frac{p_{up} - p_{down}}{0.5\rho U_{bulk}^2} \qquad (2)$$

It expresses the relationship between the local pressure force to inertial force. An ideal frictionless flow would have an Euler number of 1 whereby all the pressure energy is converted into velocity. Any energy loss in the flow due to friction would lead to values greater than one. For the rigid diaphragm, the Euler number is independent of Reynolds number over this range, and the value of Eu ~ 200 is consistent with findings by Morrison (2003) for d/D = 0.31. For the compliant diaphragms (open symbols), however, the Euler number decreases with increasing Reynolds number. Additionally, as the diaphragm compliance increases (μ decreases), the Euler number decreases more strongly. From Figs. 3-2 and 3-3, it is clear that the Euler number decreases because of orifice expansion.

To account for this expansion, we can calculate a discharge coefficient (C_d) as the ratio of actual flow rate through the orifice to the ideal (or potential) flow rate based on

the measured pressure drop. In this case, we assume that our measured pressure drop equals the difference between the pressure upstream of the orifice and the pressure at the orifice location. The measured pressure difference includes losses mainly due to flow separation upstream, friction, and turbulence. Fig. 3-5 shows C_d versus Reynolds number for the rigid and the most compliant (μ = 0.016 MPa) diaphragms with d/D = 0.31. In the range 170 < Re < 680 range, the Druck differential pressure transducer and Transonic ultrasonic flow meter were used, and in the range between 990 < Re < 8800, the Vivitro pressure transducers and Carolina Medical electromagnetic flow meter were used. The results, plotted with error bars, suggest that the stated uncertainty in the Vivitro/Carolina Medical measurements is larger than the actual uncertainty, so that the results in the 990 < Re < 3000 range appear reasonably accurate. Since C_d is calculated based on the actual orifice area at each Reynolds number, its value remains fairly constant, in fact it decreases slightly over the range studied for both the rigid and compliant diaphragms. The C_d values for the rigid diaphragm are similar to those reported in the literature in which P_{down} was located at x/D = 0.5 (Perry et al., 1984). Interestingly, the compliant diaphragm (μ = 0.016 MPa) has a smaller discharge coefficient at all Reynolds numbers, indicating a smaller efficiency or a larger pressure loss. Although the curved diaphragm shape might be expected to decrease upstream separation near the pipe wall (and therefore increase C_d), the fact that C_d decreases suggests that the curved shape may generate a stronger vena contracta than the flat rigid orifice (see velocity results below).

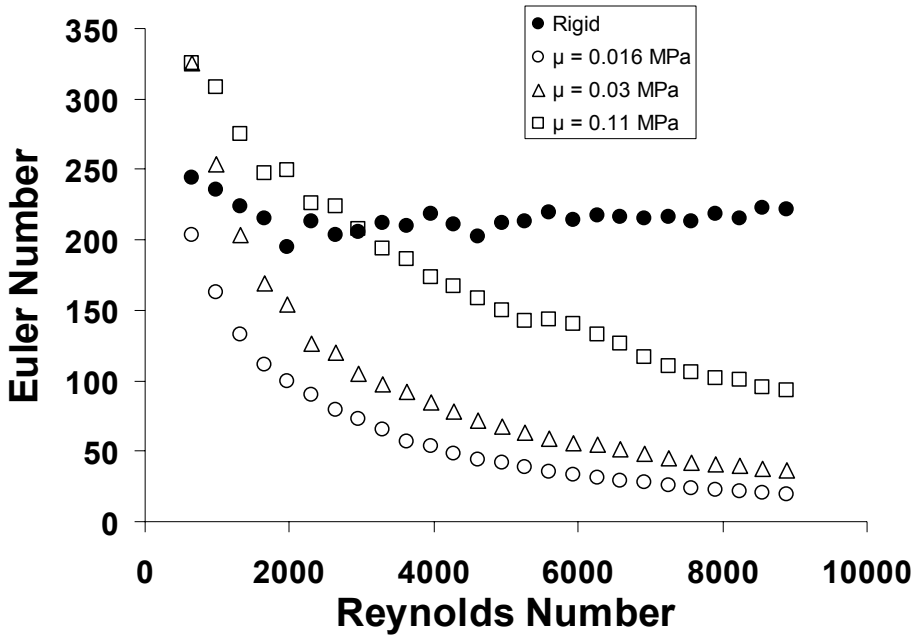

Figure 3- 4. Normalized pressure drop versus Reynolds number, d/D = 0.31.

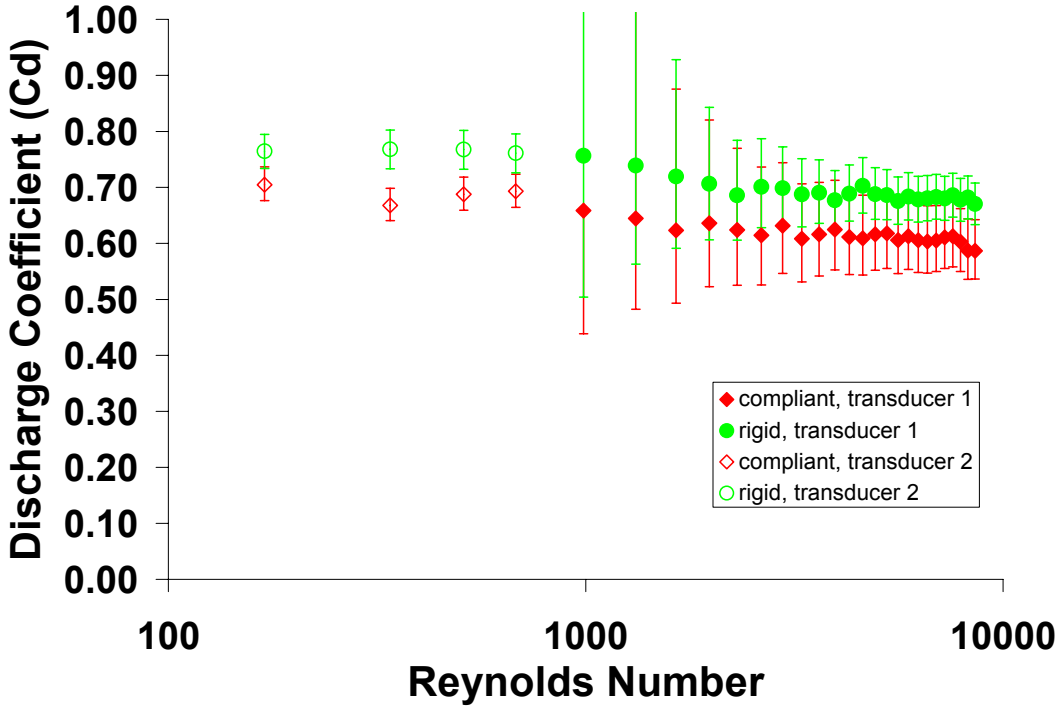

Figure 3- 5. Discharge coefficient of the compliant (μ = 0.016 MPa) and rigid diaphragms for Reynolds number range of 170 to 8800, d/D = 0.31. Low range (Re = 140 to 680) and high range (Re = 990 to 8800) were acquired using separate pressure and flow rate instrumentation.

3.1.2.2 Upstream Flow

PIV velocity fields acquired upstream of the diaphragm were averaged over the 500 samples for both Re = 600 and 3900. All velocities are normalized by U_{bulk}. The mean and RMS streamwise velocity profiles are shown in Fig. 3-6 at two streamwise locations for both Re = 600 (left) and Re = 3900 (right). For Re = 600, the mean curve, U/U_{bulk}, resembles Poiseuille flow (circles). The two streamwise locations plotted (-8.87 D and -8.64 D) indicated by the open and solid circles show excellent overlap. The RMS velocity values u_{rms}/U_{bulk}, plotted as squares, are also small as expected for the laminar flow, and result mainly from uncertainty in the PIV correlations. For Re = 3900, the mean streamwise profile is blunter as is characteristic of turbulent flow. Again, the profiles overlap for the two streamwise locations, indicating that the shape is not changing with increasing streamwise distance. Near the centerline, the measured RMS values are dominated by variations due to uncertainty in the PIV measurements, However, the peak u_{rms}/U_{bulk} level is shown to be 0.23 at r/D = 0.44 in Fig. 3-6. This value is significantly larger than that at Re = 600 as expected for turbulent flow. Note that error bars were not plotted because they span a range smaller than the size of the corresponding symbols.

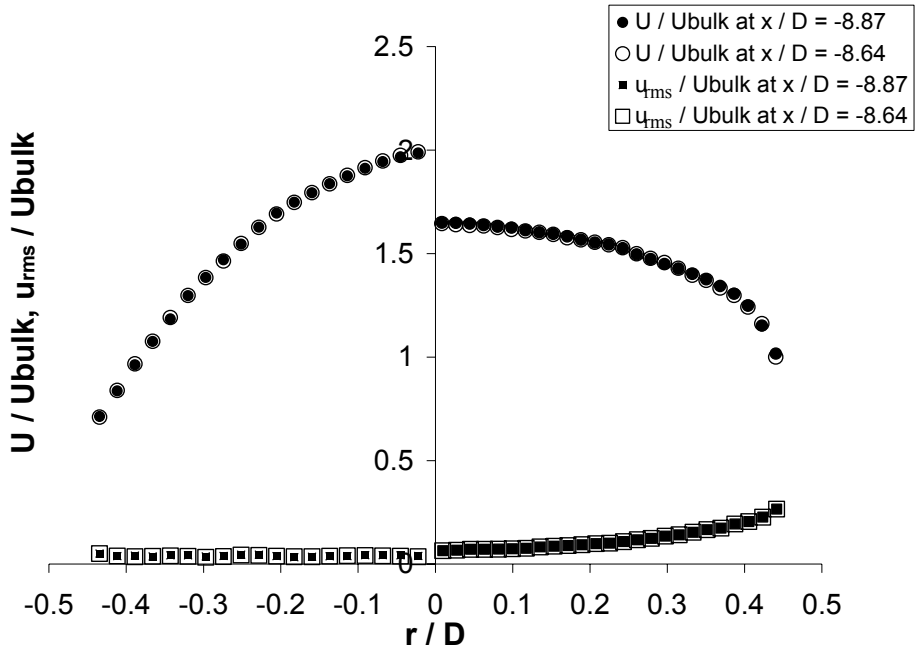

Figure 3- 6. Upstream mean streamwise and urms velocity profiles for Re = 600 (left) and Re = 3900 (right). Measurements obtained to only r/D ~ ± 0.45 due to uncertainty in near wall results.

3.1.2.3 Downstream Flow Fields

Fig. 3-7 shows mean velocity vectors at five streamwise locations for four flow cases. Each plot also includes gray-scale contours of the streamwise RMS velocity (u_{rms}) throughout the measurement field. In the literature considering flow through nozzles or orifices, displacements and velocities are typically scaled by the orifice diameter d and the mean jet velocity through the orifice U_o. In the current study, however, all data are normalized by the pipe diameter D and the mean pipe velocity U_{bulk} since the orifice-based scales vary with Re and diaphragm compliance. The four cases: Re = 600 and rigid diaphragm, Re = 600 and compliant diaphragm, Re = 3900 and rigid diaphragm, and Re = 3900 and compliant diaphragm are labeled as LR, LC, TR, and TC in subsequent discussion. Note that the deformed diaphragm positions are also plotted in the LC and TC cases.

In Fig. 3-7a, the LR case yields jet-like flow downstream of the orifice with a relatively uniform profile for $r/D < 0.16$ at $x/D = 0.15$. At larger radii, the velocity magnitude decreases suggesting the presence of a shear layer already near $x/D = 0$. The jet profile widens as the shear layer spreads becoming more Gaussian in shape. The values of u_{rms}/U_{bulk} are large across a relatively narrow layer up to $x/D = 0.45$. Beyond this location, the layer of significant RMS values spreads rapidly. The relatively sudden spread suggests the rapid growth of instabilities and presence of vortical structures in the shear layer. This growth occurs relatively early compared with the growth in jets exiting contoured nozzles (Crow and Champagne, 1971). By $x/D = 0.65$, u_{rms} is significant all the way to the centerline.

The LC results in Fig. 3-7b are somewhat similar to those observed for LR in that a jet-like flow ensues downstream of the orifice. A key difference, however, is a significant inward radial velocity (indicated by inward pointing vectors) immediately downstream of the orifice, indicating a vena contracta effect caused by the concave diaphragm shape. This radial velocity is quantified in Fig. 3-8b described below. Also, the streamwise velocity is lower at the centerline than at $r/D = 0.15$. By $x/D = 0.34$, the mean velocity profile has become more uniform for $r/D \leq 0.15$, and the inward component has disappeared. In fact, the vectors have a small outward component. The RMS contours in Fig. 3-7b indicate that disturbances grow faster in the LC case than in

the LR case. Note that $u_{rms}/U_{bulk} > 1$ already at x/D = 0.55 for LC, and further downstream, u_{rms}/U_{bulk} is larger both along the centerline and close to the pipe wall for LC than for LR.

For turbulent upstream conditions, the mean velocity profile near the rigid orifice exit (TR in Fig. 3-7c) is similar to the LR case. However, the shear layer spreads outward earlier, already by x/D = 0.25, as indicated by the broadening of the u_{rms} contours. Unlike in both of the low Reynolds number cases, the u_{rms}/U_{bulk} values remain small near the centerline to the limit of the field of view. The RMS results overall indicate possible earlier growth of instabilities in the shear layer, but perhaps the roll up of smaller structures in comparison to those in LR and LC. Mi et al. (2001) performed PIV measurements on unbounded jets issuing from round sharp-edged plates (Their jet Reynolds number based on orifice diameter d was 72,000 as compared with 12,000 for the case in Fig 3-7c). The peak values of u_{rms}/U_o measured by Mi et al. were slightly larger than in the present flow, and the rate of spread in the shear layer was slightly lower (see Fig 3-8). In the present wall-bounded flow, we expect that wall interactions would increase the rate of shear layer growth. Specifically, conservation of mass at each pipe section combined with mass entrainment in the jet causes some mean flow in the negative streamwise direction at large values of r (seen in all cases presented in Fig. 3-7). This countercurrent effect typically serves to accelerate shear layer growth (Strykowski and Wilcoxon, 1993).

Similar to the LC case, the TC case in Fig. 3-7d reveals significant inward radial velocity downstream of the deformed orifice, and the mean streamwise component is lower at the centerline than at the edge of the jet ($r/D \approx 0.16$). The initial profile is broader as a result of orifice area expansion leading to lower local velocity magnitudes. Similar to the TR case, the core of the jet appears relatively undisturbed near the centerline to the limit of the field of view. This difference in behavior (vs. LC and LR) is at least partly explained by the larger initial jet diameter (= the effective orifice diameter d_{eff} for this Reynolds number) since shear layer development depends directly on this scale, not D. The u_{rms}/U_{bulk} levels are in general smaller and spread less quickly than in the other three cases presented.

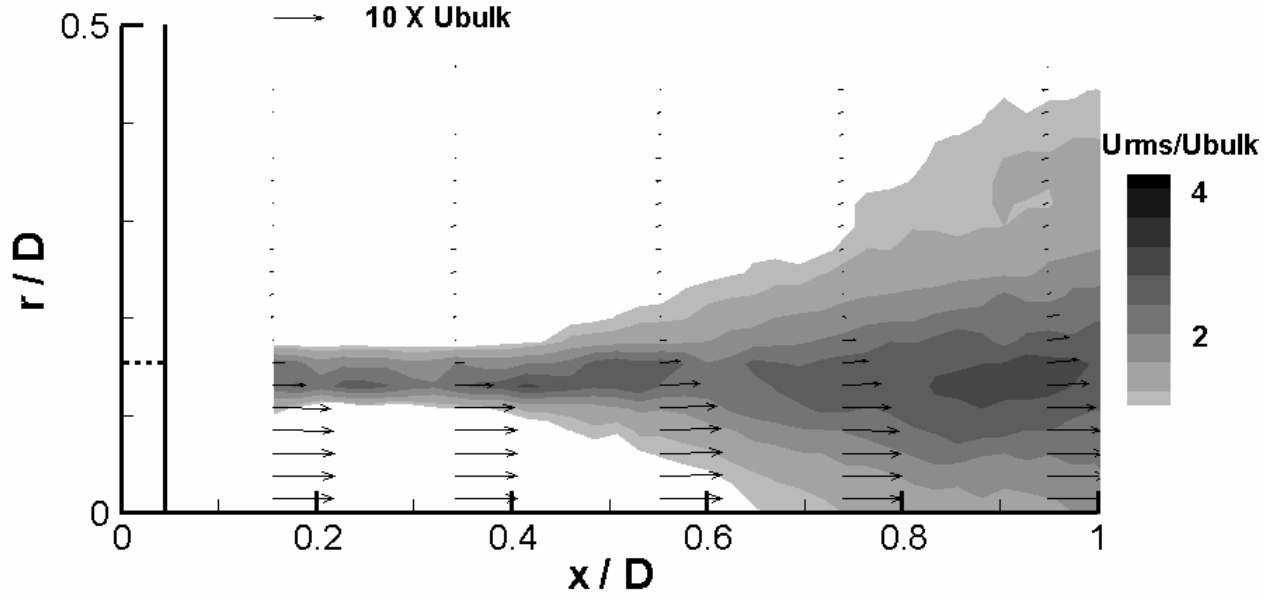
10 X Ubulk
0.5
0
r / D
0
0.2
0.4
0.6
0.8
1
x / D
Urms/Ubulk
4
2

(a) LR

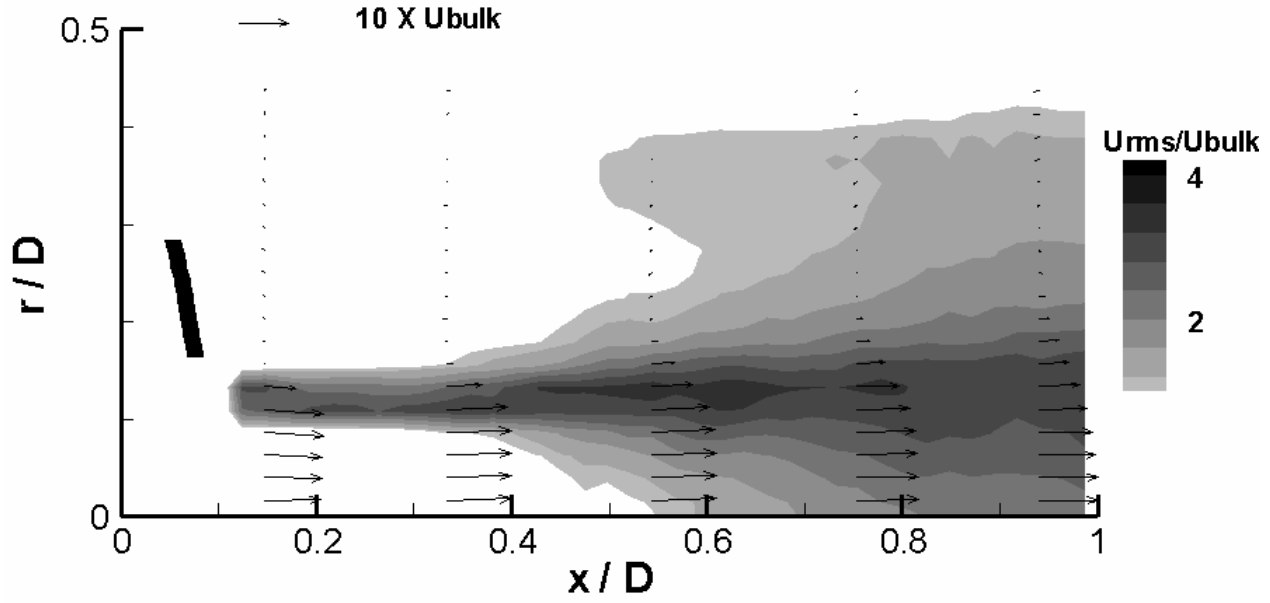
10 X Ubulk
0.5
0
r / D
0
0.2
0.4
0.6
0.8
1
x / D
Urms/Ubulk
4
2

(b) LC

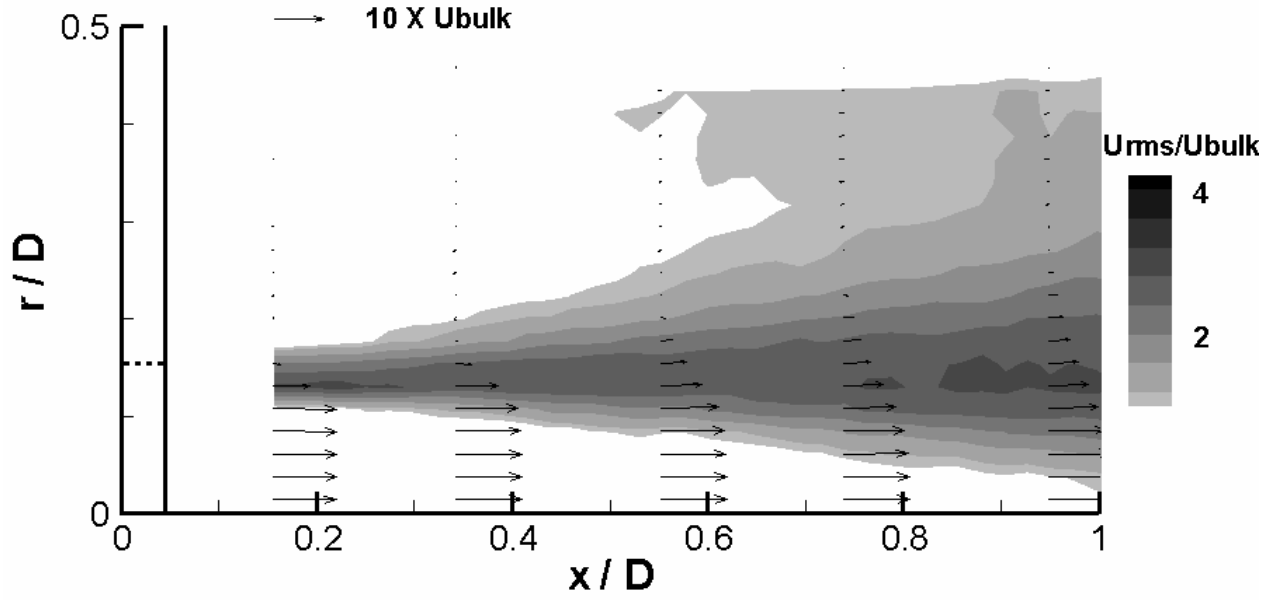

(c)TR

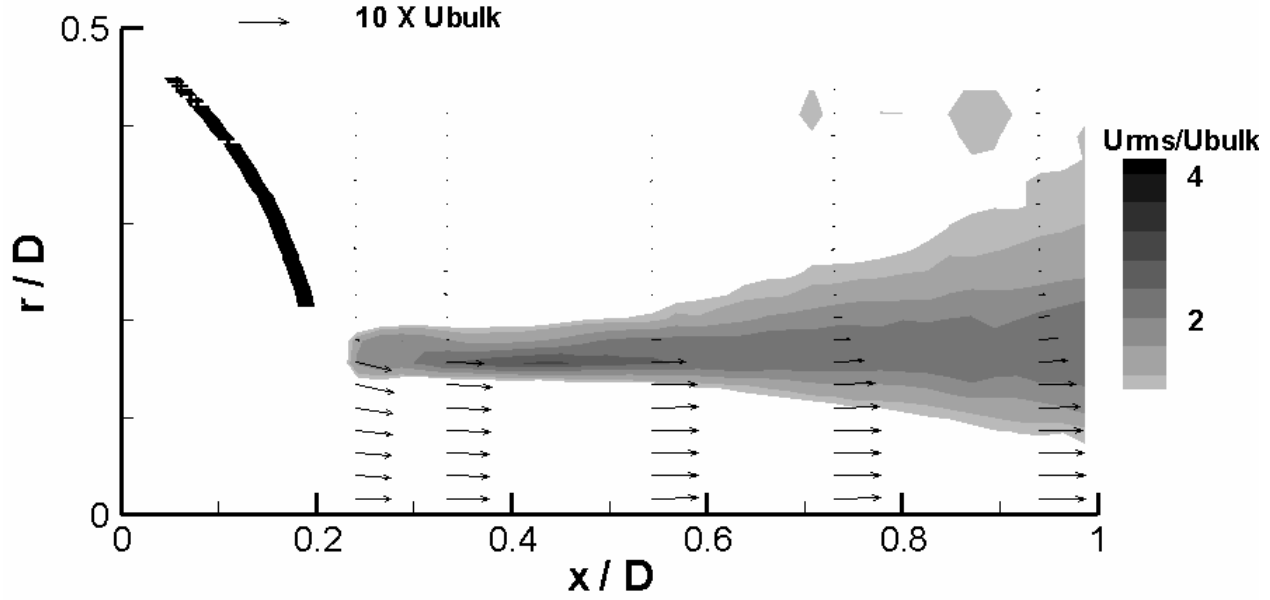

(d) TC

Figure 3- 7. Downstream mean velocity vectors with urms/Ubulk contours. Lowest contour plotted is urms/Ubulk = 1. Contour increments are 0.13. (a) LR: Re = 600, d/D = 0.31; (b) LC: Re = 600, d/D = 0.31; (c) TR: Re = 3900, d/D = 0.31; (d) TC: Re = 3900, d/D = 0.31

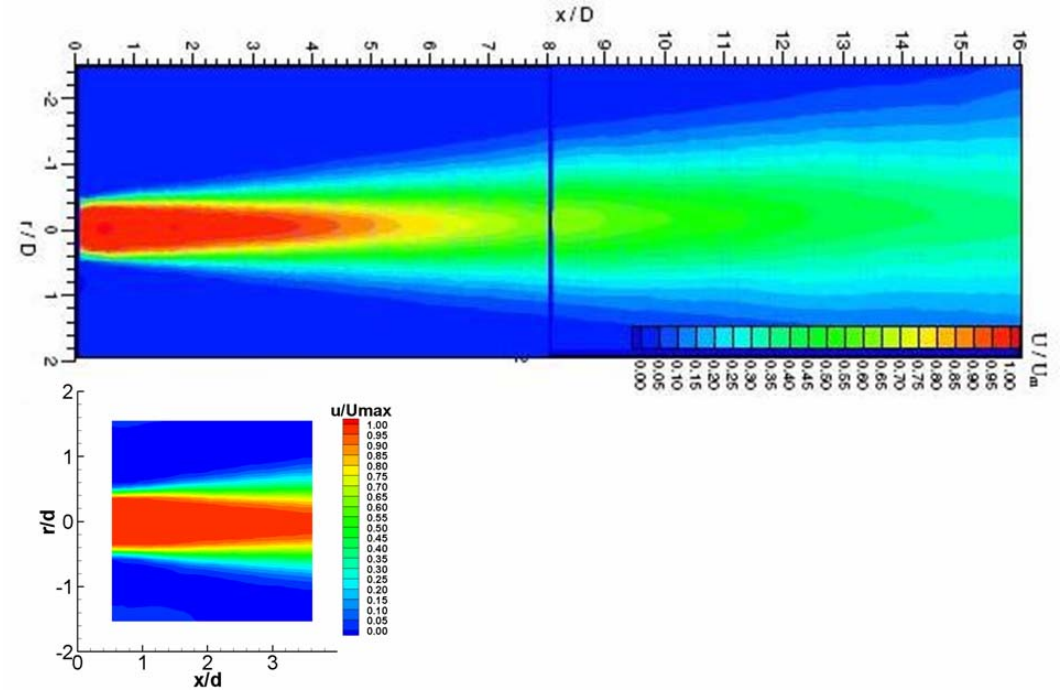

(a)

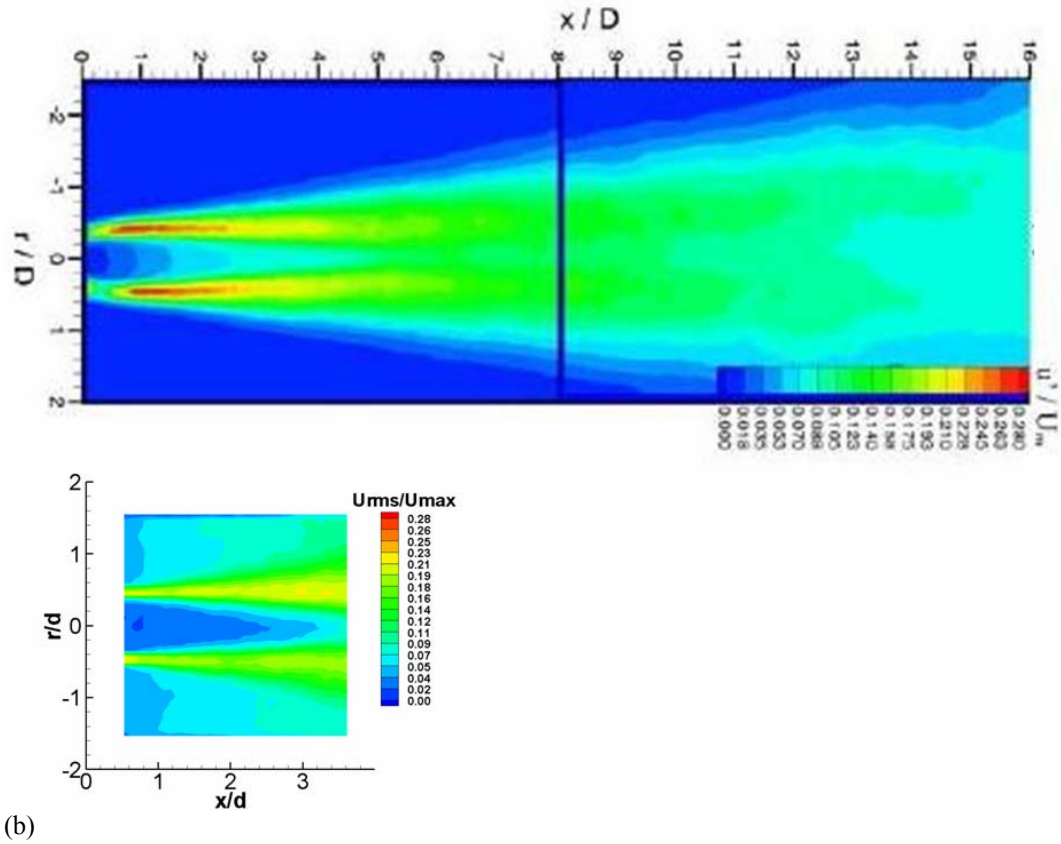

(b)

Figure 3- 8. (a) U velocity contour and (b) u_{rms} contour comparison with Mi et al. (2007) shown with the larger flow field. Contour normalized by maximum velocity for comparison.

To examine the differences in the downstream flow in more detail, the mean and RMS values of the individual velocity components are plotted for all four cases immediately after the orifice exit and further downstream. Figures 3-9 and 3-10 show the profiles resulting from laminar and turbulent upstream conditions respectively. In both figures, circles and triangles represent the exit and +0.8D (or +71 for TC) downstream from the exit locations respectively. Open symbols represent the rigid diaphragm, and closed or solid symbols represent the compliant diaphragm.

In Fig. 3-9a, comparing U/U_{bulk} for the laminar rigid and compliant cases, the LR profile (open circles) is initially uniform for $r/D \leq 0.1$, while the curved diaphragm upstream of the LC profile (closed circles) yields higher streamwise velocity near r/D = 0.1 than at the centerline. As discussed earlier, at this relatively low Reynolds number, the radial expansion of the orifice is minimal so that the initial width of the jet in these two cases is comparable, although in this view, the shear layer (layer with strong radial velocity gradient dU/dr) appears slightly narrower in the LC case. Further downstream at x/D = 0.95, the LC (closed triangles) and LR (open triangles) profiles are very similar. Beyond r/D = 0.25, there is an evidence of an average reverse flow for both cases indicating a persistence of recirculation to this point. In Fig. 3-9b, the plots of V/U_{bulk} emphasize the inward radial flow for $r/D < 0.15$ at x/D = 0.14 for the compliant case (closed circles). The inward flow is strongest near r/D = 0.12 with a magnitude $\sim U_{bulk}$. Beyond r/D = 0.15, the flow initially moves radially outward in the mean for this case. In comparison, the mean radial velocity is initially small in the LR case (open circles).

The RMS profiles for the LR and LC cases are shown in Figs 3-9c and d, respectively. Initially, the RMS values are small in both cases except in the narrow shear layer near r/D = 0.13. Further downstream, both u_{rms} and v_{rms} are large for both cases. The significant radial fluctuations corresponding with the large values of v_{rms} give further evidence of the presence of coherent vortical motions. In general, the u_{rms} values are somewhat higher than the v_{rms} values. Also, u_{rms} values for LC are slightly larger than for LR. Notice also that the peaks in the various RMS profiles have moved radially outward with increasing streamwise distance.

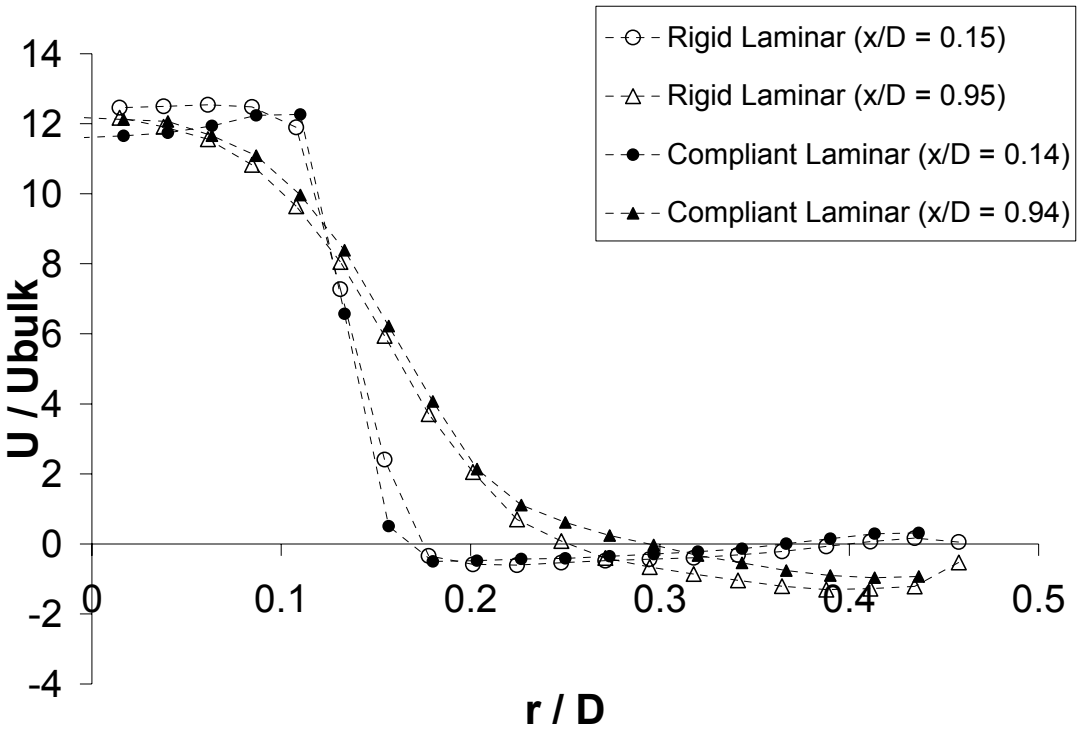
Rigid Laminar (x/D = 0.15)
Rigid Laminar (x/D = 0.95)
Compliant Laminar (x/D = 0.14)
Compliant Laminar (x/D = 0.94)
U / Ubulk
r / D
14
12
10
8
6
4
2
0
-2
-4
0
0.1
0.2
0.3
0.4
0.5

(a)

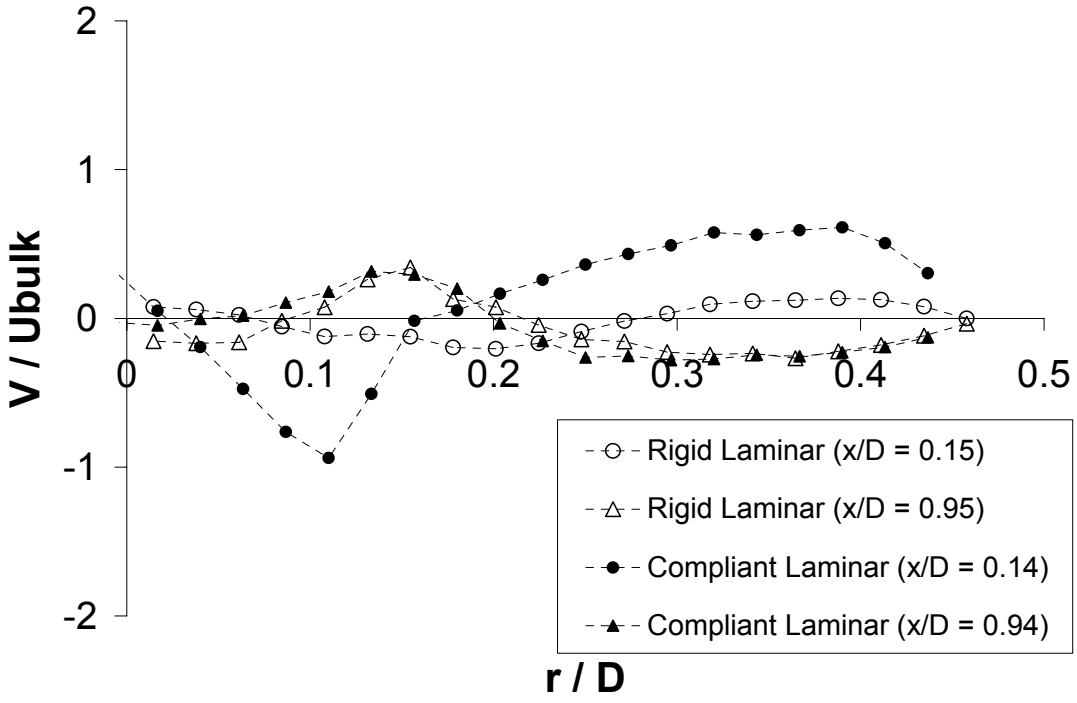
V / Ubulk
r / D
2
1
0
-1
-2
0
0.1
0.2
0.3
0.4
0.5
Rigid Laminar (x/D = 0.15)
Rigid Laminar (x/D = 0.95)
Compliant Laminar (x/D = 0.14)
Compliant Laminar (x/D = 0.94)

(b)

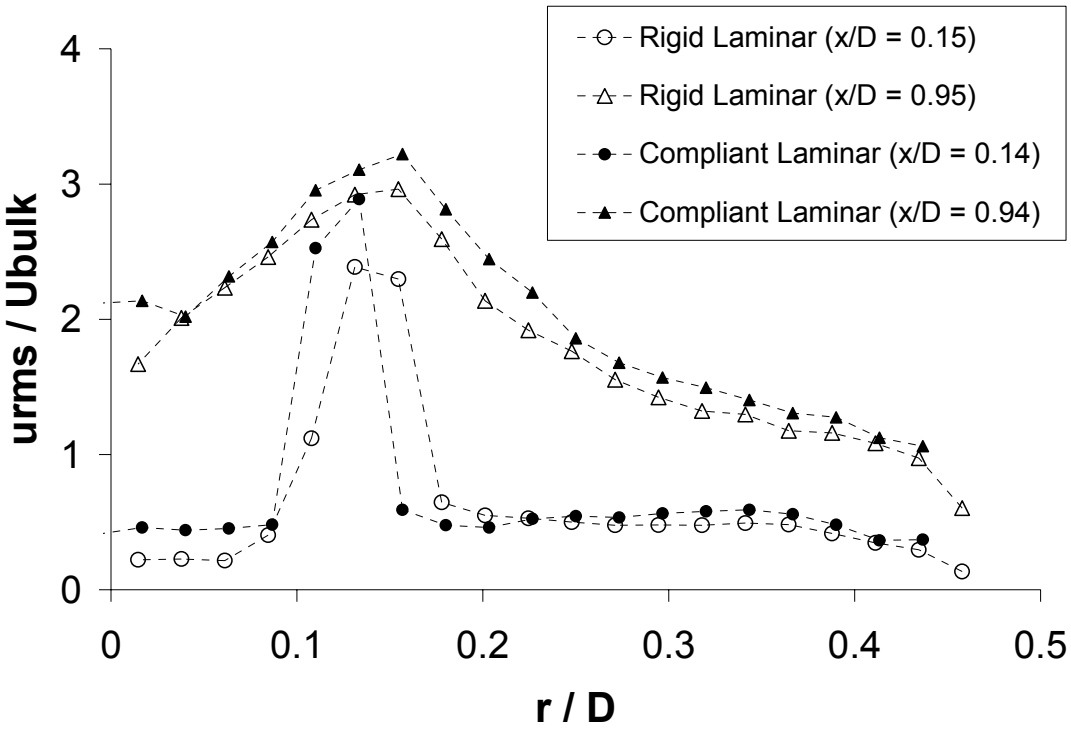

(c)

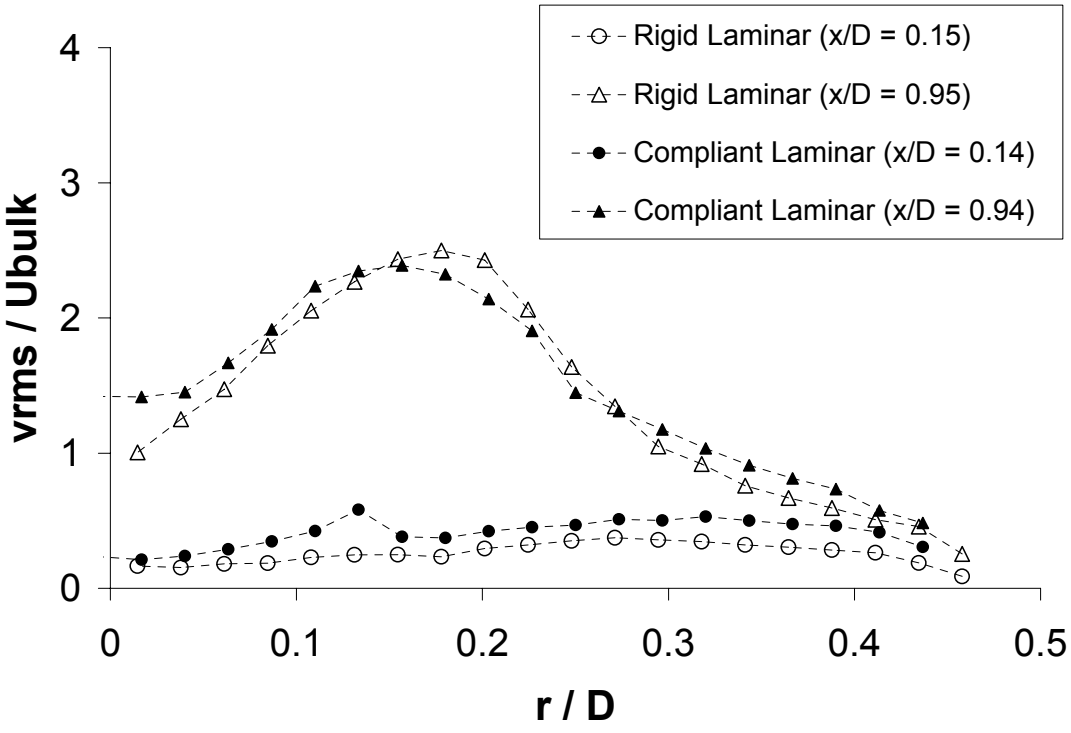

(d)

Figure 3- 9. Mean and RMS velocity profiles, Re = 600, d/D = 0.31. (a) streamwise mean U (b) radial mean V; (c) u_{rms}; (d) v_{rms}.

In Fig 3-10a, U/U_{bulk} is plotted for the higher Reynolds number TR and TC cases. The exit profile for TR (open circles) is indeed narrower than that for TC (closed circles). Also, the mean streamwise profile for TR broadens into a shape similar to that observed for LR at this location (see Fig. 3-9a). It is notable that, because of the significant orifice expansion, the TC profile maintains weaker streamwise velocity magnitudes over its inner portion and correspondingly, weaker reverse velocities over its outer portion. Fig 3-10b reveals a radial velocity profile for TC (closed circles) that is similar to LC (in Fig. 3-9b): the inward radial velocity increases linearly with increasing radius to the limit of the jet. The peak inward velocity has magnitude ~$1.7U_{bulk}$. The outward radial component at larger radii has smaller magnitude than was observed in the LC case (Fig. 3-9b). The TR case yields small values of V at both streamwise locations. The downstream trends observed in Fig. 3-10b are similar to those for LC and LR in Fig. 3-9b. For example, at larger r/D values, the mean flow is moving outward at the earlier and inward at the later streamwise location.

At the orifice exit, the streamwise RMS component u_{rms}/U_{bulk} (Fig. 3-10c) is small except in a relatively narrow shear layer for both TR (open circles) and TC (closed circles). The peak value for TR is initially larger than that in TC as might be expected because the peak RMS value scales with the velocity difference across the shear layer (Pope, 2005) and this velocity difference is larger for TR. Further downstream, each shear layer has broadened, and the TR case yields higher u_{rms} values than the TC case, but both cases have similar magnitudes of v_{rms} (Fig. 3-9d). Unlike the LC and LR cases discussed previously, the RMS values at the centerline remain relatively small at the downstream end of the field of view.

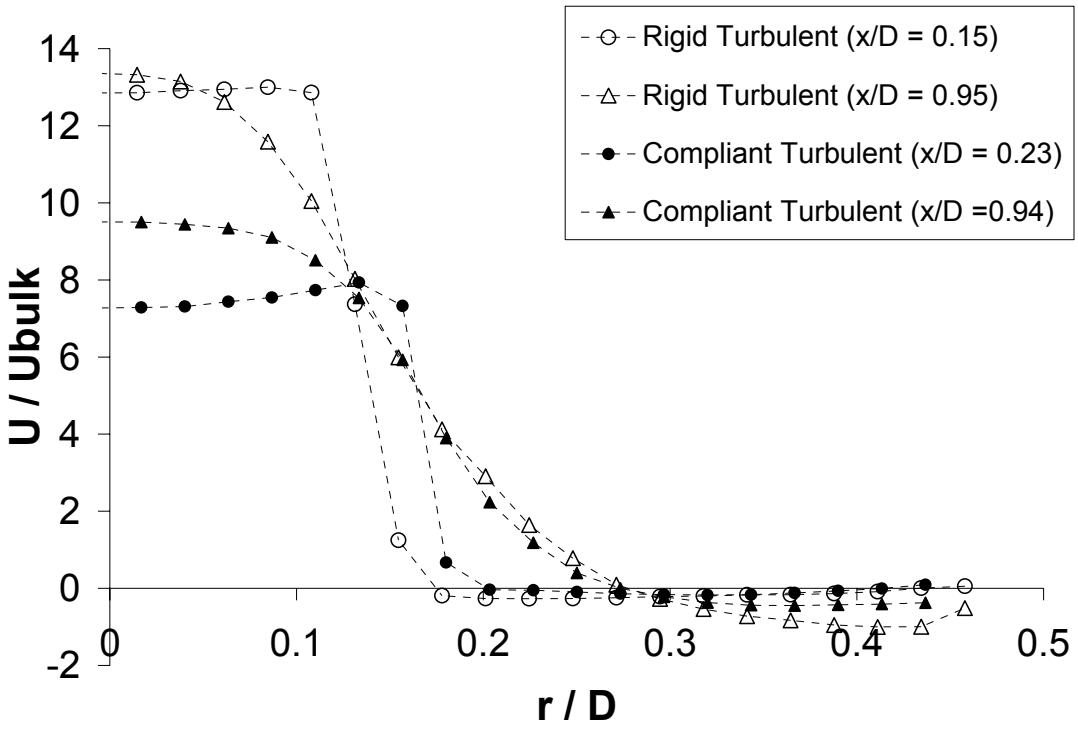
Rigid Turbulent (x/D = 0.15)
Rigid Turbulent (x/D = 0.95)
Compliant Turbulent (x/D = 0.23)
Compliant Turbulent (x/D =0.94)
U / Ubulk
r / D
14
12
10
8
6
4
2
0
-2
0
0.1
0.2
0.3
0.4
0.5

(a)

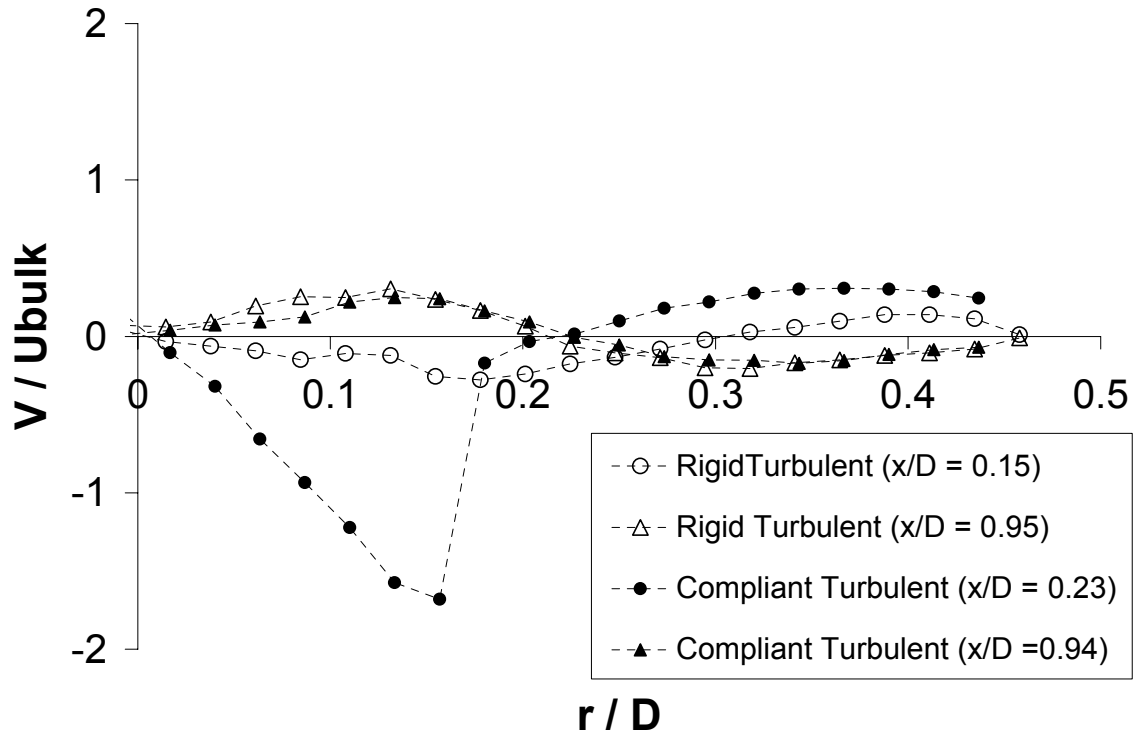
RigidTurbulent (x/D = 0.15)
Rigid Turbulent (x/D = 0.95)
Compliant Turbulent (x/D = 0.23)
Compliant Turbulent (x/D =0.94)
V / Ubulk
r / D
2
1
0
-1
-2
0
0.1
0.2
0.3
0.4
0.5

(b)

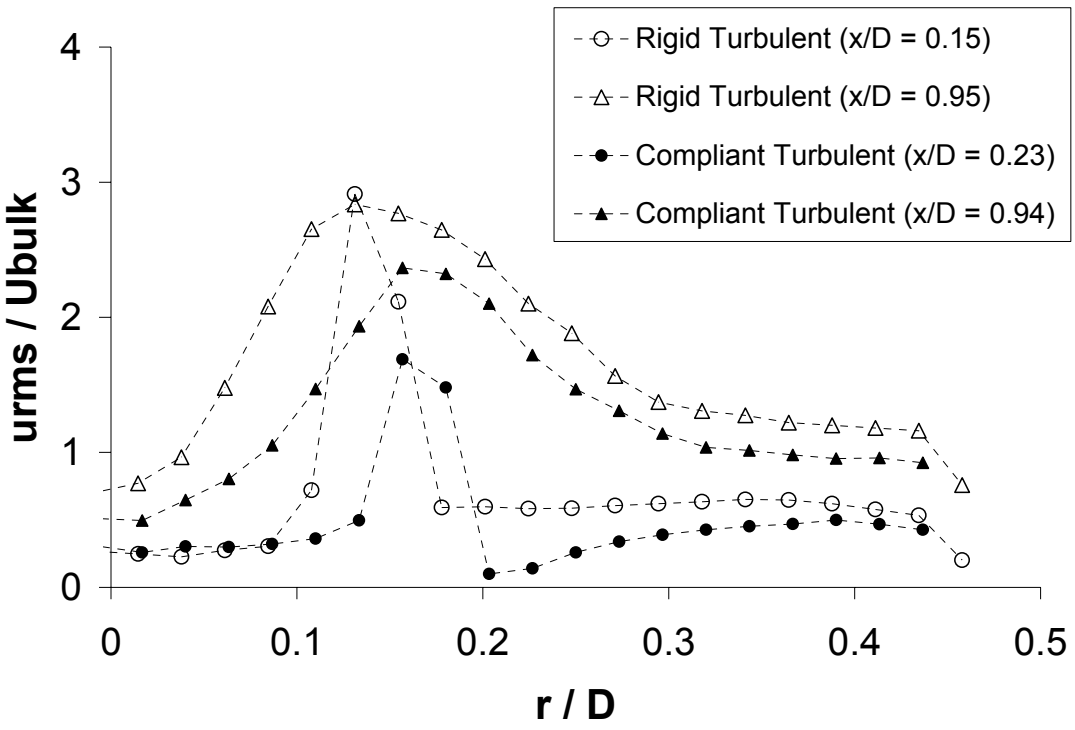

(c)

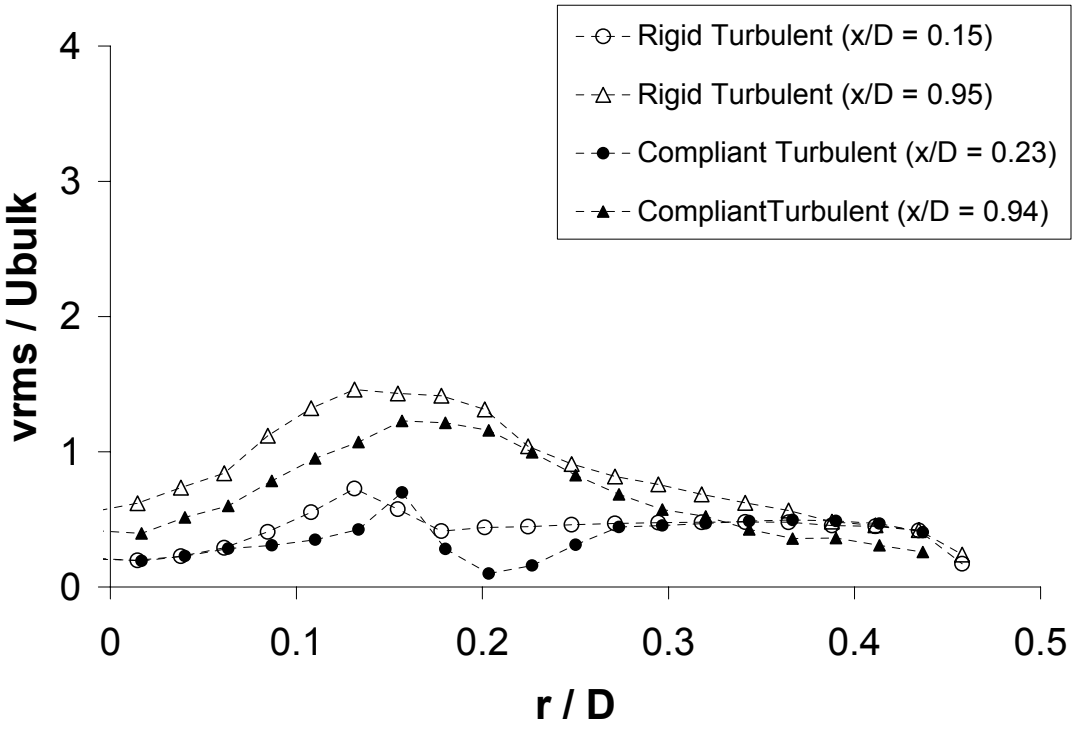

(d)

Figure 3- 10. Mean and RMS velocity profiles, Re = 3900, d/D = 0.31. (a) streamwise mean U (b) radial mean V; (c) u_{rms}; (d) v_{rms}.

In order to quantify a mean vena contracta effect, Fig. 3-11 plots the streamwise distribution of the quantity U_m/U_c where U_m is the maximum centerline velocity within the field of view, and U_c is the local centerline velocity. The rigid cases LR and TR show very little spatial acceleration in centerline velocity beyond the exit of the orifice. By contrast, the laminar compliant case (LC) shows significant acceleration up to x/D = 0.3, and the turbulent compliant case (TC) shows significant acceleration up to x/D = 0.5. Thus, even taking into account the increased axial displacement of the orifice at higher Re, the TC case exhibits acceleration over a longer distance suggesting a longer vena contracta effect. Based on the values of centerline mean velocity, the potential core of the jet appears to be preserved up to x/D = 0.95 for both turbulent cases but not for the laminar cases. The behavior of the TR case is similar to that observed in previous experiments on jets by DeOtte *et al.* (1991)and Mi *et al*. (2001).

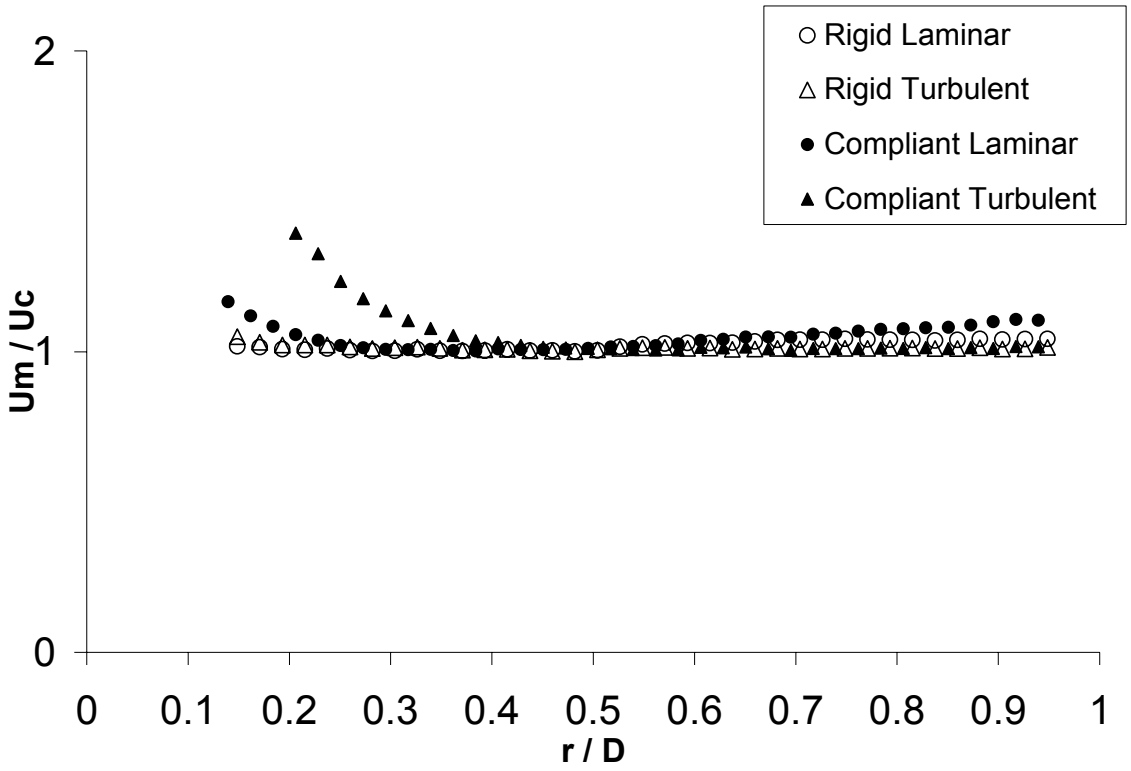

Figure 3- 11. Inverse mean velocity distribution along the centerline (Uc). U_m is the maximum centerline velocity within the field. Profiles for d/D = 0.31.

Instantaneous velocity vector fields along with normalized z-voritcity (ω_z) are plotted for each of the four cases. The instantaneous fields shown were chosen as fairly representative of the many fields acquired for each case, and they highlight some flow features that would affect the mean and RMS velocity statistics presented previously. For Re = 600, the spread in increased RMS values occurring near x/D = 0.5 for LR and LC (Fig. 3-7) is consistent with the roll up of relatively large coherent vortex rings, which can be observed with the planar velocity vectors and vorticity contour region of the instantaneous fields in Fig. 3-12. Both fields show a vortex ring spacing of approximately $0.4D = 1.3d_{eff}$. The rings appear to generate streamwise velocity variations that are felt both at the centerline and at large radii outside of the jet. Although the rings appear reasonably axisymmetric, three dimensional variations are also present. Reverse flow is present between the jet and the pipe wall in both of the flow cases. Trailing the vortex ring is the unsteady shear layer, which results in the rollup of the vortex ring. For the turbulent cases shown, it is difficult to isolate any coherent structures from the unsteady shear layer for both rigid and complaint diaphragms.

Fig. 3-13 shows the same instantaneous velocity vector fields as in Fig. 3-12 , but overlaid with contours of swirl strength, which is defined herein as the imaginary part of the eigenvalue of the two-dimensional velocity gradient tensor (Adrian et al., 2000). The swirl strength is normalized by U_{bulk} and pipe diameter D and plotted above a threshold of 50. Regions of positive swirl strength correspond with locations in which flow swirls about an axis normal to the measurement plane. Therefore, they are good indicators of vortex core regions and filter out vorticity induced by the jet shear layer.

The swirl criterion highlights the location and magnitude of the vortex ring for both laminar cases. The instantaneous fields downstream of the turbulent pipe flow yield qualitatively different results. In the TR case, numerous smaller cores are identified downstream of the orifice by the swirl criterion. Some of the cores appear to be parts of rings because they have a counterpart of similar size and strength on the opposing side of the jet at a similar streamwise location. The streamwise spacing of these cores varies over a range of 0.1D-0.35D. The individual cores cause weaker, more localized disturbances compared with the stronger cores in the LC and LR case. In the plot shown, the flow near the jet centerline appears undisturbed by the shear layer to the limit of the

field of view (x/D = 1). The TC case (Fig. 3-13d) exhibits a wider jet downstream of the expanded orifice. As in the TR case, a number of small, relatively weak cores are present, but it is unclear whether they are parts of coherent rings or helical structures. In most of the TC instantaneous fields, the flow at the centerline appears largely undisturbed all the way to x/D = 1.

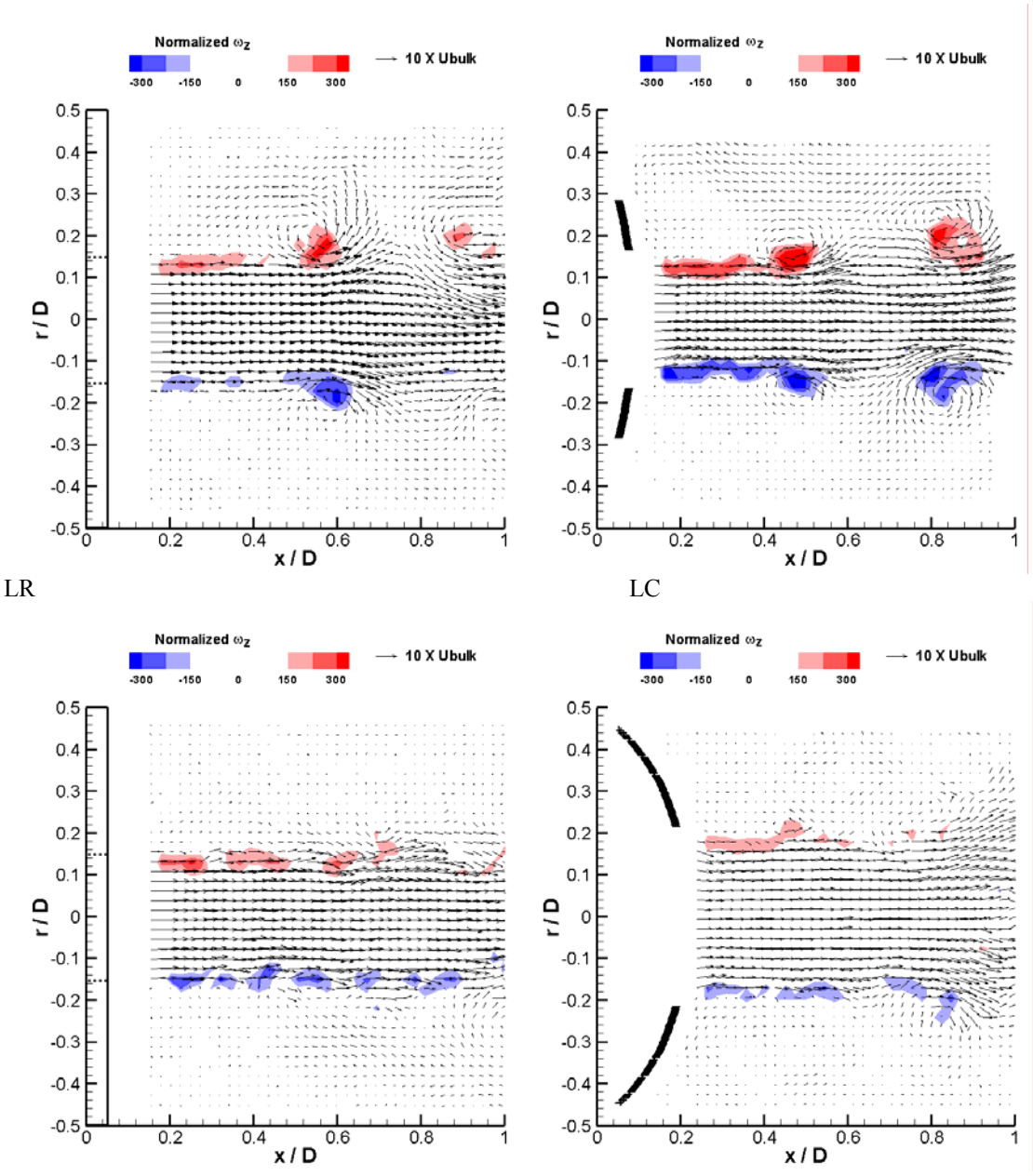

Figure 3- 12. Instantaneous velocity vector fields with vorticity contours for LR (d/D = 0.31), LC (d/D = 0.31 and deff / D = 0.31), TR (d/D = 0.31), and TC (d/D = 0.31 and deff / D = 0.42) cases. Vorticity is normalized by Ubulk and D. Vorticity levels between ±150 have been cut-off. Contour increments are 50. Based on the pixel displacement accuracy, the uncertainty in a given normalized velocity vector for LR, LC, TR, and TC was 0.22, 0.20, 0.24, and 0.16 U_{bulk}, respectively.

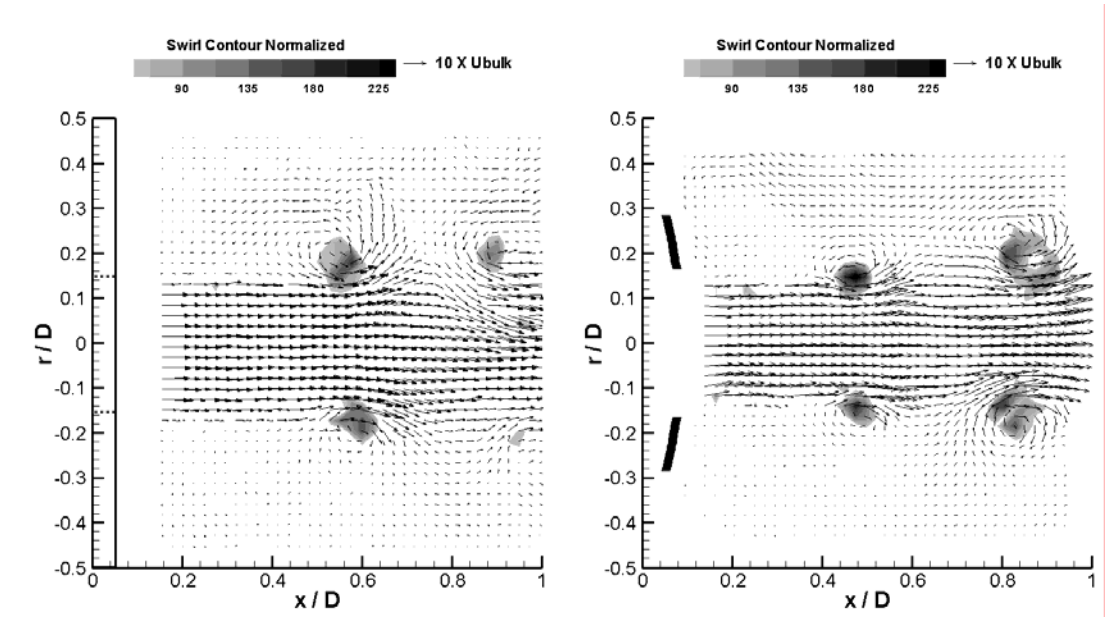

LR LC

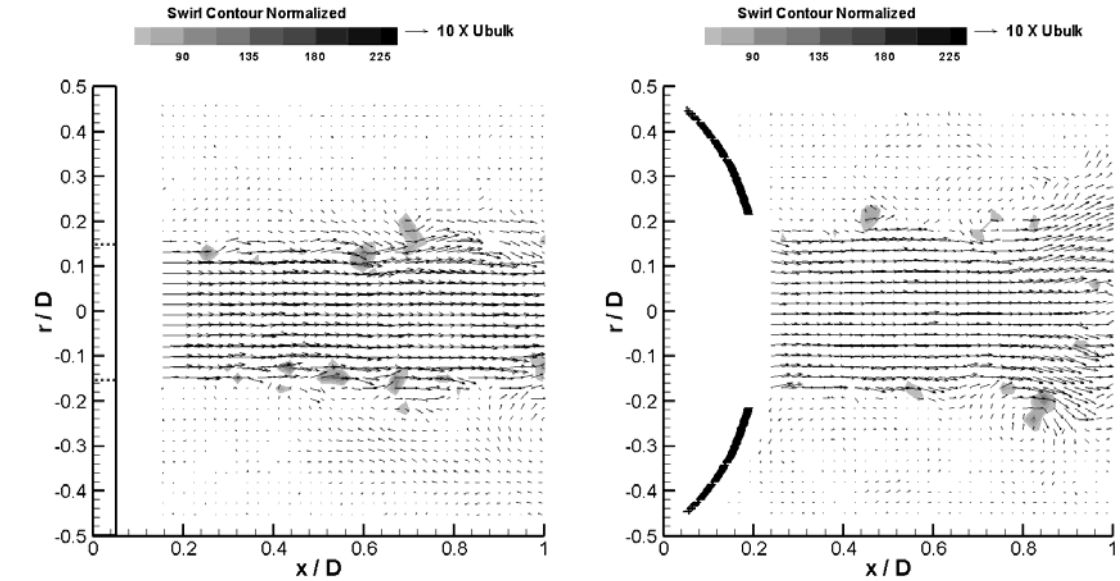

TR TC

Figure 3- 13. Instantaneous velocity vector fields with swirl contours for LR (d/D = 0.31), LC (d/D = 0.31 and deff / D = 0.31), TR (d/D = 0.31), and TC (d/D = 0.31 and deff / D = 0.42) cases. Swirl is normalized by Ubulk and D. Minimum swirl value plotted = 50. Contour increments are 22.5.

Downstream mean velocity vectors for a larger orifice size (d/D = 0.69) are plotted along with u_{rms}/U_{bulk} contours in Fig. 3-14a. In this case, the pipe Reynolds number is larger (8800) in order to generate significant deformation of the diaphragm. Fig. 3-14b shows the velocity profiles at x/D = 0.15 and 0.98. The jet profile is flatter at the exit (x/D = 0.15) than in the LC and TC cases with d/D = 0.31 and has a peak value of $U/U_{bulk} = 2$. As with the d/D = 0.31 cases, there is measurable inward radial velocity near the diaphragm lip and a shear layer develops with increasing streamwise distance. Since u_{rms} scales with the local mean velocity which is $\sim 2U_{bulk}$, the u_{rms} contours are plotted to lower limits than those in Fig. 10. For comparison purposes, the lower limit in Fig. 3-14a is set at 2/7 as shown in Fig. 3-7d (d/D = 0.31) where the local mean velocity was $\sim 7U_{bulk}$. When the two cases are compared, we can see that the two shear layers spread at similar rates, but the shear layer for d/D = 0.69 interacts more quickly with the pipe wall as would be expected. Individual profiles of the mean streamwise and radial components (Fig. 3-12b) indicate a persistence of reversing flow at x/D = 0.98, but no mean radial velocity.

The RMS plots in Fig. 3-14c show low values immediately downstream of the orifice (open symbols). The profile of u_{rms}/U_{bulk} contains a sharp peak centered at r/D = 0.35 that corresponds with the location of strong mean velocity gradient dU/dr in Fig. 3-14b. At x/D = 0.98, both u_{rms} and v_{rms} are significant at larger radii, indicative of the shear layer there. Both quantities remain low for r/D < 0.2, however, suggesting a relatively steady core region. Again, this can be contrasted with the TC case at x/D = 0.94 (see Fig. 3-10c and d) in which RMS values are elevated at the centerline, and the shear layer is focused closer to the centerline. The instantaneous vector field in Fig. 3-14d shows coherent vortex cores near x/D = 0.45 and x/D = 0.8. The upstream core induces a counter rotation in the low velocity zone further upstream bounded by the diaphragm and the wall.

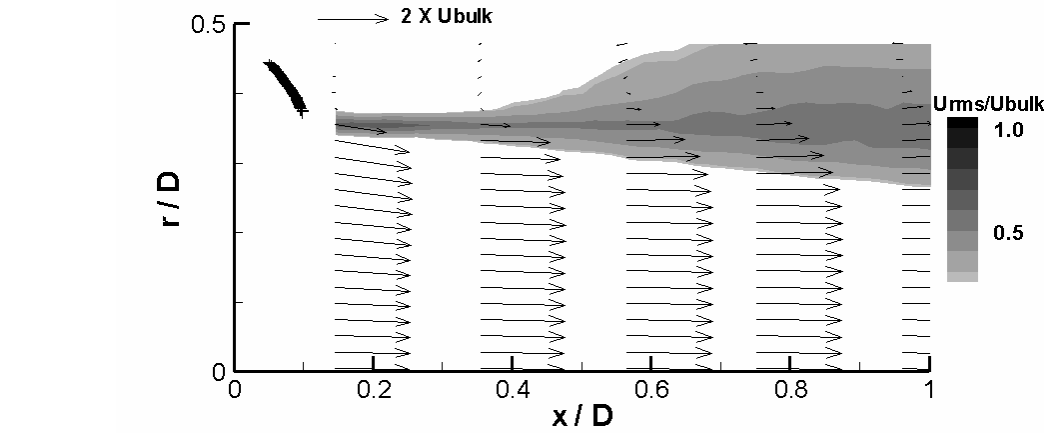

(a)

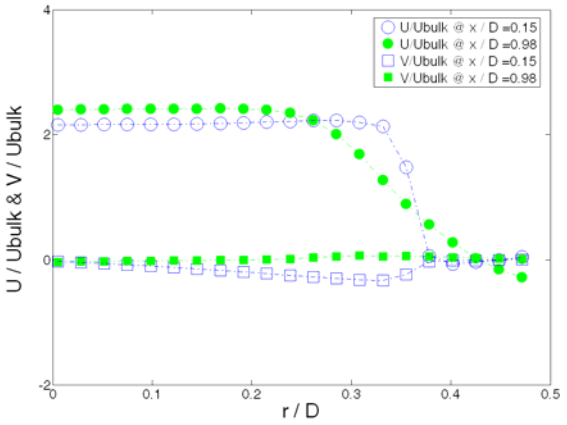

(b)

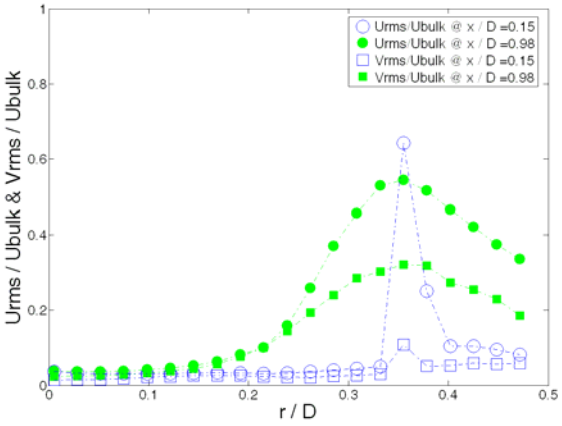

(c)

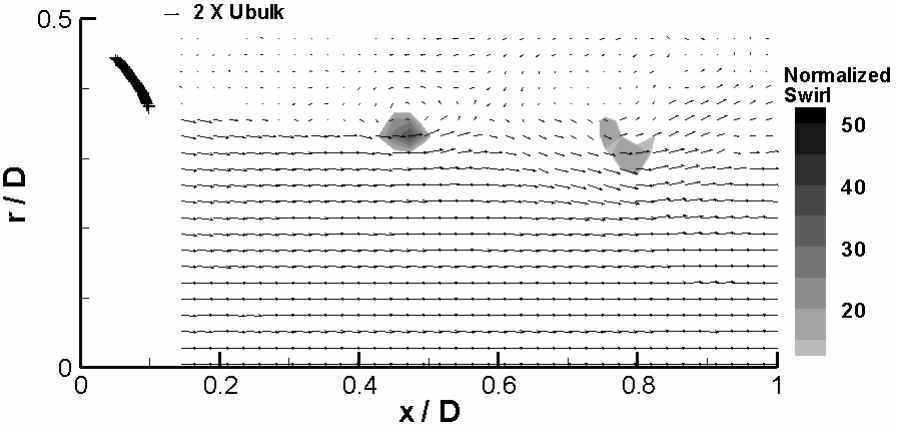

(d)

Figure 3- 14. Re = 8800, d/D = 0.69. (a) Mean velocity vector field with urms/Ubulk contours, lowest contour plotted = 0.28. Contour increments are 0.11 (b) mean velocity profiles, (c) RMS velocity profiles with PIV, and (d) instantaneous velocity vector field with normalized swirl contours. Lowest swirl value plotted = 14. Contour increments are 5.

3.1.2.4 Downstream Velocity Spectra

Fig. 3-15 shows spectral measurements resulting from the hot-film anemometry time records for the LR, LC, TR, and TC cases. In the plots, the power spectral density function is normalized using frequency f and signal variance σ^2. Both cases with upstream laminar flow (LC and LR) yield a distinct and dominant peak at 9.8 Hz, indicating indeed that vortices are developing with a regular frequency and spacing. In both laminar cases, there is very little energy above 40 Hz. The two cases with turbulent upstream conditions (TR and TC) yield broader, relatively featureless spectra that extend to higher frequencies. The TC case, in which the orifice area was larger and jet mean velocity values were lower, contains more energy at lower frequencies than the TR case as expected.

If the peak frequency of 9.8 Hz observed for LR and LC is normalized using the effective orifice diameter and the mean velocity through the orifice, the corresponding Strouhal number ($St = f * d_{eff} / U_o$) is 0.34 for both cases. This value of St corresponds closely with the frequency of the jet column mode observed, although typically further downstream, in free jets exiting contoured nozzles (Crow and Champagne, 1971, Danaila et al., 1977). The value St = 0.34 can be interpreted as the dimensionless passage frequency of vortex rings at a given streamwise location. If, for example, the vortex passage frequency is 9.8 Hz, and the vortex passage velocity is $\sim 0.5U_{mean}$, then the streamwise vortex spacing would be the velocity divided by the frequency or 0.5D (= $1.6d_{eff}$) which is comparable to the spacing observed in the instantaneous PIV fields (Fig. 3-12a and b).

When the power spectral density is replotted vs. Strouhal number as defined above (see Fig. 3-16), the range of energy-containing frequencies observed for TR falls within the envelopes spanned by the two lower speed cases (LC and LR) suggesting some similarity in streamwise vortex spacing (although the TR case favors a range of frequencies rather than a single frequency). The TC case, however, yields Strouhal numbers with higher values, suggesting the presence of eddies or fluctuations with smaller streamwise spacing and that the jet column mode has not yet developed. A spatial delay in jet development could be expected in the TC case for several reasons: due to the axial deformation of the diaphragm, this jet initiates further downstream than

in the other cases studied; the effective jet diameter is larger; and the jet exhibits the longest vena contracta.

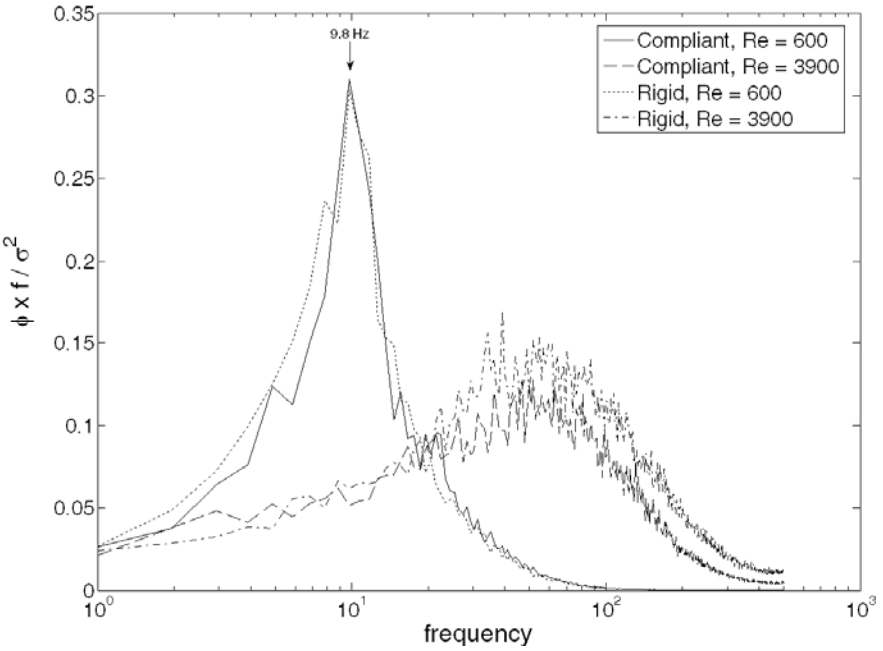

Figure 3- 15. Power spectra of the flow measured at x/D = 0.9 and radial location of strongest fluctuation energy. All cases are for d/D = 0.31. The variance in the data is σ^2.

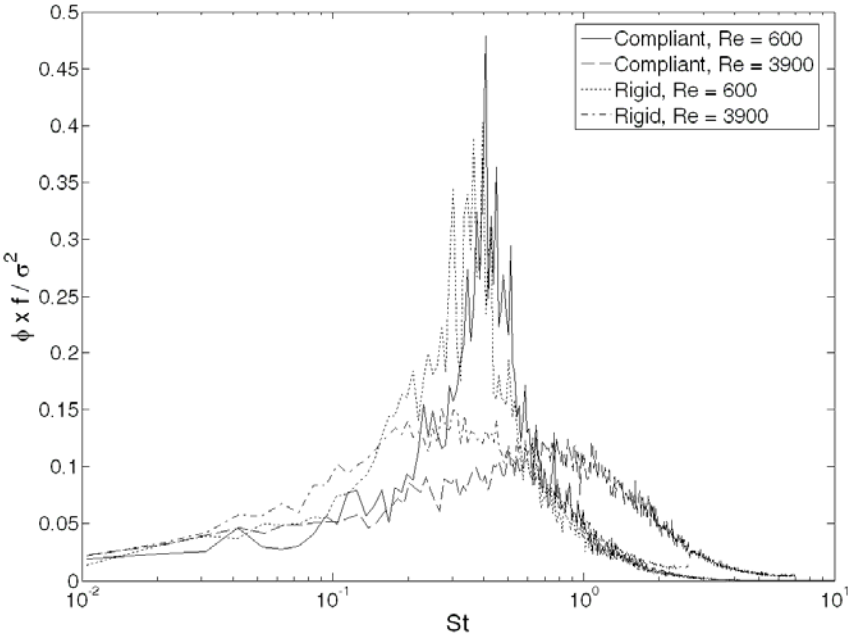

Figure 3- 16. Power spectra vs. Strouhal number based on deformed orifice diameter and mean velocity through orifice. St = (f * d_{eff}) / U_{mean}. Signals measured at x/D = 0.9 and radial location of strongest fluctuation energy. All cases are for d/D = 0.31. The variance in the data is σ^2.

3.1.3 Pulsatile Flow

The pulsatile flow testing was conducted with the same working fluid as the steady flow (0.9% w.t. saline solution). The pulsatile flow loop set up was a modification to the cardiovascular pulse duplicator (CPD) system. The ventricular impedance unit (VIA) and aortic compliance were removed, resulting in a different impedance of the system as compared with the CPD. The testing valve was the MED 4901, the most compliant diaphragm (μ = 0.016 MPa) of d/D = 0.31. The pulsatile forcing condition was a pump waveform having a frequency f =1.167 Hz for the first harmonic as shown in Fig. 2-7. The α = 33 based on the first harmonic is calculated as follows

$$\alpha = \frac{D}{2}\sqrt{\frac{2\pi f}{\nu}},$$

$$D = 0.0254m,\ f = 1.167, \nu = 1E-6\ {}^{m^2}\!/_{s}$$

where, D = 2.54 cm is the diameter of the pipe and ν is the kinematic viscosity of the working fluid at room temperature. The Womersley number expresses the ratio of the oscillatory inertial force to the shear force. A value of 33 indicates that the local inertial forces dominate the shear forces in this flow regime. The flow had a forward stroke volume of 16.7 mL and a measured time averaged flow rate of Q_{avg} = 0.54 L/min with a peak flow rate of 4 L/min. The peak flow rate corresponded to a Reynolds number of 3400 based on D. Q_{avg} and D values were used to normalize the data presented.

3.1.3.1 Diaphragm Deformation, Pressure Drop, and Flow Rate

The pressure drop across and flow rate immediately upstream of the diaphragm averaged over ten cycles are plotted in Fig. 3-17. The error bars in the pressure drop and flow rate include the rms fluctuations in the measurements. The data show good repeatability in the measurements. The percent expansion in orifice diameter, which was measured from the PIV images is also plotted in Fig. 3-17. Both the pressure drop and flow rate are in phase. The flow rate at θ = 0º has a negative value of -0.57 L/min with a corresponding pressure drop of -0.12 mmHg. The negative flow indicates a reverse flow at the beginning of the cycle when the downstream pressure is greater than the upstream pressure. The flow rate rises to positive values, which indicate the forward movement of the fluid. The rise of the flow rate and pressure drop curves are similar until 50º at which

point the pressure drop rises much faster than the flow rate curve. At the increased flow rates, the diaphragm acts with a greater resistance to the flow resulting in a steeper rise of the pressure drop. The flow reaches a peak value of approximately 4 L/min. The peak flow rate occurs at a positive pressure drop of 12.5 mmHg during the phase angle $\theta \sim 115^{\circ}$. After this phase both the pressure drop and flow rate decrease and cross zero at $\theta \sim 195^{\circ}$. The reverse flow of the fluid ensues and peak negative pressure drop and flow rate values of -1.6 mmHg and -1.46 L/min, respectively occur at $\theta \sim 280^{\circ}$. From approximately 200° to the start of the new cycle, the pressure drop and flow rate curves have similar trends. The rise and fall of both pressure drop and flow rate magnitudes are more gradual during the reverse flow as compared to the forward flow.

The maximum measured diaphragm orifice expansion of 10% in diameter occurs at 103° as shown in Fig. 3-17. The orifice expansion measurements were made when the diaphragm deformation was visible during the forward flow of the fluid (positive flow rates) and each measurement was made approximately 16° apart recorded by the PIV cameras. The maximum deformation or orifice expansion might have occurred between measurements at 103° and 119°. The expansion in orifice diameter for the pulsating flow is less than that of the steady flow at similar instantaneous flow rate. A trace of the deformed diaphragm position indicating the difference is shown in Fig. 3-18. At similar flow rates (4.6 L/min for the steady flow and 4 L/min for pulsatile flow), the steady upstream flow results in much larger deformation (beyond what is expected by the 0.6 L/min difference) of the diaphragm as shown by the larger opening and outward deflection. The smaller opening for the pulsatile flow case results in higher instantaneous pressure drops of 12 mmHg as compared to 6.5 mmHg for the steady flow case. The reduced deformation of the pulsating diaphragm at similar flow rates may be a result of the unsteady pressure field.

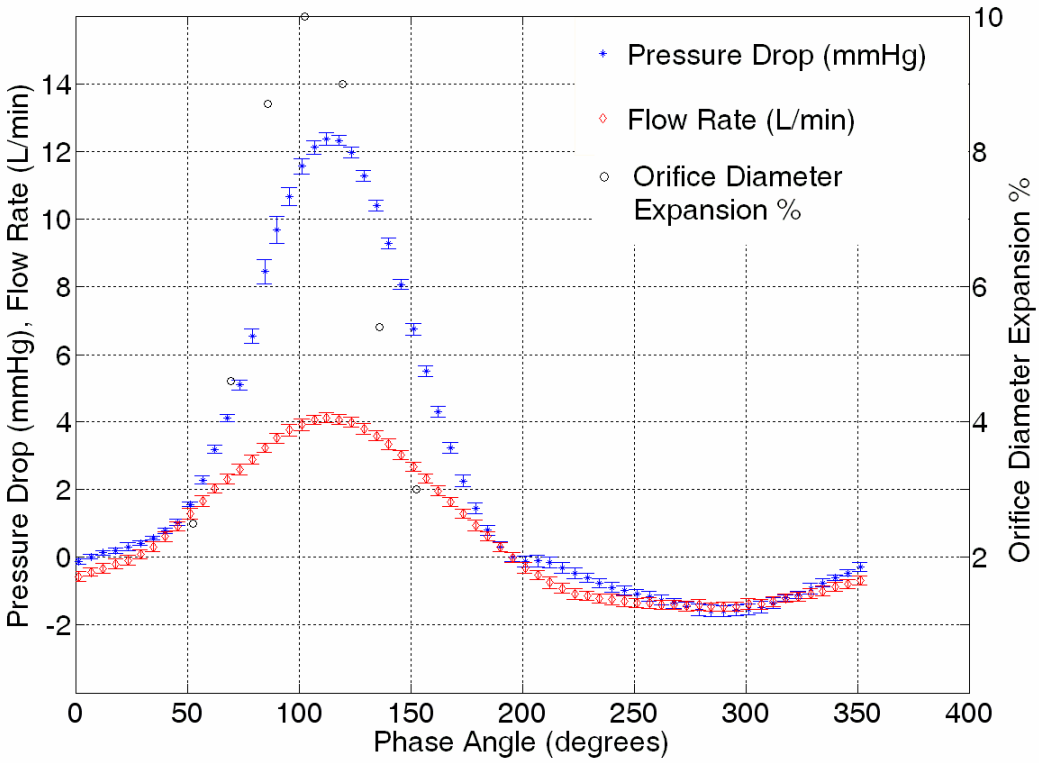

Figure 3- 17. Pressure drop and flow rate signatures. Error bars indicate the fluctuations in the measurements averaged over ten cycles. Diaphragm orifice diameter expansion plotted at certain phases during the forward flow. The orifice expansion measurements were made independently from the flow rate and pressure drop measurements.

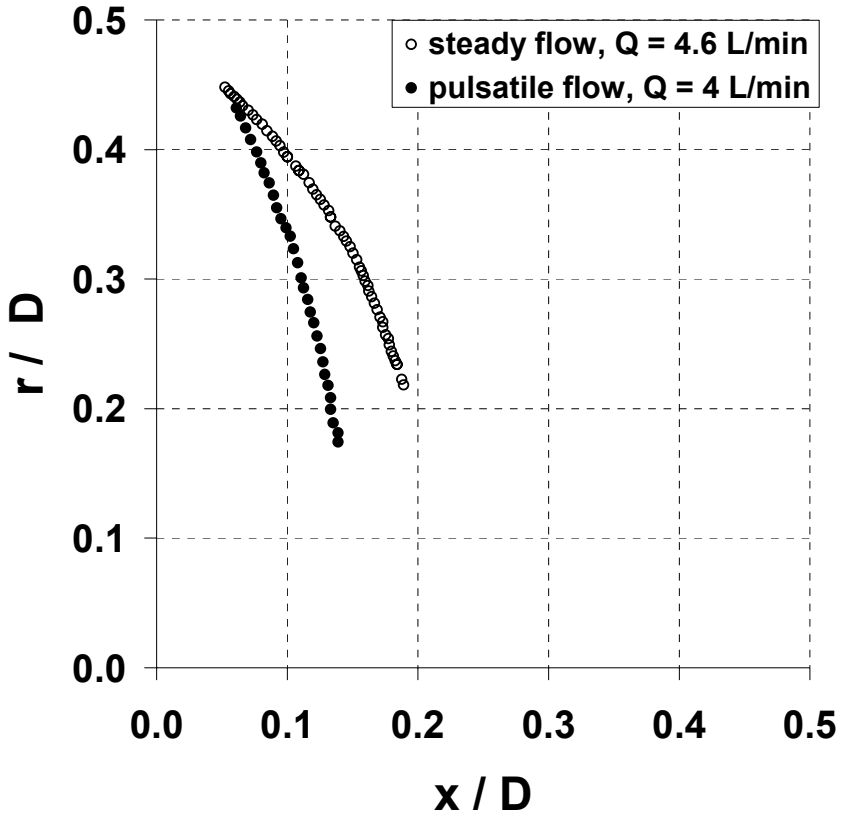

Figure 3- 18. Diaphragm deformation states for pulsatile and steady flow at similar instantaneous flow rates.

3.1.3.2 Flow Fields

A clear difference between the pulsatile jet and the steady jet is the presence of a leading vortex ring. The leading vortex ring explained earlier in the introduction Section 1.2.3 is a result of the rollup of the separated shear layer exiting the round orifice. Phase-averaged PIV results of 40 realizations were used to track spatially the vortex ring within the downstream field of view. The phase-averaged data sets were captured at 4º intervals, between $\theta = 44º$ and 64º. This was the period when the vortex ring was within the field of view. Note, phase-averaged data captures the instantaneous flow features, which repeat from cycle to cycle and filters out non-repeating flow features. There is high repeatability in the deformed diaphragm location from cycle to cycle as recorded by the PIV cameras indicating the diaphragm boundaries should not result in flow variations.

The phase-averaged velocity vector fields and vorticity ω_z contours are shown in Fig. 3-19 for θ = 44º and 64º. ω_z levels between ±400 have been cut-off. Contour increments are 200. In the pulsatile flow generated, the leading vortex ring is present in the field of view for θ = 44º. The leading vortex ring is attached to a trailing jet. The centers of the ring core are marked by green crosses. The centers are separated by approximately 0.47D, which is the measure of the ring diameter and is larger than the undeformed orifice diameter of 0.31D. By θ = 64º, the vortex ring has traveled approximately 0.75D in the streamwise direction and the diameter of the ring is approximately 0.58D, an increase of 11% in D. The deformed diaphragm orifice diameter measures 0.36D (at θ = 64º). The vortex ring diameter increase is a result of the spreading in the jet shear layer along with the opening of the diaphragm orifice. The spanwise location of the ring shows an upward shift. This may be a result of the diaphragm deformation not being perfectly symmetric. The edges of the vortex ring extend near the pipe wall. The growth of the vortex ring is supplied by the vorticity generated by the accelerating piston and the entrainment of the ambient fluid. The vorticity contours indicate that the vorticity is supplied by the shear layer into the growing vortex ring. The radial growth in the vortex ring is limited by the pipe wall. At θ = 64º, the vortex ring's core shape expands and this trend may continue beyond the field of view. The vortex ring is clearly attached to the trailing core, indicating that the formation number or the time of maximum circulation of the vortex ring before pinch-off has not been reached. It is expected that the vortex ring pinch-off occurs further downstream (Dabiri and Gharib, 2005).

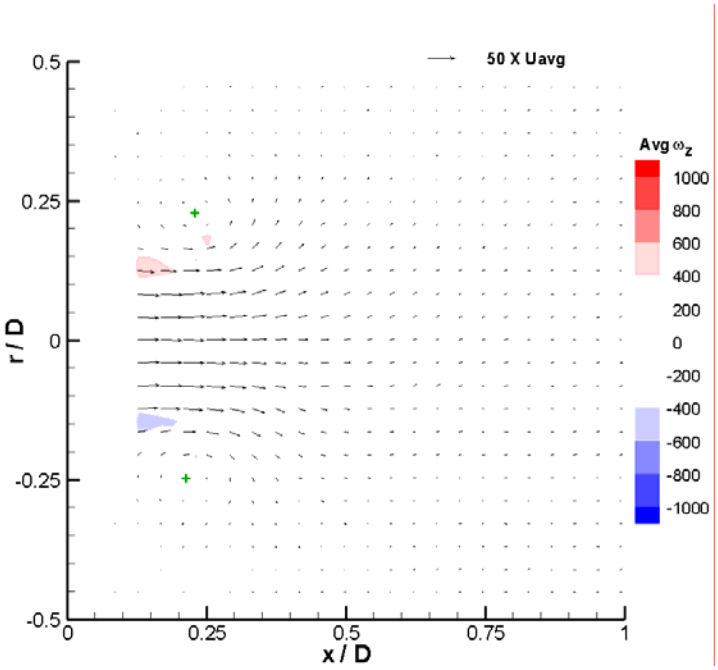

(a)

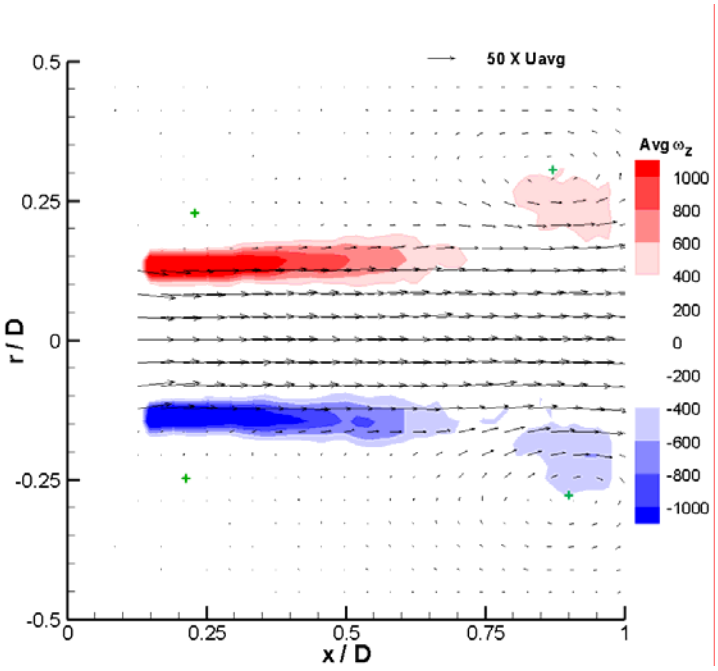

(b)

Figure 3- 19. Phase averaged growth of leading vortex ring downstream of the diaphragm. (a) velocity vector field and vorticity ω_z contour at $\theta = 44^o$ and (b) $\theta = 64^o$. The green cross-marks indicate the planar center locations of the vortex ring. Note at $\theta = 64^o$, the earlier cross-marks along with the current core center locations at $\theta = 64^o$ are plotted. ω_z levels between ±400 have been cut-off. Contour increments are 200.

Three flow phases at θ = 53º, 103º, and 169º were examined for the effects of the pulsatility on the diaphragm and flow behaviors. The corresponding instantaneous Reynolds numbers based on the flow rate and pipe diameter for each phase were 1200, 3400, and 1275, respectively. The flow is examined through the phase-averaged velocity vector field and streamwise fluctuations. The streamwise velocity fluctuation u_{rms} (normalized by the average flow rate velocity) > 10 is plotted in Fig 3-20. The deformed diaphragm states are overlaid on the plots for the phases where the diaphragm appears in the field of view. As the flow accelerates and exits the diaphragm valve orifice, the higher velocity fluctuations between cycles are isolated near the exiting shear layer shown for θ = 53º. Near the peak flow phase (θ = 103º), the cycle-to-cycle variation in the streamwise velocity occurs along the spreading shear layer. During this phase of θ = 103º and a corresponding instantaneous Reynolds number of 3400, the spread in u_{rms} is similar to that of the TC case of the steady flow in Fig. 3-7d based on the scaled equivalent rms cut-off criteria. The flow phase of θ = 169º occurs during deceleration and has an instantaneous Reynolds number of 1275. When comparing the accelerating and decelerating flows at similar Reynolds numbers, the cycle-to-cycle variation is greater throughout the field of view for the decelerating flow. This phenomenon is consistent with the fact that the accelerating flow suppresses velocity fluctuations and is more stable than decelerating flow at similar Reynolds numbers. This is because the existing coherent structures in accelerating phase of the flow may take a finite time to decay and persist throughout the decelerating phase (Fung, 1997).

An examination of an instantaneous flow field at θ = 53º with the vorticity contour identifies the location of the leading vortex ring and the trailing shear layer as shown in Fig. 3-21a. The leading vortex ring is approximately symmetric about the r-axis, but this may not always the case due to perturbations in the unsteady flow. The asymmetry may lead to a larger 'average' vortex ring size as compared to the instantaneous flow fields. Fig. 3-21b shows an instantaneous flow field at θ = 103º. The velocity vectors are longer indicating the faster flow with inward radial components at the jet exit occurring for phase of 53º as well. The jet is present throughout the field of view with larger and more spread ω_z values indicating the shear layer. The velocity vectors downstream spread radially outwards resulting in the increase of the shear layer.

ω_z of lesser magnitude are also present inside the core of the jet. Fig. 3-21c shows an instantaneous flow field at $\theta = 169^o$. Like the higher flow rate case for $\theta = 103^o$, the shear layer is present throughout the field of view. Lesser magnitude ω_z is found inside the jet. There is a zone of reverse flow in the downstream periphery of the jet with magnitudes comparable to that of the forward flow and ω_z values above the indicated threshold present. The zone of the reverse flow in the periphery of the jet and vorticity containing structures present within the core and in the periphery of the jet lead to a larger radial spread in rms values shown in Fig. 3-20c.

The main flow features observed upstream during the reverse flow are similar to that of the downstream forward flow as evident from a leading vortex ring followed by a trailing jet.

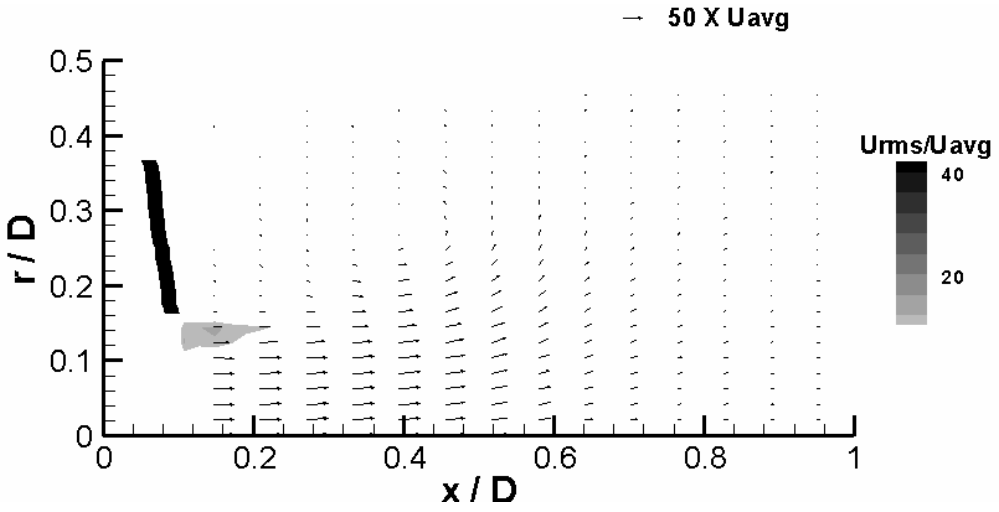

(a)

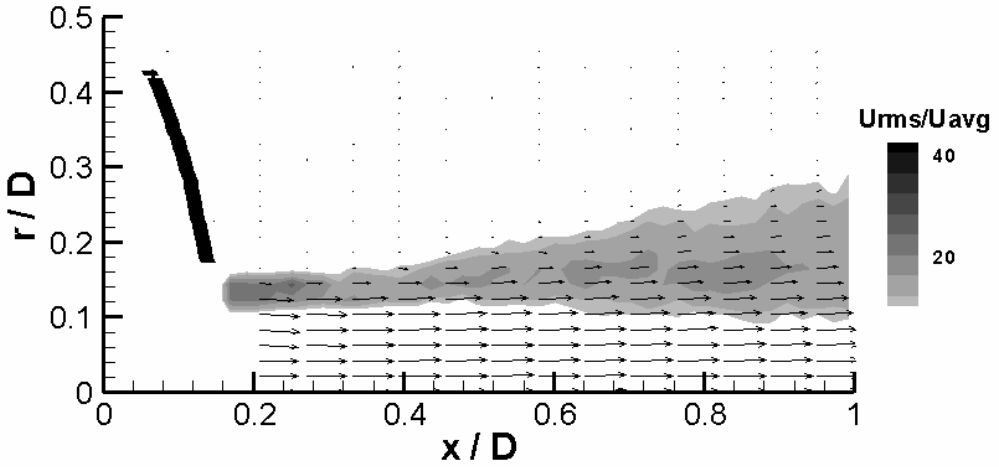

(b)

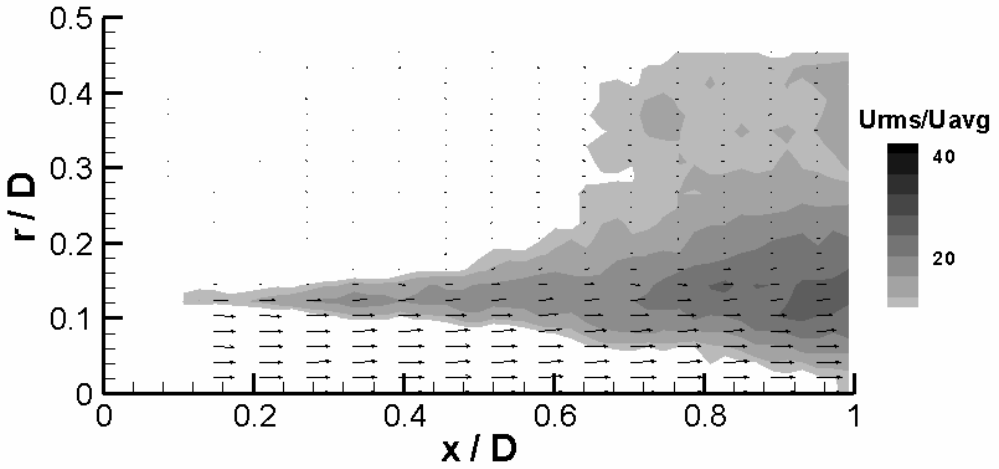

(c)

Figure 3- 20. Downstream mean velocity vector field an u_{rms} contour. Lowest contour plotted is u_{rms}/Uavg = 10. Contour increments are 4. Plotted phases are at (a) 53º, (b) 103º, and (c) 169º. Note every third vector plotted along the x-direction.

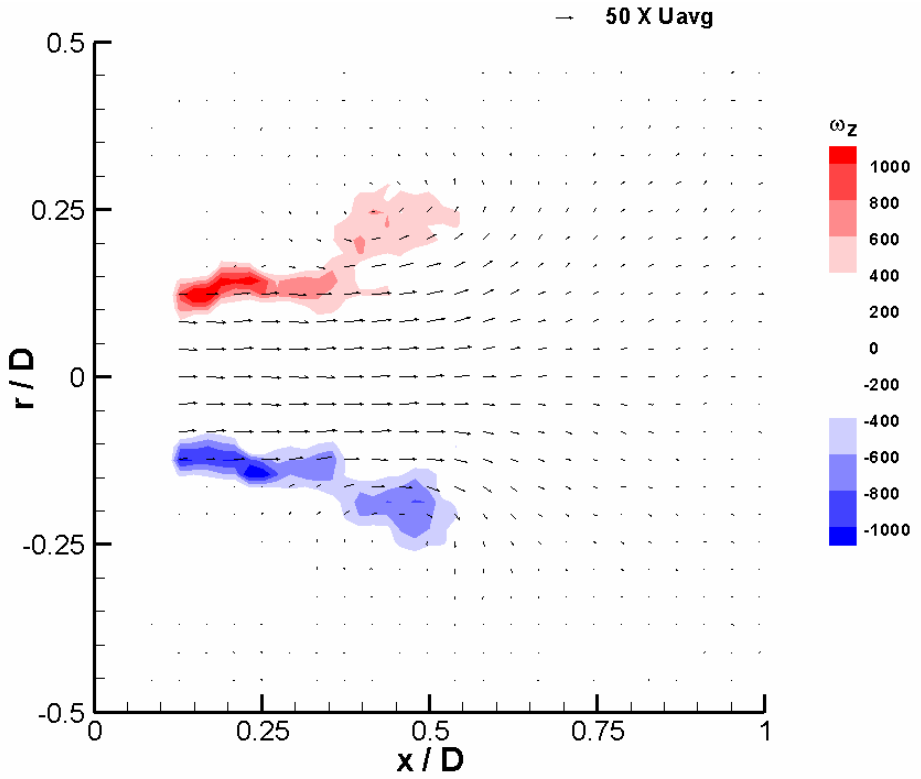
50 X Uavg
0.5
0.25
0
-0.25
-0.5
r / D
0
0.25
0.5
0.75
1
x / D
ωz
1000
800
600
400
200
0
-200
-400
-600
-800
-1000

(a)

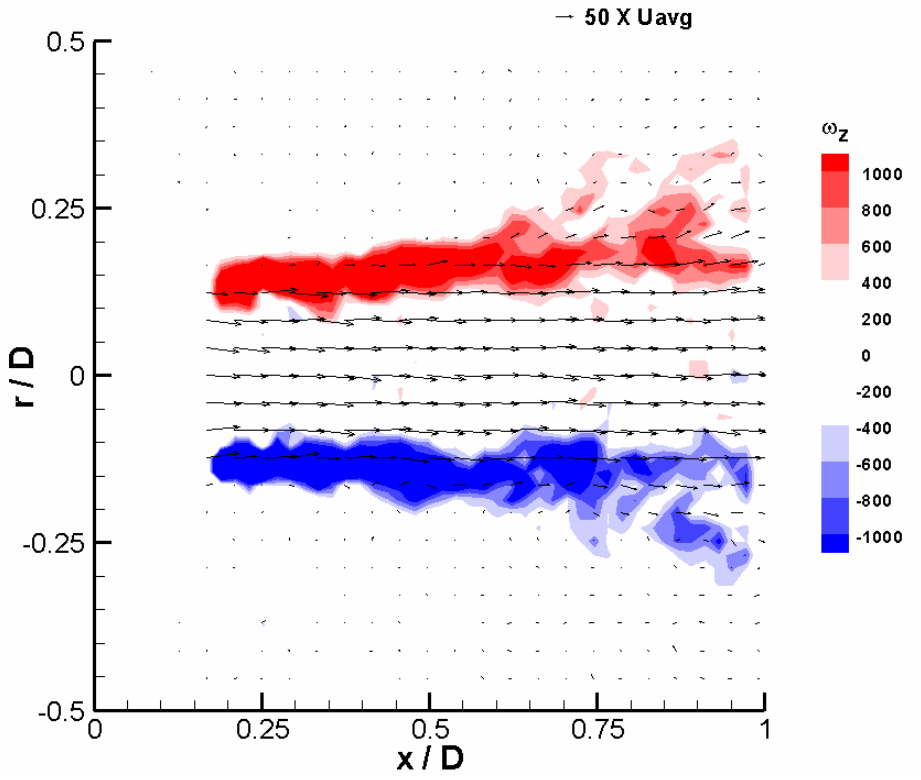
50 X Uavg
0.5
0.25
0
-0.25
-0.5
r / D
0
0.25
0.5
0.75
1
x / D
ωz
1000
800
600
400
200
0
-200
-400
-600
-800
-1000

(b)

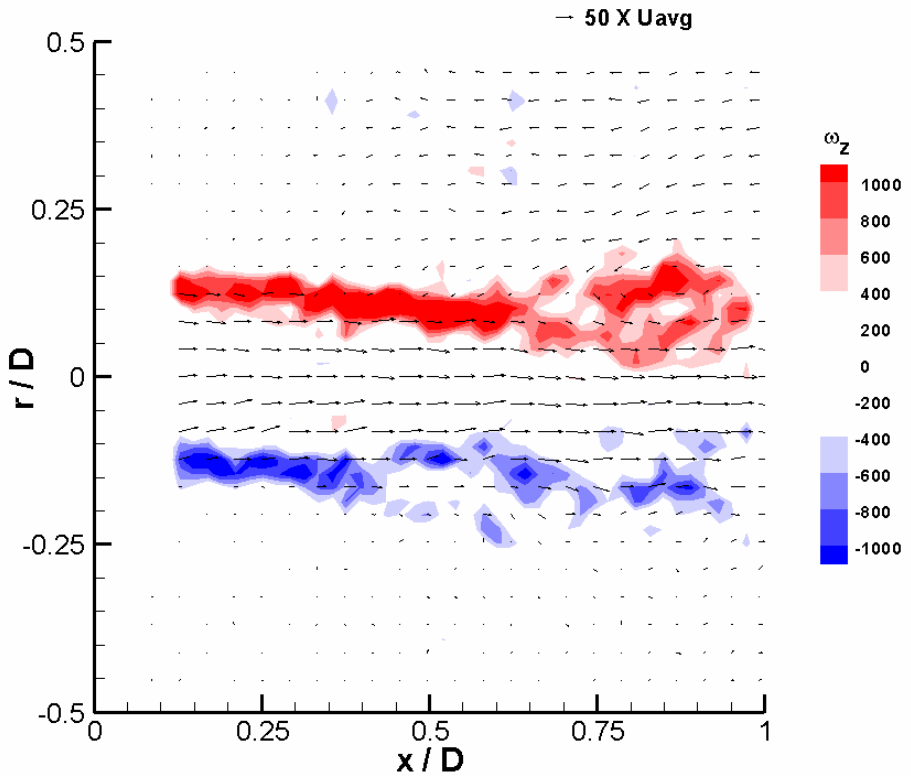

(c)

Figure 3- 21. Downstream instantaneous velocity vector flow fields with vorticity ω_z contour. ω_z levels between ±400 have been cut-off. Contour increments are 200. Plotted phases are at (a) 53°, (b) 103°, and (c) 169°. Note every second vector plotted along the x and y-directions.

3.2 Transparent Silicone Valve

The diaphragm valve described above allows multidirectional flow and does not function as a proper valve. An ideal valve should allow unidirectional flow. The transparent silicone valve (SV) serves this purpose. Additionally, these valves were fabricated to match specific geometry of the tissue engineered valve equivalents (VE) of D = 2 cm and to quantify flow features within SV, which may occur through the VEs. Therefore, the flow conditions were chosen to match right ventricular physiological conditions of 70mL of stroke volume at 70 beats per minute or 1.167 Hz leading to an approximate time-averaged flow rate near 5 L/min. The material property response obtained through tensile testing of the Sylgard 184 transparent SV as compared with the VEs and other silicone products is shown in Appendix E-1. The SV is stiffer than all the

silicone materials used for fabricating the diaphragm valve as indicated by the higher instantaneous modulus in the 0 to 0.1 MPa stress range. The SV is stiffer at lower stresses (< 0.04 MPa) as compared to both stressed directions of the VE, but at higher stresses the behavior of the SV matches more closely along the radial direction. The SV is less stiff than the VEs in the circumferential direction at higher stresses (> 0.04 MPa). The following sections present pressure drop and flow signatures along with deformation states of the silicone valve placed in the cardiovascular pulse duplicator replicating right ventricular loading conditions. The three-dimensional flow fields at certain phases through the SV flow cycle are presented.

3.2.1 Silicone Valve Pressure Drop and Flow Rate

The pressure drop across the SV and the flow rate, averaged over ten cycles, are plotted in Fig. 3-22. One cycle corresponds to a time duration of 0.87 seconds with input frequency and waveform matching the pulsating diaphragm valve case (1.167 Hz). The minor tick marks on the x-axis represent phases from φ = 0 to 25 and are spaced 14º (or 0.033 seconds) apart during the cycle. The systolic period spans approximately 100º (φ2 to φ11) from SV leaflet opening to closure. During this period the flow rate is positive. From the second phase to the sixth phase, there is a steep acceleration in the flow rate. The flow rate peaks at about 23 L/min between the sixth and seventh phases matching right ventricular physiological flow rates. From the seventh phase to the tenth phase or towards the end of systole the flow decelerates. The valve closes between the tenth and eleventh phase. The flow rate is registered as negative or in the reverse direction between these two phases. For the six subsequent phases during diastole, the flow rate oscillates about 0 L/min and is damped in time. For the remaining nine phases, or the end of diastole, the flow rate is nominally zero, and then the cycle repeats.

A positive pressure drop corresponds with the upstream pressure greater than the downstream pressure. The pressure drop is initially negative, but rises to zero during the end of diastole (φ0 to φ2). Note, unlike the pulsating diaphragm valve, the SV does not allow reverse flow when the pressure drop is negative during this phase. From the third to just after the ninth phase, the upstream pressure is greater than the downstream pressure resulting in positive values of the pressure drop. Unlike the diaphragm valve, the

pressure drop measurements slightly lead the flow measurements in time due to the inertia of the fluid (result of the added impedance in the system), with peak pressure drops of 40 mmHg occurring before the peak flow rate. The peak pressure drop preceding the peak flow rate is also found in clinical measurements (Murgo, 1998). The peak pressure drop is expected to coincide with maximum flow acceleration (Nichols and O'Rourke, 2005), but is slightly later than the peak acceleration in this flow. The measured pressure drops are much larger than ideal pulmonary measurements of a few mmHg during systole. The SV can be classified as significantly stenotic due to the high systolic pressure drops. From the ninth phase onwards, the downstream pressure is larger than the upstream pressure resulting in negative values of the pressure drop. The pressure drop is positive for approximately 21% of the cycle and negative for the remaining 79%. There are higher frequency oscillations in the pressure measurements reaching maximum values of approximately -75 mmHg at T = 0.38 and 0.45 seconds, which get damped towards the end of diastole. The higher frequency pressure and flow oscillations are in part due to the suction effect on the SV by the cardiovascular pulse duplicator. With this the high impedance in the ventricular filling during the reverse stroke of the pulsatile pump leads to a sudden drop in upstream SV root pressure (below external root pressure). The SV upstream ventricular root section contracts radially at the same time the leaflets close as will be described below. The spikes occur because of a sudden closing of the valve leaflets, referred to as the pressure hammer effect, and the contraction of the root. The oscillations get damped in time. These high frequency pressure drop oscillations are non ideal physiologically; however, during aortic valve closure, a spike in the aortic pressure is registered and referred to as the dicrotic notch. However, this spike is damped almost immediately.

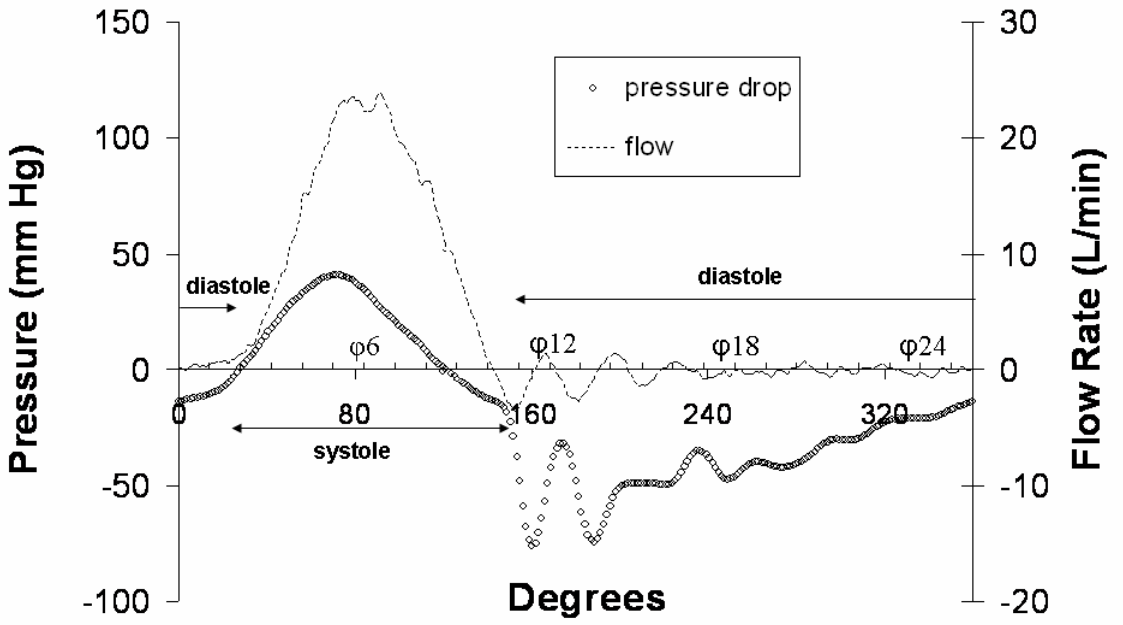

Figure 3-22. Silicone valve pressure drop versus flow rate. Degrees and corresponding phase labeled on the x-axis. Minor x-axis tick marks are spaced every 14 º (0.033 sec) apart. Data averaged over ten cycles.

3.2.2 Silicone Valve Pulsatile Flow and Deformation

A schematic of the undeformed SV and corresponding Cartesian coordinates are shown in Fig. 3-23. The coordinates have been switched from cylindrical for the diaphragm valve case to Cartesian because the SV is not axisymmetric. Fig. 3-23a shows the plane at the flow center of the SV, perpendicular to the commissures labeled as pC2C. The attachment of the leaflets to the root wall is located near x/D = 0.5. Fig. 3-23b shows the plane at the flow center of the SV and parallel to the commissures labeled as C2C. Fig 3-23c shows the end-on view of the SV including the initial gap between the two leaflets. The SV dimensions are normalized by the undeformed internal diameter D = 2 cm. The detailed SV dimensions are given in Figs. 2-18 and 2-19.

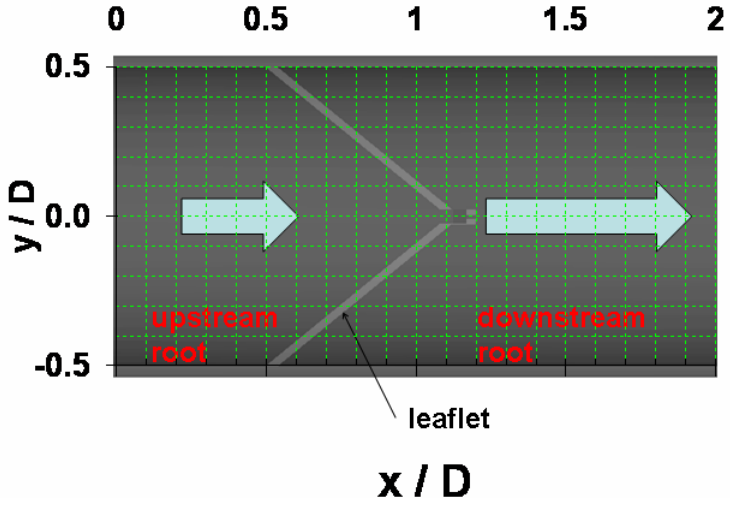

(a)

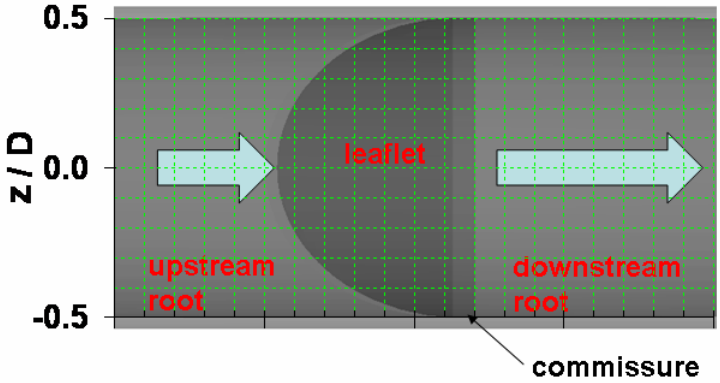

(b)

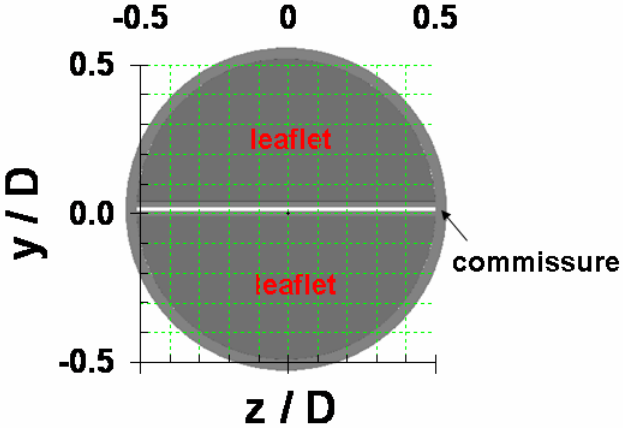

(c)

Figure 3-23. Undeformed schematic of the silicone valve. (a) plane perpendicular to commissure pC2C, (b) plane parallel to commissure C2C, and (c) end on plane views. D = 2 cm.

Digital video data was captured at 30 Hz during a cycle of the SV deformation. A total of 26 phases were captured, but only two are presented. The images for all 26 phases are shown in Appendix F. The corresponding phase and corresponding angle for each image is labeled in the caption of each figure. The images in Fig. 3-24a,b,c show the pC2C plane, C2C plane, and end-on view, respectively all acquired at φ6 (83º of systole) of different individual cycles. There was repeatability in the deformation state of the SV at a particular phase from cycle to cycle. The images in Fig. 3-25a,b,c show the same planes but at φ12 (166º of diastole). The approximate location of the SV root internal wall and 2D boundary of the outer leaflet surfaces are marked with red dots. Since the SV and the working fluid were closely index matched, the boundaries were difficult to observe or mark accurately. The leaflet opening and closing tip velocities can be measured by tracking the red circles' linear displacements between successive phases. The yellow arrows indicate the angle formed by the SV leaflets and root.

Fig. 3-24c shows an end-on trace-out of the open orifice area at φ6. The locations of the leaflets are also marked. The actual SV diameter spans the dimension of the Cartesian grid for the end on views. However, due to visual obstruction, only 80% of the undistended SV diameter is observable. The areas marked in red are likely open areas of the SV, which are not visible and therefore were not included when computing the percent open area. The percent open area is defined as the open area divided by the total SV undistended flow area. Since the obstructed open area (red) is not accounted for, the calculated value underpredicts the actual open area with respect to the undistended flow area. The underpredicted area for φ6 is approximated to be 2% of the total SV undistended flow area. Also, the SV root wall deformation is dynamic (with expansion and contraction of the root) leading to uncertainty in the approximation of the actual orifice area. Note that the end on view images were acquired using saline solution instead of water glycerin as the working fluid. The saline solution was used because it was not closely refractive index matched to the SV and enabled clearer identification of the leaflet boundaries. Since the forcing conditions were matched for both solutions, the deformation of the SV should not be affected by the change of working fluid. Fig 3-25c shows an end on view of φ12 with no open orifice area marked because the leaflets are

closed. The velocity of the leaflet opening, root expansion distance, bending angle of the leaflet, and open flow area are discussed in detail in the subsequent paragraphs.

The SV leaflets are open at φ6 during systole shown in the pC2C plane. The leaflets show a concave curvature with respect to the upstream flow of 23 L/min. During this phase, the valve leaflets experience pressure drops of 33 mmHg (upstream = 64 mmHg and downstream = 31 mmHg). The leaflet reverses in curvature becoming convex to the upstream flow at φ12 during diastole, when the flow rate is nominally zero and the pressure drop is -50 mmHg (upstream = -7 mmHg and downstream = 43 mmHg). The leaflet opening dimensions measure approximately 0.52D (consistent with both pC2C view and end-on) and 0.93D (0.8D is measured with the end-on view) along the y and z axis, respectively for φ6. There is an asymmetry in the opening with a larger area for $z / D < 0$ than for $z / D > 0$. The opening is fairly symmetric about the y-axis. The end-on view for φ12 shows asymmetry about the y-axis in the leaflet closing. The top leaflet appears to push against the bottom leaflet. This may be a result of the slight imperfection in the fabrication of SV leaflet tips.

The SV root is distended outwards near the root attachment for both φ6 and φ12 shown on the pC2C plane. In this plane, at x/D = 0.5, the root has distended in dimension to 1.1D and 1.11D during systole and diastole, respectively. The two phases experience downstream pressures of 31 mmHg (φ6) and 43 mmHg (φ12) resulting in this diameter expansion. It is possible that the pressure induced large radial expansions during systole may result in high hoop stresses at the location of the commissure approximately at x/D = 1.1 and y/D = 0. The large pressure drops of -50 mmHg during diastole may result in large tensile stresses at the commissure. At the streamwise location of x/D = 0.5 on the C2C plane, the diameter has not expanded for φ6; however, there is a reduction in diameter to 0.88D for φ12. The reduction in diameter is a result of the negative pressure (-7 mmHg) experienced in the upstream portion during diastole. The negative pressure (lower with respect to the external root pressure) is generated by the backwards stroke of the piston pump of the cardiovascular pulse duplicator. In the C2C plane, at the commissure x/D = 1.1, both φ6 and φ12 contract in diameter to approximately 0.93D. Both φ6 and φ12 show downstream root diameter expansion along the C2C plane. The geometry of the SV results in root contraction along the commissure

to commissure direction (at x/D = 1.1) and expansion along the perpendicular direction (at x/D = 0.5) to facilitate maximum SV opening and flow throughput during systole.

The angle formed by the root inner wall and outer surface of the leaflet is approximately 18º as measured on the pC2C plane for φ6. The initial undeformed state of this angle was 51º. It is expected that the root expansion during systole acts to minimize the change in bending angle between the leaflet and the root, and may result in lower stresses at this location. The same angle measured for φ12 is approximately 55º. From opening to closing, the leaflets bend approximately 37º and withstand the high pressure drops of +33 mmHg when open and -50 mmHg when closed.

These two phases registered the most pronounced deformation of the SV during systole and diastole. The negative pressures, as a result of the piston pump backward stroke during diastole, led to contraction of the upstream root. This rapid contraction then expansion was not damped immediately, and fluctuations in the root diameter and leaflets are registered in the fluctuations in the pressure signatures. The rapid closing of the SV leaflets also had a concomitant effect. These fluctuations are eventually damped by mid diastole.

The leaflet tip velocity and percent open area for the SV are plotted versus time in Fig. 3-26. The leaflet velocities were captured over seven phases during systole. The SV open area was measured over eight phases during systole. The velocity is normalized by U_{avg} = 22 cm/s (based on the time-averaged flow rate and SV inner diameter of 2 cm). A peak leaflet tip velocity of $0.28U_{avg}$ is reached at φ5 or 69º. The opening velocity decreases to nearly zero at φ7 or 97º. When the leaflets close, their maximum velocity is $0.2U_{avg}$, similar to the maximum opening velocity. The maximum area measured was 35% at φ9 or 125º.

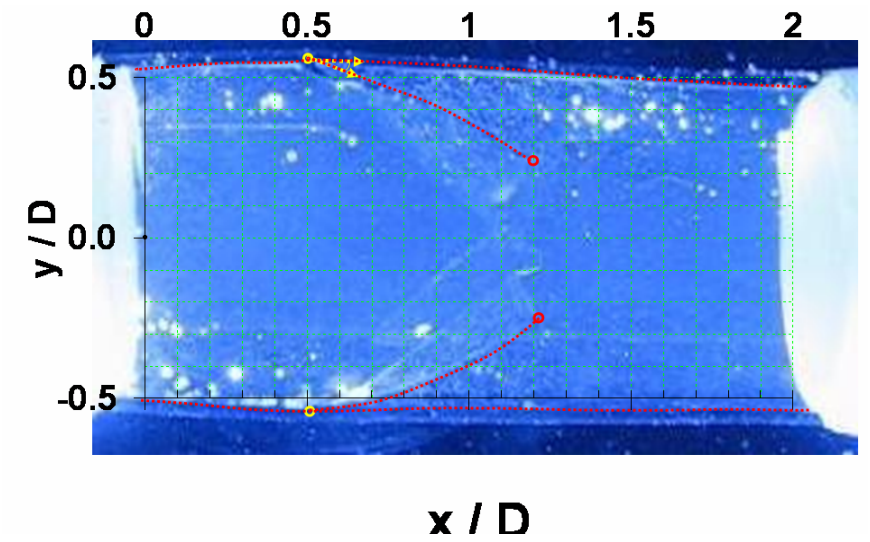

(a)

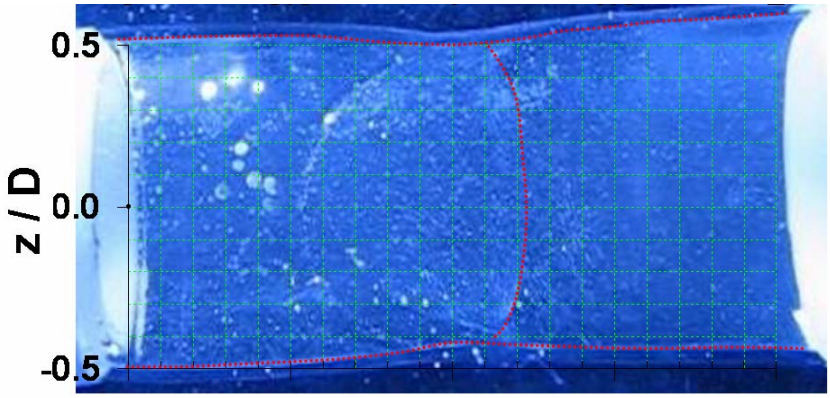

(b)

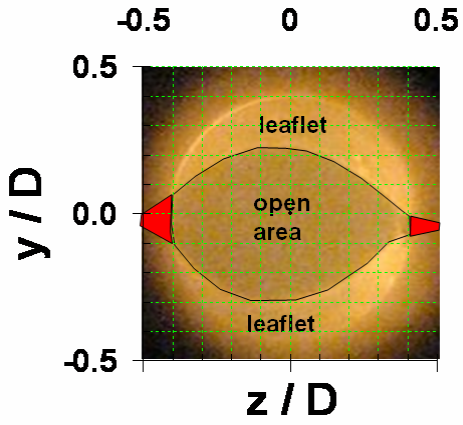

(c)

Figure 3-24. Silicone valve deformation state at φ6 or 83° of systole. (a) pC2C plane, (b) C2C plane, and (c) end-on plane of the SV. The leaflet outer surface and root inner boundaries are outlined in red dots. The red circle indicates the leaflet tip locations where the tip velocity is measured. The yellow circles indicate location of leaflet root attachment. The yellow arrows indicate the opening angles. The shaded red region in (c) indicates potential open orifice area not measured. D = 2 cm.

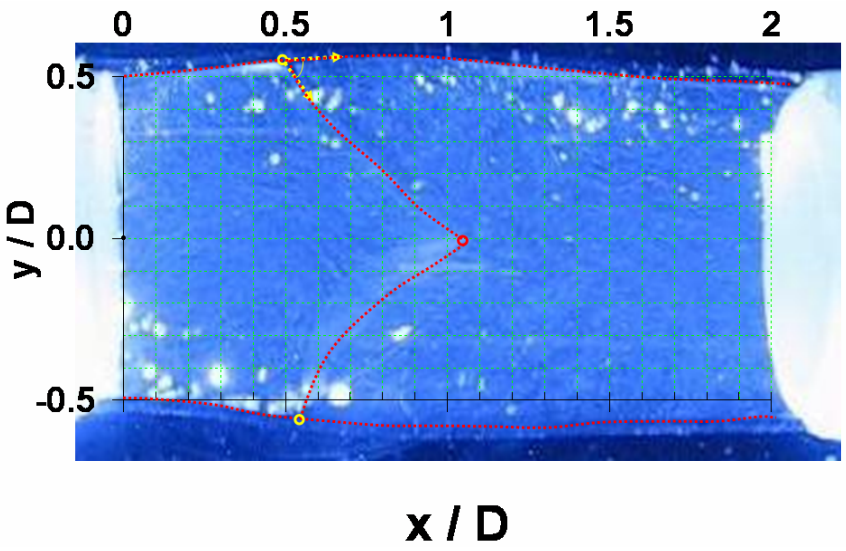

(a)

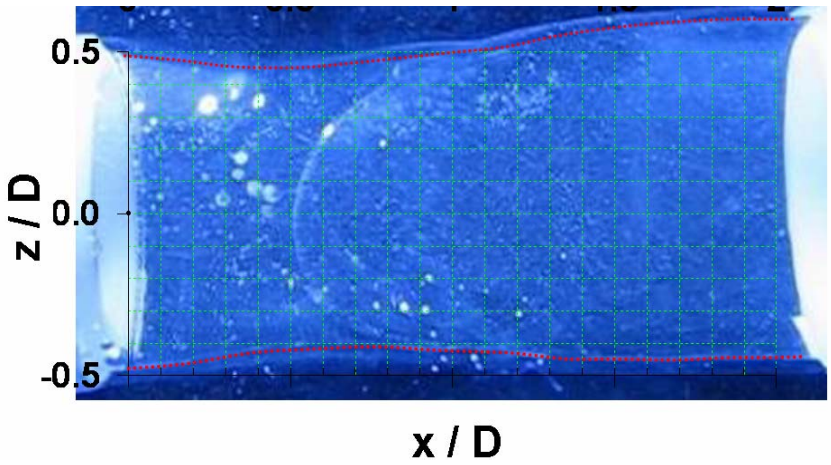

(b)

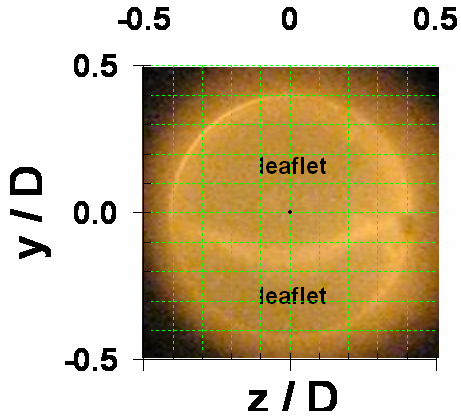

(c)

Figure 3-25. Silicone valve deformation state at φ12 or 166º of diastole. (a) pC2C plane, (b) C2C plane, and (c) end-on plane of the SV. The leaflet outer surface and root inner boundaries are outlined in red dots. The red circle indicates the leaflet tips where velocity of tip displacement is

measured. The yellow circle indicates location of leaflet root attachment. The yellow arrows form the closed angle. D = 2 cm.

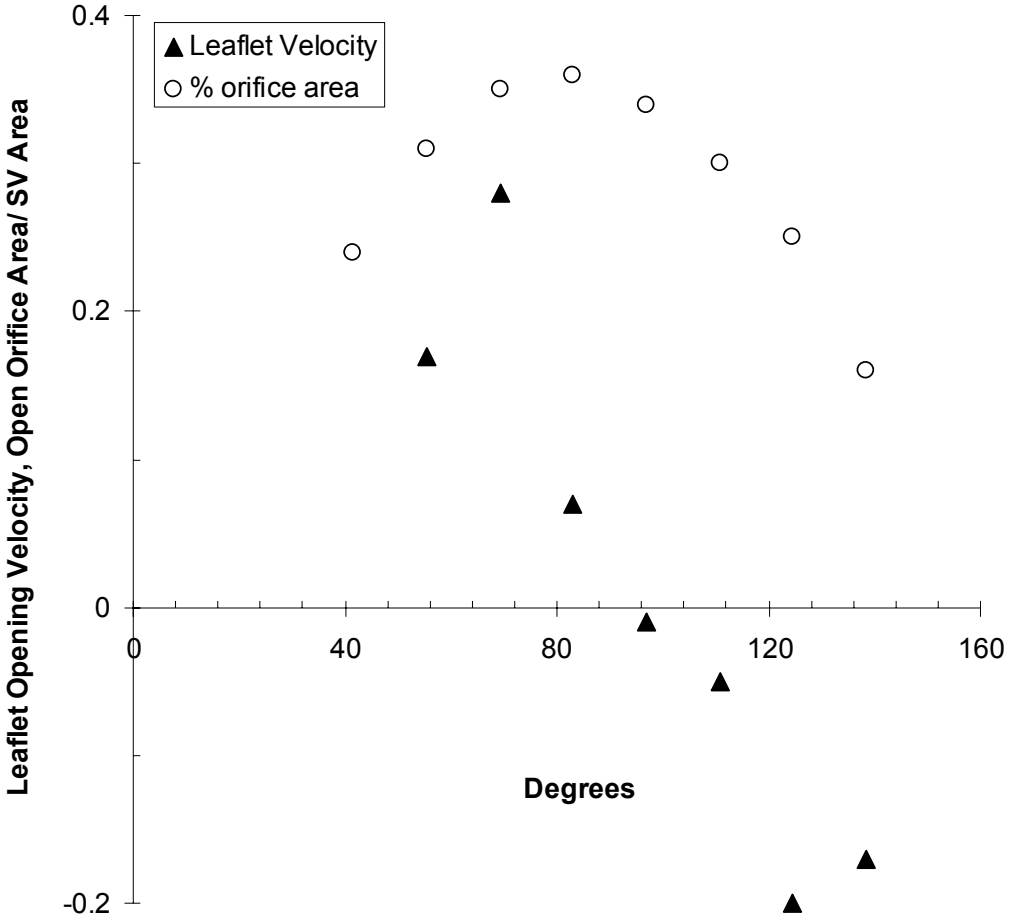

Figure 3- 26. SV leaflet tip opening velocity and open area tracked at 30 Hz during systole. Leaflet opening velocity normalized by U_{avg} = 22 cm/s. Open area normalized by SV undistended area. Negative velocity indicates closing leaflets.

3.2.3 Silicone Valve Flow Characteristics

3-dimensional 3-component (3D3C) velocity measurements were made for seven phases of the cycle. The phases examined were at φ0 (0º), φ2 (28º), φ6 (83º), φ8 (111º), φ16 (222º), φ19 (263º), and φ22 (305º) seconds. Flow field measurements through the SV will be quantified in detail for two phases, φ8 (systole) and φ19 (diastole). Fig. 3-27

shows raw V3V images of the open (φ8) and closed (φ19) phases of the SV with particle density (shown as brighter pixels) as viewed by one of the V3V cameras. Although particles appear dim near the top and bottom, valid data was obtained there. The larger brighter specks are small air bubbles that became attached to the inner walls of the SV in this visualization and were difficult to remove. The processed data velocity vectors were masked at this location eliminating data with the uncertainty caused by the location of the air bubbles.

The SV pC2C deformed state recorded by the V3V camera corresponds well with the image recorded by the digital video camera at the same phase (see Appendix F-1 for φ8 and φ19), although a different cycle was captured with the digital video camera.

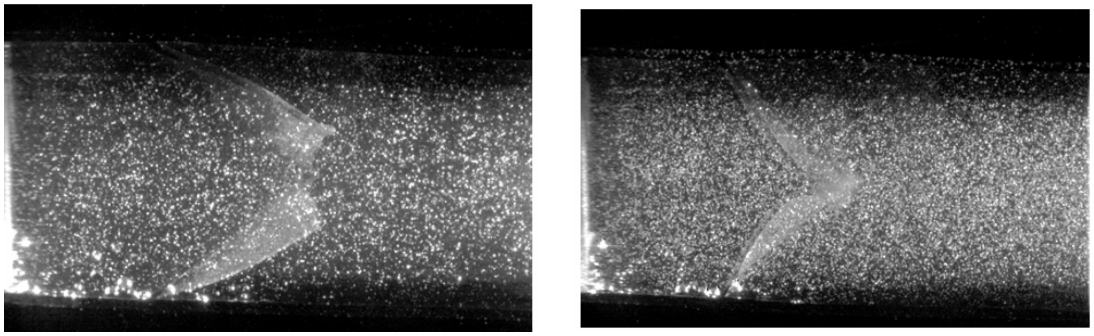

(a) (b)

Figure 3- 27. V3V raw image of valve deformation and tracer particles. (a) systole at φ8 (111°) and (b) diastole at φ19 (263°).

3.2.3.1 Systole

Fig. 3-28 shows instantaneous two-dimensional velocity vector fields along with vorticity contours (threshold of ±20) on the pC2C and C2C planes during systole (φ8). The two-dimensional boundaries (green tracing) of the SV, including the root and the leaflets as seen in the raw V3V image (for pC2C) and digital camera images (for C2C) have been traced on the figures. In the following discussion the pC2C and C2C planes will be referred to as (x, y) plane and (x, z) plane, respectively. The SV opening is approximately 0.37D. The leaflets are bulged outwards towards the downstream direction. The root is larger in diameter than the undistended state of the SV as projected on the (x, y) plane. The (x, z) plane shows minimal expansion in diameter. The leaflet tip

projected on this plane results in an arc. These boundaries are similar to that of φ6 shown in Fig. 3-24.

The upstream velocity has a dominant x-component approximately $5U_{avg}$ with the higher velocities slightly skewed towards y / D = 0.5 for Fig 3-28a. The asymmetry is due to an asymmetric inlet condition from the pulse duplicator VIA component (See Fig. 2-8). The predominantly streamwise velocity vectors turn inwards as they approach the SV leaflets. The vector magnitudes immediately upstream and downstream of the leaflet wall are very small. The vector magnitudes are examined in closer detail in Fig. 3-38, FSI Section 3.2.3.3. A significant amount of vorticity ω_z is generated near the upstream leaflet walls before the fluid exits the SV leaflets. The red and blue contours represent clockwise and counter-clockwise rotation respectively. This vorticity in the upstream flow extends into the shear layer downstream where the thickness of the high vorticity zone expands. The flow accelerates through the SV and generates a jet downstream. The vectors along the jet periphery have inward and upstream components almost to the end of the field of view indicating recirculating zones.

The boundary of the SV root and leaflet in the (x, z) plane, tracked separately by digital video data, are overlaid on the velocity vector field with the ω_y contour shown in Fig. 3-28b. The vectors are fairly uniform in size and direction throughout this field except near the root wall location of the SV and in particular near the leaflet opening. Near x/D = 1.25, the vectors are directed outwards in the z-direction which is consistent with the local radial extension of the SV root. Velocity vectors do not extend to the walls, since illuminated particles were sparse in those locations, and no particle tracks were generated. For this reason, vectors are not seen on or near the SV walls, so that the no-slip condition is not observed. There is sparse distribution of high ω_y values near the SV opening. The distribution of ω_y may occur near the walls where measurements were not obtained.

The mean velocity vector fields and vorticity contours of five realizations along both planes for φ8 are plotted in Fig. 3-29. The mean flow profiles (with instantaneous deformed diaphragm state overlaid) are consistent with the flow behavior in the individual realizations, which suggest repeatability in the pulsatile flow from cycle to cycle during this phase of systole. Additionally, the diaphragm deformed state shows

repeatability from cycle to cycle and therefore only one of the boundaries from the five realizations was traced.

Fig. 3-30a shows a three-dimensional instantaneous view of the same flow. Two vector fields at (y, z) plane of x/D = 0.25 and 1.25 are shown. These vectors are mostly directed in the streamwise direction. An isocontour of streamwise velocity with magnitude of $5U_{avg}$ is plotted in green. The contour shows that the momentum is spread over a wide area upstream of the SV but then is squeezed through the slot-like opening yielding a narrower distribution in both y and z directions that eventually spreads downstream. Fig. 3-30b shows a slice near the jet exit (x/D = 1.25) of the streamwise velocity contour. The lowest contour plotted is $1U_{avg}$ resulting in a rectangular profile of the jet having maximum streamwise velocity reaching $13U_{avg}$ near the center of the flow. Based on the volumetric flow domain measured (i.e., approximately 80% of the initial root volume) and the streamwise velocity filter of $1U_{avg}$, the jet area can be approximated to cover at least 30% of the undistended root flow area. This is consistent with SV open area measured with the digital video data at this phase.

Fig. 3-31 shows x, y-velocity vector field at z/D = 0 along with 3D swirl and 3D principle shear stress. The 3D swirl normalized (by U_{avg} and D) isocontour = 7 in grey passes through the location of the downstream recirculation zones on the jet periphery and may indicate the presence of an elliptical vortex ring. Since the flow volume measured was limited in the z-direction, it is difficult to conclude, if in fact, the elliptical ring is connected at large z-values. There is some evidence of high swirl values upstream, which may be a result of the unsteadiness of the upstream flow. The principal shear stress derived through the velocity gradients (see Appendix C) gives a coordinate invariant representation of the physical shear forces acting in the flow. The isocontour of $0.5\tau_{sys\_max}$ is plotted in red, where τ_{sys_max} is the maximum systolic shear stress measured. Due to the relatively coarse resolution of the velocity vectors, the actual magnitudes of principal shear stresses, calculated through spatial gradients may be underestimated. A more quantitative analysis of vector resolution and its effects on higher order calculation (e.g., velocity gradients and vorticity) is shown in Section 3.3.3. For qualitative comparison from phase to phase, the absolute principal shear stresses are

normalized by the maximum value during systole. The location of the high shear stresses corresponds to the location of the swirling flow.

For comparison purposes, the streamwise velocity of the flow at x/D = 1.25 during peak flow (φ6) is plotted in Fig. 3-32a. Both the jet width along y/D and the peak velocities are larger compared with φ8. Velocities below $1U_{avg}$ were filtered out. The peak velocity in this phase reaches $17U_{avg}$ and the jet width along the y/D axis spans approximately 0.5D. Note, that there is an asymmetry in the flow profile with higher velocities in the region defined by negative y/D and z/D quadrant. Also, the significant velocity magnitude extends beyond the undeformed boundary of the root as a result of root expansion. The lower resolution of the V3V vectors may and the way they are interpolated result in unrealistically high velocities close to the walls. Fig. 3-32b shows 3D principal stress isocontour = $0.5\tau_{sys\_max}$. These high values span across the shear layer of the jet and clearly scale with the higher velocity of the jet as compared to φ8.

V3V data was not acquired when jet initially exited the valve because *a priori* knowledge of this phase was uncertain. It is possible that a leading vortex ring-like structure with a trailing jet may have been present, much like the case for the pulsating diaphragm.

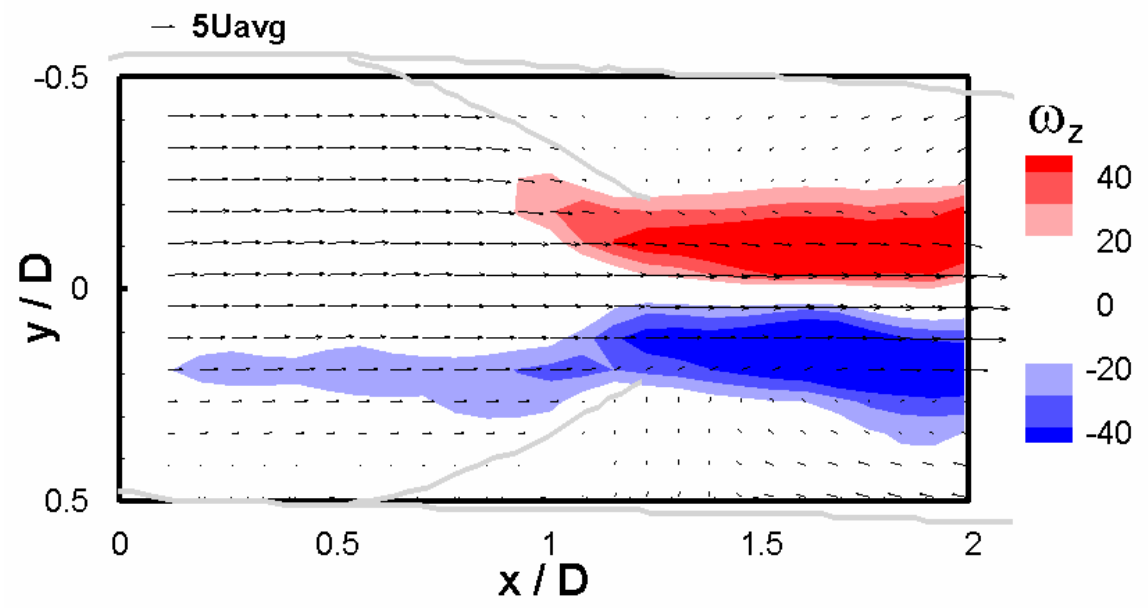

(a)

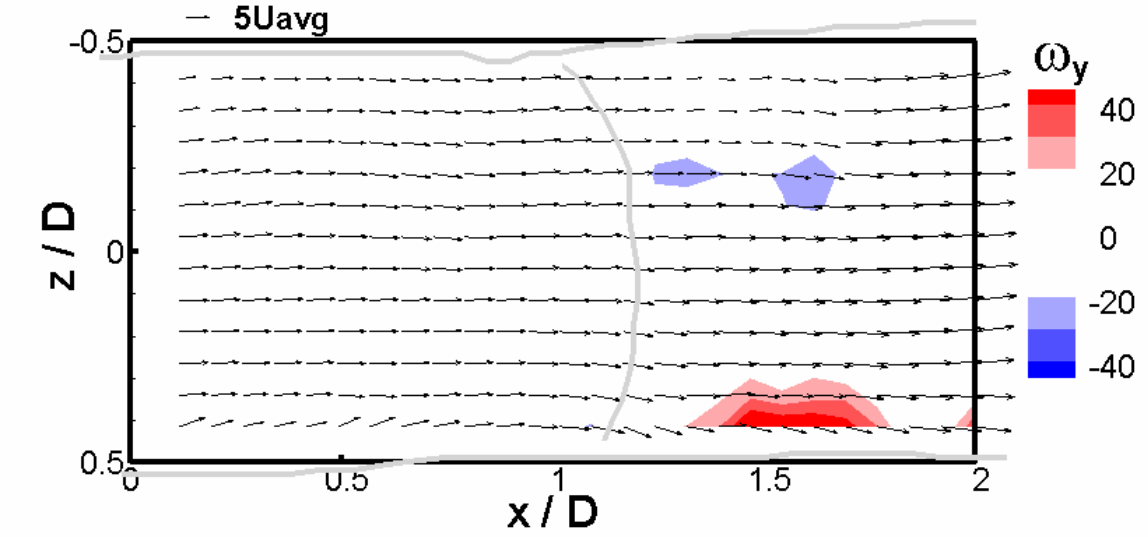

(b)

Figure 3- 28. Systole phase φ8. (a) x, y-velocity vector field (pC2C plane) along with ω_z contour at the z/D = 0 plane and (b) the (x, z) velocity vector field (C2C plane) along with ω_y contour at the y/D = 0 plane.

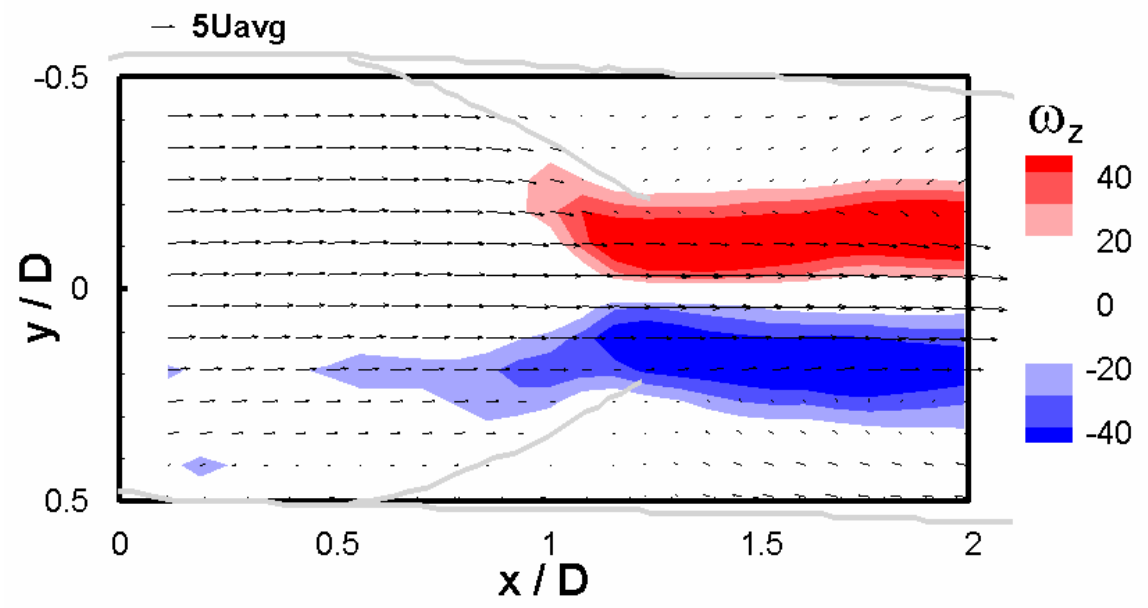

(a)

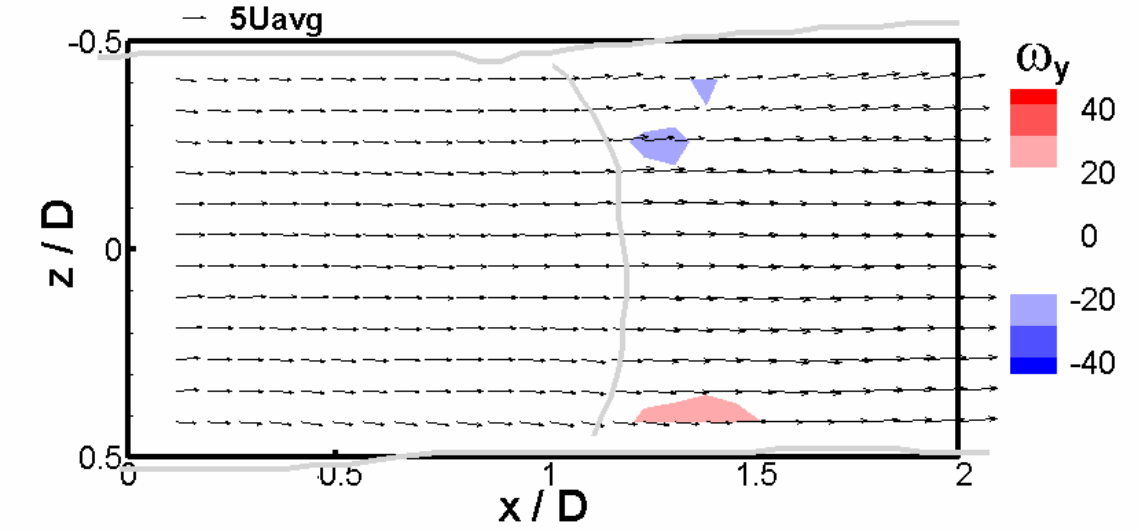

(b)

Figure 3- 29. Systole phase φ8 (a) mean x, y-velocity vector (pC2C plane) field along with mean ω_z contour at the z/D = 0 plane, (b) the mean x, z-velocity vector field (C2C plane) along with mean ω_y contour at the y/D = 0 plane. Data average of five realizations.

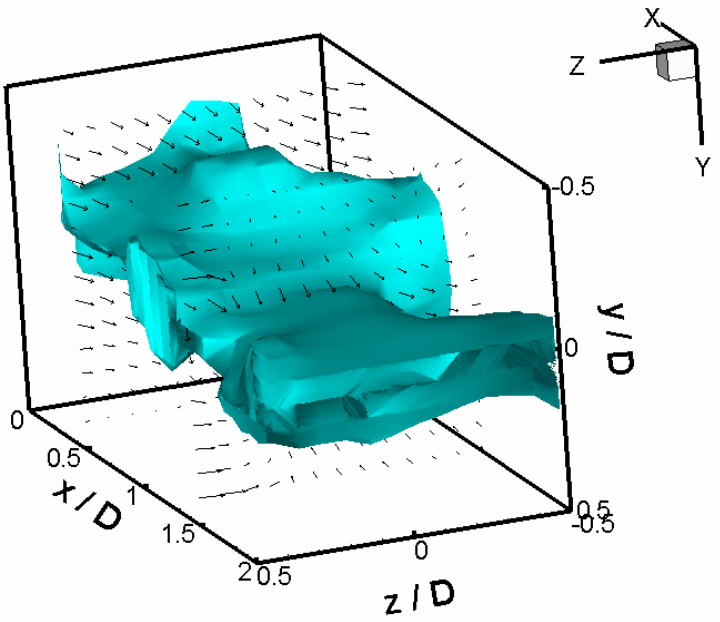

(a)

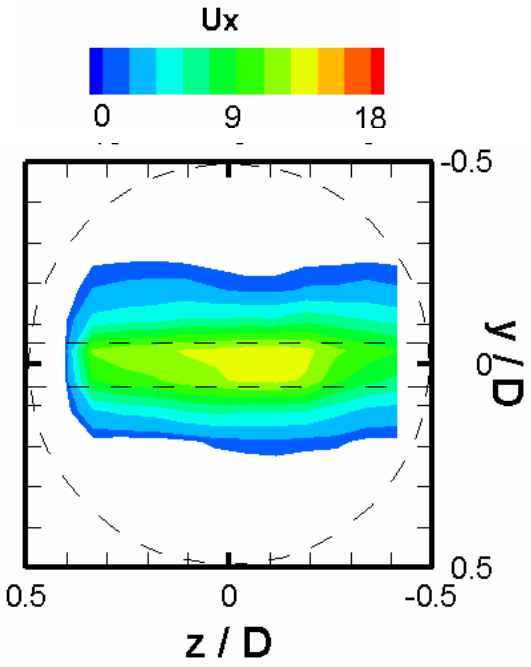

(b)

Figure 3- 30. (y, z) velocity vector fields at x/D = 0.25 and 1.25 planes with streamwise velocity isocontour U = 5Uavg in green, (b) streamwise velocity on (y, z) plane at x/D = 1.25 for phase φ8. Lowest U plotted = 1Uavg with increments of 1.

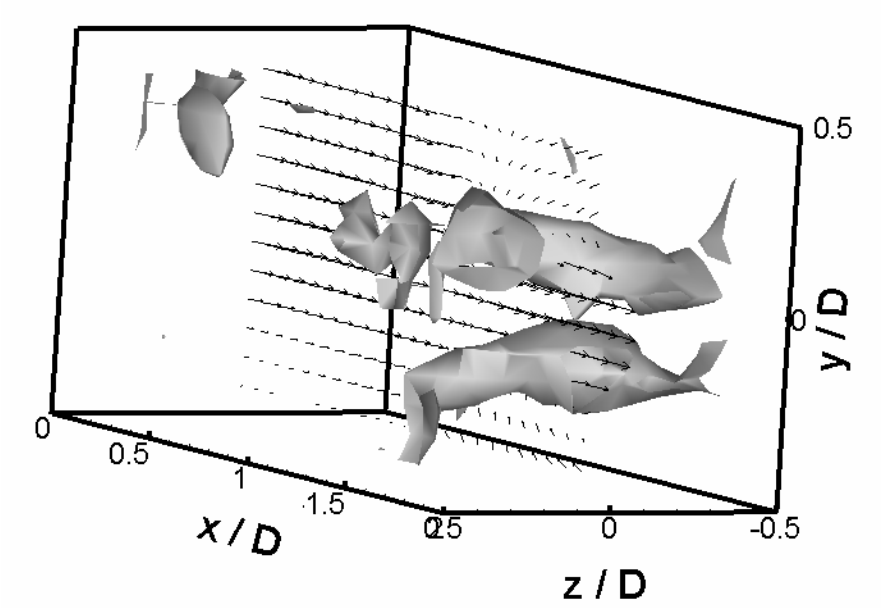

(a)

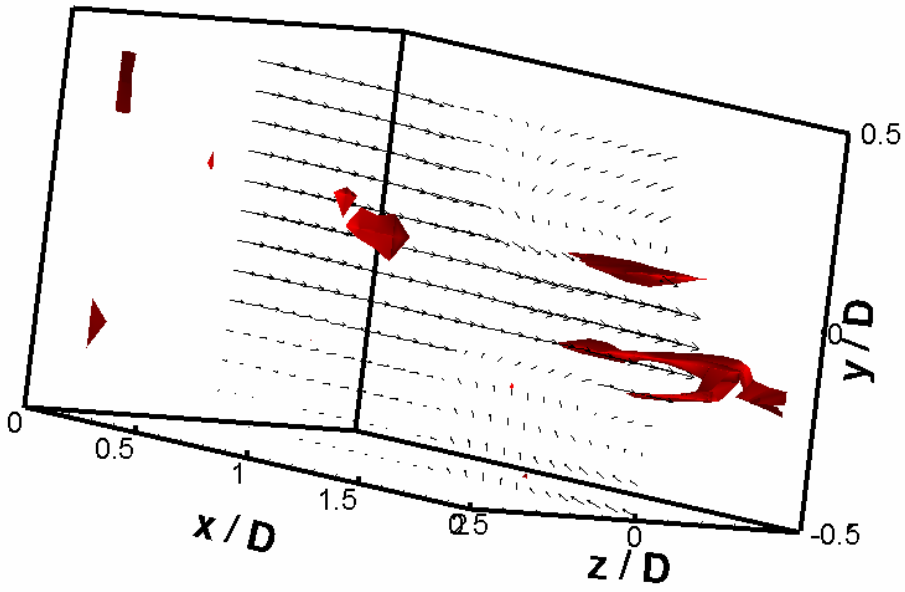

(b)

Figure 3- 31. (x, y) velocity vector field (pC2C plane) at z/D = 0, (a) 3-D swirl normalized isocontour = 7 and (b) 3D principal shear stress = 0.5τsys_max for phase φ8.

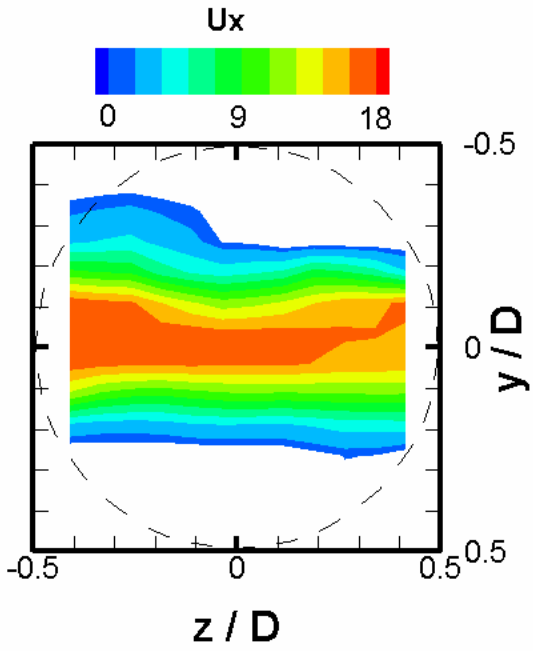

(a)

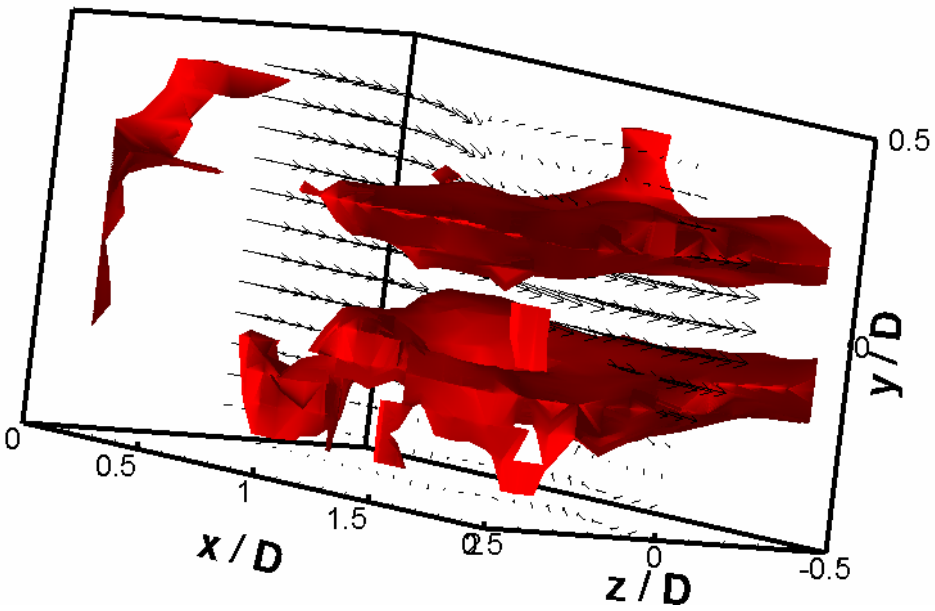

(b)

Figure 3- 32. (a) Streamwise velocity on y, z-plane at x/D = 1.25. Lowest U plotted = 1Uavg with increments of 1 and (b) 3D principal shear stress isocontour= 0.5τsys_max phase φ6.

3.2.3.2 Diastole

Fig. 3-33 shows two-dimensional velocity vector fields along with vorticity contours on the (x, y) plane for φ19 (diastole). Similar to the data presented for systole, the SV root wall and leaflets are traced in green. The markings for the (x, y) plane indicate the root is larger in diameter than the undeformed SV state. The leaflets reverse in curvature and are now convex with respect to the upstream flow. In the (x, z) plane, the root diameter is narrower near x/D = 0.5, but is comparable to the original diameter both upstream and downstream of this streamwise location. The velocity vectors are much smaller in magnitude as shown by the $0.5U_{avg}$ reference vector, as compared to $5U_{avg}$ for the open phase. Also, the vorticity scale is decreased by more than an order of magnitude for the closed phase as compared to the open phase. Clockwise and (weak) counter-clockwise rotating structures are present upstream and downstream of the closed leaflet respectively as shown in the (x, y) plane. The x, z-velocity vector field shows higher velocity but multidirectional vectors in the upstream location as compared to the downstream location.

The mean velocity vector fields and vorticity contours averaged over five realizations at φ19 along both planes are plotted in Fig. 3-34. The mean flow profiles are consistent with the flow behavior in the individual realizations, which suggest repeatability in the pulsatile flow from cycle to cycle during systole. However, a clear difference is that rotating eddies along with the vorticity values are eliminated in the mean for the downstream region, unlike the upstream clockwise rotating eddy. This indicates that the direction and size of the rotating structures downstream is more random. In the upstream region of the (x, z) plane the mean flow is moving towards the right.

Fig. 3-35 shows a 3D view with the (x, y) plane at z/D = 0 velocity vector field for φ19. The 3D swirl isocontour = 0.6 is plotted. The isocontour passes through the rotating velocity vector field. This swirl further indicates the presence of a rotating three-dimensional structure. The time evolving nature of the swirling structure upstream during diastole is shown in Fig. 3-36. The plots a, b, and c correspond to φ16, φ22, and φ0 respectively. At φ16 the swirling structures are smaller, less organized, and dispersed throughout the flow volume. At φ19, shown in Fig. 3-35, the downstream swirling

structures have dissipated and the upstream swirling structure has become organized, while growing in strength and size. In the later phases of φ22 and φ0, shown in Figs. 3-35c,d the swirling structure's strength and size is reduced.

Fig. 3-37 shows the 3D principal shear stress isocontour = 0.4τdia_max, where τdia_max is the maximum principal stress during diastole. The phases presented correspond to the same phases as the time-evolving 3D swirl structures. At this phase, the locations of the higher principal stresses do not necessary coincide with the location of the swirling structures. The duration of higher principal stresses at a particular location is shorter than the time between the phases. These higher principal stresses are therefore short lived.

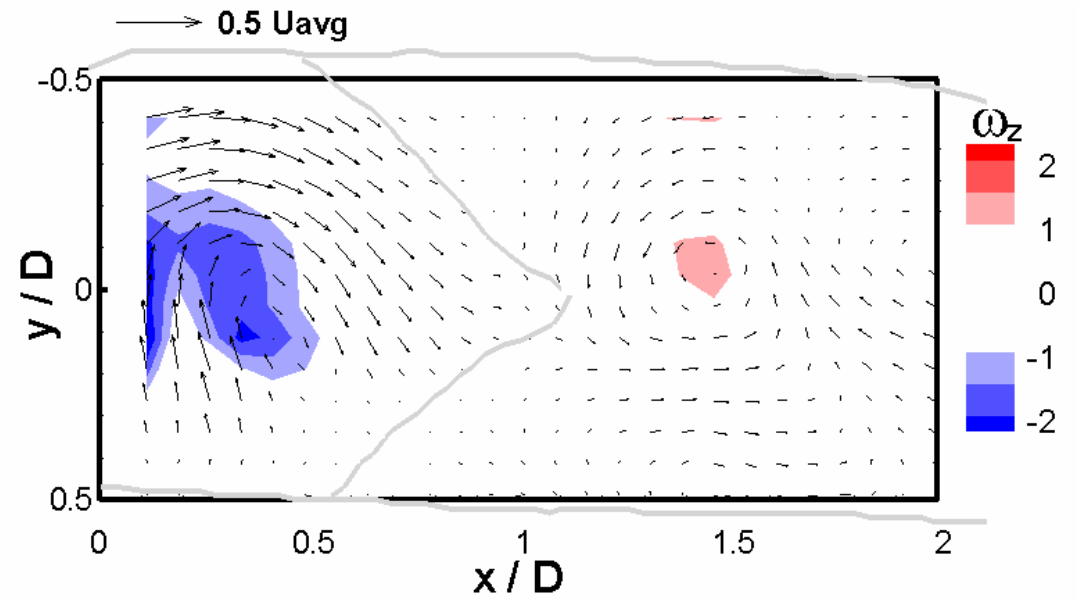

(a)

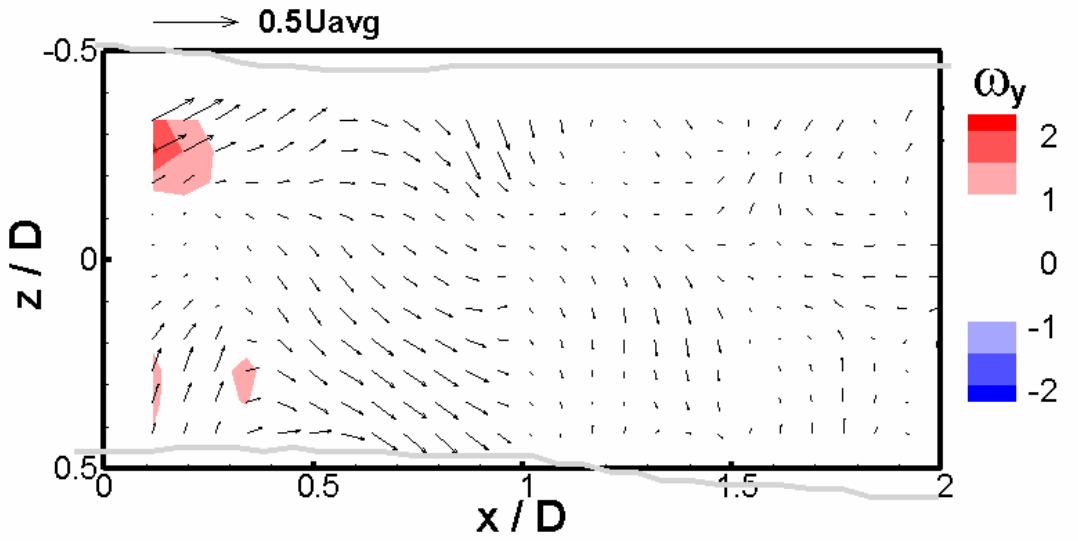

(b)

Figure 3- 33. Diastole phase φ19 (a) x, y-velocity vector field (pC2C plane) along with ω_z contour at the z/D = 0 plane, (b) the x, z-velocity vector field (C2C plane) along with ω_y contour at the y / D = 0 plane.

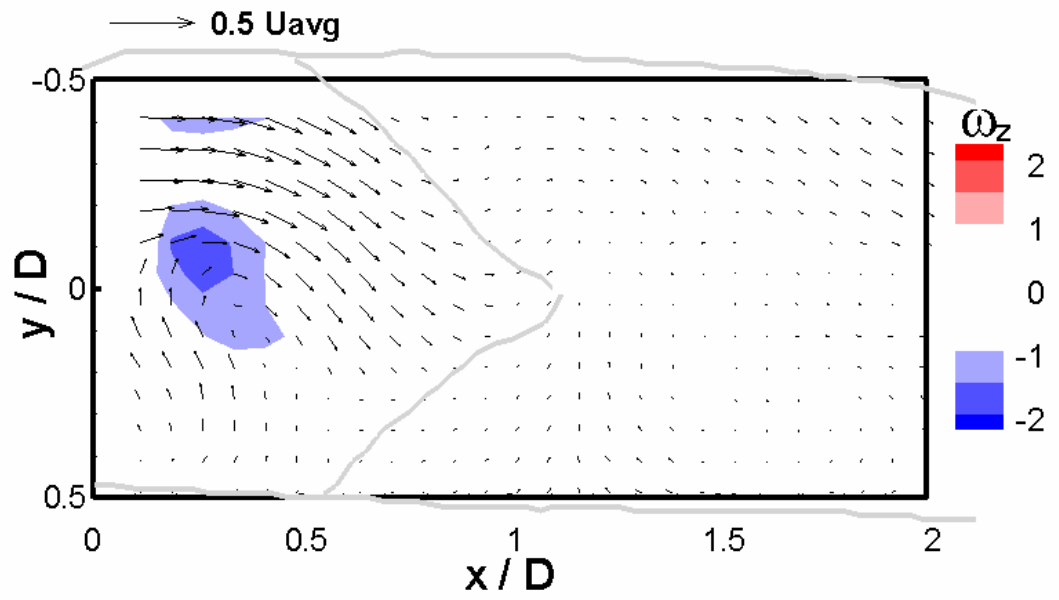

(a)

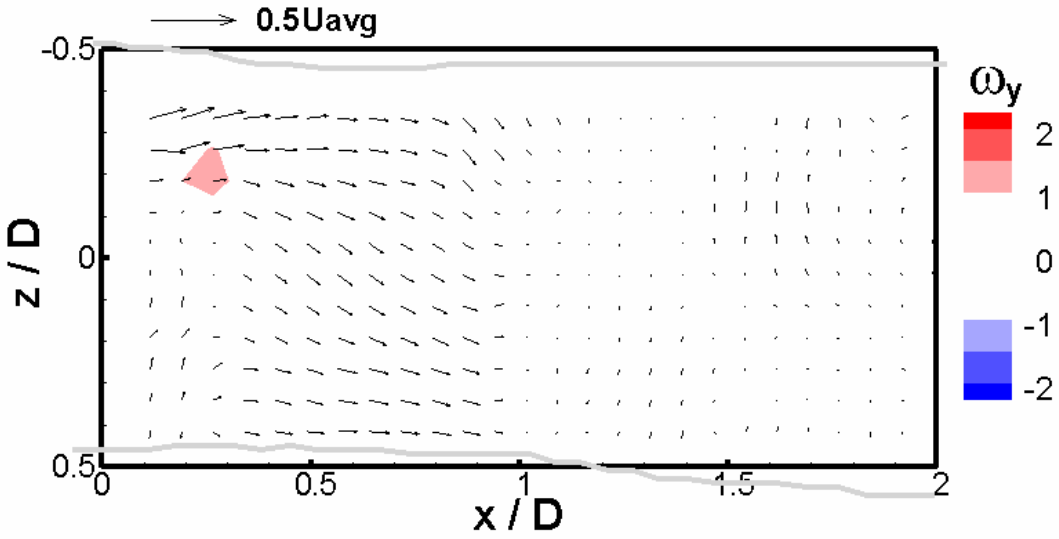

(b)

Figure 3- 34. Diastole phase φ19 (a) mean x, y-velocity vector field (pC2C plane) along with mean ω_z contour at the z/D = 0 plane, (b) the mean x, z-velocity vector field (C2C plane) along with mean ω_y contour at the y/D = 0 plane. Average of five realizations.

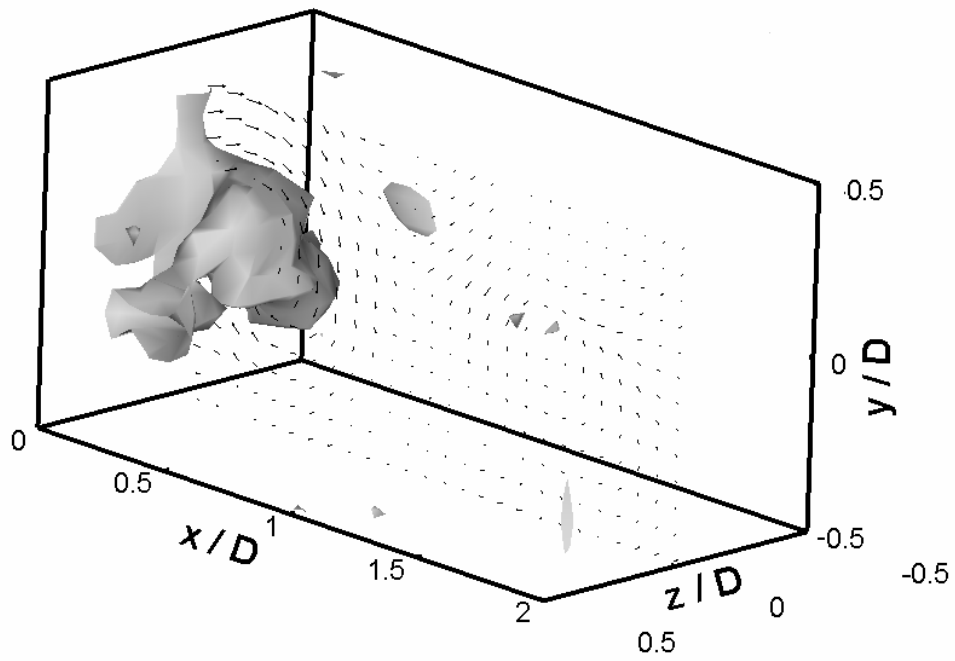

Figure 3- 35. (x, y) velocity vector field (x, z) plane at z/D = 0 with 3D swirl isocontour = 0.6 for phase φ19.

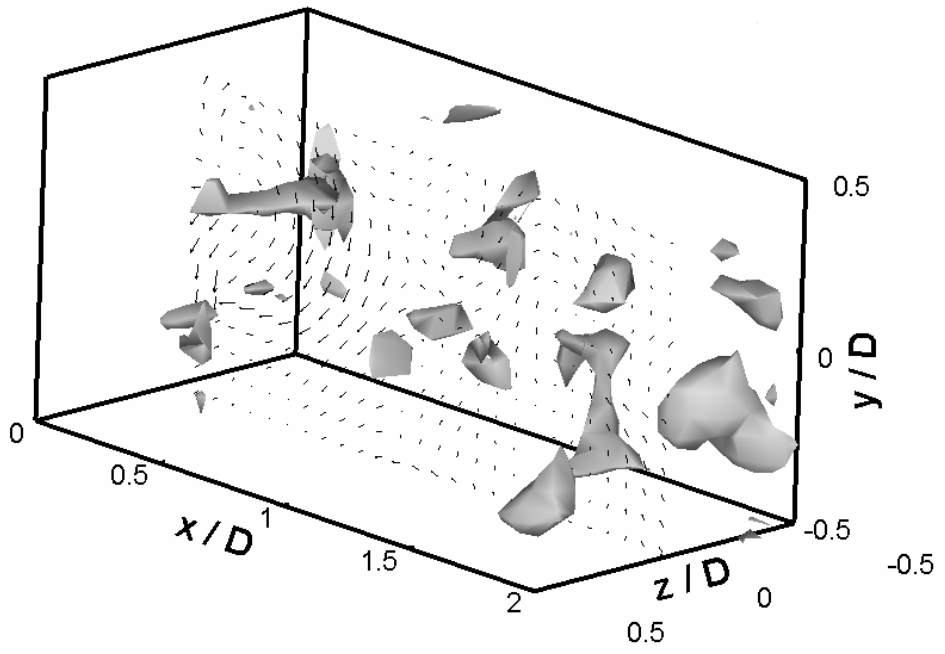

(a)

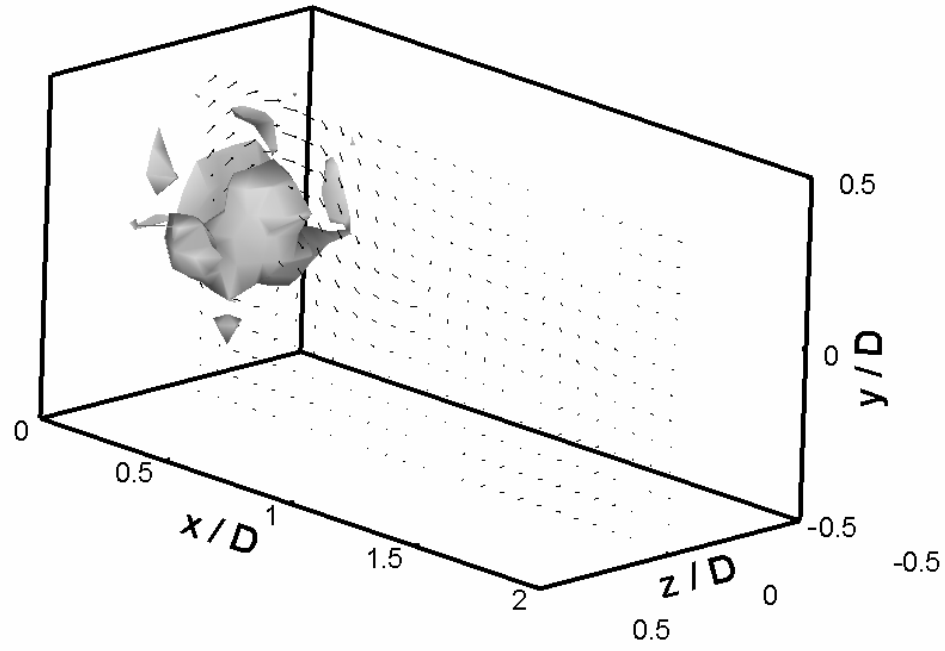

(b)

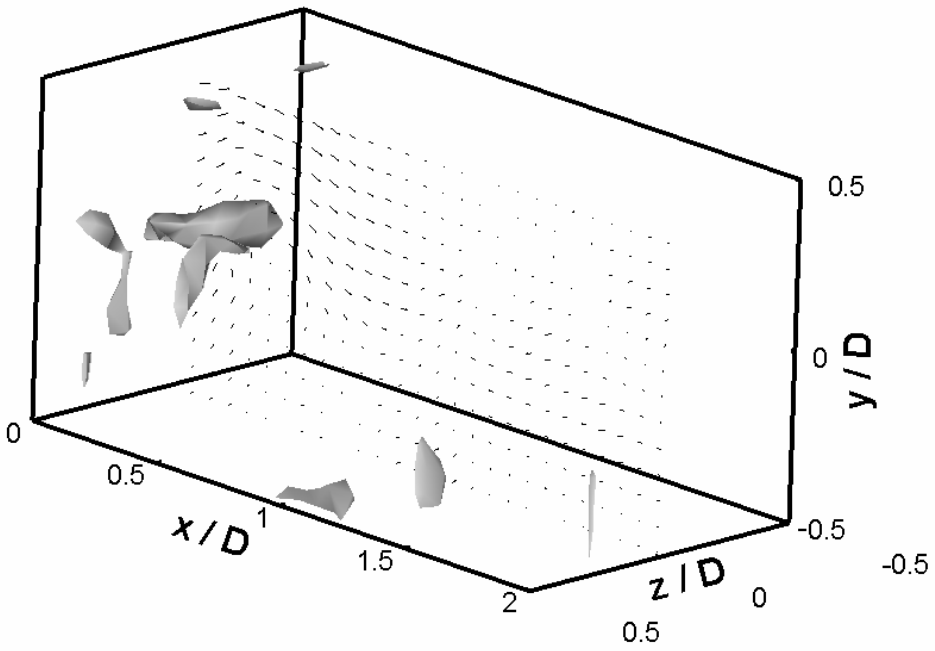

(c)

Figure 3- 36. (x, y) velocity vector field (pC2C plane) at x/D = 0 with 3D swirl isocontour = 0.6. (a) φ16, (b) φ22, and (c) φ0.

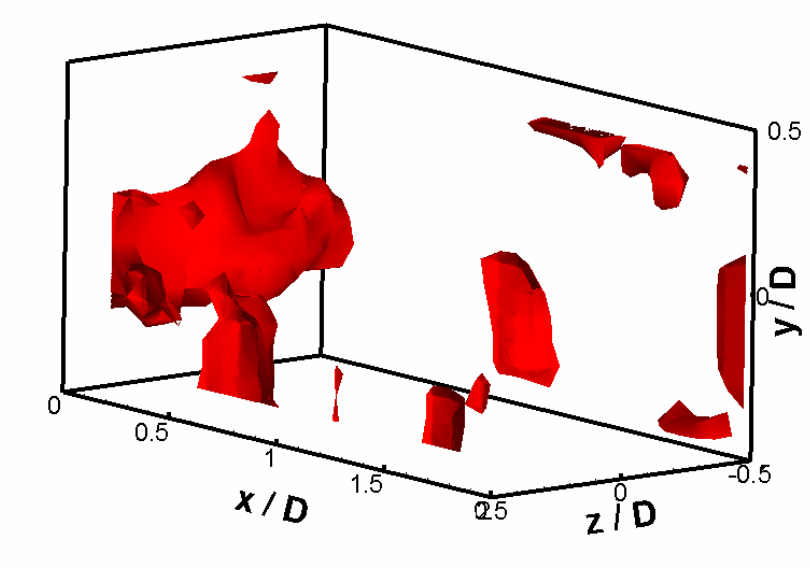

(a)

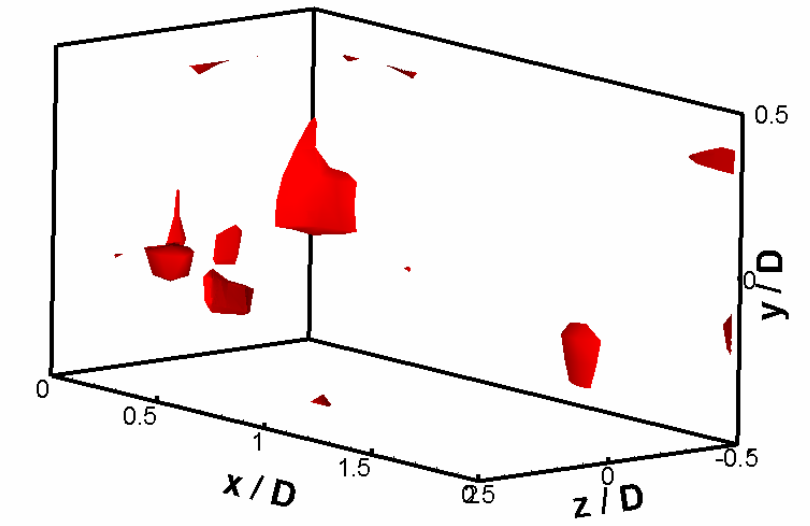

(b)

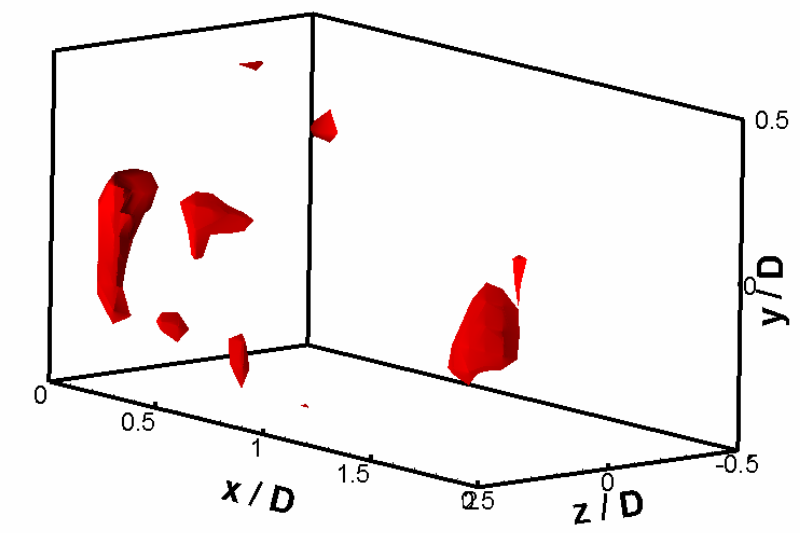

(c)

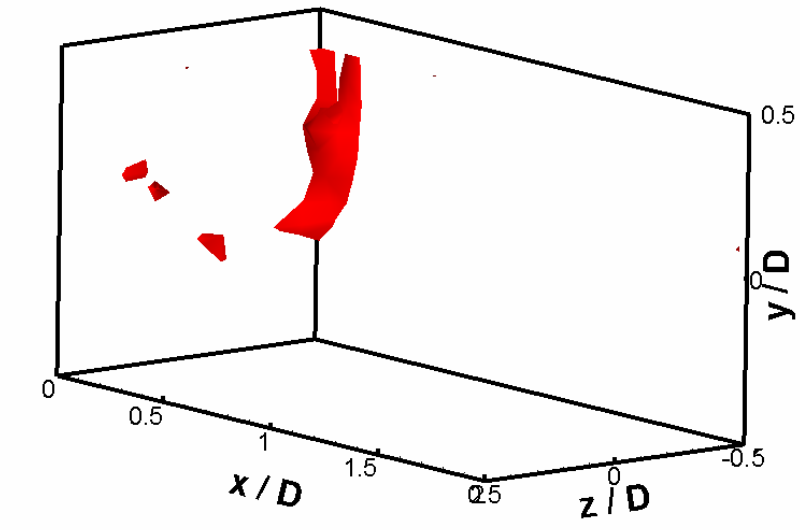

(d)

Figure 3- 37. 3D principal shear stress isocontour = 0.4τsys_max. (a) φ16, (b) φ19, (c) φ22, and (d) φ0.

3.2.3.3 Fluid Structure Interaction

Fig. 3-38 shows the velocity vector field and deformed SV state during early systole phase φ2. The leaflet movement was identified between the two successive captures of the V3V raw data separated by 2,500 μs. The deformed SV state of the first image captured on the (x, y) plane is shown in grey. The velocities of the leaflets were interpolated from the velocity of the moving fluid at the location of the leaflet wall. The leaflet wall normal velocity was calculated based on the measurement of the angle formed by the leaflet wall and root wall approximated to 42º. The leaflet velocities are higher at the tips and reaches values of 0.3U. This is in the range of tip velocities measured at later phases tracked using video data (see Fig. 3-26). Notice also that the moving SV leaflets displace the fluid immediately downstream of the SV radially outwards. This is clearly seen in the upper region.

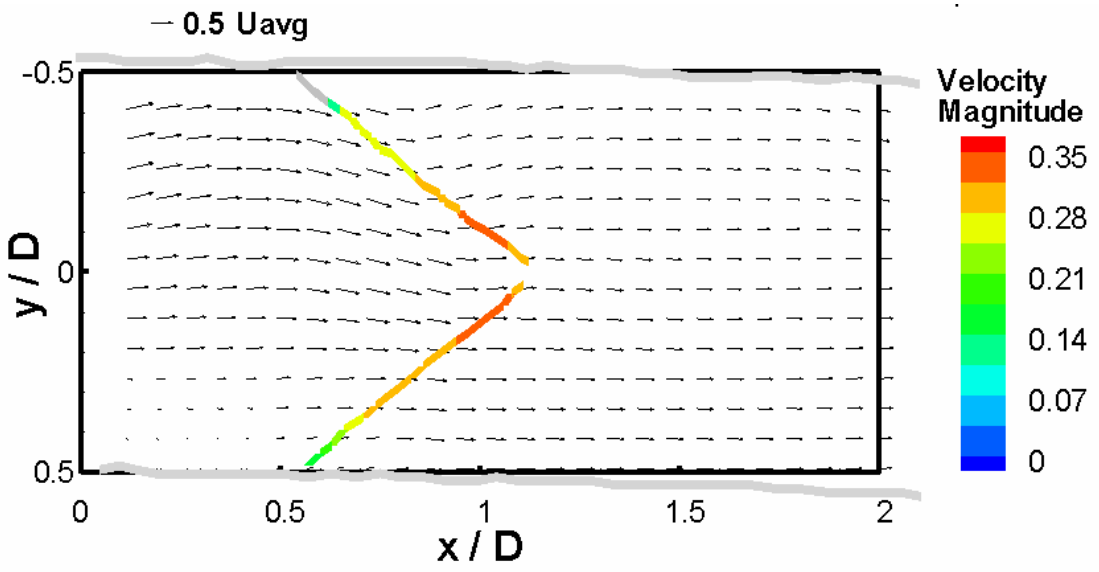

Figure 3- 38. (x, y) velocity vector field with leaflet velocity contour of the pC2C plane for φ2.

3.3 Tissue Engineered Valve Equivalents

The results presented below were for the 39 valve equivalents (VEs) harvested from the Tranquillio tissue engineering laboratories. The VEs were classified as either bileaflet (2L) or trileaflet (3L), and generation one (G1) or generation two (G2). G1 valves were harvested after static incubation, whereas G2 valves were grown in a bioreactor in addition to the static incubation. Fig. 3-39 shows images from the downstream or aortic view of the VEs. Unlike the transparent silicone valves, the VE root is not able to support its weight and therefore must be held open with forceps. The silicone valve is stiffer because it has a thicker root of 0.1 cm as compared to 0.03 cm for the valve equivalent. Note that the VEs are more compliant with a lower instantaneous modulus at lower stresses (stress < 0.04 MPa) than the silicone valve as shown in Appendix E-2. At higher stresses the circumferential direction of the VE leaflet is stiffer than the silicone valve, but comparable in the radial direction. Fig. 3-39a shows a 2L VE with leaflets open. The VE leaflets are able to coapt almost completely with the weight of a few drops of fluid in the belly of the leaflet as shown in Fig. 3-39b. The 3L VE shown in Fig 3-39c also coapts under the weight of the fluid as shown in Fig 3-39d. The two ends of the VEs were mounted onto rigid ends using sutures and the root placed in an external fluid bath. The attachment of the VE completed the valve testing flow loop. In this exposed root setup, the internal root pressure has to be approximately 3 mmHg greater than the external bath hydrostatic pressure for the VE root to be held circumferentially open (approximately the original root diameter) and support its weight. Fig. 3-40a shows where the external pressure $\geq$ internal pressure resulting in root collapse. Once the VEs were mounted, the root had to be extended in length to approximately the original harvested length. Fig. 3-40b shows a reduced length leading to the buckling of the VE. Fig. 3-40c shows the initial no flow state with both the internal pressure and root length specification met.

(a)

(b)

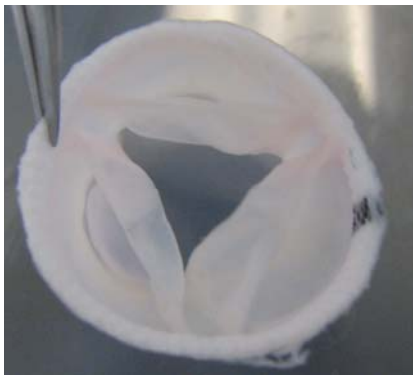

(c)

(d)

Figure 3- 39. Downstream view of valve equivalent. (a) natural open state of bileaflet VE, (b) bileaflet VE closed by the weight of the fluid held in the belly of the leaflet, (c) natural open state of trileaflet VE, and (d) trileaflet VE closed by the weight of the fluid held in the belly of the leaflet.

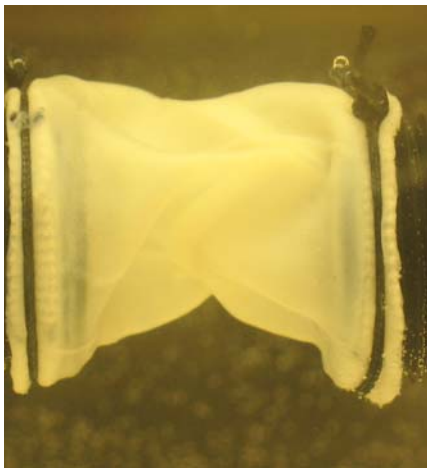

(a)

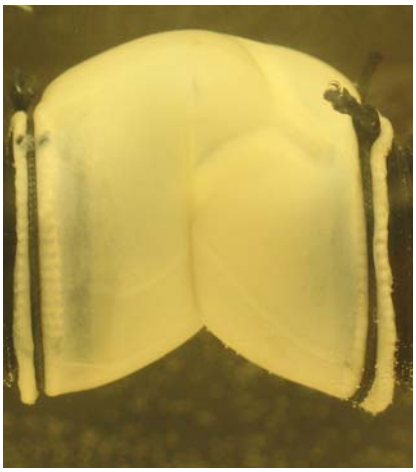

(b)

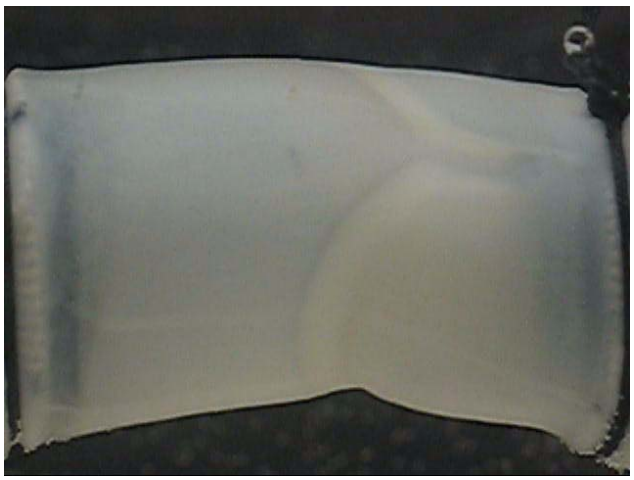

(c)

Figure 3- 40. Valve equivalent mounted with root exposed to external fluid. (a) VE root collapse with external fluid pressure ≥ internal fluid pressure, (b) incomplete lengthwise extension of root, and (c) internal – external pressure = 3mmHg with complete extension of root.

3.3.1 Steady Flow Performance

Steady flow tests were conducted on the VEs, and pressure drop and flow rate along with orifice area were measured. Fig. 3-41 shows the downstream view of the VEs. The orifice areas are marked for both 2L and 3L VEs. The leaflets shown in Fig. 3-41a,c do not coapt in the initial static state of zero flow having an internal pressure of 3

mmHg greater than the external pressure. The flow is ramped from 0 L/min to 9.5 L/min and the opening areas of the leaflets at 9.5 L/min flow rate are shown in Fig. 3-41b,d. At the maximum flow rate, the 2L VE commissure comes into view (see bottom left corner of Fig. 3-41b). The commissures coming inwards to the center of the flow is similar to the silicone valve case near peak pulsatile flow. However, none of the 3L VE commissures comes into view at maximum flow rate.

Pressure drop (solid symbols) and orifice area (open symbols) are plotted as a function of the flow rate in Fig. 3-42. The pressure drop measurements across the VEs show approximately a linear rise with increasing flow rate. At the same flow rate, the pressure drop across the 2L VE (solid black rectangle) is higher with a maximum value of 3.9 mmHg at 9.5 L/min compared to 3L VE of 1.7 mmHg at 9.5 L/min (solid red triangle). The orifice area is the measured open orifice area normalized by the undeformed orifice area (root internal diameter of 2 cm). Note, the viewable orifice area is smaller than the area obtained from the expanded root diameter due to the increase of internal pressure with the flow. At zero flow, the VE's inability to coapt for both 2L and 3L types is shown by an orifice area of 0.14 and 0.33, respectively. The orifice area for both 2L and 3L shows a non-linear increase with the flow rate. Above approximately 5 L/min, there is a slower increase in orifice area with increasing flow rate as compared at the lower flow rates for both 2L and 3L. The orifice area expands to approximately 0.47 and 0.64 for 2L and 3L, respectively. The orifice area expansion of 37% at 4 L/min steady flow for the 2L VE closely matches the silicone valve area expansion of 35% at peak flow rate of 24 L/min.

Upon closer examination of the pressure drop measurements near the 5 L/min, there is an increase in the slope of each curve. This increase is more evident for the 2L VE. Overall, the nonlinearities in the curves may be due to a combination of multiple effects. The nonlinear VE material properties at higher stresses indicate that the leaflets yield less or have higher instantaneous modulus (see Appendix E-2). The non-axisymmetric VE geometry, for example for the 2L VEs may result in the commissures coming closer together as shown in Fig. 3-41b. Having three leaflets for VEs (physiologically ideal) accommodates larger orifice areas resulting in larger flow throughput at lower pressure drops meaning less energy loss as compared with 2L VEs.

However, the compaction of the 3L VE leaflets during the incubation period results in smaller leaflet lengths and the majority do not initially coapt. With the initially compromised leaflet size (mainly for the 3L VEs), the measurements taken may not be a true indication of the performance of fully coapting leaflets. Due to the limitation of the number of VE samples, multiple VE steady flow analysis was not performed. However, the author believes that the results from the two VEs presented were representative in the trends for 2L and 3L VE steady flow performance for the batches of VEs which have been harvested.

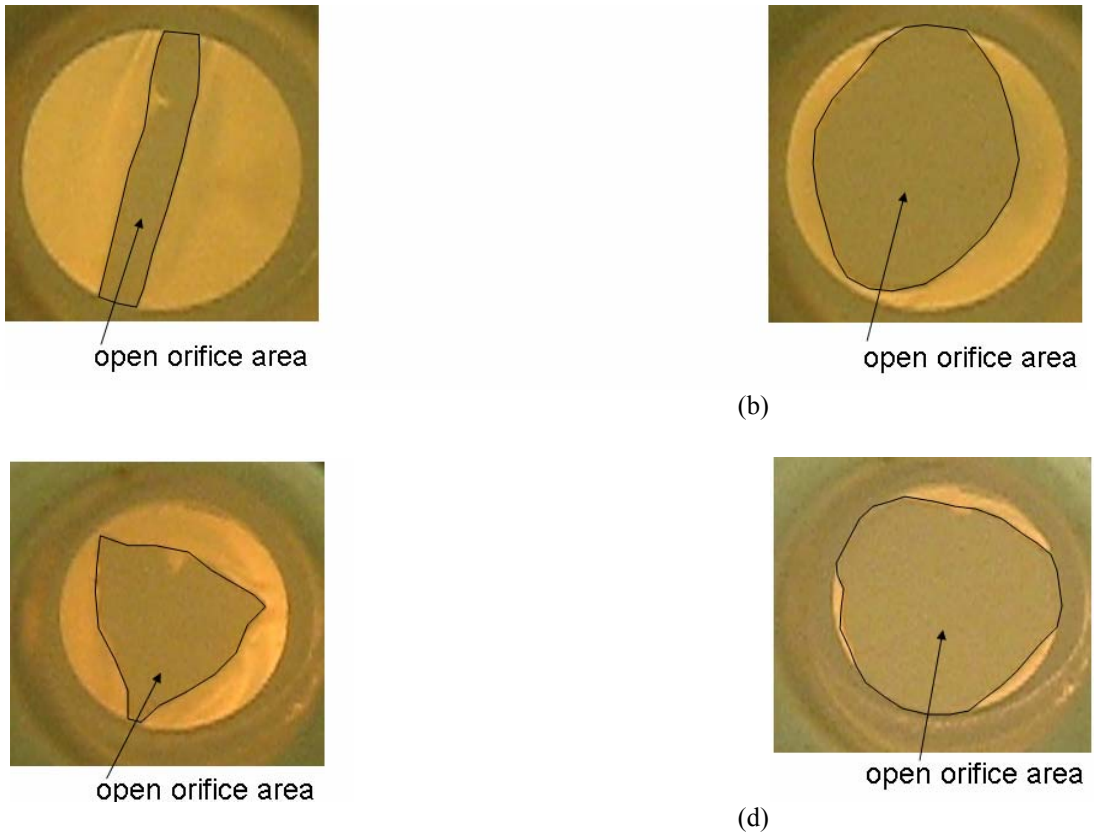

Figure 3- 41. Downstream end on view of VEs. a) no flow bileaflet, b) maximum steady flow of 9.5 L/min through the bileaflet, c) no flow trileaflet, and d) maximum steady flow of 9.5 L/min trileaflet.

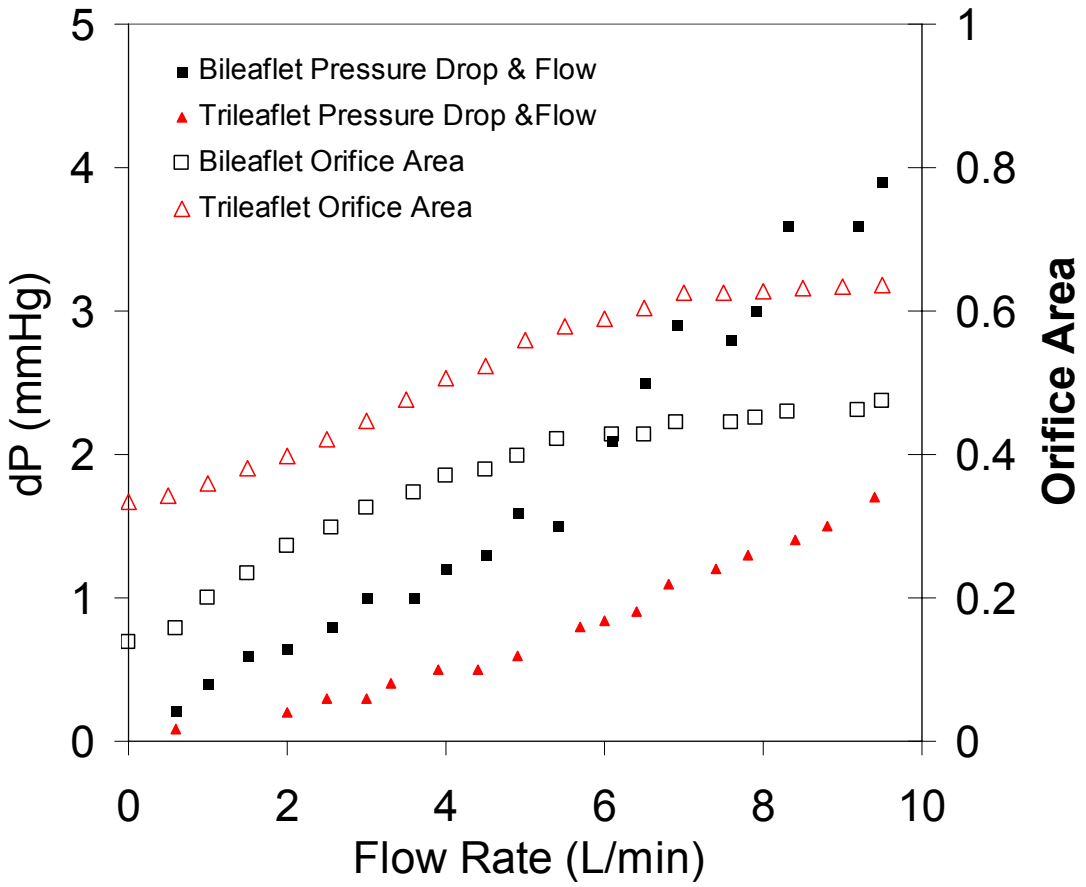

Figure 3- 42. Pressure drop versus flow rate of bileaflet and trileaflet valve equivalents. Percent increase in open orifice area measured and normalized by undeformed VE area.

3.3.2 Pulsatile Flow Performance

The steady flow testing and initial pulsatile testing of the exposed VE roots to an external fluid bath showed that the VEs were not able to coapt. The distended root and compacted leaflets prevented the VEs from coapting at zero steady flow conditions and during diastole for pulsatile flow conditions. To eliminate VE root expansion and accommodate leaflet coaptation, the VEs were sutured onto a silicone sleeve as shown in Fig. 2-12 of the Methods Section. The VE and silicone sleeve were inserted inside a rigid acrylic tube of inner diameter 2.54 cm. The VE, silicone, and acrylic unit will be referred to as the housed VE. The housed VE prevented radial distension of the VE root beyond

the initial inner diameter of 2 cm. The longitudinal tension on the VE supported its weight and allowed the root to remain open.

Fig. 3-43 shows images downstream or aortic view of the VEs in the cardiovascular pulse duplicator. The top row shows the open and closed states during systole and diastole, respectively of the 2L VE. The bottom row shows the open and closed states during systole and diastole, respectively of the 3L VE. Note that both housed VE leaflets coapt completely during diastole.

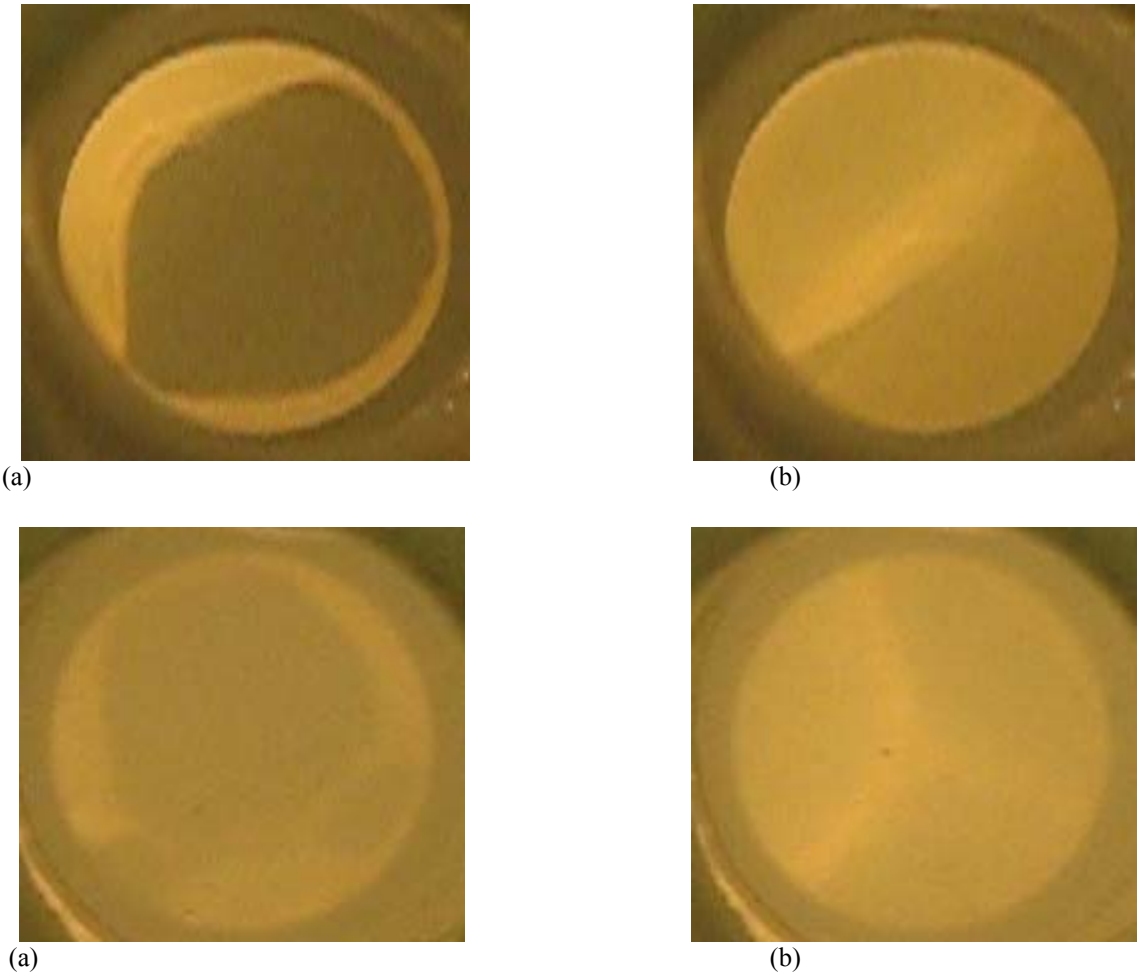

Figure 3- 43. Downstream end on view of valve equivalent leaflets in cardiovascular pulse duplicator flow. (a) open bileaflet, (b) closed bileaflet, (c) open trileaflet, and (d) closed trileaflet.

The bulk flow performance of the VEs in the pulse duplicator is presented in Fig. 3-44a. The plot presents the peak systolic pressure (black solid circles) with corresponding flow rates (red solid triangles) achieved by the VEs before failure. The data points outside the gray area indicate G1 VEs and inside indicate G2 VEs. The open circles around the solid black circles indicate fully coapting VEs. The solid circles without open circles indicate non-coapting VEs. The rectangles around the solid red triangles indicate VEs exposed to external fluid, and all others indicate housed VEs. The 3L VEs are labeled along the Valve Number axis. All non-labeled VEs are 2L (bileaflets)

G1 VEs in general were able to withstand lower flow rates and pressures before rupture as compared to the G2 VEs. G1 VEs 2L-1,2,3, and 3L-4 were mounted with roots exposed to an external fluid bath. None of the VEs reached 30 mmHg or 25 L/min, which are right ventricular physiological conditions. The documented failure location was consistently at the root. The mode of failure was root rupture at the upstream Dacron sewing cuff and root interface for VE 2L-2. The Dacron and root interface may be a problematic failure location due to streamwise tensile stresses. The rupture occurred at the downstream location, and tear proceeded along the commissure for VE 3L-4. The corresponding images of the failure locations are shown in Fig. 3-45. Five of the eleven housed G1 VEs were able to coapt, but experienced early failure. All these failed at pressures below 20 mmHg and flow rates of 10 L/min. The failure location of the coapting G1 2L-5 is shown in Fig. 3-45. There is a tear at the downstream root wall at the location of the commissure. None of the 3L VEs with documented pressure drop and flow measurements were able to coapt. Only one 3L VE was able to coapt as shown in Fig. 3-43; however, the pressure drop and flow measurements were not documented. In general, the non-coapting housed G1 VEs sustained pressures above 30 mmHg and flow rates above 15 L/min unlike the coapting VEs. The failure locations of the non-coapting housed VEs 6, 13, and 14 are shown in Fig. 3-45. VEs 3L-6 and 2L-13 show that the leaflets tore off from the root wall. VE 3L-14 shows a tear in the downstream root of the valve near the bottom location of the VE leaflet cusp.

G2 VEs had considerable improvement in pressure drop and flow rate measurements as compared to G1 VEs. This result is supported by the fact that the G2 VEs harvested from the cyclic stretched bioreactor had enhanced mechanical strength

(Syedain et al., 2008). Of the 11 G2 VEs, only one failed below 30 mmHg peak pressures and 15 L/min peak flow. The coapting VE 2L-26 failed after five hours of testing at the peak pressure and flow rate of 20 mmHg and 16.5 L/min. These low forcing conditions were conducted to acquire downstream PIV data, which required the VE to sustain long time duration of testing. Coapting VEs 2L-17, 21, and 25 survived approximately 3 hrs, 1 hr, and 1 hr of testing, respectively. These coapting 2L VEs recorded pressures and flow rates above 30 mmHg and 15 L/min (most cases near physiological flow rates of 25 L/min), respectively. The mode of failure for VE 2L-17 was leaflet tear from the root wall and VE 2L-25 had tear of the root wall at the location of the commissure. Both tear locations are shown in Fig. 3-45. These failures occur during VE leaflet closure with the sustained diastolic pressure drops. Note that the total testing time included the incremental ramp-up (to peak pressure/flow rate) along with the time the VEs sustained at the peak pressures/flow rates. Even though the incremental ramp-up stroke volume value (increase in stroke volume) was closely matched from one VE to another, modifications to the time between ramp-up steps had to be made. The flow setup requires dynamic adjustment of the flow such as removing air bubbles, which become entrapped at increased forcing conditions.

All the non-coapting valves (n = 7), including one exposed root G2 VE, sustained pressures and flow rates at or above 30 mmHg and 15 L/min, respectively. VE 2L-20 with exposed root had leaflets that did not coapt similar to G1 exposed root VEs. The failure location was at the commissure due to the root expansion. The commissure was a location of frequent VE failure. It is possible that the tissue deposition in the commissure is significantly less than at the adjacent locations where the leaflets attach to the root as seen in planar root cut-out images (e.g., 2L-13, 3L-14) of Fig. 3-45. The bileaflet VE geometry may also result in large hoop stresses at this location that lead to rupture. Even for the non-coapting valves, at high forcing conditions, the leaflet tear from the root wall was present as shown for VE 2L-18 and 22 in Fig. 3-45. In the case of VE 2L-19, the tear occurred at the downstream root Dacron-cuff interface.

Of the nine coapting 2L VEs (both G1 and G2), eight peak diastolic pressure drop values are plotted versus the peak cycle systolic pressure in Fig. 3-44b. Individual valve names are labeled. The peak pressure drop experienced by the coapting VEs at the onset

of diastole is measured as the maximum downstream – upstream pressure. The plot shows an increase of diastolic peak pressure drop with an increase in peak systolic pressure. The peak diastolic pressure drops have larger absolute values than the peak systolic pressures because the upstream pressures become negative resulting in a larger difference in pressures (downstream – upstream) during the backward stroke of the pump of diastole (see Fig. 3-46 at T ~ 0.45 sec). All but one G2 coapting valve sustained peak diastolic pressure drops over 40 mmHg (corresponding peak systolic pressures over 30 mmHg). The peak systolic pressures and diastolic pressure drops typify and exceed the values of 35 mmHg and 15 mmHg, respectively for native pulmonary heart valve (Nichols and O'Rourke, 2005). This further indicates that the coapting G2 VEs, with greater mechanical strength, performed better in the cardiovascular pulse duplicator than the G1 VEs. The G2 VE 2L-26 failed under long (5hrs) testing at lower forcing conditions noted in the previous paragraph. Three G1 valves were exposed to native pulmonary pressure drops at or above 30 mmHg, but experienced lower than physiological peak systolic pressures.

To summarize, the plots in Fig. 3-44 and failure images in Fig. 3-45 indicate that G2 valves performed better than G1 valves in general. VE exposed to the fluid bath experienced root failure at either the commissure or root-Dacron interface. The VE leaflets for the non-housed valves were always intact. VEs that were housed facilitated leaflet coaptation, although this was not always the case if the leaflets had compacted too much. The housed leaflets generally tore at the leaflet-root interface, mainly at the location of the commissure. For these VEs the root and Dacron interface were predominantly intact.

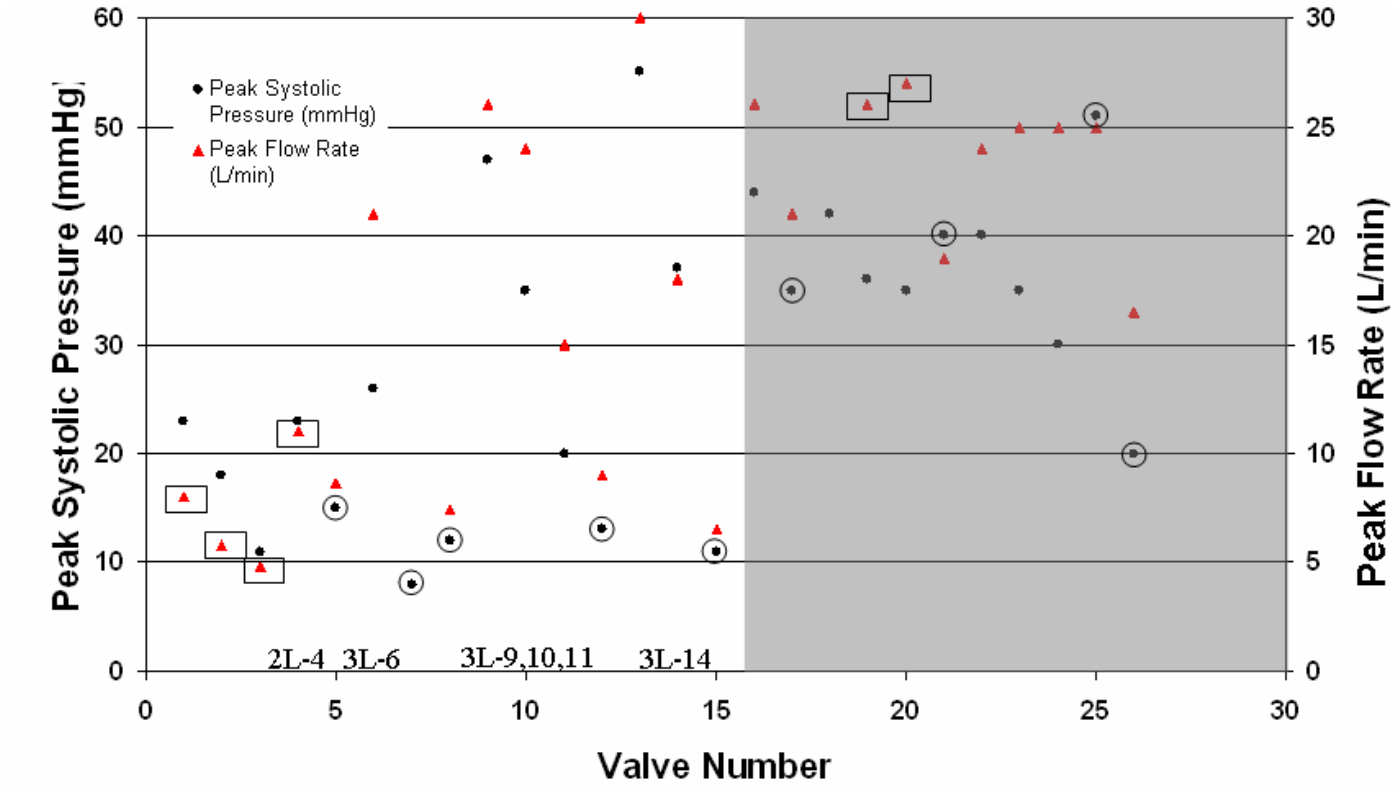

(a)

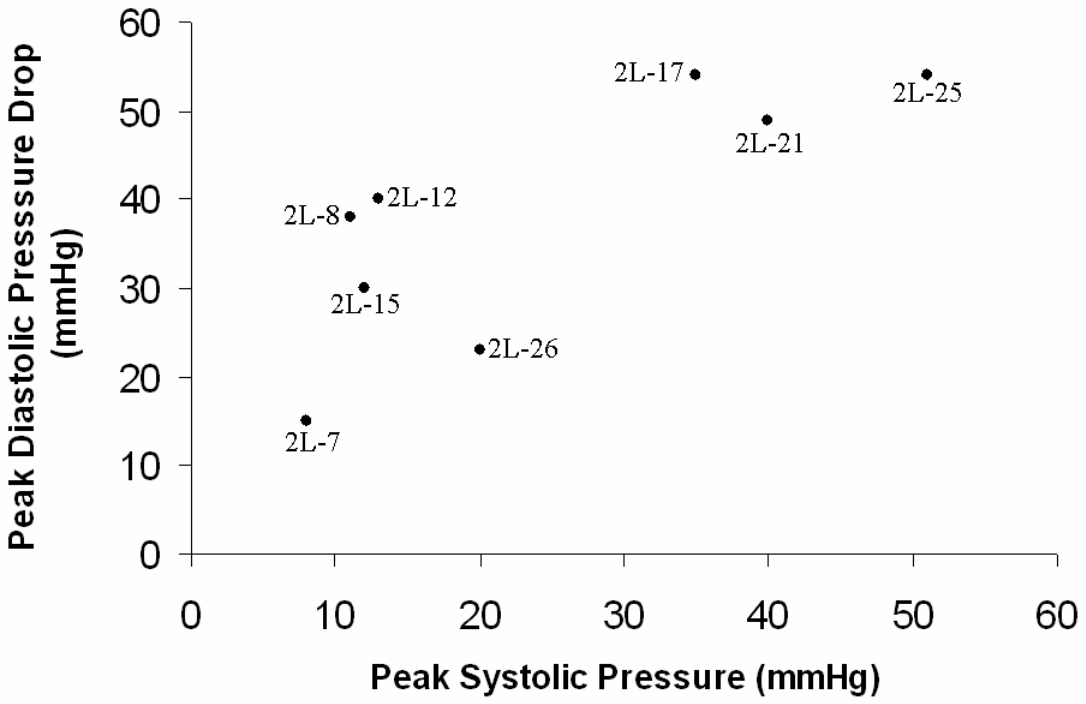

(b)

Figure 3- 44. (a) Peak systolic pressures and flow rates for 26 valve equivalents tested. Data points in the shaded area indicate Generation 2 VEs. Open circles indicate coapting valve leaflets. Rectangles

indicate VE roots exposed to external fluid. (b) Peak diastolic pressure drops measured as downstream pressure – upstream pressure for coapting leaflet VEs.

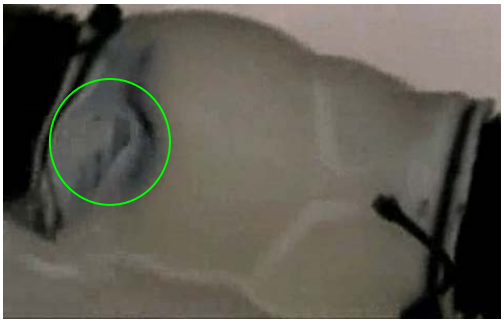

2L-2

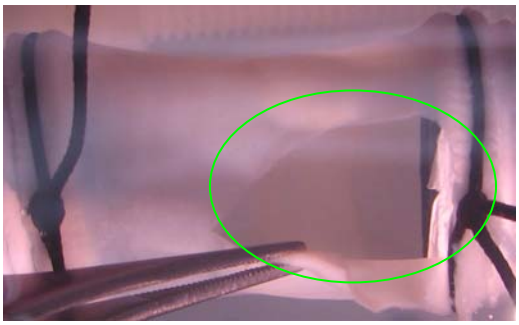

3L-4

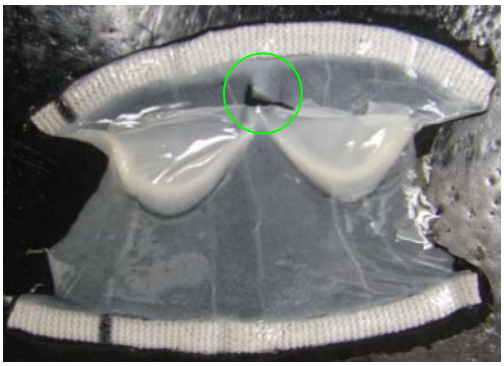

2L-5

3L-6

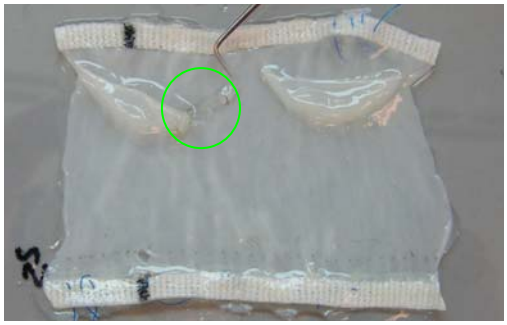

2L-13

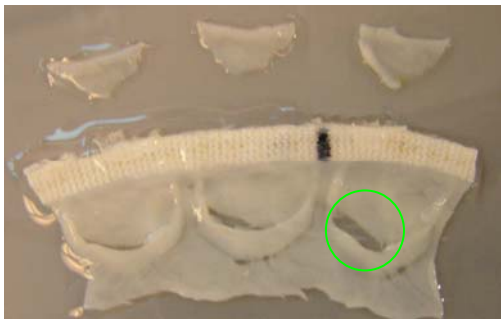

3L-14

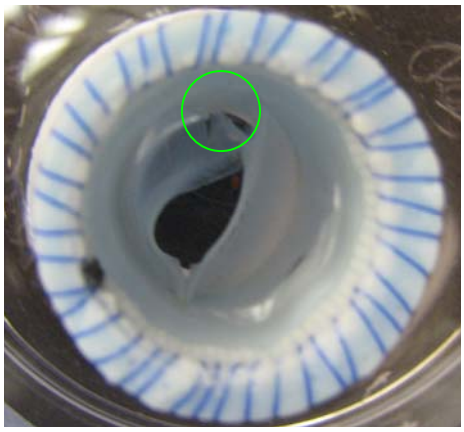

2L-17

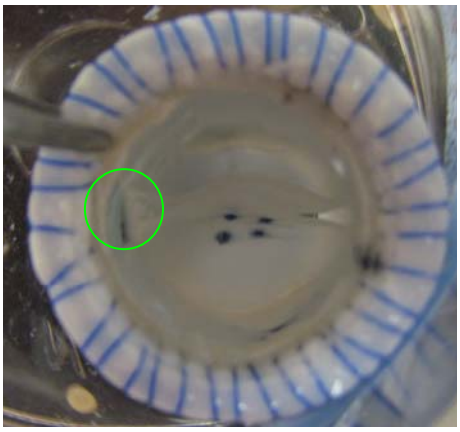

2L-25

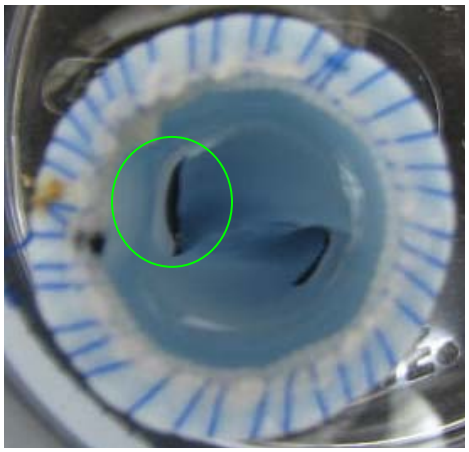

2L-18

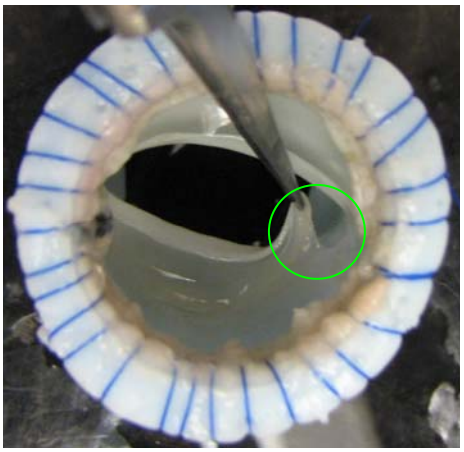

2L-22

2L-19

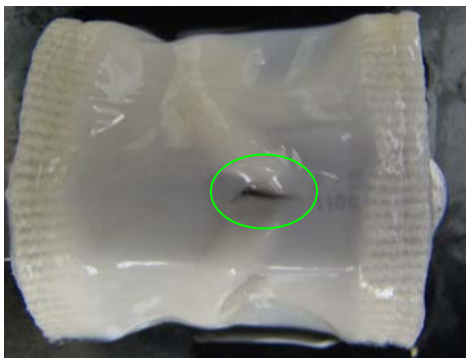

2L-20

Figure 3- 45. Valve equivalent failure locations marked in green. Images with VE side views are oriented with flow directed from left to right. Images with VE cut-open along the root oriented with flow directed from bottom to top. Images of end-on view show downstream or aortic view.

Fig. 3-46a shows a plot of pressure drop and flow rate signatures averaged over 10 cycles for a successful trial in the pulse duplicator (data of VE 2L-17). Additionally, the percent open orifice area is plotted throughout the cycle. The flow rates during systole reach approximately 24 L/min at about 0.2 seconds, which is typical for flow through native pulmonary valves. The peak pressures upstream and downstream reach near 40 mmHg, which are typical values in native pulmonary valves. The pressure drop at peak flow (at 0.2sec) is 9 mmHg. This is higher than that for native pulmonary valve, which measures a few mmHg. The orifice opens approximately 60% of its maximum root area, which is significantly larger than that of the stiffer transparent silicone valve. An even larger opening of the VE may result in matching physiological pressure drops of a few mmHg. The closing of the VE results in pressure oscillations. The peak pressure difference during the closure of the valve is 60 mmHg and a minimum of 10 mmHg diastolic downstream pressure is maintained throughout the cycle. The 10 mmHg pressure is comparable to native pulmonary valves, whereas the high 60 mmHg pressure drop is an artifact of the *in vitro* pulse duplicator system. The VEs are able to withstand higher dynamic pressure drops than what occurs in the right ventricle-pulmonary valve location. These results presented are applicable to G2 housed coapting 2L VEs in general.

A comparison of the VE and SV pressure drop and flow rate signatures is shown in Fig. 3-46b. The flow rate curves for both valves are comparable. Unlike the VE, the SV has higher frequency oscillations during diastole because the root is exposed and more susceptible to vibrations during valve closure. The SV encounters much higher systolic pressure drops at similar peak flow rates as a result of smaller orifice opening (35% for SV as compared with 60% for VE). The systolic pressure drop is greatest at an earlier time point for the VE than for the SV. During diastole, the SV still encounters higher diastolic pressure drops, and both valves show high frequency pressure oscillations. In general, the VEs have closer to physiological pressure drop and flow rate signatures than the SV.

Fig. 3-47 shows the 2L VE performance in comparison to a St. Jude Medical bileaflet mechanical valve (MV). The average flow rates of 4.8 L/min with 3 mL regurgitant volume and 5 L/min with 2 mL regurgitant volume for 2L VE and MV,

respectively, are comparable. The maximum systolic pressures reach 40 mmHg with 9 mmHg pressure drop across the VE and 45 mmHg with 5 mmHg pressure drop across for the MV. Both valves sustain a minimum downstream pressure of 10 mmHg during a cycle. The maximum open area for the VE is 60% and 77% for the MV. It is expected that if the VE were exposed to external fluid and not housed inside a silicone/acrylic unit, the maximum percent open area would increase and systolic pressure drops would decrease and reach closer to MV values. However, as it stands these current valves would not be able to coapt.

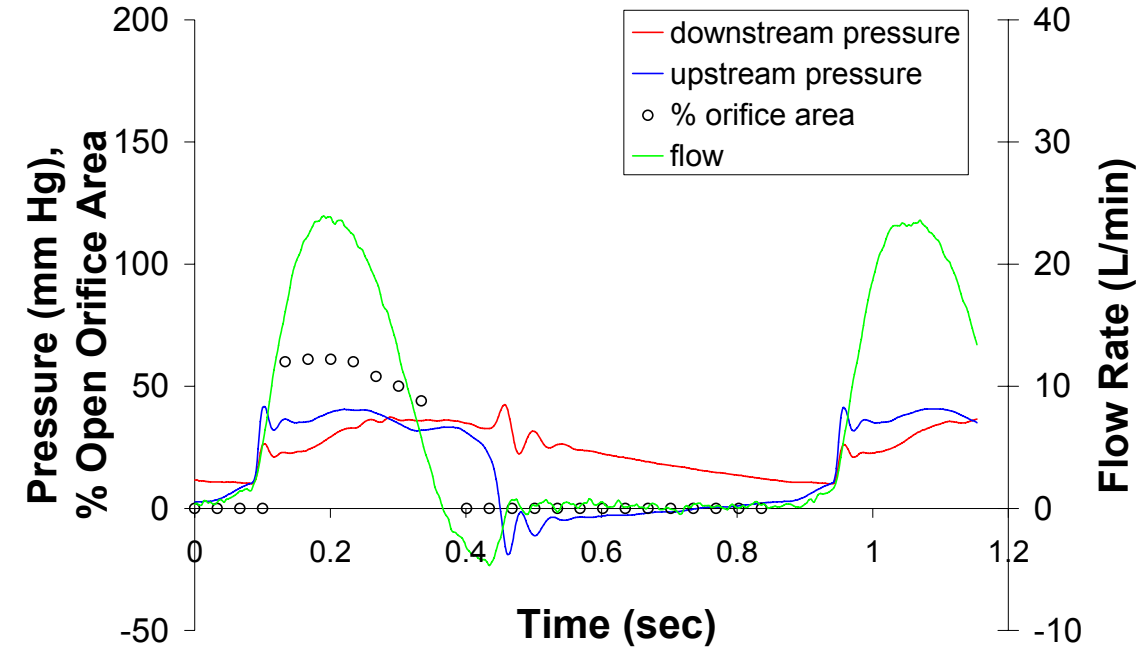

(a)

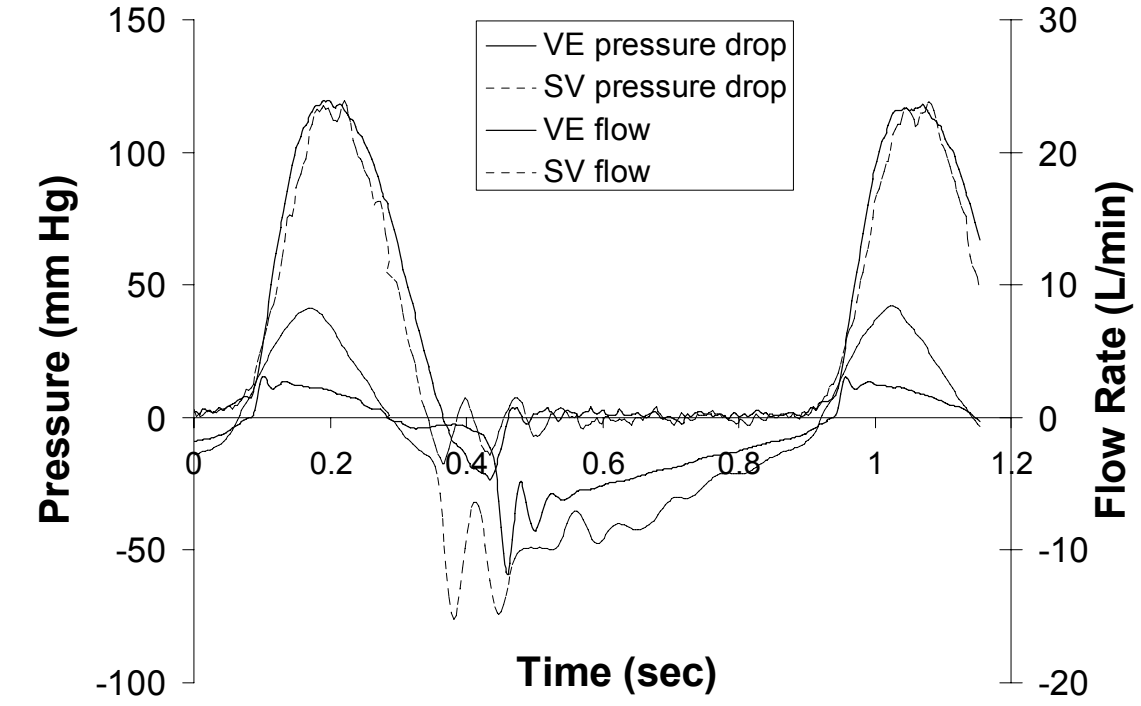

(b)

Figure 3- 46. (a) Pressure and flow rate signatures of coapting valve equivalent 2L-17 inside rigid silicone housing. Open orifice area normalized by VE initial flow area and (b) pressure drop and flow rate comparison of valve equivalent (VE) and transparent silicone valve (SV).

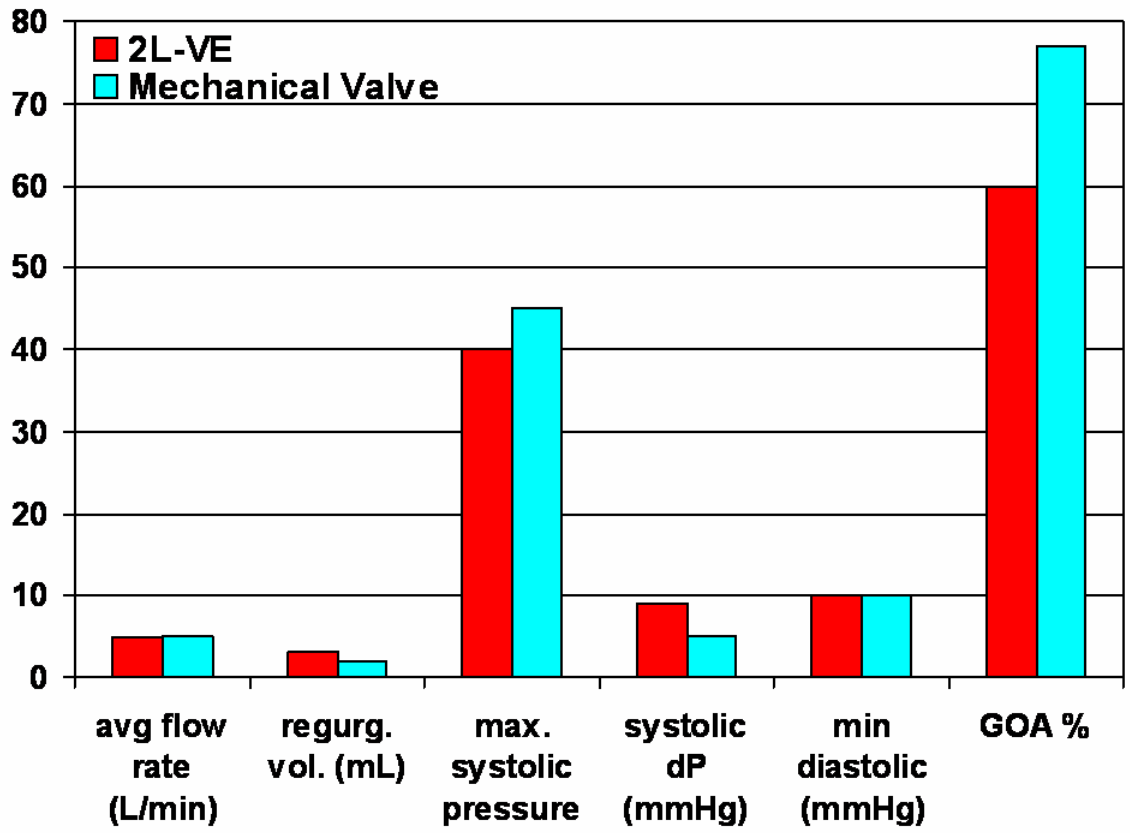

Figure 3- 47. VE comparison with St. Jude Medical bileaflet mechanical valve.

The expansion of the root diameter for VE 2L-19 and 2L-20 shown in Fig. 3-48a,b was measured along the length of the root. The percent change in diameter at 30 mmHg peak pressure during the flow cycle is plotted in Fig. 3-48c. The commissure to commissure (C2C) diameter expansion was measured for 2L-19. The perpendicular plane (pC2C) root diameter expansion was measured for 2L-20. The x-location = 0 cm corresponds with the upstream most location of the VE root, where the VE is attached to the rigid Teflon mount. The flow is from left to right along the length of the root. The leaflets are attached to the root at approximately x = 1.15 and 1.64 cm for pC2C and C2C, respectively. The location of the commissure is at x = 1.64 for VE 2L-19 (C2C). Note, since these are two different VEs, it is not necessary that location of the commissure be at the same point along the valve root as a result of tissue compaction during incubation.

The root expansion results in significant strains up to 30% at the downstream location of x = 2 cm for pC2C. At the locations of the leaflet attachment, the strains are reduced to approximately 15% and 18% for C2C and pC2C planes, respectively. These values are both larger than those in the silicone valve, which had expansion of 10% at a similar phase for pC2C. In fact, there is a contraction in diameter (7%) for the SV at the location of the commissure for C2C. The VEs tested for diameter expansion had very compacted leaflets which may result in different deformation behavior from those that have not compacted, but were not tested. Essentially, with the compromised leaflets, the geometry of the VE was closer to a simple cylinder than the SV. This may be why the contraction observed for the SV in the C2C plane was not the case for the VE. Furthermore, this difference is supported by the fact that VE and SV encountered different internal upstream/downstream pressure conditions at the similar phase resulting in a larger systolic pressure drop for SV than VE. The SV upstream/downstream pressures read 76/36 mmHg and 36/25 for the VE (see Section 3.2.2 Silicone Valve Pulsatile Flow and Deformation). This difference in root diameter expansion for the two planes of the two VEs might be due to the non-axisymmetric geometry of the valve, geometry difference due to compaction of the two VEs (i.e., different size leaflets), and the inhomogeneity in the tissue thickness (i.e., the root-leaflet interface becomes much thicker). These results show stark differences between the homogenous and isotropic material with two symmetric planes of the SV as compared to the non-homogenous and non-isotropic material with uncertain planar symmetry (due to tissue compaction) of the VE. Also, both materials have non-linear mechanical response and are not similar in behavior under the stresses applied.

(a) (b)

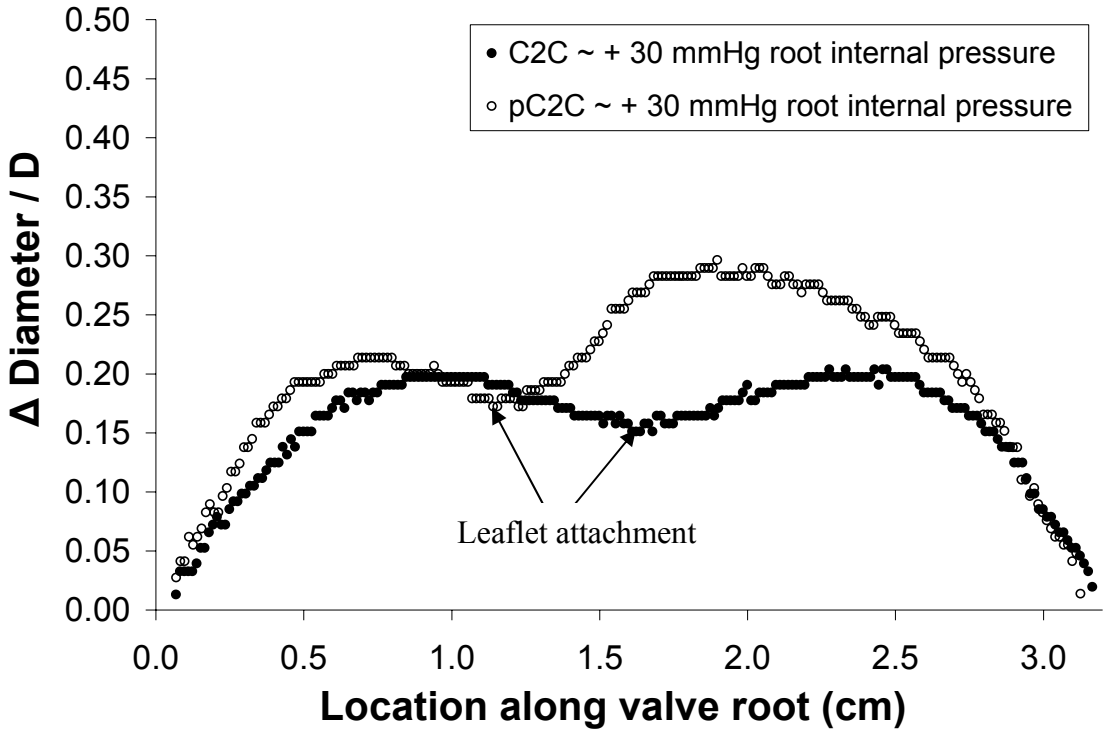

(c)

Figure 3- 48. a) commissure to commissure view (C2C) VE 2L-19, b) perpendicular to commissure view (pC2C) VE 2L-20, and c) root diameter expansion of the valve equivalent. Location of 0 cm is the furthest upstream point. Note, diameter of the valve equivalent is D = 2 cm.

3.3.3 Instantaneous Flow Fields Downstream of Bileaflet Valve Equivalent

Instantaneous pulsatile flow velocity fields immediately downstream of the coapting housed VE silicone housing were examined using particle image velocimetry at time-averaged flow rate Q = 1.7 L/min. The average flow rate was approximately 3-times less than pulmonary flow rates. The velocity measurements were made across two planes, the commissure to commissure plane (C2C) and the plane perpendicular to the commissures (pC2C). The instantaneous velocity vector fields at peak systolic flow rate along with vorticity contours at peak flow are shown for these planes in Fig. 3-49. Both a and b have vector fields and vorticity contours computed using finer and coarser gridded vectors. The vector spacings were 0.013D and 0.027D, which is half the vector resolution due to the 50% overlap criteria for both the fine and coarse resolutions, respectively. D = 2 cm is the internal diameter of the VE. The flow is plotted beyond the limit of ±1D in y-direction because the downstream flow domain exiting the VE is 2.54 cm in diameter (the internal diameter of the pipe). The measurements for both the planes were made at the same phase, but during different flow cycles. The velocity is normalized by the time-averaged velocity ($U_{avg} = Q / (0.25\pi D^2)$). The vorticity ($\omega$) is normalized by the time-averaged velocity and root diameter. The results show a broad distribution of the flow across the plane aligned with the widest opening (C2C) and a narrower distribution in the perpendicular plane (pC2C). There is an asymmetry in the flow with both the centerlines of the flow shifted below the r / D = 0. There is a wide distribution of vorticity magnitude (peaks of ± 50 for the coarser grid and ± 150 for the finer grid) and direction across the shear layer on both the viewing planes. The high vorticity values are filtered out with the coarser grid.

The velocity vector magnitudes of approximately 5Uavg downstream of the VE compare well with that of the silicone valve. The vorticity magnitudes downstream of the VE are greater than those of the silicone valve along the measurement planes. The jet diameter along both planes are similar for the VE and SV. Note that the vorticity contour level has been changed from what was presented in Fig. 3-28. The vorticity magnitude with the coarser grid downstream of the VE (Fig. 3-49b) is comparable to that observed for the silicone valve in the SV data (Fig. 3-28). The vorticity field appears much

smoother across the jet shear layer shown by the SV data as compared to the VE. However, this might be due to the lower spatial resolution of the SV data.

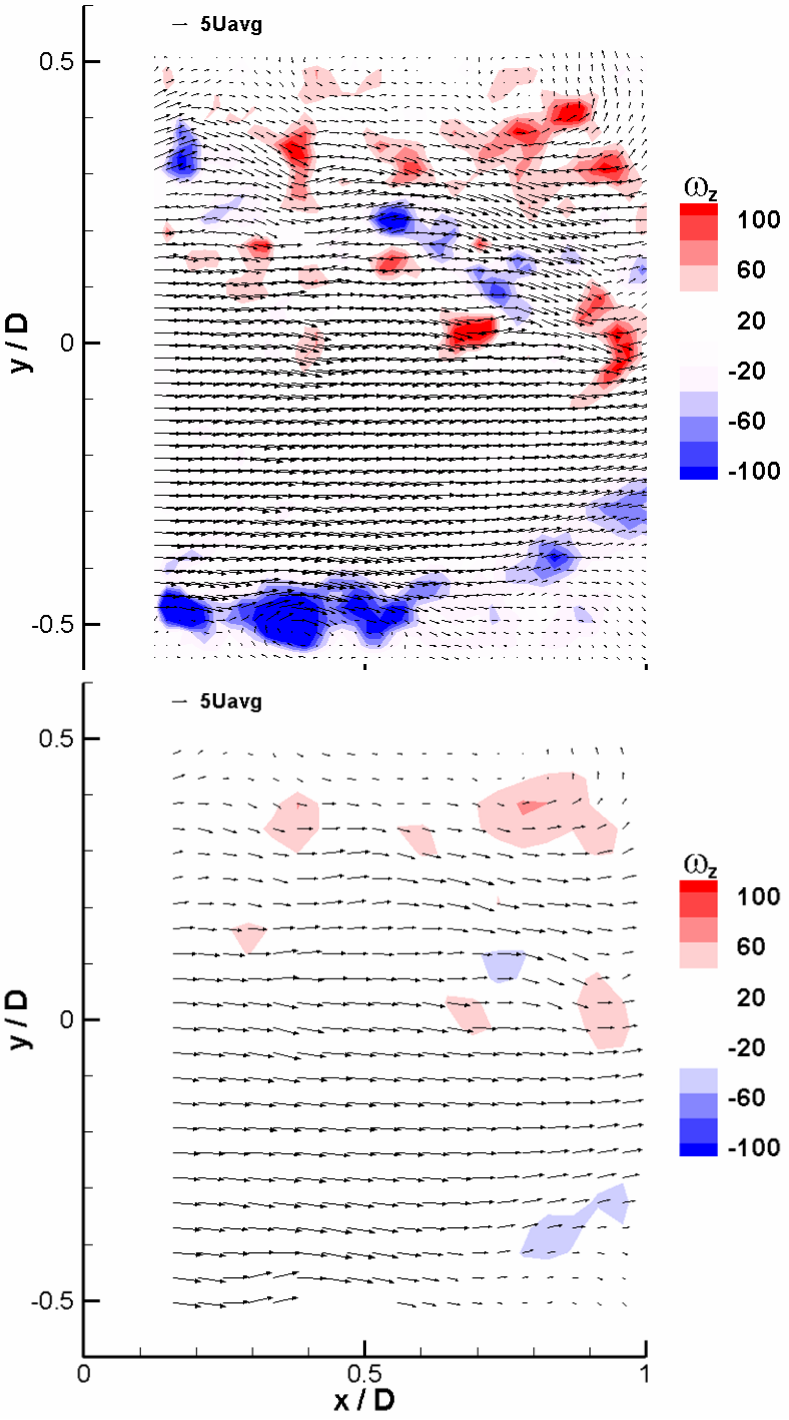

(a)

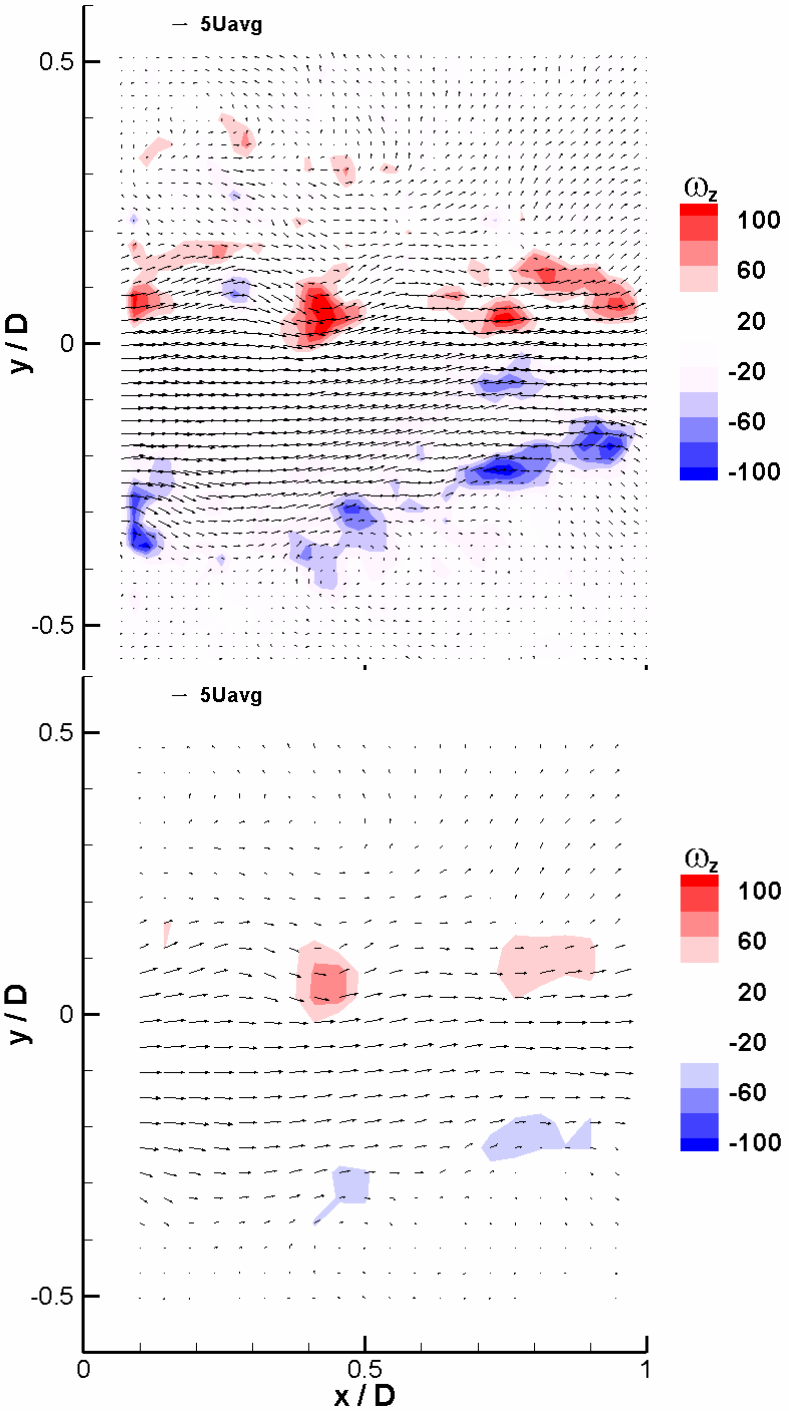

(b)

Figure 3- 49. Instantaneous valve equivalent downstream velocity vector fields and vorticity contour across two perpendicular planes captured at the same phase of different cycle. Fine and coarse vector fields shown for both. (a) commissure to commissure plane and (b) perpendicular to commissure plane. Velocity and vorticity normalized by using the time averaged flow rate and valve equivalent

diameter. Uncertainty in velocity vector = 0.15Ubulk. Uncertainty in vorticity for 64x64 and 128x128 are 9.9D/Ubulk and 5D/Ubulk, respectively.

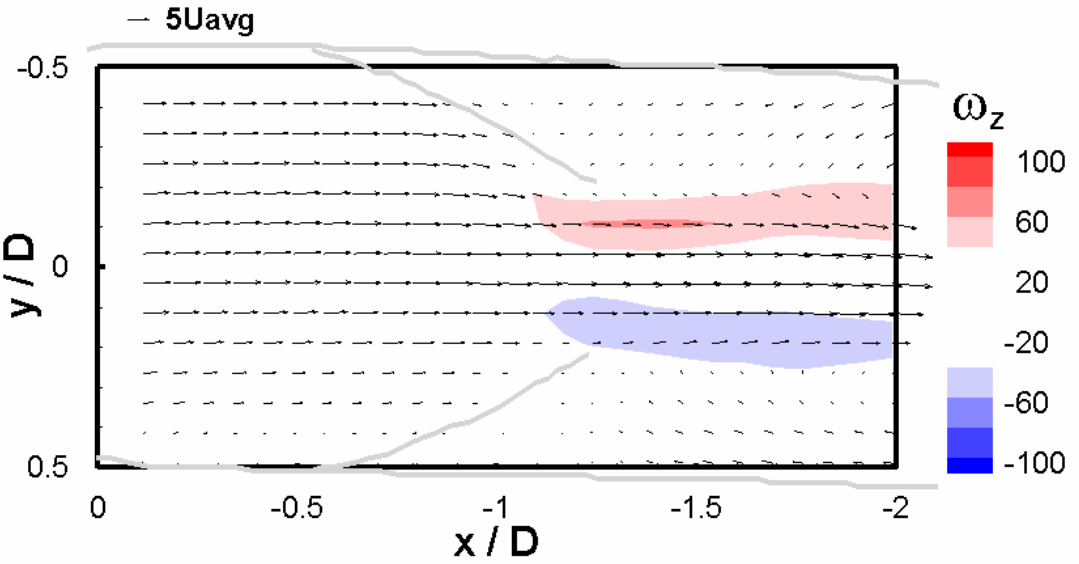

(a)

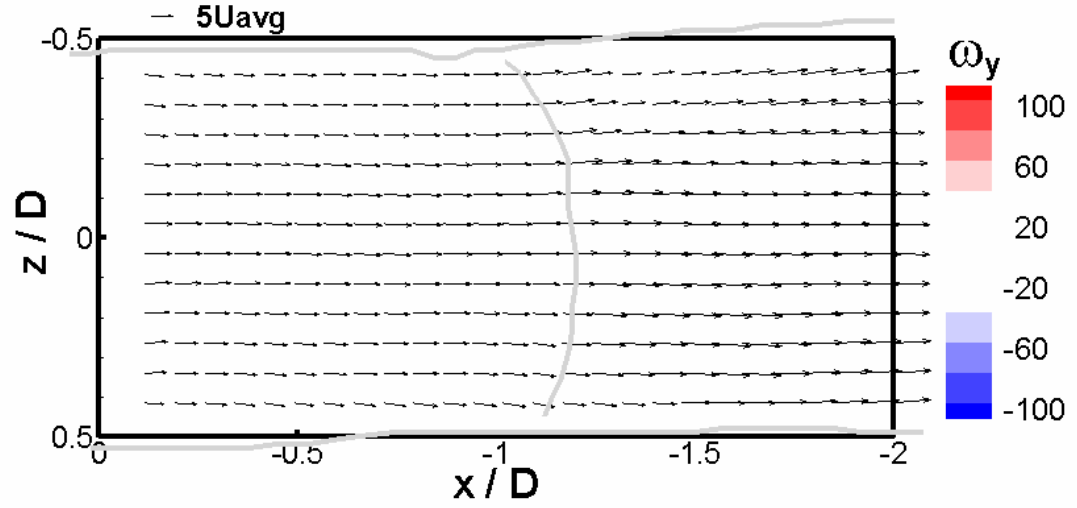

(b)

Figure 3- 50. Systole phase φ8. (a) x, y-velocity vector field (pC2C plane) along with ω_z contour at the z/D = 0 plane and (b) the (x, z) velocity vector field (C2C plane) along with ω_y contour at the y/D = 0 plane.

Chapter 4: Summary and Conclusions

Detailed results of tensile material properties, structural deformation, and fluid velocity for flows through deformable polymer and tissue engineered valves have been presented. Additionally, the bulk performance (e.g., pressure loading) and potential failure modes of the novel tissue engineered heart valves have been quantified. The data presented served two purposes: the experimental data could be used for validation of computation incorporating fluid-structure interaction, and the data could be used to assess the potential of the tissue engineered heart valve as a bioprosthetic.

4.1 Deformable Polymer Silicone Valves Subjected to Fluid Flow Interaction

Polymer silicone valves of different material tensile characteristics and simple diaphragm-like geometry with an orifice allowed bi-directional flow. The upstream conditions such as volumetric flow rate (Reynolds number), flow direction and pulsating frequency (Womersley number) were controlled while the neo-Hookean material modulus was varied to control the degree of diaphragm deformation at a given Reynolds number.

For upstream steady flow, both the material compliance and Reynolds number affected the diaphragm deformation state. At low Reynolds number (Re = 600), the diaphragm valve deflected downstream into a concave shape, but orifice area expansion was minimal. At higher Reynolds number (Re = 3900), the material compliance resulted in significant axial deflection as well as expansion of the orifice area which led to lower pressure drops compared with flow through a rigid orifice. The pressure drop across the diaphragm appeared to dominate shear forces along its surface resulting in a concave (as opposed to convex) deformation for all compliant cases studied including orifice diameters up to 0.69D. The diaphragm appeared very steady in its spatial position although the downstream velocities indicated unsteadiness in the flow.

The effect of diaphragm deformation on downstream flow was also documented. A jet with significant inward radial velocity was present immediately downstream of the deformed diaphragm valves and absent for the rigid cases within the field of measurement. This inward flow was associated with vena contracta in the compliant

cases. For low Reynolds number, laminar upstream flow conditions, the rigid and slightly deformed compliant diaphragm valves both supported the formation of relatively large scale vortices with passage frequency of St = 0.34. Ensemble-averaged velocity statistics showed that local RMS profiles were similar in both cases although the profiles spread faster in the radial direction, and the magnitudes were slightly larger in the compliant case. For higher Reynolds number, turbulent upstream conditions, the compliant diaphragm valve deformed significantly, and the orifice area increased by 75% compared to the rigid diaphragm area. The orifice area expansion led to a jet that was initially wider and slower than the comparable rigid case. Since RMS values typically scale on the mean jet velocity, the magnitudes were lower in the compliant case. Vortical structures forming immediately downstream of each orifice were typically less organized and more closely spaced than in the cases with laminar upstream conditions. While the range of Strouhal numbers observed in the shear layer of the turbulent rigid case collapsed well with the laminar cases, the range observed in the turbulent compliant case was higher indicating a delayed development of the jet downstream.

For the upstream pulsatile flow case, both diaphragm deformation and flow characteristics showed features distinct from the steady upstream flow case. The diaphragm deformation of the most compliant material tested at peak flow rate of 4 L/min (time averaged flow rate of 0.54 L/min at a forcing frequency of 1.167 Hz) showed significantly less deformation in the orifice area expansion and deflection than that of upstream steady flow at a similar flow rate. This difference may be attributed to the unsteady pressure fields of the pulsating flow. The pressure drop across the diaphragm valve appeared to dominate the shear forces, resulting in a concave deformation for the pulsating flow, similar to what occurs for the steady flow. There was very good repeatability in the diaphragm deformation at each phase measured from cycle to cycle, which was difficult to achieve with valves of more complicated geometry and pulsating flow studies cited in the literature (Ge et al., 2008). This lack of repeatability was shown previously to bias velocity statistics resulting in less accurate data for validation of fluid-structure interaction codes.

During the initiation of the forward phase of the pulsating flow, a leading vortex ring followed by a trailing jet was documented downstream of the diaphragm. This was

not the case for the upstream steady flow. As the vortex ring traveled through the field of view, the ring diameter increased due to the radial spreading of the shear layer and opening of the diaphragm valve orifice. The growth of the vortex ring was supplied by the vorticity generated by the accelerating piston and entrainment of ambient fluid; however, the growth was limited in the radial direction by interaction with the pipe wall boundary. This resulted in the vortex ring expanding along the streamwise direction. This leading vortex ring had a larger diameter than the coherent rings generated in the steady flow cases. The growth of the shear layer away from the centerline of the jet resulted in lower variations in streamwise velocities near the centerline compared with the steady flow case. Similar shear layer growth away from the centerline was documented for temporally increasing nozzle diameter in pulsatile flow experiments conducted by Dabiri and Gharib (2005). The flow during acceleration was steadier, with lower velocity fluctuations than during the deceleration phase at similar instantaneous flow rates. The higher fluctuations during deceleration may be caused by existing coherent structures from the early acceleration and peak phases, which have not yet decayed and interact with newer structures.

Polymer silicone valves with higher transparency and stiffer material properties than those of the diaphragm valves were tested in the cardiovascular pulse duplicator. The silicone valve geometry was more complex matching ideal tissue engineered valve geometry and designed to allowed unidirectional flow. The forcing conditions replicated right ventricular loads in that the stroke volumes and flow frequency were 70mL and 1.167Hz, respectively, and resulted in peak and average physiological volumetric flow rates of 23 L/min and 4.2 L/min, respectively, with blood analogue water-glycerin as the working fluid.

The deformation state at multiple phases of the silicone valve was quantified by viewing along three perpendicular planes. During forward flow, the positive pressure drop (upstream > downstream) resulted in the valve opening. Similar to the diaphragm valve, the silicone valve leaflets deflected forwards, concave to the upstream flow. Once again, we suspect that the pressure drops, which were much higher than physiological values, dominated the mode of deformation. The largest systolic pressure drop of approximately 40 mmHg was because of the compromised orifice opening ~35%

of undistended root area. The leaflet tip velocity was quantified by spatially tracking the tip and it closely matched with fluid velocities near the leaflets. The non-symmetric deformation of the root introduced by the complex geometry was evident. There was a 7% reduction in commissure to commissure distance of the root while an expansion was present on the perpendicular plane at the same streamwise location at φ6 of systole. This valve geometry may not be ideal because it leads to high pressure drops and reduction in root diameter during forward flow. The leaflets formed a slot-like elliptical profile unlike the circular profile of the diaphragm valve. The downstream flow features were affected by this elliptical shape as discussed below. During diastole, the leaflets were under negative pressure drops (upstream < downstream) resulting in reversed curvature, providing further evidence that the pressure drops dominate shear forces. This would be the case during diastole which has no net forward or reverse flow and large pressure drops (~ -50 mmHg).

Instantaneous velocity fields identified the primary features of the unsteady three-dimensional flow through the silicone valve during multiple phases of the cycle. The 3D3C measurements showed the slot-like elliptical jet flowing through the SV leaflets during the open phase of systole. The elliptical jet was wider along the commissure to commissure direction than its perpendicular face, corresponding with the bileaflet geometry of the SV. High vorticity levels along the inner surfaces of the leaflets during this phase were indicative of relatively high principal shear stresses in those locations and the potential for high shear stress on the endothelial wall lining of the similar geometry tissue engineered valve. Also, any blood cells exposed to the shear layer flow may experience high shear stresses. Immediately downstream of the leaflet, there was a large stagnation zone in which platelets, which could be activated by high shear along the jet, may accumulate and aggregate resulting in thrombus formation. The swirl criterion identified an elliptical vortex structure, which developed on the shear layer around the periphery of the jet. These areas of recirculation might help transport particles both away from and towards the stagnation zones.

Velocities and principal shear stresses were much lower during the closed phase, although recirculation zones were present both upstream and downstream of the closed leaflets. The strongest vorticity components were aligned with the commissure to

commissure axis. The upstream recirculation zone size and circulation were consistent for instantaneous and phase-averaged realizations, and the presence of a three-dimensional rotating structure was further indicated by the swirl criterion. The rotating structure grew and then decayed over the course of diastole. The downstream recirculation zone was less organized and showed multi-directional velocity components. Even with the lower principal shear stress during diastole, the prolonged exposure to these lower levels of oscillatory stresses may promote platelet activation, leading to thrombus formation. Although, the higher values of principal shear stresses were short-lived during diastole. It has been noted that the shear stress exposure on the endothelial wall helps endothelial cell alignment, become more adherent to the vessel wall, and promote fibrous proliferation. This results in the inability of monocytes and lipoproteins penetration into the tissue bed, a requirement for the onset of artherosclerosis (Freidman and Fry, 1993). On the other hand, in areas of higher velocity fluctuations and stasis zones, endothelial cell alignment is less evident, and these precursors to the onset of artherosclerosis may penetrate the tissue bed. Therefore, both high levels of principal shear stresses experienced during short duration of systole and lower levels of shear stresses experienced during the longer duration of diastole are important in assessing platelet activation, red blood cell lysis, and endothelial cell alignment.

We have demonstrated that the velocity gradient terms, such as vorticity magnitude, may be affected by the spatial resolution of the velocity vectors. The relatively coarse spatial resolution of the 3D3C measurements must underpredict actual vorticity and principal shear stress levels. Additionally, the working fluid in the experiment was a Newtonian continuum, whereas blood contains discrete cells and proteins that may lead to non-Newtonian behavior at shear rates below 50 sec^{-1} (Chandran et al., 2007). This may affect shear stress calculations at low flow during diastole because blood viscosity is higher at the lower shear strain rates. These factors, along with the non-similar materials of the silicone and tissue engineered valves, make direct prediction of potential clinical response of the tissue engineered valve based on silicone valve results difficult.

The experimental data presented in this research can be used to validate fluid-structure interaction codes in which substantial structural deformation and strain are

present along with relatively complex flow at significant Reynolds numbers. The experimental geometry and parameters were chosen to be as simple as possible for the steady and pulsating diaphragm valve flows and highly complex for the pulsating silicone valve, while including the physiological pressure and flow signatures. The results from the steady diaphragm valve flow need to be compared against a three-dimensional extension of the code developed by Liu et al. (Liu et al., 2007) that overlays deforming and fixed grids needed for the deforming valve and the pipe flow, respectively. As described in the introduction, an eventual application for such a code includes the modeling of flows through heart valves, which exhibit structural and fluid related strains, contact between leaflets, and jetting fluid surrounded by recirculation zones of intermittent turbulent flows. Clearly the code for the tissue engineered heart valve application would need to include additional complexity related to more complicated geometry, non-linear material and anisotropic macro and micro-scale properties of the leaflets and valve root, all under pulsating intermittent turbulent flow conditions. At the same time, it is our hope that the present results will be useful in development of models for additional applications including flows through elastic tubes and expandable bladders as well as industrial flows through deformable orifices used, for example, to regulate flow rate or liquid breakup in sprays.

4.1 *In Vitro* Performance of the Tissue Engineered Heart Valve

Bileaflet and trileaflet tissue engineered valve equivalents (VE) were tested in both steady flow and in a cardiovascular pulse duplicator. A population of 39 VEs tested may seem to be sufficient; however, only one or two VEs were harvested per batch monthly throughout two years of tissue engineering valve development. Since the VE was living tissue, there was no guarantee that any two valves harvested from a particular batch were exactly alike in their structural makeup and geometry. For example, the natural cellular response was to compact the structural components of the tissue and this led to some VEs with over-compacted leaflets. The over-compacted leaflets made the VE incompetent or regurgitant. Also, the tissue deposition was not uniform or homogenous throughout the valve. This compromised the strength at certain areas of the valve such as at the commissure, where the reduced tissue deposition was usually

noticed, but was not always the case. Through the improved incubation process (e.g., growth medium and incubation times) and the further development of the VE in a bioreactor that mechanically stimulates tissue growth (Syedain et al., 2008), improved mechanical properties of the VE were measured in both tensile testing and in the cardiovascular pulse duplicator. The data from the pulse duplicator testing indicated that the valves harvested after development in the bioreactor were able to withstand higher pressures, pressure drops, and flow rates throughout the loading of the right ventricular cardiac cycle.

The most successful VEs sustained right ventricular/pulmonary conditions approaching five hours of testing. The ultimate achievement in the VE pulse duplicator performance would be to withstand the higher loading conditions of the left ventricle and not fail under fatigue throughout the patient lifetime. Direct comparison of fatigue in the pulse duplicator with potential clinical implications is inappropriate. The *in vitro* setup accelerates cellular death due to both a non-sterile environment and the isotonic solution used for the working fluid as opposed to the cellular growth medium. We suspect the VEs become non-viable within a few hours of testing; therefore, only the remnant matrix material is being tested without the effect of new matrix deposition and turnover, as would be the case for the living VEs. As it stands, the current generation of tissue engineered valve equivalents have limited durability in the pulmonary position (right ventricular loading) and immediate failure in the aortic position (left ventricular loading). Even with a living valve in the pulse duplicator, we suspect the matrix turnover rate would not be fast enough to account for the limited fatigue life of the VEs. In the following Chapter (Future Directions) the failure modes of the VEs and potential improvements in their structural design are discussed.

Chapter 5: Future Directions

The cardiovascular pulse duplicator served the purpose of replicating physiological pressure and flow signatures. For future testing of valves, a few modifications to the system may have to be considered as follows:

1. The ventricular impendence chamber (VIA) results in asymmetric inflow conditions for the testing valves. The opening of the VIA should be modified to allow axisymmetric inflow conditions.
2. Currently the working fluid for testing the valves and the hydraulic fluid that the piston pumps against is the same. When a high viscosity fluid (e.g., water glycerine) is used, the pump has to push against a high flow resistance. The build up of flow resistance adds to the overall impedance in the flow system. This may result in large upstream negative pressures during the backstroke of the pump. Furthermore, testing the valve at pathological conditions requiring higher stroke volumes and pulsing frequency may go beyond the pump's forcing ability when using the high viscosity fluids. A *possible solution would be to use a separate hydraulic fluid with lower viscosity. This would require a separation of the hydraulic fluid from the working fluid by a ventricular chamber. It might be appropriate to make the chamber of a transparent silicone sac replicating the left ventricle anatomy and closely matching the compliance (see Kadem et al. (2005)). In using a compliant ventricular chamber, the VIA is not necessary. The compression of the hydraulic fluid by the pump during the systole would generate increasing pressures resulting in the 3-dimensional contraction of the compliant ventricular sac and facilitate development of 3-dimensional inlet flow conditions. This flow would be more similar to left ventricular physiology. Additionally, the testing valves would have to be placed within the sac and anastomosed by sutures making the valve and ventricular unit more similar to clinical attachment than the current rigid mounting approach.*
3. The air bubbles trapped in the cardiovascular pulse duplicator system required removal with catheters inserted into the system. When bubbles become entrapped, the pulse duplicator flow has to be stopped and air bubbles removed.

Air bleeding ports placed upstream and downstream may help capture passing bubbles. As stated in modification Number 2, using a compliant ventricular sac may eliminate the need to use the VIA, where mixing of air and water in the compliance chamber occurs upstream of the testing valve.

4. The negative upstream pressures registered during the back stroke of the pump are also a result of the resistance in forward flow through the mitral valve. *A possible solution is to use a larger diameter mitral valve. A larger orifice will result in less resistance to the flow and lower negative pressures generated by the suction effect.*
5. Meaningful *in vitro* accelerated fatigue testing could be implemented, which would have advantages over clinical tests. The accelerated fatigue testing simulates several years of virtual life of a prosthetic valve in a short period of time. *For example, a cycling rate of 10 Hz or 600 beats per minute can simulate ten months of clinical data in approximately one month of in vitro testing. In accordance to ISO 5840, the 33% systolic duration and maximum pressure gradient following valve closure of 120 mmHg could be regulated with the current system. High frame rate cameras recording at kilohertz frame rate could monitor the valve opening and closing. Additionally, accelerated fatigue testing could give an idea of both the failure modes and the growth and remodeling of the valve equivalent by saving the time and money required for clinical tests. Getting meaningful fatigue testing results would require keeping the valve equivalents viable throughout the testing time. Sterilization of the pulse duplicator and use of growth media in the working fluid are vital components in keeping the valves viable.*
6. Capturing video data at the time of failure with synchronized pressure and flow measurements is critical for a proper assessment of the valve failure mode under normal loading and accelerated loading. *Using LabView and a synchronization board, both the digital video capture and analogue pressure and flow signatures could be synchronized appropriately.*
7. The current volumetric velocity measurements have very low spatial resolution. To get a better understanding of flow physics at the smaller scales, the system has

to be modified. *There are multiple possible solutions to increasing the spatial resolution or magnification. The simplest would be to use a higher density of seeding particles. The limit of increasing particle density is reached when individual velocity vectors cannot be measured because of particle overlap. The limit in the resolution is also affected by the particle size. Another solution is to scale up the current conduit dimensions, while maintaining physiological Reynolds and Womersley number by decreasing fluid velocity and pulsing frequency. This will increase the spatial resolution for the same particle density. This requires both the testing valve and flow chamber to be modified in dimensions. For dynamic flow similarity, it is also possible to use a working fluid of lower kinematic viscosity; however, the fluid optical requirements for conducting velocity measurements must be met. The flow field within or downstream of the scaled-up valve would identify secondary flow structures, which might not have been registered in the current scale. Additionally, the camera distance to the valve can be reduced while maintaining the valve within the focal depth of the camera. To accomplish this, however, the current hardware must be modified.*

8. The current velocity field measurements have low temporal resolution allowing data capture at less than 7.5 Hz. The time evolution of vortical structures can not be captured. *Higher temporal resolution cameras working at 1 KHz would be sufficient to capture time variations of the coherent structures in the flow.*

The current generation of tissue engineered valve equivalents (VEs) may be implantable in the pulmonary position and the implantation has been done successfully in short-term clinical testing of animal models (Syedain, 2009). The successful performance of the valve throughout the lifetime of a patient is questionable, especially if implanted in the aortic position.

1. The valve equivalent root stiffness is compromised by the reduced thickness (300-400 microns) of the root as compared to native valve roots (few millimeters). This leads to the VE's early failure under high internal pressures. *A few solutions to this problem have been proposed by our colleagues at the Tranquillo*

Laboratory. The fibrin-based VEs can be cast out of stiffer biodegradable and biocompatible polymers like PGA, PLGA, and PLA. See Mol et al. (Mol et al., 2005) for published works . Also, fibrin based sheets can be rolled over the VE roots similar to what is done to increase thickness of vascular grafts (L'Heureux et al., 2006). The limiting factor in increasing tissue thickness may be the nutrient transport across the tissue layer, which is accomplished mainly by an inefficient diffusion process. If nutrient incorporates convection (transmural flow), thicker tissues may be harvested. There is ongoing work in the Tranquillo Laboratory to improve VE root tissue thickness.

2. The valve equivalent leaflets compact during the tissue engineering process and some VEs become incompetent due to overcompacted non-coapting leaflets. *Photo cross-linking of fibrin gel has been suggested to stiffen the VE matrix and inhibit excessive compaction of the leaflets. Preliminary work conducted in the Tranquillo Laboratory indicates that photo cross-linking is effective in slowing down the compaction process.*
3. Majority of the 3L VEs were not able to coapt during diastole. Once again this is a result of over-compacting leaflets. *Progress should be made towards making coapting 3L VEs because they offer less resistance to flow with a larger opening as well as a more axisymmetric flow conditions, typifying native valve flow.*

References:

Abramovich, G. N., 1963. The theory of turbulent jets. Cambridge, Mass.

Adrian, R. J., Christensen, K. T., Liu, Z. C., 2000. Analysis and interpretation of instantaneous turbulent velocity fields. Experiments in Fluids 29, 275-290.

Batchelor, G. K., Gill, A. E., 1962. Analysis of the stability of axisymmetric jets. J. Fluid Mech. 14, 529-51.

Bellhouse, B. J., Talbot, L., 1969. The fluid mechanics of aortic valve. J. Fluid Mech. 35, 721.

Bernstein, E. F., Marzec, U., Johnston, G. G., 1977. Structural correlates of platelets functional damage by physical forces. Trans. Am. Soc. Artif. Intern. Organs 23, 617-25.

Bluestein, D., Rambod, E., Gharib, M., 2000. Vortex shedding as a mechanism for free emboli formation in mechanical heart valves. Journal of Biomechanical Engineering 122, 125-134.

Borazjani, I., Ge, L., Sotiropoulos, F., 2007. Curvilinear immersed boundary method for simulating fluid structure interaction with complex 3D rigid bodies. J. of Computational Physics 227, 7587-7620.

Brown, C. H., Leverett, L. B., Lewis, C. W., C.P., A., Hellums, J. D., 1975. Morphological, biochemical, and functional changes in human platelets subjected to shear stress. J. Lab. Clin. Med. 3, 462-474.

Carmody, C. J., Burriesci, G., Howard, I. C., Patterson, E. A., 2006. An approach to the simulation of fluid-structure interaction in the aortic valve. Journal of Biomechanics 39, 158-169.

Chandran, K. B., Khalighi, B., Chen, C. J., Falsetti, H. L., Yearwood, T. L., Hiratzka, L. F., 1983. Effect of valve orientation on flow development past aortic prostheses in a model human aorta. J. of Thoracic and cardiovascular surgery 85, 893-901.

Cheng, R., Lai, Y. G., Chandran, K. B., 2003. Two-dimensional fluid-structure interaction simulation of bileaflet mechanical heart valve flow dynamics. J. Heart Valve Dis. 12, 772-80.

Clark, R. E., 1973. Stress-strain characteristics of fresh and frozen human aortic and mitral leaflets and chordae tendinae: implications for clinical use. J. Thorac. Cardiovas. Surg. 66, 202-8.

Crowe, C. T., Sommerfeld, M., Tsuji, Y., 1998. Multiphase flows with droplets and particles. Boca Raton, Fla.

Crow, S. C., Champagne, F. H., 1971. Orderly structure in jet turbulence. J. Fluid Mech. 48, 547-91.

Dabiri, J., Gharib, M., 2005. The role of optimal vortex formation in biological fluid transport. Proceedings of the royal society B 272, 1557-1560.

Dabiri, J., Gharib, M., 2005. Starting flow through nozzles with temporally variable exit diameter. J. Fluid Mech. 538, 111-36.

Danaila, I., Dusek, J., Anselmet, F., 1977. Coherent structures in a round, spatially evolving, unforced, homogeneous jet at low Reynolds number. Phys. Fluids 9, 3323-41.

Dasi, L. P., Ge, H., Simon, A., Sotiropolous, F., Yoganathan, A. P., 2007. Vorticity dynamics of a bileaflet mechanical valve in an axisymmetric aorta. Phys. Fluids 19:067105, 2007.

Dasi, L. P., Ge, H., Simon, A., Sotiropolous, F., Yoganathan, A. P., 2007. Vorticity dynamics of a bileaflet mechanical valve in an axisymmetric aorta. Phys. Fluids 19, 1-17.

de Hart, J., Peters, G. W. M., Schreurs, P. J. G., Baaijens, F. P. T., 2000. A two-dimensional fluid-structure interaction model of the aortic heart valve. Journal of Biomechanics 33, 1079-1088.

de Hart, J., Peters, G. W. M., Schreurs, P. J. G., Baaijens, F. P. T., 2003. A three-dimensional computational analysis of fluid-structure interaction in the aortic valve. Journal of Biomechanics 36, 103-112.

DeOtte, R. E., Morrison, G. L., D.L.Panak, G.H.Nail, 1991. 3-D laser Doppler anemometry measurements of the axisymmetric flow field near an orifice plate. Flow Meas. Instrum. 2, 115-123.

Dumont, K., Vierendeels, J., Kaminsky, R., van Nooten, G., Verdonck, P., Bluestein, D., 2007. Comparison of the hemodynamic and thrombogenic performance of two bileaflet mechanical heart valves using a CFD/FSI model. Transactions in ASME 129, 558-565.

Freidman, M. H., Fry, D. L., 1993. Arterial permeability dynamics and vascular disease. Atherosclerosis 104, 189-94.

Fung, Y. C., 1997. Biomechanics Circulation. Springer, New York.

Ge, L., Dasi, L. P., Sotiropolous, F., Yoganathan, A. P., 2008. Characterization of hemodynamic forces induced by mechanical heart valves: Reynolds vs. viscous stresses. Annals of Biomedical Engineering 36, 276-297.

Ge, L., Jones, S. C., Sotiropoulos, F., Healy, T. M., Yoganathan, A. P., 2003. Numerical simulation of flow in mechanical heart valves: grid resolution and the assumption of flow symmetry. Journal of Biomechanical Engineering 125, 709-18.

Ge, L., Leo, H. L., Sotiropoulos, F., Yoganathan, A. P., 2005. Flow in a mechanical bileaflet heart valve at laminar and near-peak systole flow rates: CFD simulations and experiments. J of Biomechanical Engineering - Transactions of the ASME 127, 782-97.

Gharib, M., Rambod, E., Shariff, K., 1998. A universal time scale for vortex ring formation. J. Fluid Mech. 360, 121-40.

Gross, J. M., Shermer, C. D., Hwang, N. H. C., 1988. Vortex shedding in bileaflet heart valve prostheses. ASAIO Trans. 34, 845-50.

Han, B., 2001. Instantaneous energy separation in a jet flow. Mechanical Engineering Herbertson, L. H., Deutsch, S., Manning, K. B., 2008. Modifying a tilting disk mechanical heart valve design to improve closing dynamics. Journal of Biomechanical Engineering 130, 054503-1 054503-4.

Jennings, L. M., Butterfield, M., Walker, P. G., Watterson, K. G., Fisher, J., 2001. The influence of ventricular input impedance on the hydrodynamic performance of bioprosthetic aortic roots in vitro. J. Heart Valve Dis. 10, 269-275.

Kadem, L., Knapp, Y., Pibarot, P., Betrand, E., Garcia, D., Durand, L., Rieu, R., 2005. A new experimental method for the determination of the effective orifice area based on the acoustical source term. Experiments in Fluids 39, 1051-1060.

Kafesjian, R., Wieting, D. W., Ely, J., Chahine, G. L., Frederick, G. S., Watson, R. E., 1989. Charcterization of cavitation potential of pyrolitic carbon. Proc. Int. Symp. Heart Valve Dis. 12-16.

Kaminsky, R., Kallweit, S., Rossi, M., Morbiducci, U., Scalise, L., Verdonck, P., Tomasini, E., 2008. PIV measurements of flows in artificial heart valves. Topics Appl. Physics 112, 55-72.

Keane, R. D., Adrian, R. J., 1990. Optimization of particle image velocimeters. Part I: Double pulsed systems. Meas. Sci. Technol. 1, 1202-15.

Kheradvar, A., Gharib, M., 2007. Influence of ventricualr pressure drop on mitral annulus dynamics through the process of vortex ring formation. Annals of Biomedical Engineering 35, 2050-64.

Kilner, P. J., Guang, Z., Mohiaddin, R. H., Firmin, D. N., Longmore, D. B., 1993. Helical and retrograde secondary flow patterns in the aortic arch studied by three-directional magnetic resonance velocity mapping. Circulation 88, 2235-47.

Kim, H., Lu, J., Sacks, M., Chandran, K. B., 2008. Dynamic simulation pericardial bioprosthetic heart valve function. Journal of Biomechanical Engineering 128, 717-24.

Klepetko, W., 1989. Leaflet fracture in Edwards-Duromedics bileaflet valves. J. Thorac. Cardiovasc. Surg. 97, 90-94.

Krueger, P. S., Gharib, M., 2003. The significance of vortex ring formation to the impulse and thrust of a starting jet. Phys. Fluids 15, 1271-81.

Kunlun, L., Amatya, D. M., Longmire, E. K., Barocas, V. H., 2009. Numerical and experimental investigations of fluid-structure interaction in a tube containing a flexible orifice. Journal of Fluids and Structure XX, XX.

Leo, H. L., Dasi, L. P., Carberry, J., Simon, H. A., Yoganathan, A. P., 2006. Fluid dynamic assessment of three polymeric heart valves using particle image velocimetry. Annals of Biomedical Engineering 34, 936-52.

L'Heureux, N., Dusserre, N., Konig, G., Victor, B., Keire, P., Wight, T. N., Chronos, N., Kyles, A., Gregory, C. R., Hoyt, G., Robbins, R. C., McAllister, T., 2006. Human tissue-engineered blood vessels for adult arterial revascularization. Nat. Med. 12, 361-365.

Liao, K. K., Xiaohuan, L., John, R., Amatya, D. M., 2008. Mechanical stress: An independent determinant of early bioprosthetic calcification of humans. Ann. Thorac. Surg. 86, 491-5.

Lim, W. L., Chew, Y. T., Chew, T. C., Low, H. T., 1994. Particle image velocimetry in the investigation of flow past artificial heart valves. Exp. Fluids 17, 282-4.

Liu, K., Radhakrishnan, H., Barocas, V. H., 2007. Simulation of flow around a thin flexible obstruction by means of a deforming grid overlapping a fixed grid. nt. J. Num. Meth. Fluids DOI: 10.1002/fld.1552, XX.

Luff, J.D., Drouillard, T., Rompage, A.M. Linne, M.A., Hertzberg, J.R., 1999. Experimental uncertainties associated with particle image velocimetry (PIV) based vorticity algorithms. Exp. Fluids 26, 36-54.

Marassi, M., Castellini, P., Pinotti, M., Scalise, L., 2004. Cardiac valve prosthesis flow performances measured by 2D and 3D-stereo particle image velocimetry. Experiments in Fluids 36, 176-186.

Mavrilas, D., Missirlis, Y., 1991. An approach to the optimization of preparation of bioprosthetic heart valves. J. Biomechanics 24, 331-339.

Merzkirch, W., 1987. Flow visualization. Orlando.

Mi, J., Nobes, D. S., Nathan, G. J., 2001. Influence of jet exit conditions on the passive scalar field of an axisymmetric free jet. J. Fluid Mech. 432, 91-125.

Mirnajafi, A., Raymer, J. M., McClure, L. R., Sacks, M., 2006. The flexure rigidity of aortic valve leaflet in the commissural region. Journal of Biomechanics 39, 2966-2973.

Mol, A., Driessen, N., Rutten, M., Hoestrup, S., Bouten, V. C., Baaijens, F. T., 2005. Tissue engineering of human heart valve leaflets: a novel bioreactor for strain-based conditioning approach. Annals of Biomedical Engineering 33, 1778-1788.

Moore, C. J., 1977. The role of shear layer instability waves in jet exhaust noises. J. Fluid Mech. 80, 321-67.

Morrison, G. L., 2003. Euler number based orifice discharge coefficient relationship. Journal of Fluids Engineering 125, 189-91.

Murgo, J. P., 1998. Systolic ejection murmurs in the era of modern cardiology: what do we really know? Journal of American college of cardiology 32, 1596-602.

Nichols, W. W., O'Rourke, M. F., 2005. Mcdonald's blood flow in arteries theoretical, experimental and clinical principles. Oxford University press inc., New Yourk.

Ohmi, K., Li, H.-Y., 2000. Particle-tracking velocimetry with new algorithms. meas. Sci. Technol. 11, 603-616.

Pereira, F., Stuer, H., Graff, E. C., Gharib, M., 2006. Two-frame 3D particle tracking. meas. Sci. Technol. 17, 1680-92.

Perry, R. H., Green, D. W., Maloney, J. O., 1984. Perry's Chemical Engineer's Handbook. 6th Edition 5-15.

Peskin, C. S., 1982. The fluid dynamics of heart valves: experimental, theoretical and computational methods. Ann. Rev. Fluid Mech. 14, 235-59.

Peskin, C. S., McQueen, D. M., 1989. A three-dimensional computational method for blood flow in heart: (I) immersed elastic fibers in a viscous incompressible fluid. J. Comput. Phys. 81, 372-405.

Pierrakos, O., Vlachos, P. P., Telionis, D. P., 2004. Time-resolved DPIV analysis of vortex dynamics in a left ventricular model through bileaflet mechanical and porcine heart valve prostheses. Transactions of the ASME 126, 714-26.

Pope, S. B., 2005. Turbulent Flows. Cambridge University Press, Cambridge.

Raffel, M., Willert, C., Kompenhans, J., 1998. Particle image velocimetry - A practical guide. Springer, Berlin Heidelberg New York.

Rambod, E., Beiai, M., Sahn, D. J., Gharib, M., 2007. Role of vortices in growth of microbubbles at mitral mechanical heart valve closure. Annals of Biomedical Engineering 35, 1131-45.

Robinson, P. S., Johnson, S. L., Evans, M. C., Barocas, V. H., Tranquillo, R. T., 2008. Functional tissue-engineered valves from cell-remodeled fibrin with commissural alignment of cell-produced collagen. Tissue Engineering: Part A 14, 83-95.

Schoen, F. J., 2008. Evolving concepts of cardiac valve dynamics. Circulation 118, 1864-80.

Simon, H. A., Dasi, L. P., Leo, H., Yoganathan, A. P., 2007. Spatio-temporal flow analysis in bileaflet heart valve hinge regions: potential analysis for blood element damage. Annals of Biomedical Engineering 35, 1333-46.

Sloth, E., Houlind, K. C., Oyre, S., Kim, W. Y., Pedersen, E. M., 1994. Three dimensional visualization of velocity profiles in the human main pulmonary artery with magnetic resonance phase-velocity mapping. Am. Heart J. 128, 1130-38.

Stein, P. D., Sabbah, H. N., 1976. Turbulent blood flow in the ascending aorta of humans with normal and diseased aortic valves. Circulation Research 39, 58-65.

Stella, J. A., Liao, J., Sacks, M., 2007. Time-dependent biaxial mechanical behavior of the aortic heart valve leaflet. J. of Biomech. 40, 3169-3177.

Stijnen, J. M. A., Hart, j. d., Bovendeerd, P. H. M., Vosse, F. N. v., 2004. Evaluation of a fictitious domain method for predicting dynamic response of mechanical heart valve. Journal of Fluids and Structures 19, 835-850.

Stradins, P., Lacis, R., Oolanta, I., Purina, B., Ose, V., Feldman, L., Kasyanov, V., 2004. Comparison of biomechanical and structural properties between human aortic and pulmonary valve. Eur. J. Cardiothoracic. Surg. 26, 634-639.

Strykowski, P. J., Wilcoxon, R. K., 1993. Mixing enhancement due to global oscillation in jets with annular counterflow. AIAA 3, 564-570.

Swope, R. D., Falsetti, H. L., 1976. Velocity profiles in prosthetic heart valves under steady flow conditions. 29th ACEMB 339.

Syedain, Z. H., 2009. Development of completely biological tissue engineered heart valve. Biomedical Engineering 1-230.

Syedain, Z. H., Weinberg, J. S., Tranquillo, R. T., 2008. Cyclic distention of fibrin-based tissue constructs: Evidence of adaptation during growth of engineered connective tissue. PNAS 105, 6537-6542.

Thubrikar, M., 1990. The Aortic Valve. Boca Raton.

Thubrikar, M., Aouad, J., Nolan, S. P., 1986. Pattern of calcific deposits in operatively excised stenotic or purely regurgitant aortic valves and their relation to mechanical stress. Am J. Cardiol. 58, 304-8.

Travis, B. R., Christensen, T. D., Smerup, M., Olsen, M. S., Hasenkam, J. M., Nygaard, H., 2004. An in vivo method for measuring turbulence in a mechanical prosthesis leakage jets. Transaction of the ASME. Journal of Biomechanical Engineering. 126, 26-35.

van Loon, R., Anderson, P. D., van de Vosse, F. N., 2006. A fluid-structure interaction method with solid-rigid contact for heart valve dynamics. Journal of Computational Physics 217, 806-23.

Wereley, S., Gui, L., 2001. PIV measurement in a four-roll-mill flow with a central difference image correction (CDIC) method. In: 4th International symposium on particle image velocimetry, September 17, Gottingen, Germany XX.

Weyman, A. E., 1994. Principles and practices of echocardiography. Lea & Febiger, Philadelphia.

Yoganathan, A. P., Chandran, K. B., Sotiropolous, F., 2005. Flow in prosthetic heart valves: state-of-the-art and future directions. Annals of Biomedical Engineering 33, 1689-1694.

Yoganathan, A. P., Corcoran, W. H., 1979. *In vitro* velocity measurements in the vicinity of aortic prostheses. J. Biomechanics 12, 135-52.

Yoganathan, A. P., He, Z., Jones, S. C., 2004. Fluid mechanics of heart valves. Annu. Rev. Biomed. Eng. 6, 331-62.

Yule, A. J., 1978. Large-scale structure in the mixing layer of a round jet. J. Fluid Mech. 89, 413-32.

Zhou, J., Adrian, R. J., Balchandar, S., Kendall, T. M., 1999. Mechanisms for generating coherent packets of hairpin vortices in channel flow. J. Fluid Mech. 387, 353-96.

Zilla, P., Brink, J., Human, P., Bezuidenhout, D., 2008. Prosthetic heart valves: Catering for the few. Biomaterials 29, 385-406.

Appendix A: Velocity Gradient Computation

The velocity gradients are calculated to compute vorticity, swirl, and shear stress values. The PIV data provide the two components of velocity over a two dimensional plane and therefore provide four terms of the velocity gradient tensor. The V3V data provide the three components of velocity over the three dimensional volume and therefore provide all nine terms of the velocity gradient tensor. The gradients for the different velocity components were computed with a central differencing scheme as follows. Streamwise gradients are,

$$\frac{\partial U(x,y,z)}{\partial x} = \frac{U(x+\Delta x,y,z) - U(x-\Delta x,y,z)}{2\Delta x}$$
$$\frac{\partial V(x,y,z)}{\partial x} = \frac{V(x+\Delta x,y,z) - V(x-\Delta x,y,z)}{2\Delta x}$$
$$\frac{\partial W(x,y,z)}{\partial x} = \frac{W(x+\Delta x,y,z) - W(x-\Delta x,y,z)}{2\Delta x}$$

where, Δx is the streamwise spatial resolution or the streamwise spacing between velocity vectors. Note that W and z are not considered for planar PIV data. The spanwise gradients are also calculated with the central difference scheme and the resolutions are Δy and Δz.

$$\frac{\partial U(x,y,z)}{\partial y} = \frac{U(x,y+\Delta y,z) - U(x,y-\Delta y,z)}{2\Delta y}$$
$$\frac{\partial V(x,y,z)}{\partial y} = \frac{V(x,y+\Delta y,z) - V(x,y-\Delta y,z)}{2\Delta y}$$
$$\frac{\partial W(x,y,z)}{\partial y} = \frac{W(x,y+\Delta y,z) - W(x,y-\Delta y,z)}{2\Delta y}$$

$$\frac{\partial U(x,y,z)}{\partial z} = \frac{U(x,y,z+\Delta z) - U(x,y,z-\Delta z)}{2\Delta z}$$
$$\frac{\partial W(x,y,z)}{\partial z} = \frac{V(x,y,z+\Delta z) - V(x,y,z-\Delta z)}{2\Delta z}$$
$$\frac{\partial W(x,y,z)}{\partial z} = \frac{W(x,y,z+\Delta z) - W(x,y,z-\Delta z)}{2\Delta z}$$

These terms can be represented in a tensor format and re referred to as the velocity gradient tensor Def,

$$Def = \nabla \vec{u} = \begin{pmatrix} \frac{\partial U}{\partial x} & \frac{\partial U}{\partial y} & \frac{\partial U}{\partial z} \\ \frac{\partial V}{\partial x} & \frac{\partial V}{\partial y} & \frac{\partial V}{\partial z} \\ \frac{\partial W}{\partial x} & \frac{\partial W}{\partial y} & \frac{\partial W}{\partial z} \end{pmatrix}$$

Appendix B: Swirl Calculation

B.1 Three-dimensional Swirl Strength

The velocity gradient tensor Def (Appendix A) has a characteristic Eigen-value cubic polynomial equation,

$$\lambda^3 + I_1\lambda^2 + I_2\lambda + I_3 = 0$$

where, I_1, I_2 and I_3 are the invariants of D as follows,

$$I_1 = trace(Def)$$
$$I_2 = \frac{1}{2}\left[I_1{}^2 - trace(DefDef)\right]$$
$$I_3 = \frac{1}{3}\left[-I_1{}^3 - 3I_1I_2 - trace(DefDefDef)\right]$$

The discriminant Δ of the polynomial equations is,

$$\Delta = \overline{I_3}^2 + \overline{I_2}^2$$

where,

$$\overline{I_3} = \frac{1}{6}\left(I_1I_2 - 3I_3\right) - \frac{1}{27}I_1{}^3$$
$$\overline{I_2} = \frac{1}{3}I_2 - \frac{1}{9}I_1{}^2$$

The polynomial can have three real roots or one real root and a pair of complex conjugate roots. If $\Delta > 0$, all roots are real and if $\Delta < 0$, the polynomial has one real root and a pair of complex roots. For the case where $\Delta < 0$, let

$$s1 = \left[\overline{I_3} + \sqrt{\Delta}\right]^{\frac{1}{3}}$$
$$s2 = \left[\overline{I_3} - \sqrt{\Delta}\right]^{\frac{1}{3}}$$

then, the roots zcomp1, zcomp2 and zcomp3 can be written as,

$$zcomp1 = [s1 + s2] - \frac{I_1}{3}$$

$$zcomp2 = -\frac{1}{2}[s1 + s2] - \frac{I_1}{3} + \frac{i\sqrt{3}}{2}(s1 - s2)$$

$$zcomp3 = -\frac{1}{2}[s1 + s2] - \frac{I_1}{3} - \frac{i\sqrt{3}}{2}(s1 - s2)$$

The complex roots take on the form

$$z_{comp} = \lambda_{cr} + i\lambda_{ci}$$

$$\lambda_{cr} = -\frac{1}{2}(s1 + s2) - \frac{I_1}{3}$$

$$\lambda_{ci} = \frac{\sqrt{3}}{2}(s1 - s2)$$

Based on work by Zhou et al. (1999) the imaginary part of the complex Eigen-vale (λ_{ci}) from the velocity gradient tensor Def may be used to identify vortices or swirling motion. In the results presented in this dissertation, the swirl strength of the vortex is denoted by λ_{ci}.

B.2 Two-dimensional Swirl Strength

Two-dimensional PIV provides only two components of velocity and gradients. A reduced version of the velocity gradient tensor Def_{2D} is used to compute the swirl values identifying vortex cores.

$$Def_{2D} = \nabla \vec{u}_{2D} = \begin{pmatrix} \frac{\partial U}{\partial x} & \frac{\partial U}{\partial y} \\ \frac{\partial V}{\partial x} & \frac{\partial V}{\partial y} \end{pmatrix}$$

D_{2D} has a characteristic Eigen-value quadratic polynomial equation,

$$\lambda^2 + I_{1\,2D}\lambda + I_{2\,2D} = 0$$

where, $I_{1\,2D}$ and $I_{2\,2D}$ are the invariants of D as follows,

$$I_{1\,2D} = -trace(Def)$$

$$I_{2\,2D} = -\det(Def)$$

For the 2D case, the discriminant of the equation Δ is given by,

$$\Delta_{2D} = I_{1\,2D}^2 + 4I_{2\,2D}$$

If $\Delta_{2D} < 0$ then the roots zcomp1 and zcomp2 are complex and is given by,

$$zcomp1, zcomp2 = \frac{I_1 \pm i\sqrt{\Delta_{2D}}}{2}$$

where, zcomp has the general form,

$$zcomp = \lambda_{cr} + i\lambda_{ci}$$

$$\lambda_{cr} = \frac{I_{12D}}{2}$$

$$\lambda_{ci} = \frac{\sqrt{|\Delta_{2D}|}}{2}$$

Like the 3D case, λ_{ci} defines swirl strength. Regions of positive swirl strength correspond with locations in which the flow swirls about an axis normal to the measurement plane.

Appendix C: Principal Shear Stress Calculation

The viscous shear stress τ is defined as,

$$\tau = \mu Def$$

Def is the velocity gradient tensor defined in Appendix A, and μ is the dynamic viscosity of the fluid. The maximum (σ_{max}) and minimum (σ_{min}) magnitudes of the real roots of the characteristic equation (see Appendix B) of the velocity gradient tensor (Def.) times dynamic viscosity are the maximum and minimum principal stresses of the tensor, respectively. The coordinate invariant local maximum shear stress can be defined as,

$$\tau_{max} = \frac{1}{2}(\sigma_{max} - \sigma_{min})$$

Appendix D: Uncertainty Analysis

The velocity at matrix position i, j is given by,

$$U_{i,j} = \frac{\Delta X_{i,j}}{M\Delta t}$$

where ΔX, M, and Δt denote particle displacement, magnification, and laser pulse separation time. The uncertainty in particle displacement at matrix position i, j is given by root sums of squares formula,

$$\delta\Delta X_{i,j} = \left[(\varepsilon_1)^2 + (\varepsilon_2)^2 + (\varepsilon_3)^2\right]^{0.5} \Delta X_{i,j}$$

where ε_1, ε_2, and ε_3 are uncertainty due to in-plane motion particle loss, out-of-plane motion particle loss, and PIV Gaussian peak finding algorithm, respectively (Luff et al., 1999). If a small pulse separation time ΔT value is chosen to reduce in-plane and out-of-plane particle loss, the uncertainty in the particle displacement is influenced by the peak finding algorithm (ε_3). The Gaussian peak finding algorithm has sub-pixel accuracy δΔX = 0.1 pix (Raffel et al., 1998) for PIV. The spatial uncertainties for V3V are 20 microns along the x and y-directions and 80 microns along the z-direction (Dan Troolin, TSI Incorporated). The velocity uncertainty at matrix position i, j is calculated as once again with the root sum of squares,

$$\delta U_{i,j} = \left\{\left[(1/M\Delta t)(\Delta X_{i,j}\delta\Delta X)\right]^2 + \left[(\Delta X_{i,j}/M^2\Delta T)(\delta M)\right]^2 + \left[(\Delta X_{i,j}/M\Delta T^2)(\delta\Delta T)\right]^2\right\}^{0.5}$$

where δM and δΔt are the uncertainties in the spatial magnification and pulse separation time, respectively. The uncertainties in the magnification factor δM, and pulse separation δΔT (order of nano-seconds) contributes less to the uncertainty than maximum error in the peak finding algorithm δΔX. With these assumptions, the uncertainty in the velocity vector is reduced to

$$\delta U = \left(\frac{\delta\Delta X}{M\Delta t}\right)$$

The uncertainty in the velocity vector δU is propagated through vorticity calculations. Additionally, 'spurious' vectors and 'dropout' vectors influence vorticity calculations. These spurious and drop-out vectors were filtered and filled in with local spatial averaging (see Section 2.5.1). The 'filled-in' vectors also influence vorticity calculation.

The sampling rate or the pulse separation time ΔT and PIV interrogation area/volume limit the temporal and spatial scales, respectively of vorticity calculation. The numerical approximation through differentiation schemes such as central difference method introduces truncation and smoothing errors in the vorticity calculation. In the current dissertation, the results for vorticity are obtained through the second order central difference method. Let K represent any velocity gradient computed between velocities at two points, U_1 and U_2, separated by d_g then K takes on the value

$$K = \frac{U_1 - U_2}{d_g}$$

and applying the root of sum of squares for the uncertainty in K

$$\delta K = \sqrt{\left[\frac{\delta U_1}{d_g}\right]^2 + \left[\frac{\delta U_2}{d_g}\right]^2 + \left[\frac{(U_1 - U_2)\delta d_g}{d_g^2}\right]^2}$$

where δU_1 and δU_2 are the uncertainties in velocities at points 1 and 2 and are equal for planar PIV measurements. These values are equal along the x and y-directions for V3V, but larger along the z-direction. δd_g, the uncertainty in the spatial separation is negligible. Summarizing, if $\delta U_1 = \delta U_2$

$$\delta U_1 = \delta U_2 = \delta U$$
$$d_g = 2d_s$$
$$\delta d_g \approx 0$$
$$\delta K = \sqrt{2\left(\frac{\delta U}{2d_s}\right)^2}$$
$$\delta K = 0.707\frac{\delta U}{d_s}$$

where d_s is the grid spacing between vectors. If $\delta U_1 \neq \delta U_2$

$$\delta K = \sqrt{\left(\frac{\delta U_1 + \delta U_2}{2d_s}\right)^2}$$

Appendix E: Material Testing Results

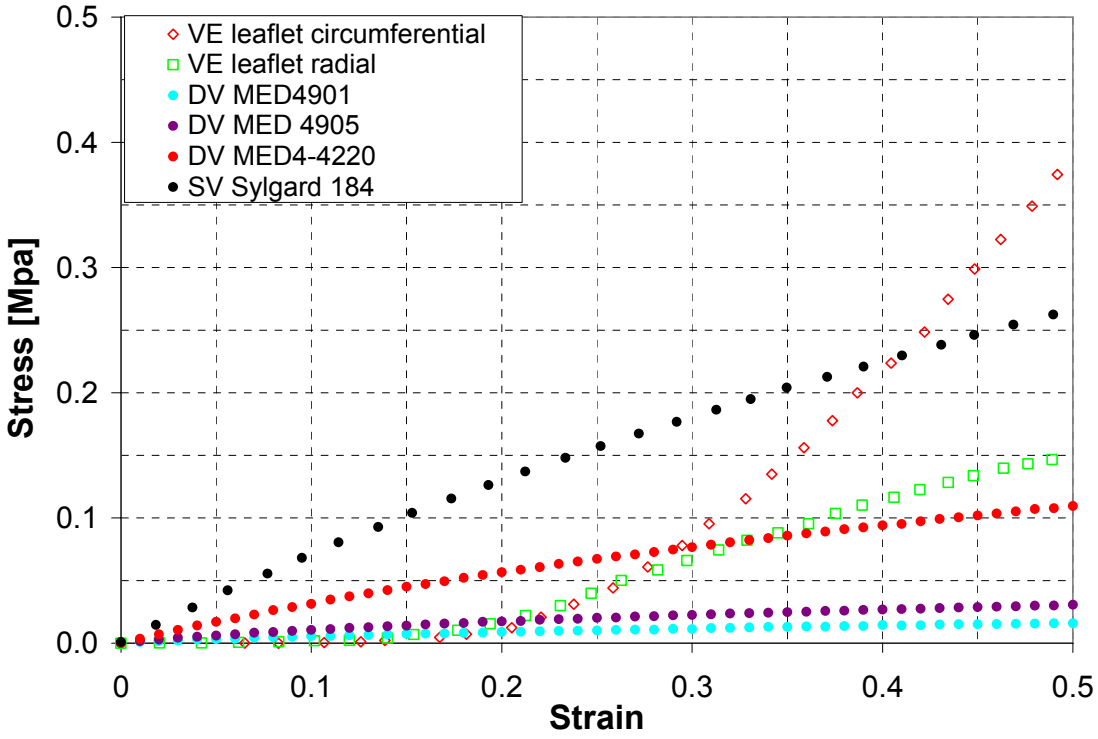

Appendix E- 1. Uniaxial material testing response. VE: valve equivalent, DV: diaphragm valve, and SV: silicone valve.

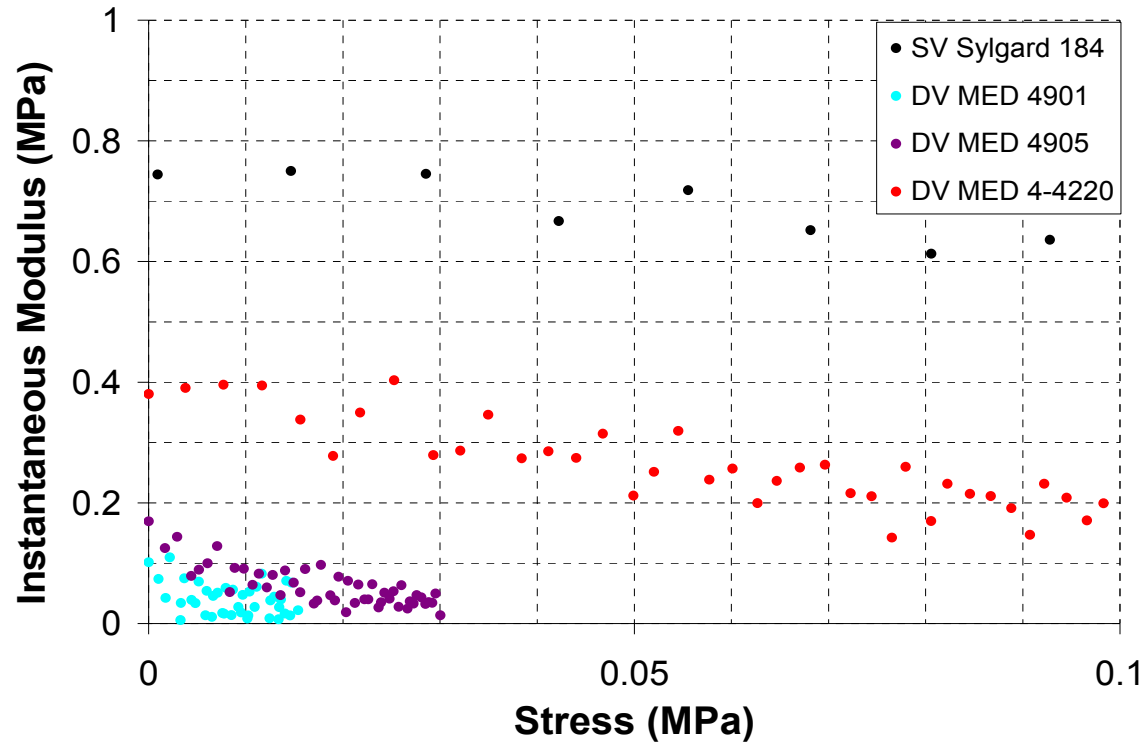

(a)

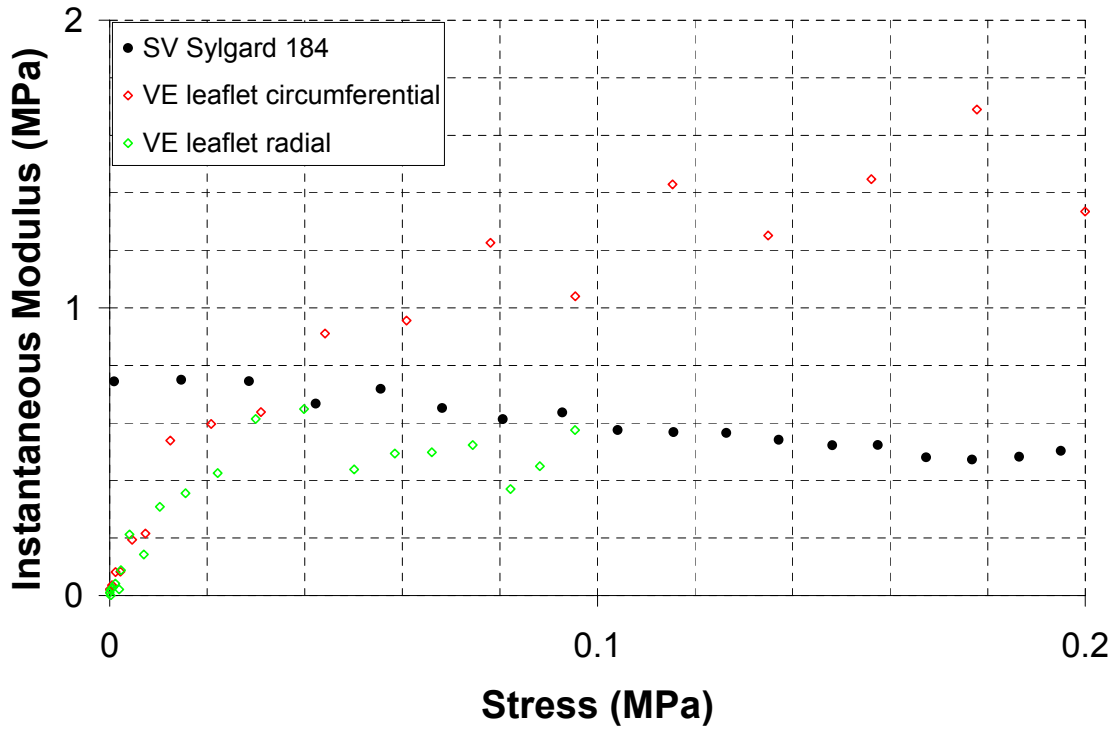

(b)

Appendix E- 2. Material modulus comparison. (a) silicone materials and (b) valve equivalent and silicone valve.

Appendix F: Silicone Valve Deformation Images

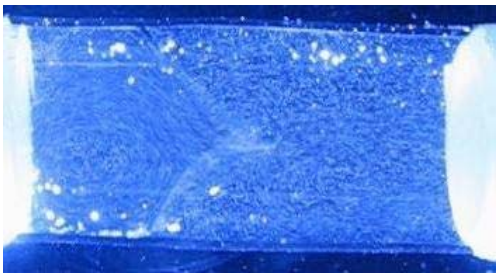

φ0 (0°)

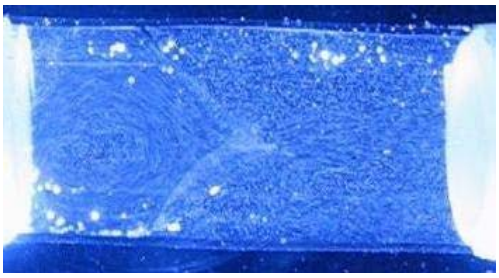

φ1 (14°)

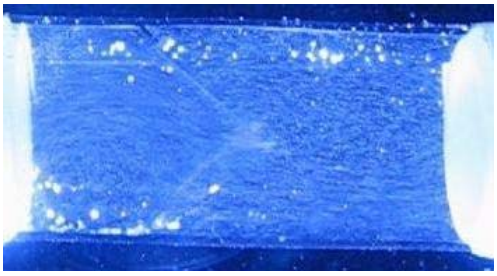

φ2 (28°)

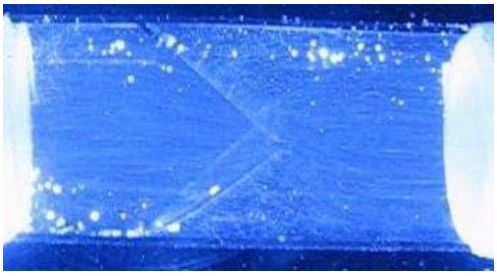

φ3 (42°)

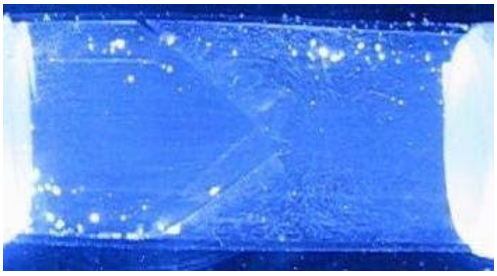

φ4 (56°)

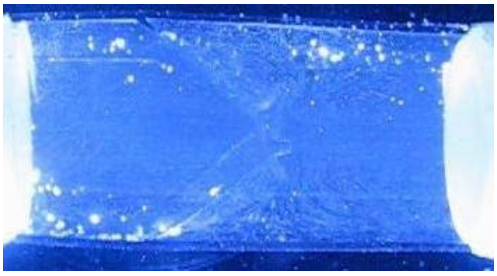

φ5 (70°)

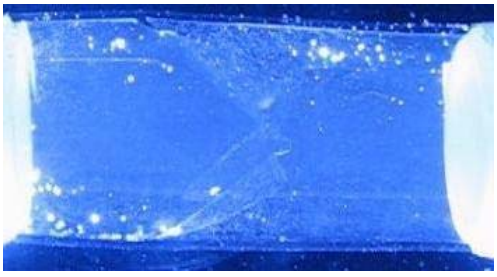

φ6 (84°)

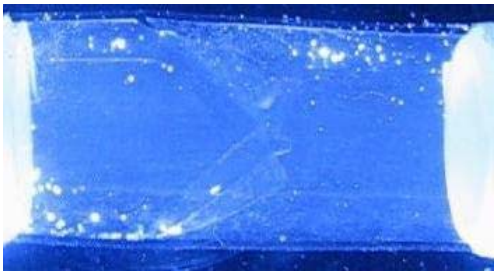

φ7 (98°)

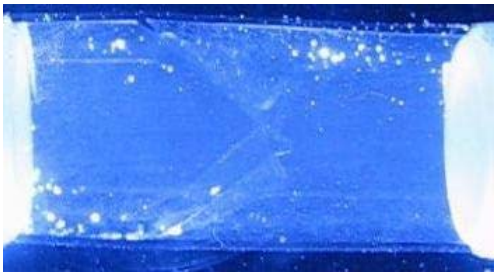

φ8 (112º)

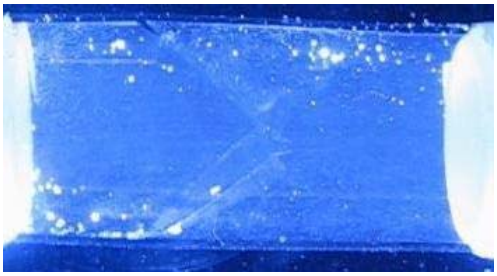

φ9 (126º)

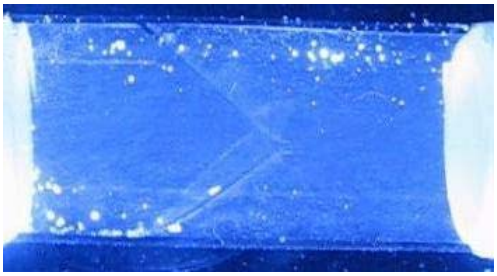

φ10 (140º)

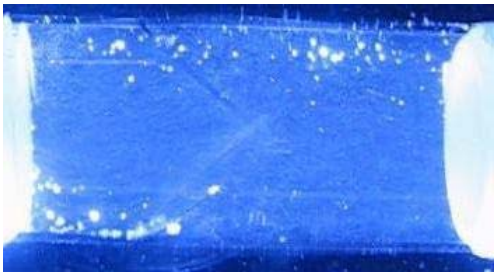

φ11 (154º)

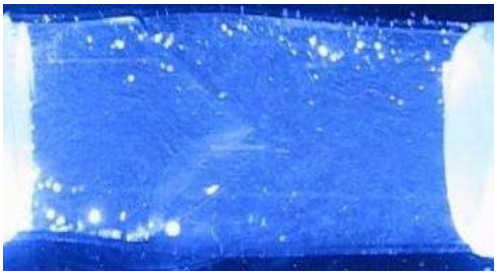

φ12 (168º)

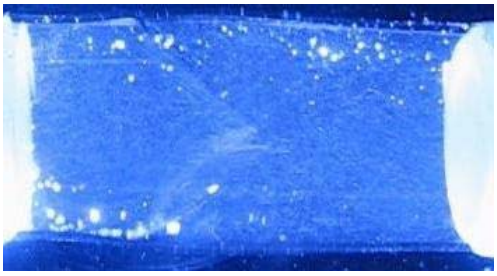

φ13 (182º)

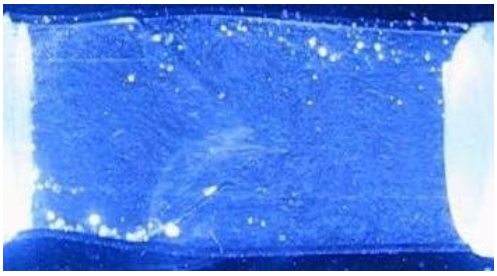

φ14 (196º)

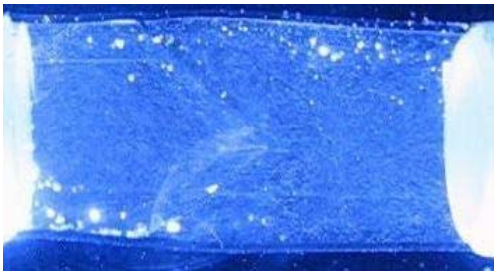

φ15 (210º)

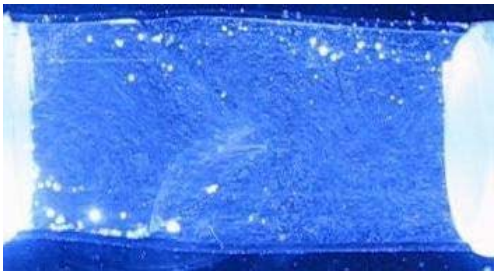

φ16 (224º)

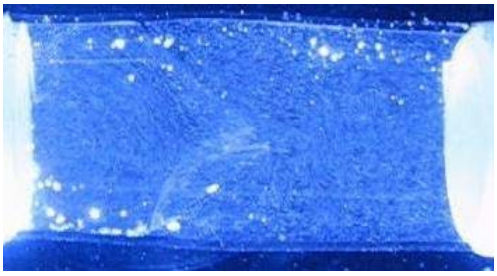

φ17 (238º)

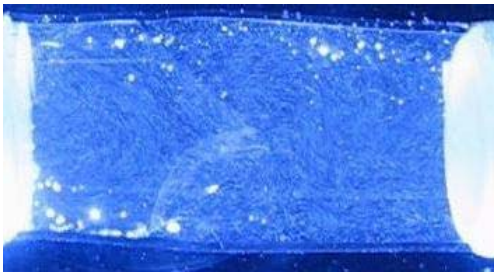

φ18 (252º)

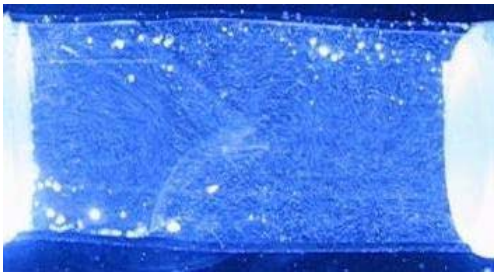

φ19 (266º)

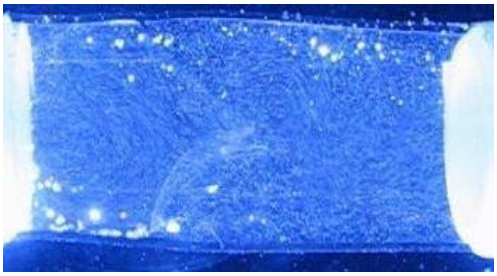

φ20 (280º)

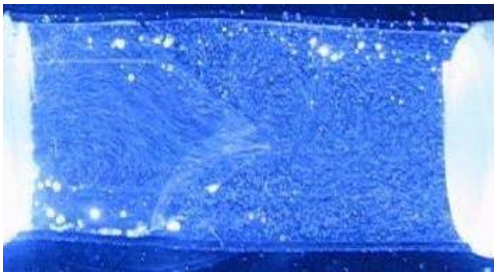

φ21 (294º)

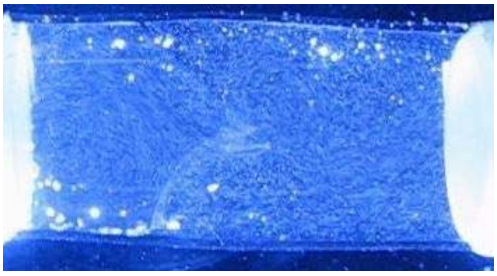

φ22 (308º)

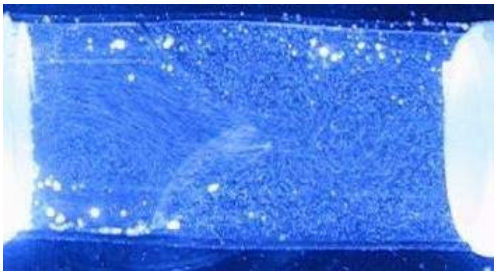

φ23 (322º)

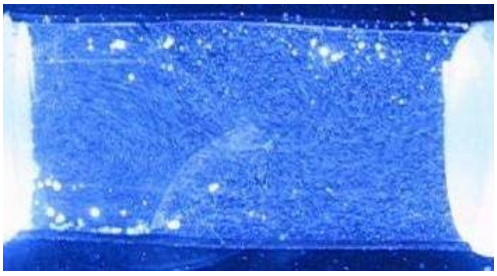

φ24 (336º)

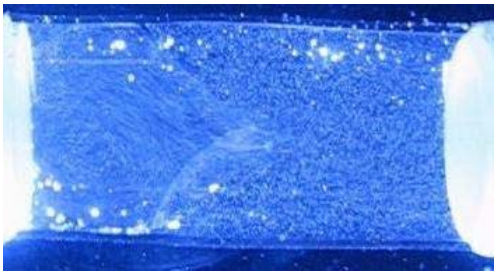

φ25 (350º)

Appendix F- 1. Transparent silicone valve flow phases showing the plane perpendicular to the commissures. The flow is from left to right. Average flow rate of 4.2 L/min at a pulsing frequency of 1.17 Hz.

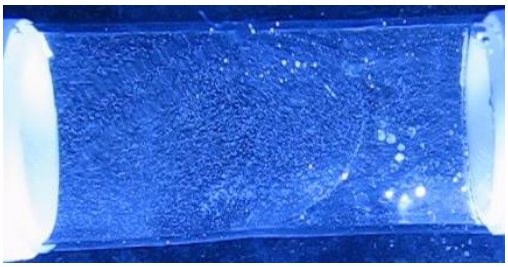

φ0 (0º)

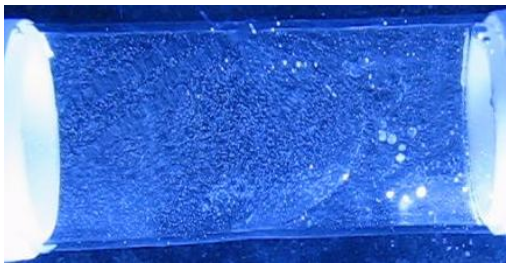

φ1 (14º)

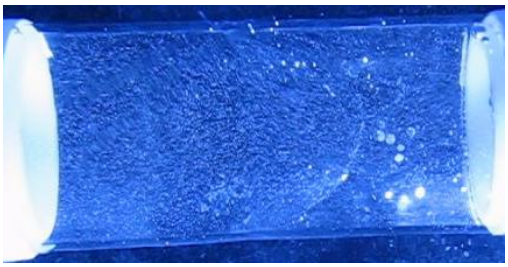

φ2 (28º)

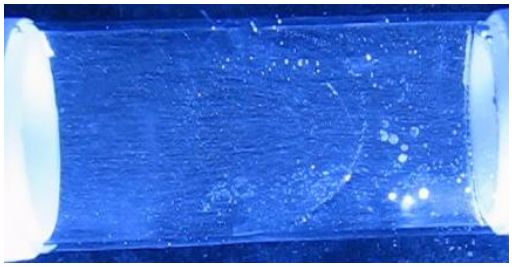

φ3 (42º)

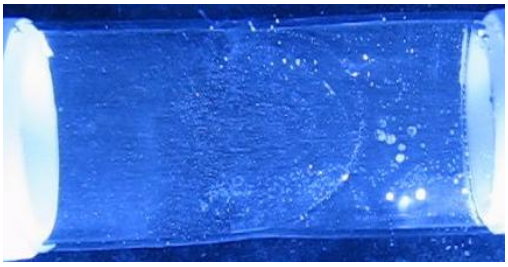

φ4 (56º)

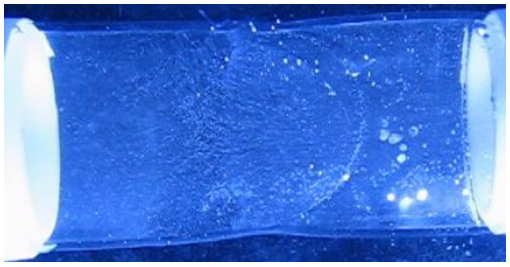

φ5 (70º)

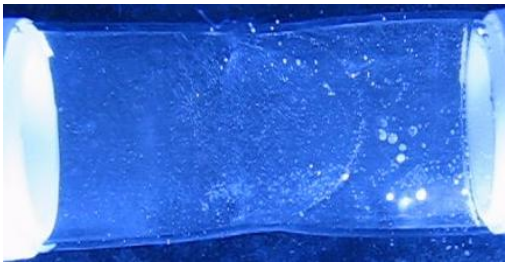

φ6 (84º)

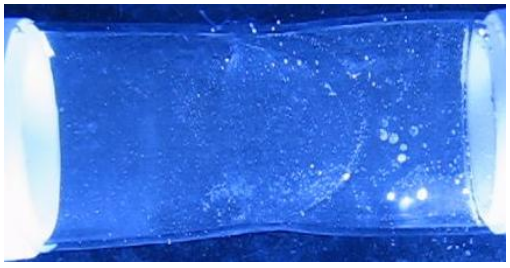

φ7 (98º)

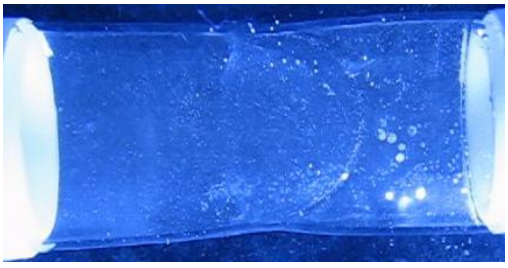

φ8 (112º)

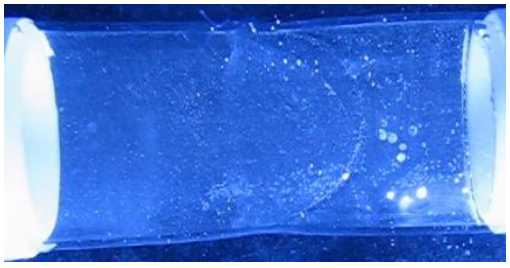

φ9 (126º)

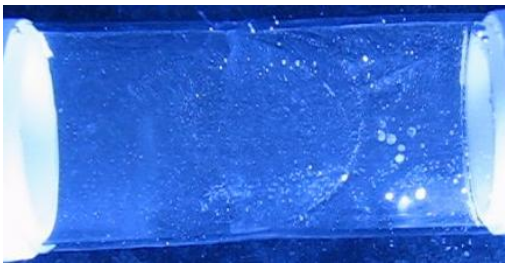

φ10 (140º)

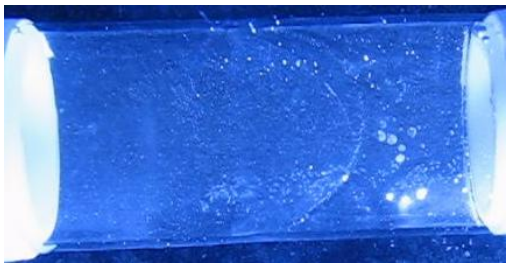

φ11 (154º)

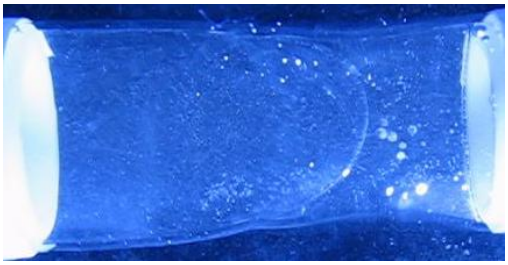

φ12 (168º)

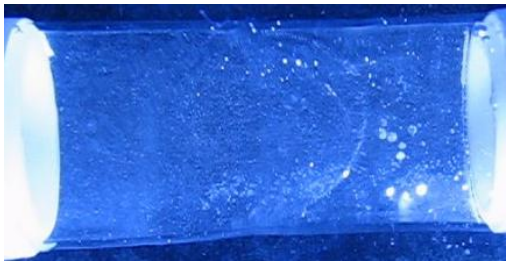

φ13 (182º)

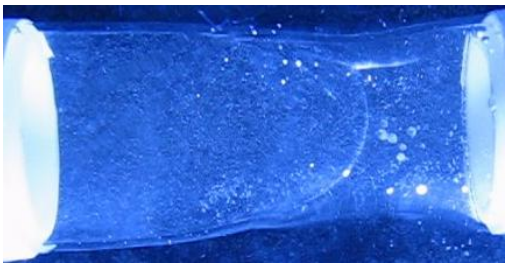

φ14 (196º)

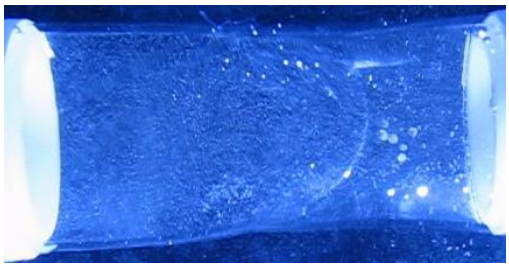

φ15 (210º)

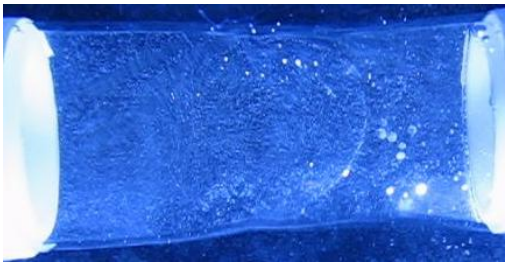

φ16 (224º)

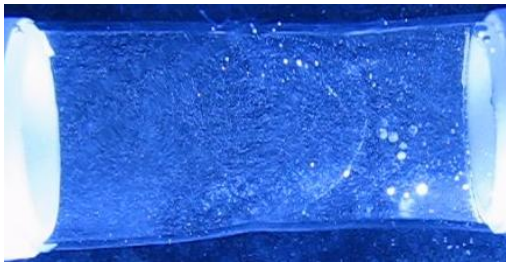

φ17 (238º)

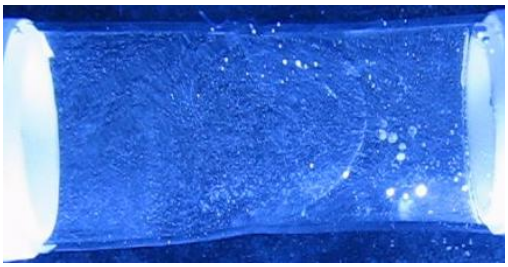

φ18 (252º)

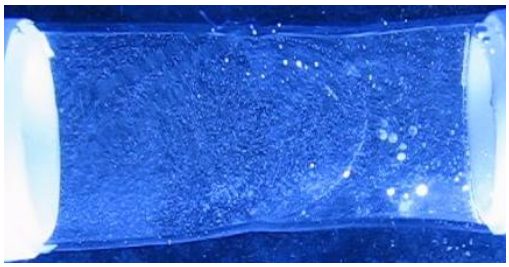

φ19 (266º)

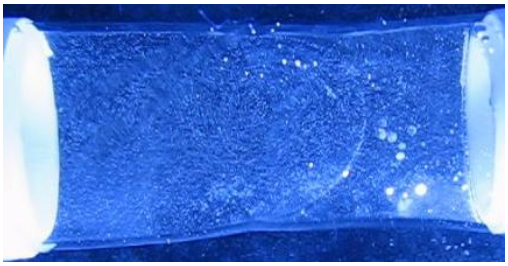

φ20 (280º)

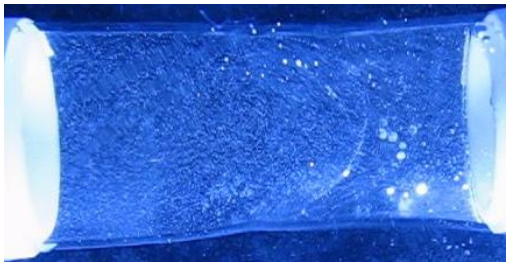

φ21 (294º)

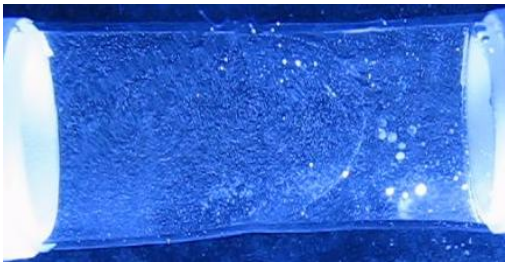

φ22 (308º)

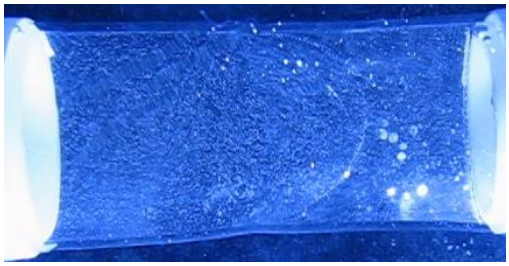

φ23 (322º)

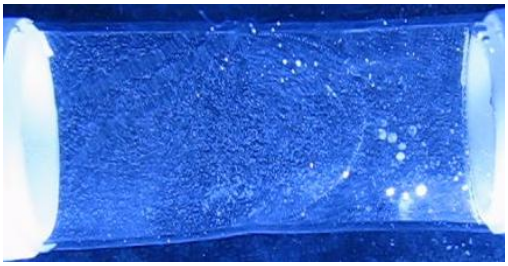

φ24 (336º)

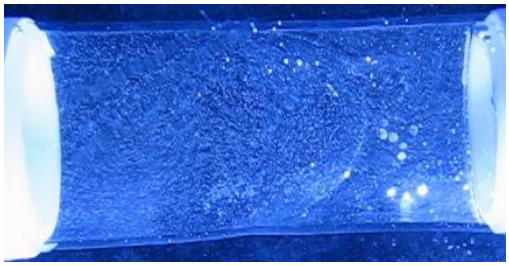

φ25 (350º)

Appendix F- 2. Transparent silicone valve flow phases showing the commissure to commissure plane. The flow is from left to right. Average flow rate of 4.2 L/min at a pulsing frequency of 1.17 Hz.

φ0 (0º)

φ1 (14º)

φ2 (28º)

φ3 (42º)

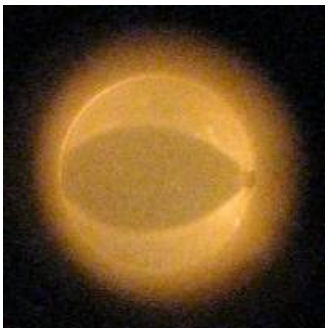

φ4 (56º)

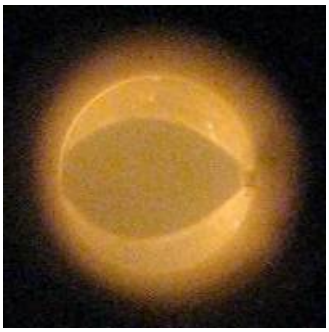

φ5 (70º)

φ6 (84º)

φ7 (98º)

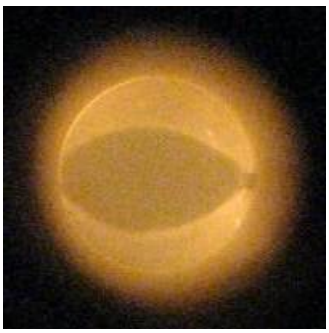

φ8 (112º)

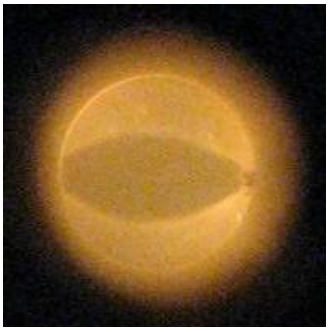

φ9 (126º)

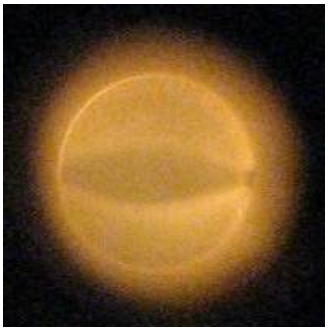

φ10 (140º)

φ11 (154º)

φ12 (168º)

φ13 (182º)

φ14 (196º)

φ15 (210º)

φ16 (224º)

φ17 (238º)

φ18 (252º)

φ19 (266º)

φ20 (280º)

φ21 (294º)

φ22 (308º)

φ23 (322º)

φ24 (336º)

φ25 (350º)

Appendix F- 3ppendix F- 4. Transparent silicone valve flow phases showing the end on view as seen from the downstream (aortic) location. Average flow rate of 4.2 L/min at a pulsing frequency of 1.17 Hz.